Technical University of Denmark

Spin structures in antiferromagnetic nanoparticles

Brok, Erik; Frandsen, Cathrine; Hansen, Thomas Willum; Lefmann, Kim

Publication date:
2014

Document Version
Publisher's PDF, also known as Version of record

Link back to DTU Orbit

DTU Library
Technical Information Center of Denmark

Technical University of Denmark

Erik Brok
Spin structures in antiferromagnetic nanoparticles

PhD thesis
Technical University of Denmark
September 2013

Supervisors

Cathrine Frandsen, DTU-Physics
Thomas Willum Hansen, DTU-Cen
Kim Lefmann, Niels Bohr Institute, University of Copenhagen

DTU Physics
Department of Physics

DTU Cen
Center for Electron Nanoscopy

Preface

This thesis is submitted in partial fulfillment of the requirements for obtaining the PhD degree in Physics at the Technical University of Denmark. Most of the work presented in the thesis have been performed at Department of Physics (DTU-Physics) and Center for Electron Nanoscopy (DTU-Cen), both at the Technical University of Denmark, Lyngby. Part of the work has been performed during my two stays of two months in total at the Department of Earth Sciences, University of Cambridge, UK in collaboration with Dr Richard J. Harrison. Several experiments have been performed at the international neutron scattering facilities Institut Laue-Langevin (ILL) in Grenoble, France, Paul Scherrer Institut (PSI), Villigen, Switzerland and ISIS, Oxfordshire, United Kingdom. SQUID-magnetisation measurements have been performed at Department of Chemistry, University of Copenhagen. The work have been performed under the supervision of my main supervisor Associate Professor Cathrine Frandsen (DTU-Physics) and co-supervisors Senior Scientist Thomas Willum Hansen (DTU-Cen) and Associate Professor Kim Lefmann from the Niels Bohr Institute, University of Copenhagen.

The thesis falls in two parts. Part I contains 7 chapters and has my investigations of spin structures in nanoparticles of antiferromagnetic materials and related systems as its main subject. Part II consists of Papers [1–7], which are the scientific papers (published as well as in preparation) that are produced from my thesis work with me as author or co-author. Much of the work covered in Part II will also be covered in Part I but in Part I the focus will be my work on spin structures in antiferromagnetic nanoparticles.

Acknowledgments

First and foremost I wish to express my gratitude to my main supervisor Cathrine Frandsen for dedicated and enthusiastic supervision and for always taking the time to discuss scientific problems pertaining to my PhD work. Her personal involvement in all aspects of my PhD project have been very motivating and helpful. I also wish to thank my co-supervisors Thomas Willum Hansen and Kim Lefmann for sharing their great knowledges of electron microscopy and neutron scattering.

A special thanks goes to Richard J. Harrison who accepted me in his office during my stays in Cambridge which because of him were both enjoyable and productive. I also owe him thanks for expanding my poor knowledge of rock magnetism and for getting me started with Rietveld refinement of magnetic structures, and for good company at beam times at ISIS, PSI and ILL.

From DTU Physics I would like to thank Steen Mørup for sharing his vast knowledge of Mössbauer spectroscopy and nanoparticle magnetism and for the great amount of work he performed during the genesis of theoretical and experimental articles of which I am one of the authors. I thank Bente Lebech for helping me understand crystallography and Rietveld refinement, and in particular for helping me calculate the magnetic structure factor of NiO. Helge K. Rasmussen have helped me on countless occasions, providing indispensable technical assistance with Mössbauer spectroscopy, X-ray diffraction and sample preparation, and for that I am grateful. Thanks are also in order to Jacob Larsen and Jelena Jordanovic for making DTU Physics an enjoyable place to be and for many interesting discussions about science, life and all the rest.

Erik Brok, September 2013

Summary in English

Spin structures in antiferromagnetic nanoparticles

In this thesis magnetic structures of antiferromagnetic nanoparticles are studied as a function of particle size and aggregation. In nanoparticles the magnetic structure can be different from that of the corresponding bulk system due to the following reasons: a) a significant surface contribution to the magnetic anisotropy, b) the low symmetry environment of surface atoms or defects in the interior of particles leading to non collinear spin structures, and c) exchange interactions between neighbouring particles. Determining the spin structures of antiferromagnetic particles is difficult, however a detailed knowledge of it can be important for applications of antiferromagnetic nanoparticles for example combined with ferromagnetic nanoparticles in nanocomposite devices. In this thesis the magnetic structure, in particular the orientation of the spins in the antiferromagnetic sublattices, is investigated in systems of magnetic nanoparticles using a variety of experimental techniques.

The spin structure in systems with spin canting, due to magnetic atoms in low symmetry surroundings, is studied in a theoretical model that is able to quantitatively explain observations of anomalous temperature dependence of the magnetisation in certain nanoparticle systems, as welll bulk systems with spin canting due to defects. In accordance with this model magnetisation measurements on goethtie (α-FeOOH) nanoparticles are presented, showing a low temperature increase in the magnetisation.

The spin orientation in plate-shaped NiO nanoparticles with thicknesses down to 2.0 nm is investigated with the XYZ-neutron polarisation analysis technique. This provides an effective way of separating the different scattering contributions (magnetic, nuclear and spin incoherent), and thus significantly improve the earlier experimental data from unpolarised neutron diffraction. The spin orientation is found to be close to the particle plane, which is the (111) plane of the FCC structure of NiO for particles with thickness ranging from 2.2 nm to bulk ($\geq$ 200 nm) particles. In the smallest particles, with a thickness of 2.0 nm, we find a reorientation of the spin to point 30° out of the plane.

Recovery of the spin reorientation, known as the Morin transition, in hematite (α-Fe$_2$O$_3$) nanoparticles was studied as function of particle growth and aggregation. Growth and aggregation of hematite particles with an initial size of $\approx$ 9 nmb in aqueous suspension was controlled by a hydrothermal treatment and by changing the ionic strenght of the suspension. Interestingly addition of NaCl to the suspension resulted in the particles aggregating in long linear chains, with neighbouring particles aligned along a common [001] axis of the hexagonal structure. The magnetic structure was investigated with Mössbauer spectroscopy, revealing a partial recovery of the Morin transition in samples with significant particle growth. The aggregation in crystallographically aligned linear chains did not introduce a Morin transition, but the addition of NaCl had the effect of partially suppressing superparamagnetic relaxation.

The spin orientation in the mineral hemo-ilmenite (α-Fe$_2$O$_3$-FeTiO$_3$) consisting of nanoscale lamellar intergorwths of hematite and ilmenite was studied with uniaxial neutron polarisation analysis to determine if the unusually high magnetisation in this antiferromagnetic-paramagnetic mineral can be ascribed to uncompensated spins in contact layers between the lamellae. From the response of the hematite spins to an applied magnetic field we confirm that uncompensated spins as well as canted spins are important in the system. This supports the hypothesis of lamellar magnetism, proposed to explain the unusual magnetic properties of the mineral.

In summary the thesis have demonstrated methods for investigation of spin structures in magnetic nanoparticles. In particular, the classical model of the temperature dependence of canted spin structures sucessfully explains many experimental observations of anomalous temperature dependence in nanoparticle and bulk systems. Morover, XYZ neutron polarisation analysis have been demonstrated to be an effective way of investigating the magnetic properties of antiferromagnetic nanoparticles, significantly improving the unpolarised neutron powder diffraction data usually obtained in investigations of magnetic nanoparticles.

Summary in Danish

Spinstrukturer i antiferromagnetiske nanopartikler

I denne afhandling studeres magnetiske strukturer af antiferromagnetiske nanopartikler som funktion af partikelstørrelse og aggregering. I nanopartikler kan den magnetiske struktur være anderledes end i det tilsvarende makroskopiske materiale af følgende årsager: a) et betydelig overflade-bidrag til den magnetiske anisotropi, b) den lave symmetri i omgivelserne for atomer på overfladen, eller deffekter i det indre af partiklerne, kan føre til ikke-collineære spinstrukturer, og c) exchange-vekselvirkninger mellem nabopartikler. Bestemmelse af spinstrukturer for antiferromagnetiske partikler er svært, men detaljeret kendskab til spinstrukturen kan være vigtig for anvendelser af antiferromagnetiske nanopartikler, for eksempel kombineret med ferromagnetiske nanopartikler i nano-komposit systemer. I denne afhandling undersøges den magnetiske struktur, især spinorienteringen i de antiferromagnetise undergitre, i systemer af magnetiske nanopartikler med en bred vifte af eksperimentelle teknikker.

Spin strukturer med spin-canting i systemer med atomer i omgivelser med lav symmetri er undersøgt i en teoretisk model, der kvalitativt kan forklare observationer af afvigende temperaturafhængighed af magnetiseringen i visse nanopartikelsystemer, såvel som i bulk systemer med spin-canting på grund af defekter. I overensstemmelse med denne model præsenteres magnetiseringsmålinger på goethit (α-FeOOH) nanopartikler, som viser en stigning i magnetiseringen ved lave temperaturer.

Spin orientering i plade-formede NiO nanopartikler med tykkelser ned til 2,0 nm undersøges med XYZ-neutron polarisationsanalyse. Dette giver en effektiv måde at adskille de forskellige bidrag til spredningen (magnetisk, nuklear og spin inkohærent), og således væsentligt forbedre tidligere eksperimentelle data fra upolariseret neutrondiffraktion . For partikler med tykkelse fra 2,2 nm til bulk (≥ 200nm) findes spinorienteringen til at være tæt på partiklerners planer, som er (111) planet i FCC strukturen af NiO. I de mindste partikler, med en tykkelse på 2,0 nm, finder vi en reorientering af spinet, så det peger 30° ud af planet.

En spinreorientering, kendt som Morinovergangen, blev undersøgt i hæmatit (α-Fe$_2$O$_3$) nanopartikler som funktion af partikel vækst og aggregering. Vækst og aggregering af hæmatitpartikler, med en oprindelig størrelse på ≈ 9 nm, i vandig suspension blev kontrolleret med en hydrotermisk behandling og ved at ændre ionkoncentrationen i suspensionen . Tilsætning af NaCl til suspensionen resulterede i aggregering af partiklerne i lange lineære kæder, med tilstødende partikler epitaksielt orienteret med en fælles hexagonal [001] akse. Den magnetiske struktur blev undersøgt med Mössbauer spektroskopi, som viser en delvis Morinovergang i prøver med betydelig partikelvækst. Aggregeringen i lange lineære kæder af partikler med fælles epitaksiel orienterion fører ikke til Morinovergang, men tilsætning af NaCl undertrykte delvist den superparamagnetiske relaxation.

Spin orientering i mineralet hemo-ilmenit (α-Fe$_2$O$_3$-FeTiO$_3$) bestående af nanoskalalamellare strukturer af hæmatit og ilmenit blev undersøgt med unaxial neutron polarisationsanalyse, for at bestemme om den usædvanligt høje magnetisering i dette antiferromagnetiskeparamagnetiske mineral kan tilskrives ukompenserede spins i kontaktlagene mellem lamellerne. Fra hæmatitspinenes rotation i et påtrykt magnetifelt bekræfeter vi at ukompenserede spins, men også cantede spins, er vigtige i systemet. Dette understøtter hypotesen om lamellar magnetisme, som er foreslået som forklaring på de usædvanlige magnetiske egenskaber af mineralet.

Sammenfattende har afhandlingen vist metoder til udersøgelse af spin strukturer i magnetiske nanopartikler. Især forklarer den klassiske model for temperaturafhængighed af cantede spinstrukturer mange eksperimentelle observationer af afvigende temperaturafhængighed af magnetiseringen i nanopartikel og bulk -systemer. Envidere har XYZ neutron polarisationsanalyse vist sig at være en effektiv måde at undersøge de magnetiske egenskaber af antiferromagnetiske nanopartikler og er en markant forbedring af upolariserede neutron pulverdiffraktionsdata som oftest bruges i undersøgelser af magnetiske nanopartikler.

Contents

Part I

Introduction

Magnetic nanoparticles (NPs) have received considerable attention in the last few decades because of their remarkable magnetic properties that differ considerably from those of the corresponding bulk materials. Understanding how the finite size affects the magnetic properties of magnetic NPs is an interesting challenge in basic science, and furthermore magnetic NPs are important for applications in fields such as magnetic data storage, biomedical imaging, and medicine. The materials under study in this thesis are NPs of antiferromagnetic (AFM) materials. AFM materials do not possess a net magnetisation and they are therefore not magnetic in the everyday sense of the word. - You cannot hang an AFM on your refrigerator. However, despite the lack of a net magnetisation there are important applications of AFM materials, in which the AFM material is coupled to other magnetic materials by exchange interaction, and it is likely that also AFM NPs can be utilised in such devices. In ferromagnetic (FM) or ferrimagnetic NPs the large dipole moment often means that the dipole interaction dominates over other interactions making these interactions difficult or impossible to investigate. Because AFM NPs do not possess a large dipole moment interactions that would otherwise be dominated by the dipole interaction can be significant and therefore the basic physics of magnetic systems of finite size are sometimes better studied using AFM than FM NPs. In particular AFM NPs can be ideal for studying exchange interactions between magnetic NPs. My field of study has been, in particular, the effect of the finite size on the magnetic structure of very small AFM particles.

In this introductory chapter I will introduce some important concepts about magnetic NPs relevant to my thesis work, give a few examples of how magnetic NPs are used in industrial applications today, and how one could envisage exciting future applications. I will also touch upon what the obstacles are for realising the most interesting applications as well as possible ways to overcome these problems. The role of AFM NPs will be given particular attention.

1.0.1 Magnetic order

Before introducing magnetic NPs we must establish what we mean when we talk about magnetic materials. The origin of magnetism in materials is the spin (and orbital) angular momentum of the atomic electrons and the magnetic properties of materials are to a large degree determined by the interactions between these spins. The important interaction is the exchange interaction which is generally described by the Heisenberg Hamiltonian:

$$\mathcal{H} = -\sum_{ij} J_{ij} \mathbf{S}_i \mathbf{S}_j, \tag{1.1}$$

where the sum is over all atomic spins in the system and J_{ij} is the so-called exchange constant for atomic spins $\mathbf{S}_i$ and $\mathbf{S}_j$. The exchange interaction has a very short range and therefore the sum can often be limited to a sum over nearest neighbours. When J_{ij} is positive, parallel spin alignment is favoured and when J_{ij} is negative, antiparallel alignment is favoured. At high temperatures the exchange energy (1.1) is smaller than the thermal energy and the spins will

be randomly aligned. This is known as a paramagnetic state. When the temperature is lower than a certain critical temperature the thermal energy is smaller than the exchange energy and it becomes favourable for the system to order magnetically. Depending on the sign of J_{ij} the order can be with parallel or antiparallel neighbouring spins. If the spins are parallel the order is said to be FM and the critical temperature is called the Curie temperature or T_C. FM order gives rise to a large net magnetic moment and this is what is used in everyday magnets. When the magnetic order is with neighbouring spins antiparallel the material is said to be AFM and the critical temperature is called the Néel temperature or T_N.

An AFM structure is commonly described in terms of two sublattices (A and B) with parallel alignment between spins in the same sublattice and antiparallel alignment of spins on different sublattices. Figure 1.1 shows a sketch of a simple AFM structure with spins in one sublattice (A) pointing to the right (blue arrows) and spins on the other sublattice (B) pointing to the left (red arrows). With the same number of spins (of the same size) on sublattice A and B the net magnetisation is $\mathbf{M}_A + \mathbf{M}_B = 0$.

Antiferromagnetism is usually caused by so-called superexchange (or indirect exchange) interactions between neighbouring magnetic atoms mediated by a non-magnetic atom between the two magnetic atoms. This typically happens in ionic crystals of metal oxides where the superexchange between the metal atoms is mediated via the p-orbitals of the intervening oxygen atoms. If the magnetisation on the two sublattices are not of the same size because they are occupied by spins of different sizes or because the sublattices are different the magnetisation of the two sublattices do not cancel each other out, and the system will have a net magnetisation. This type of magnetic order is called ferrimagnetic. More complicated magnetic structures where the arrangement of spins cannot be explained by a simple two-sublattice model also exist. In some cases more than two sublattices are needed to describe the structure and in other systems, e.g. with helical order, the idea of sublattices does not make much sense.
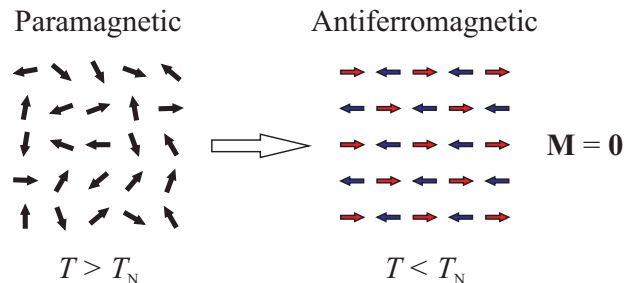
Figure 1.1: Antiferromagnetic ordering: At high temperatures the system is in a paramagnetic state. At $T = T_N$ the system orders in an antiferromagnetic structure. The total magnetic moment on the two antiferromagnetic sublattices (red and blue respectively) are equal in size and in opposite directions leading to zero total magnetisation.

An antiferromagnetic structure like that in Figure 1.1 consists of planes of parallel spins and perpendicular to the planes there is a periodic modulation of planes with spins up and down. This order can be described in terms of an AFM modulation vector, which in Figure 1.1 would be along the diagonal of the square 2D lattice of atoms. While the exchange interactions determine the relative alignment of spins on the two sublattices the absolute spin direction (in absence of an applied magnetic field) is determined by the magnetic anisotropy. The magnetic anisotropy, which will be discussed below, covers several mechanisms that tend to favour spin orientation in certain directions.

1.1 Magnetic nanoparticles

1.1.1 A single magnetic domain

When a bulk magnetic material is cooled through the ordering temperature the material becomes magnetically ordered, but the ordering happens simultaneously at many sites, creating magnetic domains with different (sublattice) magnetisation directions. The magnetic domains are separated by domain walls where the spin is rotated from the (sublattice) magnetisation direction of one domain to that of its neighbour. The spins in the domain walls are not aligned in the directions of least energy and having domain walls thus costs energy. Because of the energy cost of the domain walls there is a lower limit to the size of magnetic domains, and when particles are smaller than this size they consist of one single domain. The critical size for single-domain particles depends on the material and is generally in the range 5-1000 nm [8]. Magnetic NPs are particles of magnetic materials with dimensions in the nanometer range (1 - 100 nm) and for most materials particles in the nano regime are single-domain. Or to put it oppositely, the single-domain feature is almost a defining characteristic of magnetic NPs.

1.1.2 Magnetic anisotropy in nanoparticles

In bulk magnetic materials as well as magnetic nanoparticles the (sublattice) magnetisation always have certain preferred orientations. The orientation of the (sublattice) magnetisation along one of these so-called easy axes minimise the energy, whereas orientation along corresponding hard axes gives an energy penalty. The magnetic anisotropy is very important for the magnetic properties of a material. A large magnetic anisotropy is what makes the magnetisation of permanent magnets stable, whereas so-called soft magnetic materials have a low coercivity due to a low magnetic anisotropy, making them easy to magnetise and therefore useful for example in electromagnets and magnetic sensors. If there is only one easy axis the anisotropy is said to be uniaxial and the magnetic anisotropy energy of a NP of volume V is often given by

$$E(\theta) = KV \sin^2(\theta), \tag{1.2}$$

where θ is the angle between the (sublattice) magnetisation and the easy axis, and K is the anisotropy constant. There can be several contributions to the magnetic anisotropy, the most important often being the magnetocrystalline anisotropy. The magnetocrystalline anisotropy arises because of the spin-orbit interaction, which links the spin to the electronic orbital, which is strongly dependent on the symmetry of the crystal structure. This means that the easy directions due to the magnetocrystalline anisotropy are determined by the crystal structure, with the magnetisation often preferentially oriented along high symmetry axes of the structure. In NPs a large fraction of the atoms are located at the surface of the particles and because of the reduced symmetry on the surface this can lead to a significant contribution to the anisotropy, known as surface anisotropy. For example, the anisotropy constant K in hematite NPs is found to increase with decreasing particle size because of the surface anisotropy [9]. The surface anisotropy can be important for both the magnetic structure and dynamics in NPs and will in general depend not only on particle size, but also on the shape of the particles. So-called shape anisotropy, in which a certain magnetisation direction with respect to the shape of the particle is preferred because it minimises the magnetostatic energy, can be important in FM or ferrimagnetic particles .

1.1.3 Dynamics of magnetic nanoparticles

Because the magnetic NPs are single-domain the (sublattice) magnetisation of a particle can behave as one single macrospin with spin $S = NS_i$, where N is the number of magnetic atoms in the particle and S_i is the atomic spin. This gives rise to excitations that are not seen in bulk materials and are extremely important to be aware of when contemplating possible

applications of the particles. When the particle size becomes small enough for the thermal energy ($k_\mathrm{B}T$) to be comparable to the anisotropy energy (1.2) fluctuations of the (sublattice) magnetisation can overcome the energy barrier of KV between the two energy minima at $\theta = 0°$ and $\theta = 180°$. This leads to rapid oscillations of the (sublattice) magnetisation between the two easy directions, known as superparamagnetic (SPM) relaxation. The SPM relaxation time τ is given approximately by the Néel-Brown law [10]:

$$\tau = \tau_0 \exp\left(\frac{KV}{k_\mathrm{B}T}\right), \tag{1.3}$$

where τ_0 is typically on the order $10^{-13} - 10^{-9}$ s. The relaxation time thus depends heavily on temperature and even more so on particle diameter. Consider, for example, a 10 nm particle with an anisotropy constant of $10^5 \mathrm{J/m^3}$. If $\tau_0 = 10^{-11}$ s the relaxation time at room temperature will be about 10^{-6} s, whereas a 15 nm particle with the same anisotropy will have a relaxation time of approximately 10^7 s or roughly one year. Obviously superparamagnetic relaxation is detrimental to applications where a stable magnetisation is needed and for such applications SPM relaxation sets a limit to how small particles can be used. In experimental investigations of particles undergoing SPM relaxation the results depends crucially on the timescale of the SPM oscillations τ relative to the measurement time τ_M. If the SPM relaxation is much faster than the experimental time scale the experiment will detect the average magnetisation, i.e. zero if no magnetic field is applied. If on the other hand the relaxation time is long compared to the time scale of the experiment a static magnetisation will be measured. One often defines the so-called SPM blocking temperature T_B as the temperature where $\tau = \tau_\mathrm{M}$. The time scales of different experimental techniques vary over many orders of magnitude from the order of picoseconds for neutron scattering to nanoseconds for Mössbauer spectroscopy and around 100 seconds for DC magnetisation measurements.

At temperatures below T_B, where SPM relaxation is not important, the dynamics of nanoparticles are still very different from what is observed in bulk materials. In bulk materials the magnetic excitations known as spin waves can occur with arbitrarily long wavelengths and arbitrarily low energies and the spin wave dispersion is therefore continuous. In NPs the wave length of the spin waves are limited by the particle size. In a cubic particle of size d the allowed excitation wave vectors are $q = n\pi/d, n = 0, 1, 2, 3, \dots$. The energy gap between the $q = 0$ so-called uniform mode where all the spins are parallel, and the modes with $q > 0$ can be significant and the uniform mode becomes predominant. These precession modes, where the (sublattice) magnetisation precess as one single macrospin around the equilibrium direction defined by the magnetic anisotropy are termed collective magnetic excitations [11–13] and are typically the predominant excitation in NPs below T_B. The quantization of the spin wave spectrum leads to a linearly decreasing temperature dependence of the magnetisation of both FM and AFM NPs which is different from the $M \propto T^{-3/2}$ and $M \propto T^{-2}$ temperature dependence of the magnetisation in bulk FM and AFM materials [8].

1.1.4 Magnetic structures in nanoparticles

The dynamics are not the only difference between magnetic NPs and bulk magnetic materials. In NPs the magnetic structure, and in particular the spin orientation can also be affected by the finite size of the system.

The low symmetry surroundings of atoms at the surface of particles result in a reduced exchange field for the surface atoms, which in particles of AFM materials can lead to degenerate or nearly degenerate configurations (magnetic frustration) and non-collinear spin structures (spin canting) [15–17]. Similar structures can result from defects, cation vacancies or substituted diamagnetic ions in the interior of ferrimagnetic NPs, or bulk material [18]. The reduced exchange field in NPs can also lead to a lowered magnetic ordering temperature than in bulk materials [19].

6
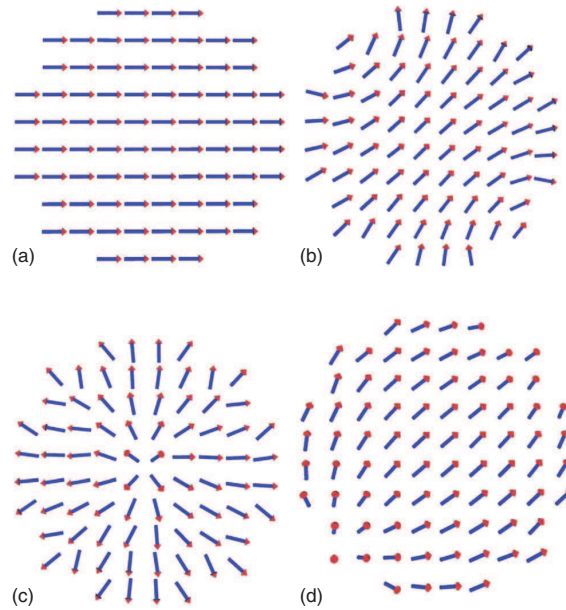
Figure 1.2: Monte Carlo simulations of spin configurations in a ferromagnetic nanoparticle with different values of the surface anisotropy. (a) No surface anisotropy. (b) A surface anisotropy smaller than the exchange energy. (c) A surface anisotropy larger than the exchange energy. (d) A negative surface anisotropy. Figure from [14].

The large surface contribution to the anisotropy in NPs can lead to changes in the magnetic structure. For example the simulations of magnetic structures of NPs with FM interactions between the spins and different anisotropies shown in Figure 1.2 shows quite different outcomes [14]. The absence of the so-called Morin transition in NPs of AFM hematite (α-Fe$_2$O$_3$) is a material where the magnetic structure in NPs is different from that in the bulk material. At the Morin transition temperature of approximately 263 K in bulk hematite [20, 21] the spin orientation changes with 90°. This transition is absent in hematite NPs smaller than about 20 nm [22] and the spin orientation in hematite NPs is thus rotated 90° with respect to the bulk structure at temperatures below 263 K.

NPs are often not isolated, but in contact with other particles, for example in a powder. In these cases interactions between the particles can be very important for the dynamics of the particles, and also for the spin structure. In FM or ferrimagnetic NPs the dipole interactions are typically dominant but in AFM NPs typically only the inter-particle exchange interactions can come into play. In interacting AFM NPs the SPM relaxation have been seen to be suppressed by the inter-particle exchange interactions [11, 23–27], and the inter-particle interactions can also change the sublattice spin orientation as seen in powder samples of interacting hematite NPs [28].

1.1.5 Industrial applications of magnetic nanoparticles

Magnetic NPs, and in particular FM or ferrimagnetic particles, have a number of present applications. Current applications of magnetic NPs include fields such as biomedical imaging [29, 30] and also experimental treatment of diseases. An example of the latter is an experimental cancer therapy called magnetic hyperthermia [31] where magnetic NPs functionalised to bind specifically to cancer cells are injected into a tumor and subjected to an alternating magnetic field. Thereby the particles produce locally a great amount of heat that may kill the cells in the tumor ideally with no severe side effects compared to other treatments like chemotherapy.

For the last few decades single-domain NPs have been used as bits in magnetic data storage with bit dimensions in commercially available hard drives reaching a size of about 30 nm × 70 nm in 2009 [8]. If the bits of information could be downsized to the scale of a few nanometers the information density in data storage could be greatly increased. There are, however, great challenges to overcome before revolutionisingly small NP based bits can be achieved. One such challenge is that posed by SPM relaxation. One method to overcome the SPM problem could be to increase the magnetic anisotropy of the used magnetic material. However, this tends to affect other important properties and make the material less useful. Another idea is to use the interaction between the FM particles and another magnetic material, e.g. AFM, to stabilise the magnetisation. For discussions of the use of magnetic NPs in magnetic data storage see e.g. [30, 32, 33].

Another possible use of magnetic NPs is in very strong magnets that could be produced without the need for large amounts of rare earth metals. In our modern society we use a huge amount of powerful magnets in numerous applications like electro-motors, wind mill turbines, mobile phones, and many more. The powerful magnets of today are made with rare earth materials like neodymium or samarium that is becoming very expensive because it is only mined very few places on Earth. It has been proposed that very strong and stable magnets can be produced from so-called nanocomposite materials consisting of NPs of one material, e.g. CoFe, with a high saturation magnetisation exchange coupled with NPs of a magnetically 'hard' material, e.g. SmCo. In this way one material (the magnetically hard one) would stabilise the other (the one with high magnetisation) and it could be possible to obtain a functionality comparable to that of the most powerful magnets today but with a reduced use of rare earth metals [34–37].

1.1.6 Antiferromagnetic nanoparticles

Most applications of magnetic NPs, including the ones described above, make use of the magnetic moment carried by FM or ferrimagnetic NPs but many future applications also rely on the magnetic coupling between NPs. AFM NPs have many of their magnetic properties in common with their FM counterparts, but in the ideal case of an AFM NP, where all the magnetic moments are pairwise antiparallel, the particle does not possess a net magnetic moment. The usefulness of AFM NPs in applications is therefore less obvious. AFM materials exchange coupled to FM or ferrimagnetic materials are, however, widely used in for example magnetic sensors, spin-valve read heads in hard drives, and could conceivably be used in other components in the emerging field of spin-tronics [38, 39]. SPM relaxation of FM Co NPs have been shown to be suppressed when the Co NPs are embedded in an AFM matrix [40], and something similar can be achieved by mixing AFM and FM (ferrimagnetic) NPs [41]. One could also think of a magnetic nanocomposite material like described in the last paragraph of Section 1.1.5, but with the magnetically hard FM material replaced by AFM NPs. Of course it would not be possible to attain as high a magnetisation as with mixtures of two materials carrying significant net magnetisations, but it might be possible to produce a very stable magnetisation of a useful size at a very low price.

Magnetic moment of nanoparticles of antiferromagnetic materials

In bulk AFM materials the magnetic moments on the two sublattices are to a good approximation equal and opposite, giving no net magnetisation. This is in general not the case for NPs of AFM materials. NPs of AFM materials can have a non-vanishing magnetisation originating from uncompensated spins at the particle surfaces or distributed over the volume of the particles. The term uncompensated spins simply refers to a system where the number of spins on one of the AFM sublattices is larger than on the other so that the cancellation of the two sublattices is not perfect leading to a finite magnetisation of the particle $\mathbf{M} = \mathbf{M}_A + \mathbf{M}_B \neq 0$. This phenomenon, which was studied by Louis Néel in 1961 [42], is stochastic in nature, and is a

consequence of the finite size of N, the number of spins in a NP. He considered three cases, where the first is a situation where vacancies are randomly distributed on each sublattice. This would results in a magnetic moment proportional to $N^{1/2}$. Another scenario is that the uncompensated moment comes about in particles where there are an uneven number of magnetic layers, or in other words, when there are one more layer with one sublattice orientation than with the other sublattice orientation. This gives an uncompensated moment proportional to $N^{2/3}$. Thirdly, one imagine that the interior of the particle is a perfect antiferromagnet, while the surface have randomly distributed vacancies, leading to an uncompensated moment proportional to $N^{1/3}$. Other types of departure from the perfect AFM structure such as spin canting can also lead to a net magnetisation of NPs of AFM materials because the spins are rotated away from the antiparallel alignment. Moreover, when the AFM sublattices perform uniform precessions around the equilibrium positions they in general have different precession angles and are thus not perfectly parallel. This leads to a net magnetisation known as thermoinduced magnetisation which has the special property that it increases with temperature [43]. Nanoparticles of AFM materials thus always possess some magnetic moment and they are thus not strictly speaking AFM. We will however continue to refer to AFM NPs even though the term NPs of AFM materials would be more correct.

1.2   About this thesis

This thesis work concerns theoretical and experimental studies of the magnetic properties and in particular magnetic structure of individual as well as assembled magnetic nanoparticles and intergrown nanostructures. Experiments have been performed on systems of α-FeOOH (goethite), NiO, α-Fe$_2$O$_3$ (hematite), FeTiO$_3$ (ilmenite) and inter-mixtures of the latter two with a variety of different techniques suitable for the study of magnetic NPs. The techniques include X-ray powder diffraction (XRD), dynamic light scattering (DLS), Mössbauer spectroscopy, neutron single crystal diffraction, neutron powder diffraction (NPD), uniaxial neutron polarisation analysis, XYZ-neutron polarisation analysis, inelastic neutron scattering (INS), transmission electron microscopy (TEM), and DC and AC magnetisation measurements. The experimental techniques will be presented in **Chapter 2**. The following investigations constitute the work of my PhD thesis.

- **Canted spin structures and goethite nanoparticles** (**Chapter 3, Papers [1–3]**)

In order to study the effect of relaxation of canted spin structures on the magnetisation of NPs and of bulk systems with localised spin canting a classical theoretical model of a two-dimensional canted spin structure was derived. The model which is presented in the first part of **Chapter 3** and in **Papers [1,2]** shows the temperature dependence of the magnetisation of the two-dimensional system which is a model system for more realistic spin structures.

The theoretical model is exemplified by magnetisation measurements on 5.7 nm goethite particles presented in the second part of **Chapter 3** and in **Paper [3]**. The particles were further characterised by XRD, TEM, INS and Mössbauer spectroscopy. The investigations of the dynamics with Mössbauer spectroscopy and INS are presented in **Paper [3]**.

- **Spin orientation in NiO nanoparticles as function of particle size**(**Chapter 4, Papers [4]**)

To study the effect of finite particle size on spin structures in AFM NPs the spin direction in plate-shaped NiO particles with thickness down to 2.0 nm was investigated. The particles were studied by XRD, TEM, NPD and XYZ-polarisation analysis, enabling us to determine the direction of AFM propagation and the AFM sublattice spin direction with respect to the particle shape as a function of particle size. These investigations are not in the form of a scientific paper but are presented in **Chapter 4**.

Our interest in the spin orientation in NiO nanoparticles were partly motivated by our investigation of spin reorientation in hematite NPs due to inter-particle exchange interactions in a hematite/NiO nanocomposite not discussed in Part I, but presented in **Paper [4]**.

- **Magnetic structure in hematite nanoparticles as function of particle aggregation and growth (Chapter 5)**

To study aggregation of AFM NPs and in particular their magnetic properties as function of particle aggregation and growth hematite particles with an initial size of ≈ 9 nm were prepared in different states of aggregation, and their magnetic properties studied with Mössbauer spectroscopy. The aggregation and growth of the particles in aqueous suspension were controlled by a hydrothermal treatment and was investigated with TEM, DLS and XRD. These investigations are not in the form of a scientific paper but are presented in **Chapter 5**.

- **Spin orientation in hematite-ilmenite(Chapter 6, Papers [5–7])**

To identify whether the source of the unusually high natural remanent magnetisation in natural samples of hematite-ilmenite can be ascribed to uncompensated spins in contact layers between nanoscale exsolution lamellae a natural single crystal of hematite-ilmenite was investigated with uniaxial polarisation analysis. This work is presented in **Chapter 6** and in **Paper [5]**.

In relation to this project cation disorder induced in ball-milled ilmenite was investigated by, XRD, NPD and Mössbauer spectroscopy (**Paper [6]**). Additionally spin orientation in bulk hematite and synthetic samples of solid solution hematite-ilmenite was investigated with NPD (**Paper [7]**). These last two projects are not about spin structures in nano sized systems and are not discussed in Part I.

Experimental methods

In this chapter I introduce the experimental techniques that I have applied to structurally characterise antiferromagnetic nanoparticles (X-ray diffraction, transmission electron microscopy, and dynamic light scattering) and to investigate their magnetic structure (neutron scattering, Mössbauer spectroscopy, and magnetisation measurements). Some of the techniques have been used for more elaborate investigations than others and the degree of detail devoted to the review of each technique here will reflect this.

2.1 Neutron scattering

Neutron scattering (NS) is a powerful method for probing the structure and dynamics of materials. In our context most importantly NS can be used to determine magnetic structure. NS has been one of the most important techniques for the investigations in this thesis, and I will therefore go into some detail with the description in this section. My review of the theory of NS, is inspired by text books such as [44, 45] and the notes from the Copenhagen University NS course [46]. Some important results of the theory of elastic NS will be presented, including the scattering cross sections for nuclear and magnetic neutron diffraction. In particular the technique of neutron powder diffraction (NPD), which has been employed in the studies of hematite/NiO nanocomposites, ball-milled ilmenite NPs, NiO NPs, and also in investigations of spin orientation in bulk hematite-ilmenite, will be given specific attention.

Inelastic NS, used in the investigations on goethite NPs will only be briefly mentioned, as the subject of this thesis is mainly magnetic structure. I will start, however, with the basic properties of the neutron.

2.1.1 Basic properties of the neutron

The neutron is a nuclear particle with zero charge, spin $s = 1/2$, and a mass $m_{\mathrm{n}} = 1.675 \cdot 10^{-27}$ kg similar to that of the proton ($m_{\mathrm{p}} = 1.673 \cdot 10^{-27}$ kg). The gyromagnetic ratio of the neutron is negative, meaning that the magnetic moment $\boldsymbol{\mu}_{\mathrm{n}}$ of the neutron is antiparallel to its spin:

$$\boldsymbol{\mu}_{\mathrm{n}} = \gamma_{\mathrm{n}} \mu_{\mathrm{N}} \boldsymbol{\sigma}, \tag{2.1}$$

where $\gamma_{\mathrm{n}} = -1.913$ is the gyromagnetic ratio for the neutron, $\mu_{\mathrm{N}} = e\hbar/m_p = 5.051 \cdot 10^{-27}\,\mathrm{J/T}$ is the nuclear magneton and $\boldsymbol{\sigma}$ is the Pauli spin operator for the neutron. For a neutron traveling with velocity $\mathbf{v}$ the associated (de-Broglie) wavelength, and wave vector are

$$\lambda = \frac{2\pi\hbar}{m_{\mathrm{n}}v} \quad , \quad \mathbf{k} = \frac{m_{\mathrm{n}}\mathbf{v}}{\hbar}, \tag{2.2}$$

and the kinetic energy is

$$E = \frac{\hbar^2 k^2}{2m_{\mathrm{n}}}. \tag{2.3}$$

Neutrons used for scattering experiments are produced, by nuclear reactors or spallation sources, in nuclear processes where the energies are in the MeV range. The neutrons energies are brought to the more useful meV range by passing the neutrons through a moderator where each neutron scatters many times and eventually reaches thermal equilibrium with the moderator material. When the neutrons are moderated to useful energies they are transported to the instruments in so-called neutron guides. A guide is simply a tube, typically of rectangular cross section, leading the neutrons from the moderator to the instrument. The inside of the guide is coated with a neutron reflecting material so that neutrons that hit the guide walls with a shallow angle are reflected and continue towards the experiment. The moderated neutrons have an energy (wavelength) distribution that is too wide to be useful for experiments, and therefore a so-called monochromator is used to select a desired wavelength for a particular experiment. As will be discussed later, the monochromator is often a Bragg reflecting crystal that is positioned to reflect the desired wavelength to the instrument.

2.1.2 Why use neutrons?

Neutron scattering is a versatile technique for probing the structure and dynamics of condensed matter and is used in a wide range of scientific disciplines, including fundamental physics, materials science, biology, Earth sciences, cultural heritage and more. Neutrons are, however, expensive to produce and the flux is very limited, especially compared to the high flux of modern X-ray sources. X-ray photons can do many of the same things as neutrons, and because X-rays are exceedingly cheaper than neutrons (price per useful photon/neutron), it is advisable to use X-rays instead of neutrons whenever possible. Fortunately, if you are a neutron scientist, there are a number of advantages of using neutrons that makes NS an indispensable tool for certain investigations. Below are listed four important advantages to NS. The list is largely stolen from [46].

1 **Suitable energy (wavelength) for probing excitations in solids.** Neutrons can be moderated to energies in the meV range similar to the energies of excitations in solids. The corresponding wavelengths are in the Ångström range, similar to the inter-atomic distances in solids. This means that neutrons are very well suited to investigate both the structure and the dynamics of solids.

2 **Scattering varies "randomly" between elements and even between isotopes of the same element.** This means that, in contrast with X-rays, light elements can be measured easily and isotopes can be used for labeling.

3 **The neutron interacts weakly.** The rather weak interaction of neutrons with most materials means that the neutron penetrates deeply into the material, probing the bulk, not just the surface, of materials. Perhaps even more importantly, it means that neutrons can penetrate through meters of air and centimeters of material (e.g. aluminium) making bulky sample environment possible.

4 **The neutron possesses a magnetic moment.** The neutron can therefore interact with magnetic fields in the sample and give information about magnetic structure and dynamics.

All of these properties of the neutron can be a great advantage and they have all been important for the studies in this thesis. Of course item 4 on the list is what makes it possible to investigate magnetic structures, which is a main topic here.

2.1.3 Neutron scattering theory

While the theory of NS was developed [47] early after the discovery of the neutron by James Chadwick in 1932 [48] experiments became practical with the advent of the first nuclear reactors.

Early experiments were performed under the secrecy of the Manhattan project and the first public articles appeared in the late 1940ies. The first neutron measurement of an AFM structure was published in 1949 [49] and in 1951 a study of a series of AFM materials was published in a classic paper by Shull, Strauser and Wollan [50]. Shull later received the Nobel prize for his efforts in developing the NS method for the study of the structure of materials [51]. The first magnetic structures investigated with NS were the antiferromagnets MnO, FeO, NiO, CoO and α-Fe$_2$O$_3$.

The scattering cross section

Any NS experiment starts with a beam of neutrons coming from a source and hitting a sample. The neutrons can then be scattered from the sample in any direction and will be detected if a detector is placed in the path of the scattered neutrons. The neutrons impinging on the sample are described by the incident flux Ψ, which is simply the number of neutrons impinging on the sample per second per unit area. The ability of a system to scatter neutrons is the so-called NS cross section:

$$\sigma = \frac{1}{\Psi} \cdot \text{number of neutrons scattered per second} . \tag{2.4}$$

Neutrons are scattered in all directions, but in any real experiment the detector, or detectors only cover a certain solid angle and the full cross section is thus never measured. Therefore we define the very important quantity known as the differential cross section:

$$\frac{d\sigma}{d\Omega} = \frac{1}{\Psi} \frac{\text{number of neutrons scattered per second into solid angle } d\Omega}{d\Omega} . \tag{2.5}$$

This quantity is what is measured in (absolutely calibrated) elastic scattering experiments. Because the interaction between the neutron and the scattering system is weak we can use the Born approximation and describe both the incident and the scattered neutron as plane waves:

$$\psi(\mathbf{r}) = \frac{1}{\sqrt{Y}} \exp(i\mathbf{k} \cdot \mathbf{r}), \tag{2.6}$$

where Y is a normalisation constant, $\mathbf{k}$ is the wave vector, and $\mathbf{r}$ is the position vector. When neutrons are scattered by a scattering system (sample) energy and momentum can be transfered between the neutron and the system, changing the state of both. A fundamental result from quantum mechanics known as Fermi's golden rule (see e.g. [52]) relates the rate of transitions from one state to another to the matrix element of the initial and final states with the interaction potential. This gives the differential scattering cross section for scattering neutrons from initial state $|\psi_i\rangle$ to final state $|\psi_f\rangle$:

$$\frac{d\sigma}{d\Omega} = Y^2 \frac{k_f}{k_i} \left(\frac{m_{\mathrm{n}}}{2\pi\hbar^2} \right)^2 |\langle \psi_i | V | \psi_f \rangle|^2 , \tag{2.7}$$

where k_i and k_f are the incident and final wave numbers, and V is the interaction potential (operator). The normalisation constant Y disappears because it also appears in the states ψ_i and ψ_f and when the scattering is elastic the expression is further simplified because the initial and final wave numbers are the same.

Neutrons can be scattered from the atomic nuclei in the sample via the strong nuclear forces, or from the magnetic moments of the electrons via electromagnetic forces. The first type of scattering is known as nuclear scattering and the second is termed magnetic scattering. In the following only nuclear scattering will be considered, but most of the formalism can be applied directly to magnetic scattering as well. Magnetic scattering will be described in section 2.1.5.

Scattering from a single nucleus

For nuclear scattering the scattering potential (from the j'th nucleus at position $\mathbf{r}_j$) is the Fermi pseudo potential

$$V_j(\mathbf{r}) = \frac{2\pi\hbar^2}{m_\mathrm{n}} b_j \delta(\mathbf{r} - \mathbf{r}_j), \tag{2.8}$$

where b_j is a constant for the j'th nucleus, called the scattering length. The scattering length originates from the interaction between the nucleus and the neutron through the strong nuclear force, and is not very well understood, and the variation in b between elements, and even between isotopes of the same element seems random. If we consider elastic scattering from a single nucleus with scattering length b_j, fixed at position $\mathbf{r}_j$ the matrix element in (2.7) can be calculated as

$$
\begin{aligned}
\langle \psi_f \left| V_j(\mathbf{r}) \right| \psi_i \rangle &= \frac{1}{Y} \frac{2\pi\hbar^2}{m_\mathrm{n}} b_j \int \exp(-i\mathbf{k}_f \cdot \mathbf{r}) \delta(\mathbf{r} - \mathbf{r}_j) \exp(i\mathbf{k}_i \cdot \mathbf{r}) d^3\mathbf{r} \\
&= \frac{1}{Y} \frac{2\pi\hbar^2}{m_\mathrm{n}} b_j \int \exp(i\mathbf{q} \cdot \mathbf{r}) \delta(\mathbf{r} - \mathbf{r}_j) d^3\mathbf{r} \\
&= \frac{1}{Y} \frac{2\pi\hbar^2}{m_\mathrm{n}} b_j \exp(i\mathbf{q} \cdot \mathbf{r}_j),
\end{aligned}
\tag{2.9}
$$

where $\mathbf{q} = \mathbf{k}_\mathrm{i} - \mathbf{k}_\mathrm{f}$ is the so-called scattering vector (see Fig. 2.1). The scattering vector is an important concept in scattering experiments. For elastic scattering ($k_\mathrm{i} = k_\mathrm{f} = k$) there is a simple relation between the scattering vector and the scattering angle:

$$q = 2k \sin(\theta), \tag{2.10}$$

where θ is half the scattering angle. In experiments the measured quantity is often scattered intensity versus scattering angle, but in analysis of diffraction data one typically works in reciprocal space and the identity (2.10) is useful when moving back and forth between real and reciprocal space. Now the differential cross section for elastic scattering from a single fixed nucleus can be calculated by inserting (2.9) into (2.7):

$$\frac{d\sigma}{d\Omega} = b_j^2. \tag{2.11}$$
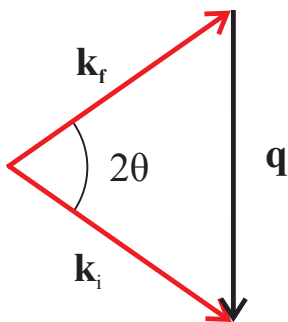
Figure 2.1: The scattering triangle shows the definition of the scattering vector $\mathbf{q}$. Here the incoming and outgoing wave vectors are equal in magnitude and the depicted scattering event is elastic.

Scattering from a system of nuclei

Of course the scattering system always consists of many nuclei and when a neutron scatters from a collection of nuclei the waves scattered from each nucleus interfere. This interference

is exactly what is utilised in diffraction experiments, where diffraction peaks are present when scattering from nuclei (or spins) in certain lattice planes interfere constructively, giving a strong scattering. For a system of scattering nuclei at positions $\mathbf{r}_j$ and with scattering lengths b_j the differential cross section becomes

$$\frac{d\sigma}{d\Omega} = \exp(-2W) \left| \sum_j b_j \exp(i\mathbf{q} \cdot \mathbf{r}_j) \right|^2, \tag{2.12}$$

where $\exp(-2W) = \exp\left(-\langle \mathbf{q} \cdot \mathbf{u} \rangle^2\right)$ is the so called Debye-Waller factor that corrects for the displacement $\mathbf{u}(t)$ of the atoms from their equilibrium positions due to thermal vibrations.

Coherent and incoherent scattering

In most NS experiments on crystalline solids one wishes to measure the strong scattering signal from the constructive interference of the scattering from nuclei (spins) arranged in a periodic lattice. However, even for a monatomic scatterer, there are almost always random variations in the scattering length between atomic sites. This gives rise to so called incoherent scattering. The variation can come about because the sample contains different isotopes of the same element and the scattering is then called isotope incoherent (II) scattering, or because the nucleus has a nuclear spin and is then called nuclear spin incoherent (SI) scattering. The II scattering has its origin in the different scattering lengths for different isotopes, whereas the SI scattering is because the scattering length also depends on whether the neutron spin is parallel or antiparallel to the nuclear spin of the scattering nucleus. Whereas the coherent scattering can be strongly anisotropic the incoherent scattering is isotropic and is often regarded as nothing more than a source of background. NPs are known to have a large amount of water adsorbed on the surface of the particles, giving rise to a very large SI scattering from hydrogen. This signal can be so large that it can pose a real problem for NS experiments on NPs and sometimes one can benefit from using polarisation analysis techniques, where the SI scattering can be eliminated (see section 2.2). If we assume that the nuclear species with scattering length b_j occurs with frequency c_j then the average (coherent) scattering length is:

$$\bar{b} = \sum_j c_j b_j, \tag{2.13}$$

and the average (coherent) cross section is:

$$\sigma_{\text{coh}} = 4\pi \left(\bar{b}\right)^2. \tag{2.14}$$

The total scattering cross section is:

$$\sigma_{\text{scat}} = 4\pi \sum_j c_j b_j^2 = 4\pi \overline{b^2}. \tag{2.15}$$

The difference between the total and the coherent cross sections is then the incoherent cross section $\sigma_{\text{inc}} = \sigma_{\text{scat}} - \sigma_{\text{coh}}$, and one can define an incoherent scattering length:

$$b_{\text{inc}} = \sqrt{\overline{b^2} - \bar{b}^2}. \tag{2.16}$$

In summary, the coherent scattering is the scattering from the average scattering length and the incoherent scattering can be thought of as a correction due to random variations in the scattering length. The coherent scattering length $\bar{b}$ is almost always referred to as simply b and this practice will be used here unless explicitly stated.

2.1.4 Scattering from a crystal

A crystal is a periodic arrangement of atoms in a lattice. Because of the periodicity of the lattice a crystal can give rise to strong coherent scattering in specific directions. If the i'th atom (nuclei) in the j'th unit cell of a crystal lattice is at a position $\mathbf{r}_{i,j} = \mathbf{r}_j + \boldsymbol{\Delta}_i$, where $\mathbf{r}_j$ is the position of the j'th unit cell and $\boldsymbol{\Delta}_i$ is the position of the i'th atom in the unit cell, the elastic nuclear cross section (2.12) reads

$$\frac{d\sigma}{d\Omega} = \exp(-2W) \left| \sum_{i,j} b_i \exp(i\mathbf{q} \cdot (\mathbf{r}_j + \boldsymbol{\Delta}_i)) \right|^2 \tag{2.17}$$

$$= \exp(-2W) \left| F_N(\mathbf{q}) \right|^2 \left| \sum_{j} \exp(i\mathbf{q} \cdot \mathbf{r}_j) \right|^2, \tag{2.18}$$

where the sum in (2.18) has been divided into a sum over the lattice, and the nuclear structure factor $F_N(\mathbf{q})$ defined as

$$F_N(\mathbf{q}) = \sum_{i} b_i \exp(i\mathbf{q} \cdot \boldsymbol{\Delta}_i). \tag{2.19}$$

The arrangements of atoms in a crystalline solid is described in terms of a basis of atoms in a unit cell that is repeated in a periodic lattice. From the (direct) crystal lattice one can define the reciprocal lattice, which is very useful in the description of scattering experiments. The reader will be assumed familiar with the definition of the reciprocal lattice as well as the indexing system where (hkl) denotes a lattice plane and $[hkl]$ denotes a direction in the lattice, whereas $\{hkl\}$ and $\langle hkl \rangle$ denotes families of symmetry-equivalent planes and directions (see any textbook on condensed matter physics, e.g. [53]).

Bragg's law

It can be shown that the lattice sum is only nonzero when the scattering vector is equal to a reciprocal vector. Intuitively it can be understood because the sum will contribute with a factor of N (N being the number of unit cells) when the condition is fulfilled, and all the contributions from other scattering vectors will cancel because $e^{i\mathbf{q}\cdot\mathbf{r_j}}$ gives contributions with different phases which sum to zero. It can be show that with N unit cells of volume V_0 the unit cell sum becomes [44, 46]

$$\left| \sum_{j} \exp(i\mathbf{q} \cdot \mathbf{r}_j) \right|^2 = \mathrm{N}\frac{(2\pi)^3}{V_0} \sum_{\boldsymbol{\tau}} \delta(\mathbf{q} - \boldsymbol{\tau}), \tag{2.20}$$

where $\boldsymbol{\tau}$ is a reciprocal lattice vector. The delta function represents the condition $\mathbf{q} = \boldsymbol{\tau}$, known as the diffraction (or Laue) condition, which is equivalent to the well known Bragg's law:

$$n\lambda = 2d\sin(\theta), \tag{2.21}$$

where d is the spacing between the diffracting planes in the crystal lattice (the so-called d-spacing) and 2θ is the scattering angle. The final version of the elastic nuclear cross section is

$$\frac{d\sigma}{d\Omega} = N\frac{(2\pi)^3}{V_0} \exp(-2W) \left| F_N(\mathbf{q}) \right|^2 \sum_{\boldsymbol{\tau}} \delta(\mathbf{q} - \boldsymbol{\tau}). \tag{2.22}$$

Experimental consideration

In the calculation of the lattice sum leading to the delta function in (2.22) it is implicitly assumed that the sample is a perfect crystal of infinite size and that the neutron beam is perfectly monochromatic and without angular divergence. Obviously none of these conditions are ever strictly fulfilled. The infinite crystal size is often a good approximation for crystals

of μm size, which contain as many as 10^{12} unit cells, and one can get crystals with very low mosaicities, but the angular divergence of the neutron beam and the monochromacity is usually far from perfect. The consequence of the failure of these assumptions is that the delta function representing the diffraction condition becomes $\delta(\mathbf{q} - \boldsymbol{\tau} - \delta\boldsymbol{\tau})$, where $\delta\boldsymbol{\tau}$ signifies that there will be diffraction in directions that deviate with a small amount from a reciprocal lattice vector. This means that the measured Bragg peaks are not delta functions, but have a finite width.

2.1.5 Magnetic neutron scattering

The magnetic interaction between the neutron and the sample is the magnetic Zeeman energy of the magnetic moment of the neutron in a magnetic field $\mathbf{B}$:

$$E_Z = -\boldsymbol{\mu}_{\mathrm{n}} \cdot \mathbf{B} = -\gamma_{\mathrm{n}} \mu_{\mathrm{N}} \boldsymbol{\sigma} \cdot \mathbf{B}. \tag{2.23}$$

The starting point for the magnetic scattering is once again (2.7), but now we have to take the spin of the neutron into account and use the correct magnetic interaction potential. The magnetic interaction potential can be shown to be (see e.g. [54])

$$V_m(\mathbf{q}) = -\left(\gamma_{\mathrm{n}} r_0/2\right) \boldsymbol{\sigma} \cdot \mathbf{M}_{\perp}(\mathbf{q}), \tag{2.24}$$

where the so-called magnetic interaction vector $\mathbf{M}_{\perp}(\mathbf{q})$ has been introduced.

$$\mathbf{M}_{\perp}(\mathbf{q}) = \hat{\mathbf{q}} \times \mathbf{M}(\mathbf{q}) \times \hat{\mathbf{q}}, \tag{2.25}$$

where $\mathbf{M}(\mathbf{q})$ is the Fourier transform of the (microscopic) magnetic moment density and $\hat{\mathbf{q}}$ is a unit vector in the direction of $\mathbf{q}$. Here we see the important result that only magnetic moments perpendicular to the scattering vector contributes to the magnetic scattering. For a magnetically ordered structure the elastic cross section for magnetic scattering of unpolarised neutrons becomes [46]

$$\frac{d\sigma}{d\Omega} = \left(\frac{\gamma_{\mathrm{n}} r_0}{2}\right)^2 g^2 f^2(q) \frac{N(2\pi)^3}{V_0} |F_M(\mathbf{q})|^2 \exp(-2W) \sum_{\boldsymbol{\tau}} \delta(\mathbf{q} - \boldsymbol{\tau}), \tag{2.26}$$

where the magnetic structure factor $F_M(\mathbf{q})$ has been defined analogously to (2.19), $f(q)$ is the magnetic form factor and g is the Landé g-factor that accounts for any orbital contribution to the magnetic moment. Here V_0 and N refer to the magnetic unit cell and $\boldsymbol{\tau}$ is a vector in the reciprocal lattice to the lattice of the magnetic structure. The magnetic unit cell for AFM structures are typically not the same as the chemical unit cell. The magnetic structure factor is a sum over the magnetic unit cell:

$$F_M(\mathbf{q}) = \sum_i \exp(-i\mathbf{q} \cdot \boldsymbol{\Delta}_i) \langle \mathbf{M}_{i,\perp} \rangle, \tag{2.27}$$

where $\langle \rangle$ denotes thermal average. The magnetic form factor $f(q)$ accounts for the extend of the orbital of the electron carrying the magnetic moment:

$$f(q) = \int \exp(i\mathbf{q} \cdot \mathbf{r}) \rho_s(\mathbf{r}) d^3\mathbf{r}, \tag{2.28}$$

where $\rho_s(\mathbf{r})$ is the normalised density of unpaired electrons. The magnetic form factor can be written as (see e.g. [45])

$$f(q) = \langle j_0 \rangle + \left(\frac{g-2}{2}\right) \langle j_2 \rangle. \tag{2.29}$$

Here j_0 and j_2 are spherical Bessel functions, and $\langle j_0 \rangle$ and $\langle j_2 \rangle$ can be calculated for the ion in question using analytical approximations or the Hartree-Fock method [55–57].
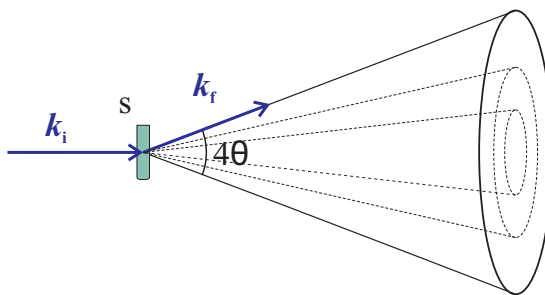
Figure 2.2: Neutron diffraction from a powder sample (S). The crystallites that are oriented for diffraction scatter neutrons into Debye-Scherrer cones.

2.1.6 Neutron powder diffraction

A powder is a collection of a very large number of crystal grains (crystallites). In a typical powder sample there will be at least billions of μm sized crystallites and in a sample of NP powder there can easily be as many as 10^{18} particles. It can usually be assumed that all crystal orientations are represented equally and this means that diffraction will occur at all angles that fulfill Bragg's law (2.21) or equivalently at all scattering vectors that satisfy $q = \frac{2\pi}{d}$. The scattering is spread into so-called Debye-Scherrer cones with opening angle 4θ. The Debye-Scherrer cone covers a solid angle that varies with θ as $\sin(2\theta)$, whereas the detector covers a constant solid angle. It can be shown [58] that the probability for a certain particle to be oriented in the diffraction condition is inversely proportional to $\sin(\theta)$. Together these two effects mean that the cross section is corrected with a factor of

$$L_\theta = \frac{1}{\sin(\theta)\sin(2\theta)}, \tag{2.30}$$

known as the Lorentz factor. Because of the random orientation of the crystallites all reflections with the same d-spacing contribute to scattering in the same Debye-Scherrer cone, and cannot be distinguished from one another. This means that the cross section for NPD of some reflection $\{hkl\}$, should be further multiplied with a factor $j_{\{hkl\}}$, known as the multiplicity of the reflection. For example the $\{100\}$ family of reflections in a cubic lattice have a multiplicity of 6. The cross section for nuclear or magnetic NPD can be obtained for a $\{hkl\}$ Bragg peak, by multiplying (2.22) or (2.26) with $j_{\{hkl\}}L_\theta$.

In Figure 2.3 is a simple sketch of a neutron powder diffractometer. Instruments like DMC at PSI and D1B at ILL used in the investigations of NiO NPs to be presented in Chapter 4 have this basic appearance plus some further features I will not discuss here.

Powder diffraction on nanoparticles

When the sample is a powder of NPs the finite crystallite size gives rise to a substantial broadening of the Bragg peaks. The peak broadening can be used to estimate the particle size in the direction perpendicular to the diffracting planes (ϵ), using the so-called Scherrer formula [59, 60]:

$$\epsilon = \frac{\lambda}{B_{2\theta}\cos(\theta)}, \tag{2.31}$$

where θ is half the scattering angle and $B_{2\theta}$ is the peak broadening due to the finite particle size in units of the scattering angle (radians). It is straight forward to show that in terms of the scattering vector this becomes

$$\epsilon = \frac{2\pi}{B_q}, \tag{2.32}$$

where B_q is the peak broadening due to the finite particle size in units of the scattering vector. From ϵ one can determine the so-called true particle size, defined as $p = V^{1/3}$, where V is the
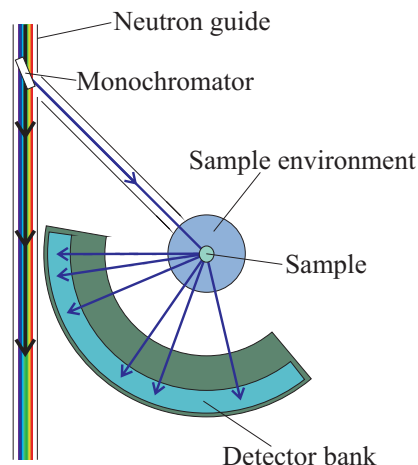
Figure 2.3: Schematic of a neutron powder diffractometer. The white neutron beam in the guide hits the monochromator, and neutrons of the desired wavelength are reflected onto the sample. The neutrons can scatter off the sample in all direction and some of them hit the banana-shaped detector and are counted. Not displayed on the sketch are slits, monitors, filters, and collimators usually equipped on powder diffractometers. The neutrons not selected by the monochromator and may remain in the guide, and travel on to other experiments further down the line.

particle volume, from

$$p = K\epsilon, \tag{2.33}$$

where K is a constant of the order unity that depends on the symmetry of the crystal structure and on the particle shape. Calculations of K (known as the Scherrer constant) for certain geometries can be found in the literature [60,61]. When using the Scherrer formula it is important to note that B is only the broadening due to the finite crystallite size. Other types of broadening from the instrument or from the sample (e.g. from lattice strain) have to be properly subtracted. However, in measurements of NPs that are only a few nanometers in size other types of broadening is often negligible and (2.31) or (2.32) can be used directly. If the sample is magnetically ordered the broadening of the magnetic Bragg peaks can give information about the magnetic correlation length in the same way as for the crystalline size.

Figure 2.4 shows neutron powder diffraction patterns of bulk ilmenite powder (a) and NPs of ilmenite produced by ball-milling (b). The finite size broadening of the diffraction peaks is evident in the diffraction pattern of the NP sample. Furthermore it can be seen that the signal to background ratio is significantly lowered in the NP sample compared to the bulk sample, because of SI scattering from hydrogen in the water adsorbed on the surfaces of the NPs.

2.1.7 Inelastic scattering

In an inelastic scattering event energy is transfered between the neutron and the scattering system so that

$$\hbar\omega = E_{\mathrm{i}} - E_{\mathrm{f}}, \tag{2.34}$$

where E_{i} and E_{f} are the initial and final energies of the scattering system respectively. For inelastic scattering one defines the partial differential scattering cross section:

$$\frac{d^2\sigma}{d\Omega dE_{\mathrm{f}}} = \frac{1}{\Psi} \frac{\text{no. of neutrons scattered per sec. into } d\Omega \text{ with energies } [E_{\mathrm{f}}; E_{\mathrm{f}} + dE_{\mathrm{f}}]}{d\Omega dE_{\mathrm{f}}}. \tag{2.35}$$

When a neutron scatters inelastically the state of the scattering system changes. Let the state of the system before and after the scattering event be $|\lambda_{\mathrm{i}}\rangle$ and $|\lambda_{\mathrm{f}}\rangle$. Then the partial differential
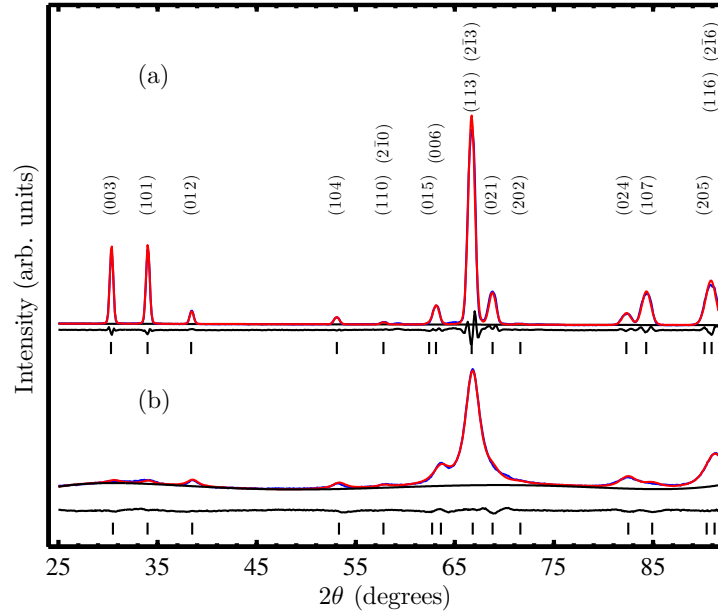
Figure 2.4: NPD patterns of FeTiO$_3$ measured at the DMC instrument at PSI in 2011 (see Paper [6]). The scattering from the bulk sample (a) gives rise to relatively sharp Bragg peaks, with their widths determined by the resolution of the instrument. The Bragg peaks of the NP sample (b) are much broader because of the finite size broadening from the particles that are about 13 nm in size. The indexing is with respect to the $R\overline{3}$ structure of ilmenite in hexagonal notation.

cross section is

$$
\left.\frac{d^2\sigma}{d\Omega dE_{\rm f}}\right|_{\lambda_{\rm i}\to\lambda_{\rm f}} = \frac{k_{\rm i}}{k_{\rm f}}\left(\frac{m_{\rm n}}{2\pi\hbar^2}\right)^2 |\langle\lambda_{\rm i}\psi_{\rm i}\,|V|\,\lambda_{\rm f}\psi_{\rm f}\rangle|^2\,\delta\left(E_{\lambda_{\rm i}} - E_{\lambda_{\rm f}} - \hbar\omega\right), \tag{2.36}
$$

where the delta function ensures that the energy difference between the final and initial state of the scattering system must equal the energy transfered to or from the neutron.

2.2 Neutron polarisation analysis

In the previous section the neutron beam was assumed to be unpolarised. Using a polarised neutron beam and analysing the polarisation of the scattered neutrons can be a great advantage, especially when dealing with magnetic scattering or samples with a large SI scattering. The use of polarisation analysis further makes it possible to determine the orientation of the magnetic moment in a crystal.

In this section I will explain the basic theory of polarisation analysis in elastic NS. First I will briefly describe the experimental setup for polarisation analysis, using the triple axis spectrometer as example, and I will continue with a discussion of uniaxial polarisation analysis, followed by a section on XYZ-polarisation analysis. The theory of polarised neutron scattering was explained in 1969 in a classic paper by Moon, Riste, and Koehler [62] and is also reviewed in the textbook by Squires [44]. In my presentation of the subject, which is heavily inspired by the above mentioned text as well as on the paper by Stewart et al. [54] Many details will be left out, and the reader is referred to the original texts if further information is desired. After the theoretical derivations the two instruments used for polarisation analysis experiments in this thesis will be described.

2.2.1 Basics of polarisation analysis

Polarisation of the beam

The basic idea in a polarisation analysis experiment is to have a polarised beam of neutrons impinging on the sample and to analyse the polarisation state of the scattered neutrons after the sample. The beam can be polarised e.g., by polarising supermirrors, by polarisation sensitive Bragg-diffraction from crystals, or by passing the beam through a cell with spin-polarised ^{3}He. The neutron is a spin $\frac{1}{2}$ particle and if a quantisation axis (say the z - axis) is chosen the spin of a neutron along that axis can be in either of the two states

$$|+\rangle = \begin{bmatrix} 1 \\ 0 \end{bmatrix} \quad , \quad |-\rangle = \begin{bmatrix} 0 \\ 1 \end{bmatrix}, \tag{2.37}$$

usually referred to as spin up and spin down. The polarisation of the beam along the z - direction can be defined as

$$p \equiv p^z = 2 \langle S^z \rangle. \tag{2.38}$$

The polarisation is a number in the range $-1 \leq p \leq 1$ and can be written in terms of the number of neutrons with spin up (N_+) and down (N_-):

$$p = \frac{N_+ - N_-}{N_+ + N_-}. \tag{2.39}$$

In experiments the beam is never perfectly polarised $(p < 1)$, but let us assume for now that $p = 1$ and later come back to the necessary corrections.

Layout of a polarised triple axis spectrometer

The triple axis spectrometer (TAS) is a classic in NS instrumentation. The three axes that gives the instrument its name are those of the monochromator, the sample, and the analyser, that can all be manipulated. The monochromator and analyser are identical Bragg-diffraction crystals that enable a specific incoming wave vector to be selected (monochromator) and a specific final wave vector to be measured by the detector (analyser). Together with rotation of the sample this enables the TAS to map out reciprocal space and by using different Bragg angles on monochromator and analyser it is possible to measure the inelastically scattered neutrons. While inelastic NS is an important use of the TAS only elastic scattering will be considered here. The basic layout of a TAS equipped with polarisation analysis capabilities is given in Figure 2.5. The polariser is a monochromator that only reflects $|+\rangle$ neutrons to the sample and similarly the analyser only reflects $|+\rangle$ neutrons to the detector. In order for the beam not to get depolarised by stray fields a magnetic field, the so-called guide field, produced by permanent magnets covers the entire beam path from polariser to detector. So called "flippers" are placed between monochromator (polariser) and sample, and between sample and analyser. A flipper is a device that allows for 180° rotation of the neutron spin from $|+\rangle$ to $|-\rangle$ or vice versa. The sample is placed in a small magnetic field from electromagnetic coils to maintain the neutron polarisation at the sample position, where guide fields would be impractical. This setup allows for measurement of cross sections for the four possible neutron spin states before and after the sample:

$$|+\rangle \rightarrow |+\rangle, \quad |-\rangle \rightarrow |-\rangle, \quad |+\rangle \rightarrow |-\rangle, \quad |-\rangle \rightarrow |+\rangle. \tag{2.40}$$

Given that the initial neutron spin (from the monochromator) is $|+\rangle$ and that the analyser reflects only $|+\rangle$ neutrons the $|+\rangle \rightarrow |+\rangle$ cross section is measured by having both flippers off. If the first flipper is kept off but the second is turned on the neutrons will be flipped after the sample and then the $|+\rangle \rightarrow |-\rangle$ cross section is measured, and similarly for the remaining two possibilities. The two processes $|+\rangle \rightarrow |+\rangle$ and $|-\rangle \rightarrow |-\rangle$ that leaves the spin state of the neutron unaltered are referred to as non-spin-flip (NSF) processes and the other two as spin-flip (SF) processes for obvious reasons.
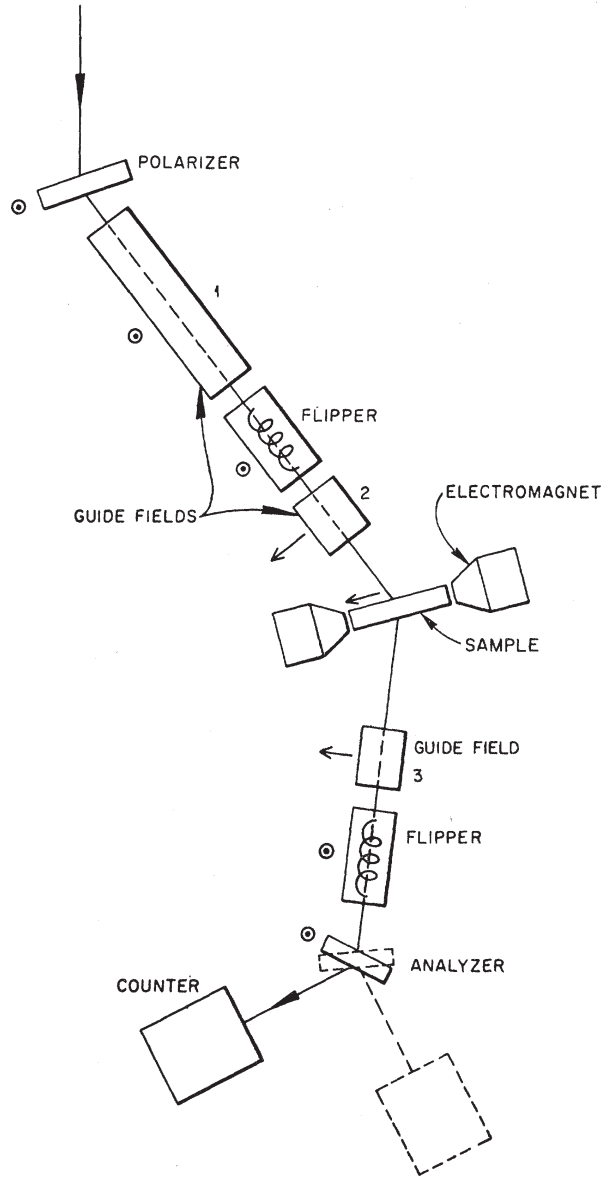
Figure 2.5: Schematic of a triple axis spectrometer equipped for polarisation analysis. Figure from [62].

The cross section for unpolarised neutrons can be found as $\frac{1}{2}$ times the sum of the four polarisation analysis cross sections. When the neutron spin is taken into account the differential cross section is (from Equation 2.7)

$$\frac{d\sigma}{d\Omega} = \left(\frac{m_{\mathrm{n}}}{2\pi\hbar^2}\right)^2 |\langle \mathbf{k}_{\mathrm{f}}\boldsymbol{\sigma}_{\mathrm{f}} |V| \mathbf{k}_{\mathrm{i}}\boldsymbol{\sigma}_{\mathrm{i}}\rangle|^2 , \tag{2.41}$$

where $\boldsymbol{\sigma}_{\mathrm{i}}$ and $\boldsymbol{\sigma}_{\mathrm{f}}$ are the initial and final spin states of the neutron respectively. To obtain the cross section we now have to calculate the scattering amplitude

$$U = \langle \mathbf{k}_{\mathrm{f}}\boldsymbol{\sigma}_{\mathrm{f}} |V| \mathbf{k}_{\mathrm{i}}\boldsymbol{\sigma}_{\mathrm{i}}\rangle \tag{2.42}$$

for each of the four processes in (2.40)

Nuclear scattering

To calculate the cross sections for the four processes (2.40) we need to take into account the difference in scattering length for nuclei with nuclear spin parallel or antiparallel to the spin of

the neutron. We denote these two scattering lengths b_+ and b_- and define the scattering length operator for a nucleus with nuclear spin $\mathbf{I}$ (see ref. [44] p. 173)

$$b = A + B\boldsymbol{\sigma} \cdot \mathbf{I}, \tag{2.43}$$

where

$$A = \frac{(I+1)b_+ + Ib_-}{2I+1} \quad \text{and} \quad B = \frac{b_+ - b_-}{2I+1}. \tag{2.44}$$

With this definition of the scattering length one can arrive at [44] the four expressions for the scattering amplitude for nuclear scattering:

$$
\begin{aligned}
\langle + |b| + \rangle &= A + BI_z, \\
\langle - |b| - \rangle &= A - BI_z, \\
\langle + |b| - \rangle &= B\left(I_x + iI_y\right), \\
\langle - |b| + \rangle &= B\left(I_x - iI_y\right).
\end{aligned}
\tag{2.45}
$$

Magnetic scattering

From the magnetic interaction potential (2.24) and using the properties of the Pauli spin matrices one can arrive at the scattering amplitudes for magnetic scattering

$$
\begin{aligned}
\langle + |\boldsymbol{\sigma} \cdot \mathbf{M}_\perp(\mathbf{q})| + \rangle &= M_{\perp,z}(\mathbf{q}), \\
\langle - |\boldsymbol{\sigma} \cdot \mathbf{M}_\perp(\mathbf{q})| - \rangle &= -M_{\perp,z}(\mathbf{q}), \\
\langle + |\boldsymbol{\sigma} \cdot \mathbf{M}_\perp(\mathbf{q})| - \rangle &= M_{\perp,x}(\mathbf{q}) + iM_{\perp,y}(\mathbf{q}), \\
\langle - |\boldsymbol{\sigma} \cdot \mathbf{M}_\perp(\mathbf{q})| + \rangle &= M_{\perp,x}(\mathbf{q}) - iM_{\perp,y}(\mathbf{q}),
\end{aligned}
\tag{2.46}
$$

where $M_{\perp,z}$ is the component of $\mathbf{M}_\perp$ in the z-direction, and similarly for the other components. Equation (2.46) states the very important rules of uniaxial polarisation analysis, namely that the NSF scattering gives information about the magnetisation parallel to the polarisation direction and the SF scattering gives information about the magnetisation perpendicular to the polarisation direction.

Combined nuclear and magnetic scattering

We can now combine (2.46) and (2.45) to obtain the spin dependent combined nuclear and magnetic scattering amplitudes:

$$
\begin{aligned}
U^{++} &= A + BI_z - pM_{\perp,z}(\mathbf{q}), \\
U^{--} &= A - BI_z + pM_{\perp,z}(\mathbf{q}), \\
U^{+-} &= B\left(I_x + iI_y\right) - p\left(M_{\perp,x}(\mathbf{q}) + iM_{\perp,y}(\mathbf{q})\right), \\
U^{-+} &= B\left(I_x - iI_y\right) - p\left(M_{\perp,x}(\mathbf{q}) - iM_{\perp,y}(\mathbf{q})\right),
\end{aligned}
\tag{2.47}
$$

where $p = \gamma_{\mathrm{n}} r_0 / 2$.

Coherent and incoherent scattering

The differential cross section for incoherent scattering is

$$\left(\frac{d\sigma}{d\Omega}\right)_{\mathrm{inc}} = \overline{b^2} - \left(\bar{b}\right)^2. \tag{2.48}$$

Using (2.45) and assuming a random distribution of nuclear spins this can be shown (see section 3.2 in [54]) to be

$$\left(\frac{d\sigma}{d\Omega}\right)_{\mathrm{inc}}^{\mathrm{NSF}} = \bar{A}^2 - \left(\bar{A}\right)^2 + (1/3)B^2 I(I+1) \tag{2.49}$$

23

for both the NSF transitions, and similarly for the SF transitions:

$$\left(\frac{d\sigma}{d\Omega}\right)_{\text{inc}}^{\text{SF}} = (2/3)B^2 I(I+1). \tag{2.50}$$

The term $\bar{A}^2 - \left(\bar{A}\right)^2$ is the II cross section and enters only in the expression for NSF scattering. This is not surprising because a nuclear scattering event cannot change the spin of a neutron. The term $B^2 I(I+1)$ is the SI cross section and enters with a factor of $1/3$ in the NSF cross section, and $2/3$ in the SF cross section and the equations (2.49) and (2.50) immediately suggest a method of separating the SI scattering, namely by subtracting half the SF cross section from the NSF cross section.

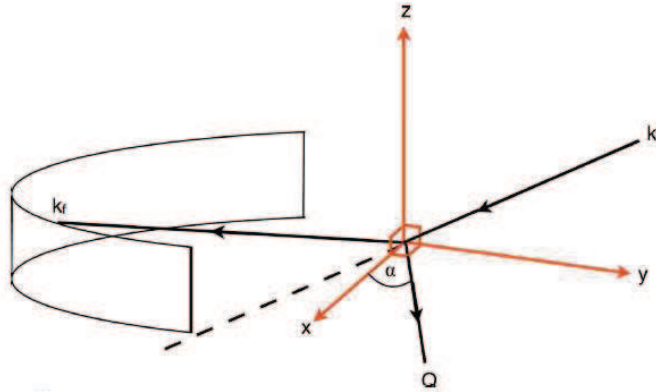### 2.2.2 XYZ-polarisation analysis

Figure 2.6: Geometry in an XYZ-polarisation analysis experiment. Figure from [54].

The technique of XYZ-polarisation analysis as described by Schärpf and Capellmann [63] makes it possible to separate magnetic, nuclear and SI background. This can be done on an instrument with a multidetector array, making it possible to employ the method to measure for example diffraction patterns or diffuse scattering. I will continue to follow the formalism of [54] in my presentation of the theory. The magnetic part of the cross section depends on the polarisation direction with respect to the scattering vector as can be inferred from (2.46), whereas the nuclear and SI parts of the cross section does not, and this is utilised in XYZ-polarisation analysis where the NSF and SF cross sections are measured in three orthogonal directions. It can be shown (see [44]) that the magnetic scattering cross sections for NSF and SF scattering are

$$\left(\frac{d\sigma}{d\Omega}\right)_{\text{mag}}^{\text{NSF}} = \frac{1}{2}\left(\frac{d\sigma}{d\Omega}\right)_{\text{mag}}\left[1 - \left(\hat{\mathbf{P}}\cdot\hat{\mathbf{q}}\right)^2\right] \quad \text{and} \tag{2.51}$$

$$\left(\frac{d\sigma}{d\Omega}\right)_{\text{mag}}^{\text{SF}} = \frac{1}{2}\left(\frac{d\sigma}{d\Omega}\right)_{\text{mag}}\left[1 + \left(\hat{\mathbf{P}}\cdot\hat{\mathbf{q}}\right)^2\right], \tag{2.52}$$

where $\hat{\mathbf{P}}$ and $\hat{\mathbf{q}}$ are unit vectors in the direction of $\mathbf{P}$ and $\mathbf{q}$, and $\left(\frac{d\sigma}{d\Omega}\right)_{\text{mag}}$ is the magnetic cross section. If the instrument is equipped with a multidetector in the xy plane and the angle between the scattering vector and the x-axis is α (see Fig. 2.6) the scattering vector will be in

this plane and the unit vector in the direction of $\mathbf{q}$ is

$$\hat{\mathbf{q}} = \begin{bmatrix} \cos\alpha \\ \sin\alpha \\ 0 \end{bmatrix}. \tag{2.53}$$

In the experiment the polarisation is brought to point alternately in the x, y and z directions:

$$\hat{\mathbf{P}}_x = \begin{bmatrix} 1 \\ 0 \\ 0 \end{bmatrix} \quad , \quad \hat{\mathbf{P}}_y = \begin{bmatrix} 0 \\ 1 \\ 0 \end{bmatrix} \quad , \quad \hat{\mathbf{P}}_z = \begin{bmatrix} 0 \\ 0 \\ 1 \end{bmatrix} \quad . \tag{2.54}$$

Now, using Equations (2.51) - (2.54), the magnetic contribution to each of the six cross sections can be calculated, and including the nuclear cross section (containing both nuclear coherent and II scattering) and the SI cross section the six cross sections for the NSF and SF scattering with the polarisation in the x, y and z directions are

$$
\begin{aligned}
\left(\frac{d\sigma}{d\Omega}\right)_x^{\text{NSF}} &= \frac{1}{2}\sin^2\alpha\left(\frac{d\sigma}{d\Omega}\right)_{\text{mag}} + \frac{1}{3}\left(\frac{d\sigma}{d\Omega}\right)_{\text{SI}} + \left(\frac{d\sigma}{d\Omega}\right)_{\text{nuc}}, \\
\left(\frac{d\sigma}{d\Omega}\right)_x^{\text{SF}} &= \frac{1}{2}\left(\cos^2\alpha + 1\right)\left(\frac{d\sigma}{d\Omega}\right)_{\text{mag}} + \frac{2}{3}\left(\frac{d\sigma}{d\Omega}\right)_{\text{SI}}, \\
\left(\frac{d\sigma}{d\Omega}\right)_y^{\text{NSF}} &= \frac{1}{2}\cos^2\alpha\left(\frac{d\sigma}{d\Omega}\right)_{\text{mag}} + \frac{1}{3}\left(\frac{d\sigma}{d\Omega}\right)_{\text{SI}} + \left(\frac{d\sigma}{d\Omega}\right)_{\text{nuc}}, \\
\left(\frac{d\sigma}{d\Omega}\right)_y^{\text{SF}} &= \frac{1}{2}\left(\sin^2\alpha + 1\right)\left(\frac{d\sigma}{d\Omega}\right)_{\text{mag}} + \frac{2}{3}\left(\frac{d\sigma}{d\Omega}\right)_{\text{SI}}, \\
\left(\frac{d\sigma}{d\Omega}\right)_z^{\text{NSF}} &= \frac{1}{2}\left(\frac{d\sigma}{d\Omega}\right)_{\text{mag}} + \frac{1}{3}\left(\frac{d\sigma}{d\Omega}\right)_{\text{SI}} + \left(\frac{d\sigma}{d\Omega}\right)_{\text{nuc}}, \\
\left(\frac{d\sigma}{d\Omega}\right)_z^{\text{SF}} &= \frac{1}{2}\left(\frac{d\sigma}{d\Omega}\right)_{\text{mag}} + \frac{2}{3}\left(\frac{d\sigma}{d\Omega}\right)_{\text{SI}}.
\end{aligned}
\tag{2.55}
$$

Now, one can separate the magnetic from the SI, and from the nuclear coherent and II cross sections by measuring all six cross sections in (2.55) and taking the appropriate linear combinations. The magnetic cross sections can be found in two ways:

$$
\begin{aligned}
\left(\frac{d\sigma}{d\Omega}\right)_{\text{mag}} &= 2\left(\frac{d\sigma}{d\Omega}\right)_x^{\text{SF}} + 2\left(\frac{d\sigma}{d\Omega}\right)_y^{\text{SF}} - 4\left(\frac{d\sigma}{d\Omega}\right)_z^{\text{SF}}, \\
\left(\frac{d\sigma}{d\Omega}\right)_{\text{mag}} &= 4\left(\frac{d\sigma}{d\Omega}\right)_z^{\text{NSF}} - 2\left(\frac{d\sigma}{d\Omega}\right)_x^{\text{NSF}} - 2\left(\frac{d\sigma}{d\Omega}\right)_y^{\text{NSF}},
\end{aligned}
\tag{2.56}
$$

For the spin independent nuclear scattering (nuclear coherent +II) we have:

$$\left(\frac{d\sigma}{d\Omega}\right)_{\text{nuc}} = \frac{1}{6}\left[2\left(\frac{d\sigma}{d\Omega}\right)_{\text{TNSF}} - \left(\frac{d\sigma}{d\Omega}\right)_{\text{TSF}}\right] \tag{2.57}$$

$$= \left(\frac{d\sigma}{d\Omega}\right)_{\text{nuc,coh}} + \left(\frac{d\sigma}{d\Omega}\right)_{\text{II}}, \tag{2.58}$$

where the subscripts TNSF and TSF refer to sum of the three NSF and SF cross sections. Finally the SI cross section can be found as

$$\left(\frac{d\sigma}{d\Omega}\right)_{\text{SI}} = \frac{1}{2}\left(\frac{d\sigma}{d\Omega}\right)_{\text{TSF}} - \left(\frac{d\sigma}{d\Omega}\right)_{\text{mag}} \tag{2.59}$$

$$= B^2 I (I+1). \tag{2.60}$$

With this method of separating the magnetic cross section from the nuclear and the SI scattering we have a powerful tool for investigations of the magnetic properties of samples that would otherwise be difficult or impossible, because of overlapping nuclear and magnetic scattering or a high SI scattering.

2.2.3 Data corrections in polarisation analysis

Because of imperfect polarisers and flippers that do not have an efficiency of 100% it is never possible to have a perfectly polarised neutron beam ($p = 1$) and the experimental data therefore has to be corrected to obtain the true NSF and SF cross sections. To quantify the deviation from perfect polarisation one defines the so called flipping ratio:

$$R = N_+/N_-, \tag{2.61}$$

which will be infinite for a perfectly polarised beam. The polarisation of the beam can be found from the flipping ratio through

$$p = \frac{N_+ - N_-}{N_+ + N_-} = \frac{R-1}{R+1}, \tag{2.62}$$

and the probability p_+ (p_-) of finding a neutron in the state $|+\rangle$ ($|-\rangle$) is

$$p_+ = \frac{1+p}{2} \quad , \quad p_- = \frac{1-p}{2}. \tag{2.63}$$

The relationship between the measured intensities I^{NSF} and I^{SF} and the true cross sections σ^{NSF} and σ^{SF} is

$$\begin{pmatrix} I^{\text{NSF}} \\ I^{\text{SF}} \end{pmatrix} = \begin{pmatrix} p_\uparrow & p_\downarrow \\ p_\downarrow & p_\uparrow \end{pmatrix} \begin{pmatrix} \sigma^{\text{NSF}} \\ \sigma^{\text{SF}} \end{pmatrix}. \tag{2.64}$$

In the correction one utilises that a non magnetic scattering event cannot change the polarisation state of the neutrons and should thus give zero spin flip scattering. The spin flip scattering from a purely nuclear (with no SI scattering) scatterer is thus a measure of the imperfect polarisation control in the experiment and can be used to correct the data. The flipping-ratio can be calculated from a measurement of a nuclear peak ($\sigma^{\text{SF}} = 0$):

$$R = \frac{I^{\text{NSF}}_{\text{nuc}}}{I^{\text{SF}}_{\text{nuc}}} \tag{2.65}$$

and the true cross sections can then be calculated by inverting equation (2.64). In practice R can be determined by measuring the intensity of a nuclear Bragg peak in a uniaxial polarisation analysis experiment. In an experiment with an array of individual analysers and detectors one can obtain R for each for each detector-analyser element by measurement of an isotropic nuclear scatterer like amorphous silica. For a full treatment of data corrections in a polarisation analysis experiment see the review by Wildes [64].

2.2.4 The polarised triple axis spectrometer IN12 at ILL

The IN12 instrument is a TAS and the layout of the instrument is similar to the one depicted in Figure 2.5. There are, however, differences in how the beam polarisation is attained and manipulated. IN12 was the instrument used for the investigation of the spin orientation in a natural crystal of hemo-ilmenite to be described in Chapter 6 and Paper [5]. In the following I will go through the most important components of the instrument, following the path of a neutron from guide to detector. For our purpose of studying static magnetic structure no energy transfer between neutron and sample is needed and the discussion will be restricted to elastic scattering.
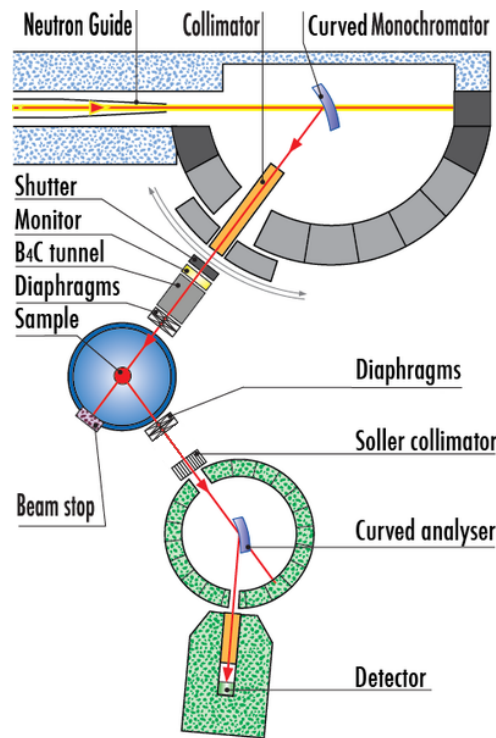

Figure 2.7: Layout of the IN12 instrument. The instrument has been moved and refurbished since our experiment in 2010 and the diagram is of the new IN12, but most components are the same. One particular difference is that in our experiment there was a Be filter in place of the B_4C tunnel in the incident beam. The equipment for polarisation analysis, not displayed in the diagram includes a polarising supermirror together with a short collimator, replacing the large collimator in the incident beam, a Mezei type spin flipper in the diffracted beam, and a guide field of permanent magnets in the entire beam path. The sample environment was a 2.5 T cryomagnet with a temperature range of 2 K - 290 K. The most important components for our experiment are described in the text. The Figure is modified from the instrument homepage [65].

Incident beam

The monochromator is a Bragg reflecting crystal that is placed in the center of the guide and reflects neutrons of the desired wavelength to the IN12 experimental area. On IN12 the (002) reflection of pyrolytic graphite (PG) with a d-spacing of 3.4 Å is used. Because of the factor of n in Bragg's law (2.21) the diffraction condition is fulfilled not only neutrons of the desired wavelength, but also for neutrons with wavelengths $\lambda/, \lambda/3, \lambda/4\ldots$ These so-called higher-order neutrons are an unwanted source of background that can severely hamper the data analysis, and one therefore utilises filters to get rid of them. The filter used on IN12 is a 10 cm long container with powder of Be, which has a Bragg-scattering cutoff at λ_{cutoff}=4.0Å [45], meaning that virtually no neutrons with wavelengths smaller than λ_{cutoff} are transmitted. The filter is cooled with liquid N_2 to minimize inelastic scattering from phonons, enhancing the transmission

for wavelengths greater than λ_{cutoff}. The beam is polarised by a so called supermirror bender positioned between the monochromator and the Be filter. The supermirror bender is a multilayer of ferromagnetic supermirrors with a critical angle of total reflection that is given by [66]

$$\theta_c^\pm = \lambda\sqrt{N(b \pm p)/\pi}, \tag{2.66}$$

where N is the nuclear density, b is the nuclear scattering length and p is the magnetic scattering length. The $\pm$ denotes the two polarisation states. The principle of polarising supermirrors is that one choses a material with $b = p$ and thus only $|+\rangle$ neutrons are reflected. In this way a polarisation $p > 0.95$ is obtained at IN12. To avoid losing the polarisation of the beam a small vertical guide field of a few mT is maintained along the entire beam path.

Sample and sample environment

The polarised neutron beam enters the sample which can be enclosed in a variety of different environments. A small magnetic field is always maintained inside the sample chamber by Helmholtz coils, to preserve the polarisation in the absence of a guide field from permanent magnets.

Diffracted beam

After the sample the neutrons that are elastically scattered hit the polarising analyser. The analyser is of the Heusler (Cu_2MnAl) type, and uses the (111) reflection, which has a d-spacing of 3.44 Å. The Heusler analyser polarises the beam in a similar way as the supermirror bender, by a carefully matched nuclear and magnetic scattering length. In our case the configuration is such that the supermirror bender only reflects $|+\rangle$ neutrons, and only $|-\rangle$ neutrons are analysed, and the instrument is thus set up to measure the SF cross section. To be able to measure the NSF cross section a so-called Mezei spin flipper is positioned between the sample and analyser. The Mezei flipper consists of two coils, one producing a vertical magnetic field that exactly cancels the guide field, and the other producing a horizontal field that is tuned so that the 4.05 Å neutrons precess exactly 180° inside the flipper, and are thus flipped from $|+\rangle$ to $|-\rangle$ or vice versa. A measurement with the flipper *off* is thus an SF experiment and a measurement with the flipper *on* is an NSF experiment. The detector is of the He^3 type, that consist of a chamber with a mixture of He^3 and another gas like Ar. The nuclear process that is utilised for detection is:

$$n + {}^3\text{He} \rightarrow {}^3\text{H} + p + \text{Energy}.$$
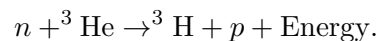
The charged particles produced in the process are accelerated by a voltage difference over the chamber, ionizing the Ar gas and creating a cascade of charged particles that can be detected.

The IN12 instrument of course also contains further components that are important in all neutron scattering experiments like radiation protection shielding, slits and apertures (diaphragms), monitors, and collimation sections. The role of the monitor is to measure the incident flux for normalisation purposes in case of instabilities in the neutron flux from the source. The collimation sections are there to improve the spatial resolution to the desired level by minimising the angular divergence of the beam.

2.2.5   The polarised diffractometer D7 at ILL

In a neutron powder diffractometer a bank of detectors covering an extended angular range is used to obtain the diffraction pattern. If one wishes to obtain a polarisation analysed powder diffraction pattern the neutrons hitting every single detector element have to be analysed. This means that contrary to for example a TAS like IN12 where a single polarising analyser is enough a polarised powder diffractometer needs a polariser in front of each detector element. This is a complicated and costly addition to an instrument and therefore equipped on only very few instruments in the world. One of these instruments is D7 at ILL.

D7 is a diffuse scattering spectrometer, typically used to study short range order or low energy excitations, but can also be used for powder diffraction. D7 is equipped with the instrumentation needed for XYZ polarisation analysis, including a detector array covering a 132° angular range with supermirror analysers in front of all detector elements. The instrument also has an option for inelastic scattering using the time-of-flight technique, with a so-called Fermi chopper in the beam providing the time structure. Here I will focus on the use of D7 as a polarised powder diffractometer with the ability of separating magnetic, nuclear and SI scattering.
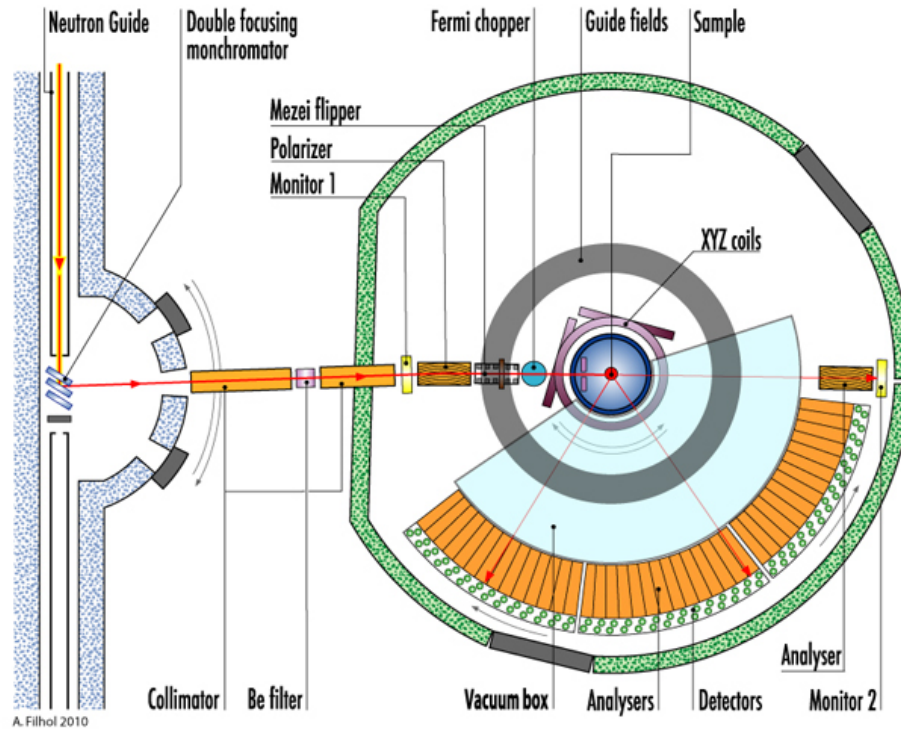

Figure 2.8: Layout of the D7 instrument at ILL. In the sketch the instrument is positioned at the central beam port and it is thus set up for a neutron wavelength of 4.855 Å. The components of the instrument are described in the text. Figure from the D7 homepage [67].

The layout of the D7 instrument has been altered several times. The instrument with the initial multi analyser-detector array is described in [63] and the current version of the instrument is described in [54]. The schematic of the D7 instrument is shown in Figure 2.8. Many of the components of D7 are identical or very similar to the corresponding elements equipped on IN12 and will not be explained here. Once again we will follow the path of the neutron from the guide to the detector.

Incident beam

On D7 three PG monochromators are placed in the guide, monochromating and focusing the beam using the PG (002) reflection. A neutron wavelength of 3.12 Å or 4.855 Å can be selected by moving the whole instrument to the appropriate beam port. The neutron beam now travels through collimation sections and enters the main tank of the instrument. Inside the instrument tank there is a supermirror polariser. The polariser and the analysers of D7 are Co/Ti super-mirrors of the bender type [68, 69] and are produced at ILL. After the polariser is the Mezei spin flipper that determines whether a measurement is NSF or SF. The chopper depicted in the diagram is only used for inelastic measurements and is taken out of the beam for elastic measurements.

Around the sample position three coils, labeled XYZ coils, produce a magnetic field that defines the polarisation direction at the sample position in order to measure the desired cross

section. By sending a current through the different coils and using the Mezei flipper the six cross sections (2.55) necessary for XYZ polarisation analysis can be measured. The guide field is in the vertical (z) direction and it is not necessary to use any of the XYZ coils to obtain a polarisation in the z direction. To get the beam polarised in the x direction the Z coil is excited to produce a vertical magnetic field that exactly cancels the guide field at the sample position and the X coil produces a magnetic field in the x-direction that rotates the z-polarised neutrons into the x-direction at the sample position. Similarly polarisation in the y-direction can be achieved by using the Y-coil. The sample environment is usually a cryostat of furnace. Magnetic fields applied at the sample position is not compliant with the XYZ method.

Diffracted beam

After the sample the neutrons travelling in the right directions are analysed by the analyser-detector array, consisting of three banks of each 22 analysers and 44 detectors. The bank of ^{3}He detectors covering an angle of $132°$ can be moved around the sample position giving a total angular range of $4° < 2\theta < 145°$. The analysers, which are supermirrors similar to the polariser, need to be magnetised all the time to remain polarisation selective (i.e. for b and p to be equal in (2.66)). This is achieved by a large number of NdFeB magnets, that at the same time produce the guide field in the instrument. After the neutron has interacted with the sample its spin is rotated into the z direction by the guide field and it will thus be reflected by the analysers into the detector if it has the right spin along this quantisation axis and together with the polariser, the spin flipper and the XYZ coils it is thus possible to measure the NSF and SF cross sections for all three polartisation directions.

2.3 X-ray powder diffraction

X-ray powder diffraction is an excellent tool for sample characterisation, and has been used throughout my PhD project. Much of the theory of neutron scattering can be applied to X-rays with only minor changes. Importantly, X-rays interact with the charge of the electron around atoms, and not just with their spins or with the atomic nuclei. This means that XRD can be used to determine the crystal structure of materials, but not the magnetic structure. The strength of the interaction between an X-ray photon and an atom depends on the electron density, and consequently the scattering length for X-rays is proportional to the atomic number. This means that X-rays have a hard time detecting lighter elements, and that it can be difficult to distinguish elements that have similar atomic numbers, not to mention isotopes of the same element. The cross section for X-ray powder diffraction is similar to the cross section for NPD and takes the form:

$$\frac{d\sigma}{d\Omega} \propto j_{\{hkl\}} |F_{\text{XRD}}(\mathbf{q})|^2 \exp(-2W) \frac{0.5\left(1 + \cos^2(2\theta)\right)}{L_\theta} \delta\left(\mathbf{q} - \boldsymbol{\tau}\right), \qquad (2.67)$$

where $0.5\left(1 + \cos^2(2\theta)\right)$ is the so-called polarisation factor for scattering of unpolarised X-rays. The X-ray structure factor, $F_{\text{XRD}}(\mathbf{q})$, is defined analogous to the structure factor for neutrons, but contains a form factor that is different for each element. The form factor is analogous to that for magnetic neutron scattering, but instead of the spin density it is the Fourier transform of the charge density and is proportional to the atomic number Z. Unlike neutron sources, X-ray sources are cheap enough that most laboratories have one, and XRD can in this way be a useful tool for day to day sample characterisation. The positions and relative intensities of Bragg peaks can be used to identify materials using databases of known crystal structures. In this way XRD is an easy and effective way of verifying sample compositions and purity. Furthermore the Scherrer equation (2.31) can be used to determine particle sizes in the same way as for neutrons.

All the XRD work done during my PhD project has been performed with the Panalytical powder diffractometer at DTU-Cen, which is set up in the Bragg-Brentano geometry and uses a conventional Cu K_α X-ray tube. A variety of slits and filters have been used in attempts

to minimize background, divergence and other undesired contributions to the X-ray beam. A know problem with the use of Cu K_α X-rays is that it gives rise to a large background from fluorescence in Fe-containing samples because the emission energy of 8.05 keV is close to the 7.112 keV K-absorption edge of Fe. This problem could have been overcome if a monochromator had been installed in the path of the scattered beam, but such a device was unfortunately not equipped on our system. This means that there is a large isotropic background in my XRD patterns of hematite and goethite.

2.3.1 The Rietveld method

The Rietveld method is a very successful method for refining the structural parameters of a approximately known crystal structure using X-ray or neutron powder diffraction data. With neutron data the magnetic structure can also be refined. The method was developed by Hugo Rietveld in 1969 and is a least squares methods that minimises the quantity [70, 71]

$$M = \sum_i w_i (Y_{\mathrm{o}i} - Y_{\mathrm{c}i})^2, \tag{2.68}$$

where $Y_{\mathrm{o}i}$ is the observed intensity and $Y_{\mathrm{c}i}$ is the calculated intensity at the point i of the diffraction pattern. The weight w_i is based on the counting statistics $w_i = Y_{\mathrm{o}i}^{-1}$. The calculated intensity takes the form

$$Y_{\mathrm{c}i} = s \sum_H L j_H |F_H|^2 \phi (2\theta_i - 2\theta_H) P_H A + Y_{\mathrm{b}i}, \tag{2.69}$$

where s is a scale factor, $H = (h, k, l)$ represents the Miller indices of the Bragg reflections contributing to the intensity at the point i. L is the Lorentz and polarization factor also present in (2.67), F_H is the structure factor for reflection H, j_H is the multiplicity of reflection H, $\phi (2\theta_i - 2\theta_H)$ is a profile function, P_H is a preferred orientation function, A is an absorption factor and $Y_{\mathrm{b}i}$ is the background at the point i. The quality of the refinement is determined by the minimization of (2.68) and is often quantified by the weighted pattern residual

$$R_{\mathrm{WP}} = \left(\sum_i (Y_{\mathrm{o}i} - Y_{\mathrm{c}i})^2 / \sum_i w_i Y_{\mathrm{o}i}^2 \right)^{1/2}. \tag{2.70}$$

R_{WP} is a useful number for following the progress of a refinement or for comparing different models to the same data but it is generally not very useful to compare R_{WP} values for different data sets.

The success of the Rietveld methods rely on a good description of the lineshape by the used profile function $\phi (2\theta_i - 2\theta_H)$. Commonly used profile functions include the Gaussian, Lorentzian and Voigtian line shapes but many more exist. The Voigt function is a convolution of a Gaussian and a Lorentzian function and often the line broadening from the intrument can be assumed to be Gaussian and the finite size broadening from the sample can typically be assumed to be Lorentzian. This assumption of a Gaussian shape of the instrument broadening is especially well satisfied for neutron scattering, where instrumental broadening of lab X-ray sources typically have a Lorentzian component. However, in powder diffraction patterns of NPs the Lorentzian size-broadening from the sample is typically so large that any Lorentzian component from the instrument is insignificant. The width of the Lorentzian can then be assumed to depend on θ according to the Scherrer formula (2.31) (plus a term that accounts for strain broadening). The width of the Gaussian have a different 2θ dependence which can be determined by measuring a standard sample with no Lorentzian broadening (e.g. bulk Si powder), and the particle size can then be determined by refining the Lorentzian width.

Many computer programs for Rietveld refinement exist. The refinements presented here have been performed with the WINPOW program, which is a modified version of the LHMP1 program [72].

2.4 Transmission electron microscopy

The human brain is very good at interpreting images and looking at an image often gives an immediate impression of the object in the image. A measurement of some physical quantity can tell us a lot about the system under study, but when we see what the object looks like we understand it on a completely different level. This is one of the reasons why imaging methods are so powerful in helping us understand nature (although we have to be aware that our brain not always interprets the image correctly). Imaging with a microscope is a powerful method to investigate the structure of small things, but the resolution of an optical microscope is limited by the wavelength, λ, of visible light. The Rayleigh criterion is a common way to describe the resolving power, δ, of a microscope [73]:

$$\delta = \frac{0.61\lambda}{\mu \sin \beta}, \tag{2.71}$$

where μ is the refractive index of the medium and β is half the collection angle of the magnifying lens. With a wavelength of a few hundred nm for visible light and a refractive index of one the resolution of a visible light microscope is limited to about half the wavelength of the light. In a transmission electron microscope (TEM) observation angles are small and the refractive index of the electrons in the vacuum of the microscope is one and the Rayleigh criterion is reduced to $\delta = \frac{0.61\lambda}{\beta}$. The wavelength of the electrons in a TEM is typically a few picometers and atomic resolution is therefore possible. That is, it is possible to distinguish individual atoms separated by only a few Ångströms. This means that the TEM is well suited to investigate features on the nanoscale.

In this thesis the TEM has been used to determine the shapes and sizes of NPs and to look at aggregated structures of NPs. Diffraction of electrons can give information about the crystallographic structure of the material and this has been used to determine the orientation of planes of the crystal structure with respect to the particle shape for hematite and NiO NPs.

In this chapter I will give an introduction to the basic interactions between the electron and the sample in a TEM, to the different mechanisms that gives contrast in TEM images, and to the imaging scheme in a TEM. For further details the textbook by Williams and Carter [73] which covers most aspects of the TEM can be consulted. The short review of the theory of electron microscopy will start with some basic properties of the electron similar to the discussion about neutrons in section 2.1.1.

2.4.1 Basic properties of the electron

The electron is charged with charge $e = -1.602 \cdot 10^{-19}$ C, spin $s = 1/2$, and mass $m_e = 9.109 \cdot 10^{-31}$ kg. Because of the negative charge of the electron the magnetic moment is antiparallel to its spin:

$$\mu = -g\mu_B s, \tag{2.72}$$

where $g = 2.0023$ can be derived from quantum electrodynamics, and $\mu_B \equiv e\hbar/2m_e = 9.274 \cdot 10^{-24}\text{Am}^2/\text{kg}$ is known as the Bohr magneton. The magnetic moments responsible for the magnetic properties of magnetic materials are mostly electronic spins in atoms and therefore the Bohr magneton is a useful unit and it will be used throughout this thesis. Similar to the neutron the electron can be characterised by its de-Broglie wavelength $\lambda = 2\pi\hbar/p$. However, because the electrons are accelerated to large velocities ($> 0.5c$) in a TEM the calculations need to be relativistic. If the electron is accelerated from rest to a velocity v in a potential U the relativistic kinetic energy of the electron is

$$m_e c^2(\gamma - 1) = eU, \tag{2.73}$$

where c is the speed of light and $\gamma = 1/\sqrt{1 - v^2/c^2}$ is the usual relativistic factor. The relativistic momentum of the electron is

$$p = \gamma m_e v = m_e c\sqrt{\gamma^2 - 1}. \tag{2.74}$$

From (2.73) we get $\gamma = 1 + eU/m_e c^2$ and substituting this into (2.74) we can arrive at

$$p = \sqrt{2m_e eU \left(1 + \frac{eU}{2m_e c^2}\right)}. \tag{2.75}$$

Now we can obtain the de-Broglie wavelength of the electron as function of the accelerating potential U:

$$\lambda = 2\pi\hbar/p = \frac{h}{[2m_e eU\,(1 + eU/2m_e c^2)]^{1/2}}. \tag{2.76}$$

With an accelerating voltage of e.g. 200 kV this gives an electron wavelength of 2 pm and it is thus not surprising that the resolving power of a TEM is superior to that of an optical microscope which uses photons with a wavelength of a few hundred nm as probe. The short wavelength of relativistic electrons does, however, not mean that modern electron microscopes can obtain a resolution in the pm range or better (by cranking up the voltage to some MV). This is because the resolution of electron microscopes is limited by imperfections (aberrations) in the electron optical elements (lenses).

2.4.2 Imaging in the TEM

The optical configuration of a TEM is similar to an optical (transmission) microscope with a source of illumination followed by a condenser lens that focuses light onto the sample which is then followed by an objective lens that produces an image of the sample. The source of illumination is an obvious difference between the TEM and the optical microscope, but also the optical elements are different. Where the lenses in a light microscope are polished pieces of glass the lenses that control the electron beam are electromagnetic fields.

A modern TEM is a complicated instrument with many optical elements to control the properties of the electron beam and to enable different modes of operation of the instrument, but here I will neglect many complications and look at a simplified version of the imaging scheme in a TEM.

Illuminating system

The illuminating system in a TEM consists chiefly of an electron gun and a system of condenser lenses that shines the beam onto the sample. The gun can be of the thermionic or the field emission type. In a thermionic electron gun the gun material (typically W or LaB_6) is heated to a temperature where the thermal energies of electrons are large enough to overcome the binding potential and escape. The gun is kept at a large negative potential (e.g. 200 kV) with respect to an anode and the electrons are then accelerated into the column of the microscope. An electron gun of the field emission type is made of a very fine tip of e.g. tungsten that is kept at a few kV negative potential with respect to an anode. The large potential gradient at the tip enables the electrons to tunnel out of the tip and the extracted electrons are then accelerated by a second anode that is kept at e.g. 100 kV with respect to the tip. Both types of guns have their advantages and disadvantages, most noticeably the field emission gun makes it possible to produce a much more coherent and bright beam of electrons than a conventional thermionic gun making the field emission gun ideal for high resolution imaging, however it comes with a price of having to operate the gun in ultra high vacuum.

After the gun a system of condenser lenses produce a beam that is as parallel as possible on the sample (or in some cases a convergent beam). An aperture, called the condenser aperture can also be inserted to block the most diverging electrons, but at the cost of a lower beam intensity.

Imaging system

Let us assume that the sample is illuminated by a parallel beam and see how the image is formed in a TEM. For now we ignore the wave properties of the electrons and consider the
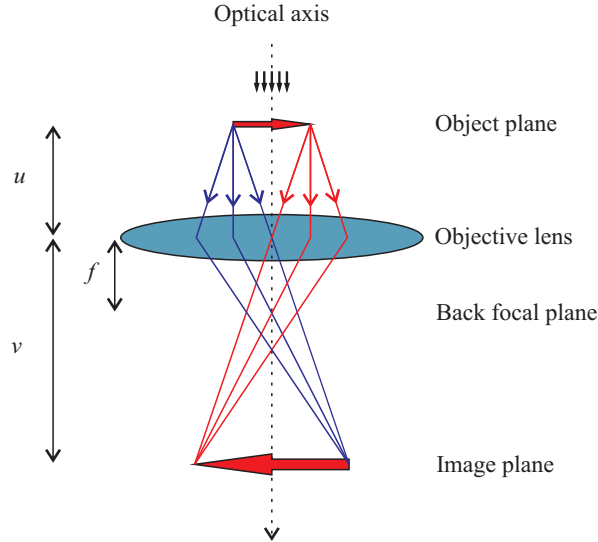
Figure 2.9: Imaging in a TEM. The sample in the object plane is hit by a parallel electron beam. The electrons transmitted through the sample form the diffraction image in the back focal plane of the objective lens and in the image plane the real space image of the sample is formed. Note that the angles are not drawn to scale as the observed angles in a TEM are typically very small ($\leq 1°$).

image formation scheme from the point of view of geometric optics in which the electrons are represented by straight line rays as in Figure 2.9. The rays from the object plane (sample) are transmitted through the objective lens placed a distance u from the sample. The focal length of the objective lens is f. Parallel rays (i.e. rays that are scattered by the same angle) are focused on a single spot in the back focal plane, creating the diffraction image of the sample. Rays originating from the same point in the sample meet at the same point in the image plane thus creating the real space image of the sample. If the viewing screen or the detector (camera) is placed in the image plane the image can be seen or recorded. The magnetic lenses in the electron microscope can be considered as thin convex lenses and Newton's lens equation can be used:

$$\frac{1}{u}\frac{1}{v} = \frac{1}{f},\tag{2.77}$$

and the magnification is given by $M = v/u$. To obtain the high magnifications in TEMs (e.g. $M = 1,000,000$) the lens is placed close to the sample so u is small and after the first magnification more lenses magnify the image further. Changing the magnification in the TEM is done by controlling the current in the coils of the magnetic lenses, thus changing f. This is analogous to rotating a different objective in front of the sample in an optical microscope.

The image is viewed on a screen coated with a substance that is fluorescent when hit by electrons or with a CCD camera. The observed intensity is proportional to time average of the square of the amplitude of the electron wave function (Ψ_i) in the image plane:

$$I(x) = \langle \Psi_i \Psi_i^* \rangle \tag{2.78}$$

where $\langle \rangle$ denotes time average (i.e. average over all the electrons hitting the screen during the acquisition time). The information to be obtained from the image is in the contrast in intensity between parts of the beam that has traveled through different parts of the sample. In the next section we will discuss mechanisms for producing contrast in a TEM.

Bright field and dark field imaging

The two most basic modes of imaging in the TEM are bright field (BF) and dark field (DF) imaging. To take a BF image an aperture, known as the objective aperture, is inserted into the

back focal plane of the objective lens (see Fig. 2.9). The aperture is centered on the optical axis and thus blocks off electrons that are scattered at high angles, and the observed intensity will be from the electrons travelling straight through the sample. In DF mode the objective aperture is displaced in the back focal plane so that the direct beam is blocked and only scattered electrons are detected. The positioning of the objective aperture in DF mode is usually done with the help of a diffraction image, making it possible to choose only electrons scattered with a certain scattering vector for the imaging. In this way some parts of the sample that did not have good contrast in the BF image may light up in a DF image. In high resolution TEM the objective aperture is removed because it limits resolution.

2.4.3 Interactions between electron and sample and contrast in TEM images

Because the electron is a charged particle it interacts through electrostatic forces with the charge of the nuclei and electrons of atoms in the sample. This interaction leads to much stronger scattering than does the short ranged nuclear forces between neutrons and nuclei, the forces between magnetic moments of the neutron and the valence electrons or even the interaction between X-ray photons and electronic charges. Because of the strong scattering of electrons by solids very thin samples are needed (typically a few hundred nm or thinner). This can of course be a disadvantage, but for NPs it is not an issue. The magnetic scattering of electrons is usually small compared to the electrostatic scattering and will not be considered here even though it can be used to image magnetic field lines in ferromagnetic samples with special TEM techniques such as electron holography and Lorentz microscopy.

The scattering cross section for electrons can be defined in the same way as for neutrons (2.4) but our objective here is to understand imaging in a TEM and we will restrict ourselves to discuss the different mechanisms that can produce contrast in TEM images. Inelastic scattering of the electrons by the sample occur in a number of processes which can be very useful in the field of analytic electron microscopy where secondary signals such as characteristic X-rays, secondary electrons and Auger electrons are measured. Here, however, we ignore the inelastic effects and consider just the elastically scattered electrons.

There are two fundamentally different types of contrast in the TEM, amplitude contrast and phase contrast and they can both be important for obtaining contrast in an image. Amplitude contrast is basically quite simple. The electrons pass straight through some parts of the sample giving a high intensity while other parts of the sample scatter electrons out of the beam leading to low image intensity from these regions. This scattering could be from crystalline material that diffracts electrons (diffraction contrast) or by amorphous material incoherently scattering electrons giving rise to a contrast that depends on the atomic number and the thickness of the scatterer (mass-thickness contrast).

Phase contrast is when the interaction between electron and sample is so weak that not the amplitude, but only the phase of the wave function is changed by the interaction. This is true only for very thin samples and is the contrast mechanism that is important in hight resolution TEM. Here it is worth noting that we cannot actually measure the phase of the wave function, and this phase problem actually means that in an ideal microscope (i.e. one without any aberrations) it is not possible to obtain contrast from phase changes. What saves us and makes high resolution imaging possible are the properties of the lenses in the TEM. To explain how phase contrast comes about we move into reciprocal space and see how the electron wave function transmitted by the sample Ψ_o is transformed to the wave function in the image plane Ψ_i. First we denote the Fourier transform of the object wave as

$$\Psi_o(q) = \mathcal{F}(\Psi_o), \tag{2.79}$$

where $\mathcal{F}$ denotes the Fourier transform from real to reciprocal space. The propagation of the wave function to the image plane is governed by the contrast transfer function (CTF) which

depends on the imperfections of the microscope. The CTF, $T(q)$, can be written (see e.g. [73]):

$$T(q) = e^{i\chi(q)}e^{-D}, \tag{2.80}$$

where $\chi(q)$ is a function that depends on the spherical aberration coefficient C_s of the microscope and on the defocus Δf (Δf is the departure from focus) and $D(q)$ is a damping function that also depend on C_s and Δf, but also on chromatic spread and the divergence of the beam. The image wave function is the inverse Fourier transform of the CTF multiplied with $\Psi_o(q)$

$$\Psi_i = \mathcal{F}^{-1}\left(\Psi_o(q)T(q)\right), \tag{2.81}$$

and the intensity on the detector is simply $\Psi_i\Psi_i^*$. What happens is in a sense that the wave function of the scattered electron is mixed with itself because of the transfer function leading to regions in the image plane of more or less constructive and destructive interference which is transfered to the image as visible contrast. The imaginary part of the CTF have been plotted as a function of q in Figure 2.10 for U = 200 kV, $C_s = 0.7$ mm, $\Delta f = -51.2$ nm, and realistic values for the other aberrations. The point where $T(q)$ first changes sign is the point resolution of the microscope. For spatial frequencies lower than this value the image can be directly interpreted with rows of atoms being imaged as dark lines. For higher spatial frequencies modelling is needed to interpret the data. When T goes towards zero no information can be obtained and the value of q where T becomes zero is hence known as the information limit.
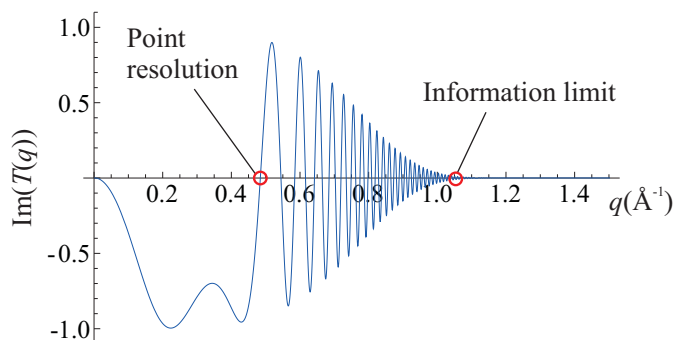

Figure 2.10: Imaginary part of the contrast transfer function with U=200 kV, $C_s = 0.7$ mm, $\Delta f = -51.2$ nm. The point resolution and the information limit are indicated on the figure. $T(q)$ first crosses the axis at q =0.48 Å^{-1} corresponding to a point resolution of 2.1 Å.

2.4.4 TEM on nanoparticles

In my PhD project I have used TEM to investigate the sizes and shapes of NPs of hematite and NiO and aggregated structures of hematite particles. All my TEM images of magnetic NPs were taken on the FEI Tecnai T20 G2 microscope at DTU-Cen shown in Figure 2.11. The Tecnai operates with a thermionic LaB_6 or W filament gun and has a point resolution of 2.4 Å.

In many cases, especially when looking at larger particle aggregates, but often also when looking at small isolated particles the largest magnifications are not the most useful because one typically wants to obtain an overview of a number of particles rather than a closeup of one single particle. In these images the scattering from the particles will give rise to mass-thickness contrast and diffraction-contrast. When one wishes to see fine details like lattice fringes high resolution phase contrast images are needed and then higher magnifications are used. To satisfy these demands I have recorded images at magnifications in the range from about M =20,000 to M =400,000. My NP samples for TEM imaging were prepared by placing a drop of NPs in suspension on a TEM grid and leave it to dry overnight. Holey carbon film on 400 mesh Cu grids with a ultrathin carbon film (less than 3 nm thick) on top, from Ted Pella Inc, were used
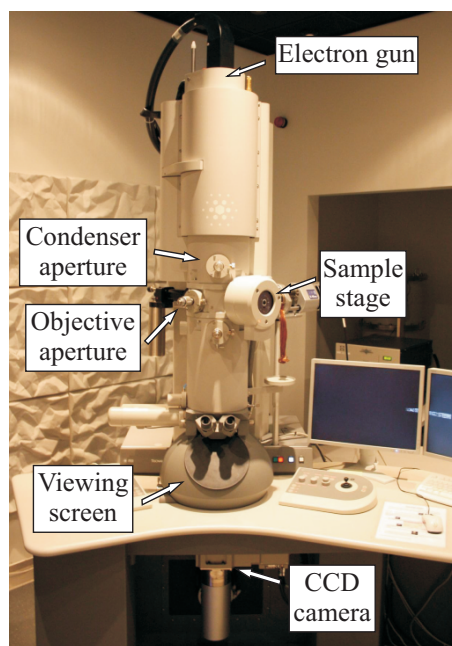
Figure 2.11: The FEI Tecnai T20 G2 microscope at DTU-Cen.

for all my samples. The ultrathin carbon on top of the holey carbon is ideal for suspending NPs for obtaining good high resolution images. All my TEM images were taken with an acceleration voltage of 200 kV. Examples of TEM image of α-Fe$_2$O$_3$ NPs at medium and high magnification are shown in Figure 2.12. The image at intermediate magnification (43,000$\times$) shows several hundred NPs dispersed on the TEM grid while the image at high magnification (400,000$\times$) shows a zoom-in on a few particles. The contrast in the medium magnification is due to mass-thickness contrast and diffraction contrast because the particles are crystalline. In the high magnification image phase contrast is important and lattice fringes from the α-Fe$_2$O$_3$ structure are visible.
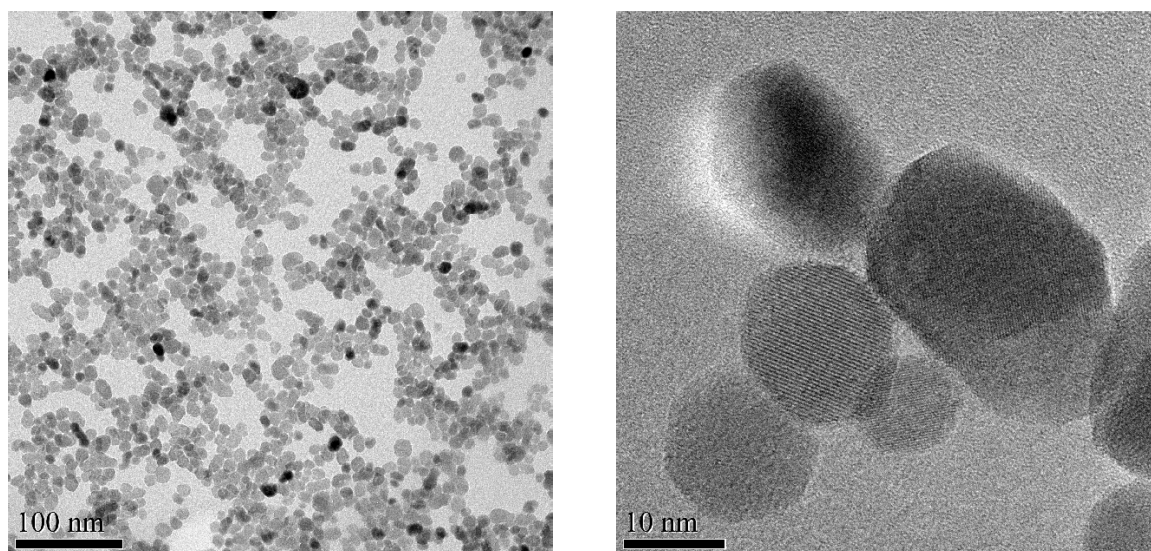

Figure 2.12: TEM images of α-Fe$_2$O$_3$ nanoparticles at magnifications of $M = 43,000$ (left) and $M = 400,000$ (right). The images are of two different samples.

37

2.5 Dynamic light scattering

Particles suspended in a liquid undergo Brownian motion due to bombardment of the particles with the solvent (e.g. H_2O) molecules, and measurement of these random fluctuations can be used to determine the size distribution of particles on the nanoscale with a technique known as dynamic light scattering (DLS). DLS is a well established technique that can be studied in textbooks. [74] Here I will explain how the technique works without too much detail. In principle a DLS instrument is quite simple. A laser shines light onto the suspended particles, the scattered light is measured on a detector, and the fluctuations in the intensity on the detector is related to the time scale of the Brownian motion, which in turn is related to the particle size. The diffusion of a spherical particle in a liquid is described by the translational diffusion coefficient (see e.g. [74]), through the Stokes-Einstein equation:

$$D = \frac{k_B T}{3\pi \eta d_H},$$ (2.82)

where D is the translational diffusion coefficient, η is the viscosity of the fluid, and d_H is known as the hydrodynamic diameter of the particle. The hydrodynamic diameter of a particle is the diameter of a spherical particle with the same translational diffusion coefficient as the particle. The hydrodynamic diameter depends on the size and shape of the particles, but also on any surface structure. Also the so-called electrical double layer consisting on ions at the particle surface and screening counter ions that are bound tightly enough to move with the particle in the suspension contributes to d_H. If the particle is a perfect sphere d_H in (2.82) can be replaced with the particle diameter d.

If the suspended particles are small compared to the wavelength of the radiation, which is typically in the visible regime, the scattering is isotropic. In this so-called Rayleigh scattering regime the scattered intensity is proportional to d^6 and inversely proportional to λ^4. [75] If the criterion for Rayleigh scattering ($\frac{d}{\lambda} << 1$) is not fulfilled the scattering is not isotropic. The scattering from spherical particles of any size is described by Mie theory, which has the Rayleigh theory as its limiting case for small particles. In a DLS experiment the measured quantity is simply the total intensity on a small detector as a function of time. The intensity $I(t)$ at time t is then compared to the intensity a small time interval, τ, later. More specifically a digital component known as a correlator measures the autocorrelation function of the scattered intensity, which is mathematically defined as:

$$G(\tau) = \langle I(t)I(t+\tau)\rangle = \lim_{t\to\infty} \int_T^T I(T)I(t+\tau)dt.$$ (2.83)

For monodisperse particles the correlation function will be an exponential decaying function of the sample time τ:

$$G(\tau) = A\left[1 + B\exp\left(-2\Gamma\tau\right)\right],$$ (2.84)

where $\Gamma = q^2 n^2 D$ has been defined. Here q is the scattering vector as defined in (2.10)[1] and n is the index of refraction of the dispersant. The constant A is the baseline of the exponential and B is the intercept and depends on the area of the detector. For a polydisperse sample the correlation function becomes

$$G(\tau) = A\left[1 + Bg_1^2(\tau)\right],$$ (2.85)

where $g_1^2(\tau)$ is a sum of exponential decays. The particle size distribution (PSD) can then be obtained from a fit of the measured correlation function to (2.84) or (2.85). The measured correlation coefficient, $\langle I(t)I(t+\tau)\rangle / \langle I(t)\rangle^2$, for a sample of hematite NPs in aqueous suspension is given in Figure 2.13.

---

[1]In DLS theory it is customary to define the scattering vector as $q = 2kn\sin(\theta/2)$with θ being the scattering vector, but here we will stick with the notation used in previous sections.
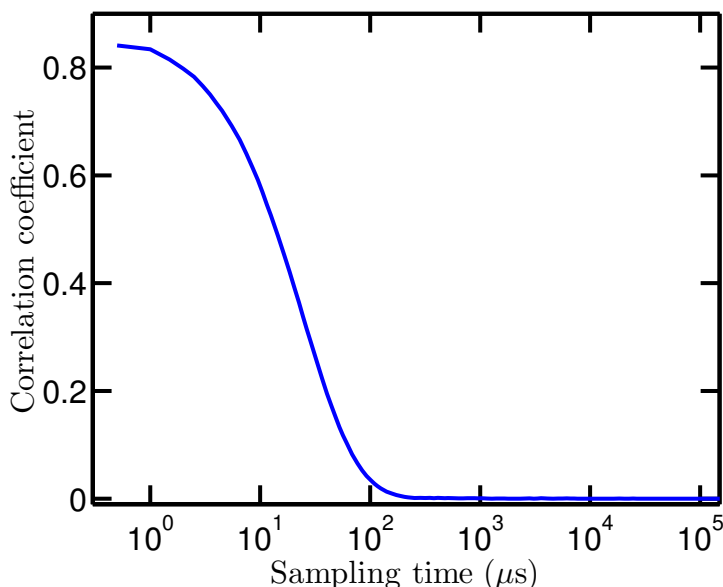
Figure 2.13: Correlation coefficient of a sample of hematite NPs in aqueous suspension measured at 25°C. The 'cutoff' point where the curve decays from its initial value close to unity depends on the particle size. The slope of the decay depends on the polydispersity of the sample.
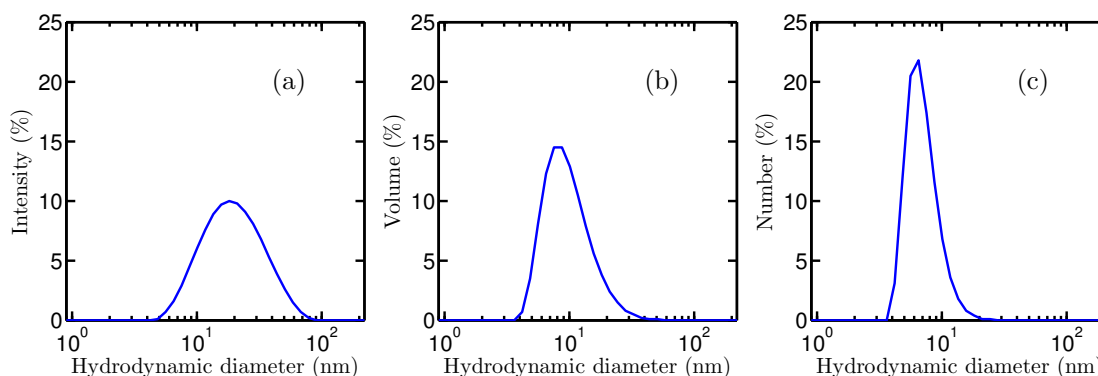

Figure 2.14: Size distribution of hematite NPs in aqueous suspension from the correlation data in Figure 2.13. (a) Intensity distribution, (b) Volume distribution, (c) Number distribution.

The size distribution obtained from the correlation data is a the distribution of the scattered intensity as function of particle size, known as the intensity distribution. The intensity distribution can be converted to volume distribution or number distribution using Mie theory. Because of the strong dependence of the intensity on d in the Rayleigh regime the largest particles dominates the intensity distribution. If one instead looks at the the volume distribution the larger particles are less dominating, but of course particles with a large diameter have a large volume, and are therefore more prominent in the volume distribution. In the number distribution the particle size is the unweighted nuber-average. When one decides which particle size to quote, it is important to be aware of these differences, but it is not given that the number distribution is always the best choice. The best value to use depends on what other types of measurements you wish to compare with, and it is also worth noting that when you do the conversion from one distribution to another you introduce a possible source of systematic error. Intensity- number- and volume distributions from the correlation data in 2.13 are presented in Figure 2.14.

39

2.5.1 DLS instrument

The light scattering work in this thesis was performed with a commercial instrument, a Malvern Zetasizer Nano ZS at DTU-Physics. The layout of the instrument is presented in Figure 2.15. Because it is commercial some details about the components of the instrument are industrial secrets. The instrument is relatively compact, with all the components fitted into a box that can fit on a desktop. The light source is a 4 mW He-Ne laser with a wavelength of 632.8 nm. The liquid sample is in a rectangular plastic cuvette, with polished sides facing the laser. The sample temperature is controlled. In our case the sample was kept at 25 °C in all measurement. In the path between the laser and the sample there is an attenuator to prevent saturation of the detector, and a focusing lens to select the measurement position in the sample. The instrument is in a back-scattering geometry, with a scattering angle of 173°. The focusing lens with the back-scattering geometry makes it possible to measure very dense samples by selecting a measurement point not very far into the sample. A small portion of the speckle pattern from the interference between the scattering from different particles is measured by the detector, which transmits its signal to the digital correlator, which computes the autocorrelation function. The analysis of the DLS data was performed with the software provided with the instrument which outputs the intensity, volume and number PSDs and corresponding intensity- volume- and number weighted average hydrodynamic diameters.
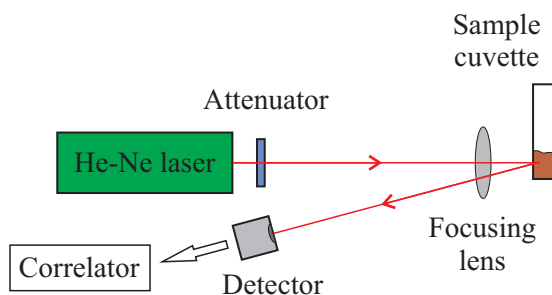

Figure 2.15: The layout of a backscattering DLS instrument like the Malvern Zetasizer Nano ZS. The components are described in the text.

2.5.2 Limitations of DLS

DLS is an easy to use method for determining particle sizes of particles in suspension, and it has the advantage of providing not only an average size but also the size distribution. It can be used to measure particle sizes in quite a wide range from below a nanometer to above a micron, and it can handle a wide range of concentrations. There are however, limitations of the usefulness of the technique. One severe limitation is that the sample has to bee in a reasonable stable suspension. If the particles are aggregating or sedimenting during the measurement, which takes a few minutes, the method does not work. If the sample is very polydisperse determining the size distribution with DLS can be problematic because the signal from the smaller of particles tends to be drowned in the strong signal from the larger particles. The particle size measured with DLS is the hydrodynamic diameter. If the particles are far from the ideal spherical particles with no surface structure the size measured with DLS may be difficult to interpret to get a useful number.

2.5.3 The ζ-potential

The ζ-potential is the potential at the edge of the electric double layer with respect to the potential in the dispersant. For a colloidal suspension of NPs the particles can be kept apart by electrical repulsion between the particles that are charged. In this type of system the ζ-potential is a measure of the stability of the suspension. The ζ-potential of a suspension can be

changed by varying the PH or the ionic strength in the medium. The Zetasizer Nano ZS has the possibility to measure the ζ-potential of suspensions by applying an alternating electrical field via two electrodes connected to a special sample cell for measurement of ζ-potential. In the presence of an electrical field the charged particles will start to move with a velocity that is related to their ζ-potential. In a ζ-potential measurement the laser beam is split in two. One goes through the sample and the other is a reference beam. The two beams are brought together on the detector, and the interference between the scattered- and the reference beam is measured. This gives information about the motion of the particles, which can be translated into the ζ-potential.

2.6 Mössbauer spectroscopy

In Mössbauer spectroscopy the resonant emission and absorption of gamma rays is used to obtain information about the electric and magnetic fields surrounding the nucleus. Because of conservation of momentum the decaying nucleus recoils with a momentum equal to that of the emitted gamma ray. This reduces the gamma energy, bringing it out of resonance with a nucleus that could have absorbed it. The same consideration is true for the absorbing nucleus. However, in 1957 Mössbauer discovered that nuclei in solids under the right circumstances can emit and absorb gamma rays without any energy loss to recoil [76,77]. Mössbauer received the 1961 Nobel prize [78] for his discovery of the recoil free emission and absorption of gamma rays, which is now known as the Mössbauer effect. The short review of the basic theory of Mössbauer spectroscopy is heavily inspired by the course notes by Steen Mørup [43].

2.6.1 The Mössbauer effect

When a gamma ray is emitted from an atomic nucleus decaying from an excited state of energy E^* to a ground state E_0 the equations for conservation of energy and momentum are

$$E^* = E_0 + E_\gamma + E_R$$
$$0 = p_R + \frac{E_\gamma}{c}, \tag{2.86}$$

where E_γ is the energy of the gamma ray, E_R is the recoil energy, p_R is the recoil momentum and $\frac{E_\gamma}{c}$, with c being the velocity of light, is the momentum of the gamma ray. For the recoiling nucleus with mass m the recoil energy is

$$E_R = \frac{p_R^2}{2m} = \frac{E_\gamma^2}{2mc^2}. \tag{2.87}$$

The condition for resonant emission and absorption is that the difference between the excited state and the ground state is (almost) equal to the energy of the gamma ray, i.e.

$$E^* - E_0 = E_\gamma + E_R, \tag{2.88}$$

where E_R is negligible. This is in general not the case, but for nuclei in a solid the mass of the nucleus m in (2.87) is replaced with the much larger mass of the entire crystal, and the resonance condition can be fulfilled within the natural line width of E^*. However, for the resonance to take place it is required that the recoil momentum is imparted to the the entire crystal as translational energy, and not to lattice vibrations (phonons). The probability of such a recoil free event is described by the Lamb-Mössbauer factor, f, which is closely related to the Debye-Waller factor previously introduced

$$f = \exp\left(-\frac{E_\gamma^2}{\hbar^2 c^2} \left\langle u^2 \right\rangle\right), \tag{2.89}$$

where $\left\langle u^2 \right\rangle$ is the mean square displacement of the nuclei. For this probability to be large it is necessary to use an isotope with a low lying excited state, and not to work at too high

temperatures. For some isotopes this can be achieved at room temperature. The natural line width of the excited state is $\Gamma = \hbar/\tau$, where τ is the lifetime of the excited state (Heisenberg's uncertainty principle). To find a suitable isotope for Mössbauer spectroscopy it is thus necessary to find one with an exited state with a lifetime long enough to obtain the required energy resolution.

2.6.2 ^{57}Fe Mössbauer spectroscopy

A very useful isotope for Mössbauer spectroscopy is ^{57}Fe, and it is by far the most widely used. The used transition is the 14.41 keV transition between the $I = \frac{3}{2}$ excited state and the $I = \frac{1}{2}$ ground state (I being the nuclear spin). The recoil free fraction of the decays (2.89) is close to 1 even at room temperature, and the 141 ns lifetime gives a relatively low spectral linewidth. ^{57}Fe thus has very suitable parameters for Mössbauer spectroscopy, and furthermore iron is a common element that is important for many industrial applications, and this is perhaps the main reason for the popularity of ^{57}Fe over other isotopes. The fraction of ^{57}Fe in naturally occurring Fe is about 2.14%, which is usually enough to produce good signals without the need for isotope substitution. The excited ^{57}Fe can be produced from ^{57}Co, which decays to ^{57}Fe with a half life of 270 days (see Fig. 2.16).
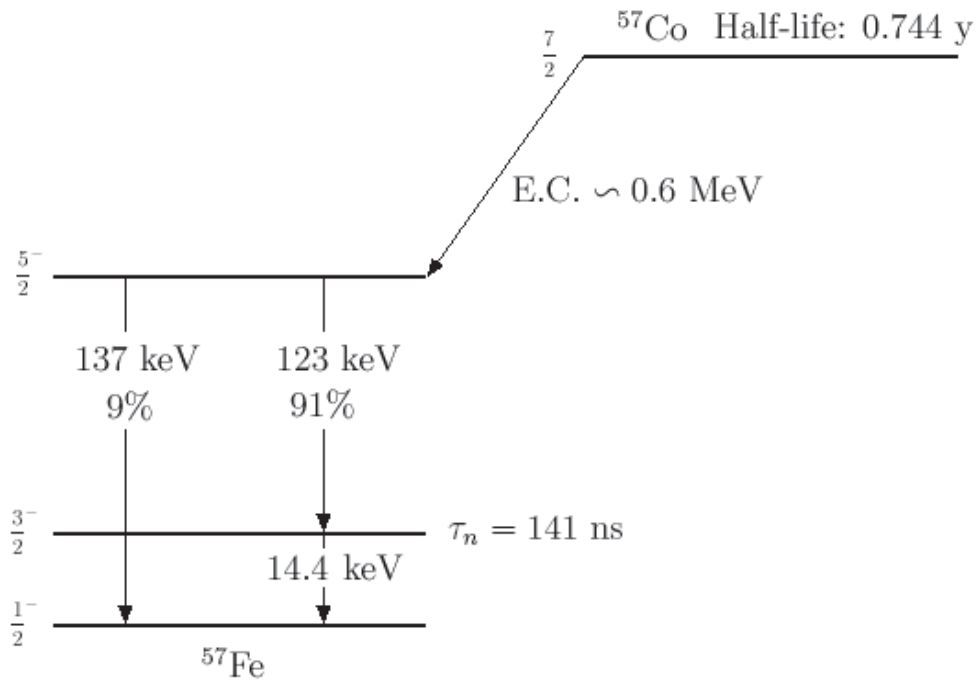

Figure 2.16: Decay scheme of ^{57}. The transition used for Mössbauer spectroscopy is the 14.4 keV transition from the excited state if ^{57}Fe with nuclear spin $I = 3/2$ to the ground state with $I = 1/2$. Figure from [43]

In Mössbauer spectroscopy the Doppler effect is used to tune the gamma ray energy in and out of resonance with the absorber. If the ^{57}Fe source is moved with a velocity v the energy of the gamma ray is shifted to

$$E(v) = E_\gamma \left(1 + \frac{v}{c}\right). \tag{2.90}$$

The energy will still be in the resonance if the Doppler shift is smaller than the halfwidth of the absorption line. It can be shown that the absorption line is a Lorentzian, and with the 141 ns life time of the ^{57}Fe excited state the the half width of the Lorentzian is 0.19 mm/s. The basic layout of a Mössbauer spectrometer is sketched in Figure 2.17
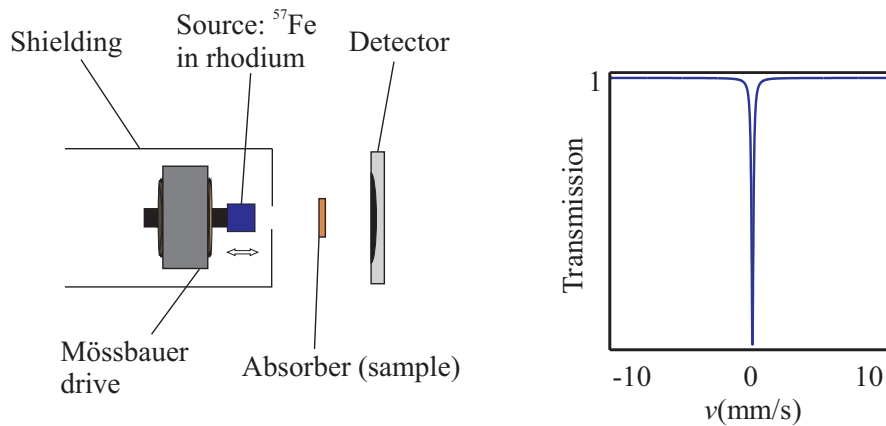
Figure 2.17: The layout of a Mössbauer spectrometer. The gamma ray energy of the source is Doppler shifted by placing it on the Mössbauer drive that moves back and forth with constant acceleration. The gamma rays are sent through the sample (absorber) and the transmission is measured by a detector on the other end. The resonance in ^{57}Fe gives rise to a single Lorentzian line 0.19 mm/s in width.

The precise energy of a nucleus is affected by electric and magnetic fields in the surroundings. These changes in nuclear energies, known as hyperfine structure, can be detected with Mössbauer spectroscopy with an energy resolution determined by the intrinsic linewidth. For ^{57}Fe Mössbauer spectroscopy the intrinsic linewidth of 0.19 mm/s corresponds to an energy resolution of 4.6 neV.

2.6.3 Hyperfine interactions

There are three principal hyperfine interactions each affecting the Mössbauer spectrum in different ways. All three can give useful information about the state of the system. The three interactions, their effect on the spectrum, and what information can be extracted from these effects will be described shortly below.

The isomer shift - Electric monopole interaction

Because of the nonzero volume of the nucleus and the nonzero density of the s-electrons inside the nucleus there are electrostatic forces between the charge distribution of the nucleus and of the the s-electrons. This is the so-called electric monopole interaction. The extend of the nucleus in the $I = 3/2$ excited state is in general different than in the ground state, leading to a small change in the gamma ray energy. The density of s-electrons at the nucleus in general differs between nuclei in different chemical environments. If the chemical environments of the source and absorber nuclei are different this leads to a relative shift of the resonance energy, known as the isomer shift. The isomer shift can be shown to be [43]

$$\delta = \frac{1}{\epsilon_0} Z e^2 \left(R_e^2 - R_g^2 \right) \left(|\psi_a(0)|^2 - |\psi_s(0)|^2 \right), \tag{2.91}$$

where ϵ_0 is the vacuum permittivity, Ze is the charge of the nucleus, R_e and R_g are the radii of the nucleus in the excited and ground states respectively, and $-e\,|\psi_a(0)|^2$ and $-e\,|\psi_s(0)|^2$ are the s-electron charge densities at the nucleus for the absorber and source atoms. The density of s-electrons at the nucleus depends on screening effects from other electrons, and the isomer shift δ can thus give information about not only the oxidation state of the atoms but also about its chemical bonds. The isomer shift is usually given relative to that of metallic iron measured at room temperature.

The quadrupole splitting - Electric quadrupole interaction

In the above it was implicitly assumed that the nuclear charge distribution was spherically symmetric. However, this is not the case for nuclei with $I > 1/2$, like in the excited state of ^{57}Fe. The non spherical symmetry of the nuclear charge is characterised by the electric quadrupole moment Q of the nucleus, which can be found as a volume integral of the nuclear charge density ρ_n:

$$eQ = \int \rho_n(r)r^2 \left(3\cos^2(\theta) - 1\right) dV, \tag{2.92}$$

where e is the proton charge. For nuclei with $I > 1/2$ Q is nonzero and can interact with any asymmetric electric field from the surrounding electrons. An asymmetric electric field can come from the charges of neighbouring atoms or from asymmetrically distributed valence electrons. This leads to a splitting of the energy levels of the $I = 3/2$ state into degenerate states with magnetic quantum numbers $m_I = \pm 1/2$ and $m_I = \pm 3/2$. The Mössbauer spectrum will thus consist of a doublet instead of a single line. The energy of a non-spherical nucleus in an electrostatic field depends on the gradient of the electric field (EFG). The EFG is in general a tensor V_{ij}, but if it is axially symmetric it can be specified with only one parameter V_{zz}. In this case the quadrupole splitting is

$$\Delta E_Q = eQ\frac{V_{zz}}{2}. \tag{2.93}$$

If the nuclear environment has cubic symmetry the EFG is zero and there is no quadrupole splitting of the spectrum.

The Zeeman splitting - magnetic dipole interaction

In the presence of a magnetic field the nuclear states split up into $2I + 1$ states because of the magnetic dipole interaction between the magnetic moment of the nucleus and the magnetic field. The energy of nucleus with magnetic quantum number m in a magnetic field, B is

$$E_m = -g_N\mu_N Bm_I, \tag{2.94}$$

where μ_N is the nuclear magneton, g_N is the nuclear g factor, which is not the same in the ground and excited state. The energy of the ground state thus splits into 2 levels with $m_I = -1/2$ and $m_I = 1/2$, and the excited state splits up into 4 levels with m_I=-3/2, -1/2, 1/2 and 3/2. Because the gamma photon can only change its angular momentum with zero or unity the selection rule $\Delta m_I = 0, \pm 1$ applies for the Mössbauer transitions, leading to a sextet of lines in the spectrum.

The magnetic field $\mathbf{B}$ at the site of the nucleus is a sum of any applied field $\mathbf{B}_{\mathrm{Appl}}$ and the total internal field, known as the hyperfine field $\mathbf{B}_{\mathrm{hf}}$. The hyperfine field is itself a combination of contributions from the orbital and spin angular momentum of the electrons and the so-called Fermi contact term $\mathbf{B}_C$. The Fermi contact term is due to the s-electron spin density at the site of the nucleus, which is nonzero for magnetic atoms, where the unpaired valence electrons polarise the s-electrons, leading to a nonzero s-electron spin density at the nucleus. $\mathbf{B}_C$ is often the dominating term and can be on the order of 50 T (e.g. in α-Fe$_2$O$_3$), which is much larger than stable magnetic fields produced in laboratories.

Combined quadrupole and magnetic dipole interaction

When quadrupole and magnetic dipole interaction is present at the same time the energy levels are more complicated to calculate. However, in the common situation where the magnetic dipole interaction is much larger than the electric quadrupole interaction the nuclear levels with $I = 3/2, m_I = \pm 3/2$ are shifted by an amount ϵ and the levels with $I = 3/2, m_I = \pm 1/2$ are shifted by the same amount in the opposite direction. Which of the levels are shifted up and down respectively depends on the sign of V_{zz}. For an axially symmetric EFG, forming an angle θ with the magnetic field the nuclear energies are

$$E_{Q,M} = -g_N\mu_N Bm_I + (-1)^{|m_I|+\frac{1}{2}}\frac{eQV_{zz}}{8}\left(3\cos^2\theta - 1\right). \tag{2.95}$$
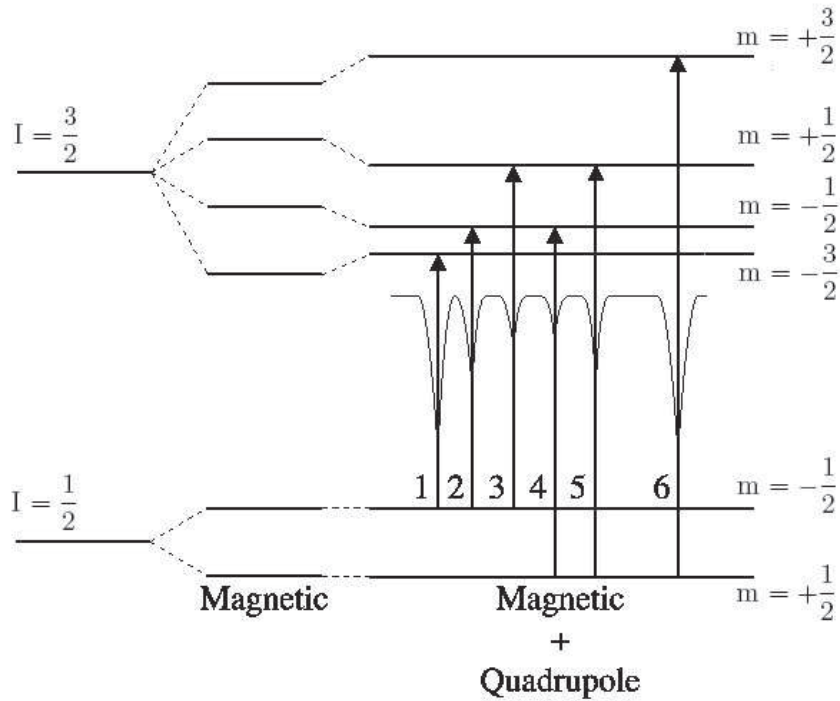
Figure 2.18: Energy levels and possible transitions in ^{57}Fe Mössbauer spectroscopy where both magnetic dipole and electric quadrupole interaction is in effect. Figure from [43]

The first term in the equation is the magnetic energy and the second is the quadrupole shift ϵ. The result of the combined quadrupole and hyperfine interactions is a Mössbauer spectrum of line lines with uneven spacing between them as indicated in Figure 2.18.

2.6.4 Magnetic relaxation

If the hyperfine field is not constant during the time scale of the Mössbauer measurement due to e.g. SPM relaxation the Mössbauer observed spectrum will depend greatly on the timescale of the relaxation τ compared to the experimental time scale, which is the nuclear Larmor precession time, $\tau_{\mathrm{L}} \approx 10^{-9}$ s. If $\tau \gg \tau_0$ the relaxation is slow from the point of view of Mössbauer spectroscopy and the spectrum will consist of a well defined hyperfine sextet. If $\tau \ll \tau_0$ the relaxation is fast and the magnetisation changes direction many times during the measurement. Consequently, only the average hyperfine field is seen, which is zero for SPM relaxation between two easy directions 180° apart. In this case the spectrum will consist of a single line, or two lines if the is quadrupole interaction in the sample. In the case where $\tau \approx \tau_0$ the absorption lines will be broadened and the resulting spectra are complicated.

2.6.5 Mössbauer instrument

The Mössbauer spectroscopy experiments presented in this thesis have been performed at the spectrometers at DTU Physics. The spectrometers were constant acceleration ^{57}Fe spectrometers with sources of ^{57}Co in a film of rhodium. The instruments were calibrated using a 12.5 μm foil of α-Fe at room temperature. Measurements were performed at temperatures from room temperature down to 20 K using liquid nitrogen cryostats (down to 80 K) or a closed cycle helium refrigerator (down to 20 K).

2.7   Magnetisation measurements

Measurements of the total magnetisation of samples of magnetic materials as function of temperature or applied magnetic field can give information about both the macroscopic magnetic characteristic of the sample but also indirectly about the microscopic magnetic properties and it is often the first experimental method used for investigating magnetic samples. The magnetic field produced by a sample is typically measured by moving the sample close to an electric circuit (a pickup coil) and measuring the resulting current induced in the coil. In very sensitive magnetometers known as superconducting quantum interference devices or SQUIDs the magnetic flux through a superconducting loop with two Josephson junctions are measured. In this way very small changes in the magnetic flux can be measured.

The magnetisation can be measured in a constant magnetic field (DC magnetisation) or in an alternating field (AC magnetisation). Here I will briefly describe the types of magnetisation measurements that were used to measure the magnetisation of ultra-small goethite NPs presented in section 3.2. The magnetisation measurements were performed using the Quantum Design MPMS XL 5 magnetometer at the Department of Chemistry, University of Copenhagen. The system employs a SQUID detector and can perform accurate AC and DC magnetisation measurements at temperatures down to that of liquid helium (4.2 K).

2.7.1   DC magnetisation

Zero field cooled an field cooled magnetisation

A common way of characterising magnetic NPs is to measure the zero field cooled (ZFC) and field cooled (FC) magnetisation as a function of temperature. In the ZFC measurement the sample is cooled from a high temperature to the lowest measurement temperature in absence of an applied magnetic field. A (usually small) magnetic field is applied and the sample is heated while the magnetisation of the sample is measured at regular temperature intervals. The FC measurement is performed similarly but with the magnetic field applied already during the cooling.

In the ZFC measurement the magnetic moments are usually assumed to be frozen in random directions during the cooling and the magnetic moment at the lowest temperature is therefore close to zero. For AFM NPs undergoing SPM relaxation there will be a peak in the ZFC magnetisation at a position that for noninteracting monodisperse particles correspond to the SPM blocking temperature. However inter-particle interactions and a particle size distribution will in general change the peak position. [8] In the FC magnetisation measurement the magnetic moments are frozen in a preferred orientation determined by the direction of the field and the measured magnetisation at the lowest temperature is high. At a temperature higher than the blocking temperature all the particles are SPM and the ZFC and FC curves coincide.

AC susceptibility

In an AC susceptibility measurement the applied field can be written as $b(t) = b_0 \sin(\omega t)$, where ω is the angular frequency and t the time. The magnetisation is measured as function of temperature angular frequency $M(\omega, T) = \chi_{\mathrm{AC}} b_0$. The complex AC susceptibility is given by

$$\chi_{\mathrm{AC}}(\omega, T) = \chi'_{\mathrm{AC}}(\omega, T) - i\chi''_{\mathrm{AC}}(\omega, T), \qquad (2.96)$$

where $\chi'_{\mathrm{AC}}(\omega, T)$ and $\chi''_{\mathrm{AC}}(\omega, T)$ are the in-phase and out-of-phase AC susceptibility respectively. Like in the FC/ZFC curves there will in be a peak in the AC susceptibility corresponding to the SPM blocking temperature and if the SPM relaxation is following the Néel-Brown expression (1.3) the anisotropy constant K and the SPM attempt time τ_0 can be determined from an analysis of the peak position as function of ω. [8,79] However this determination requires monodisperse particles or a full analysis of the shape of the AC susceptibility curves and knowledge about the size distribution. [79]

Canted spin structures and goethite nanoparticles

In this chapter I present a model of how a simple two dimensional ferrimagnetic structure can lead to an anomalous temperature dependence of the magnetisation, which is qualitatively in agreement with observations of the low temperature magnetisation of ferrimagnetic nanoparticles and diamagnetically substituted bulk ferrites. The model shows that transverse relaxation of canted spin structures can explain both an increase and a decrease in the magnetisation at low temperatures, depending on the relative size of the interactions. While the spin structure in the model is a two dimensional ferrimagnet qualitative similar results should be expected for transverse relaxation of canted surface spins in a three dimensional AFM. The model is also presented in Papers [1, 2]. In the second part of the chapter I will present some results on ultra-small goethite NPs that are in qualitative agreement with the model.

3.1 Temperature dependence of the magnetisation of canted spin structures

An anomalous temperature dependence of the magnetisation at low temperatures has been reported for ferrimagnetic NPs and diamagnetically substituted bulk ferrites. An increase in the magnetisation at low temperatures has been observed in NPs of γ-Fe$_2$O$_3$ (maghemite) [80, 81] and in ferrite NPs (MnFe$_2$O$_4$, CuFe$_2$O$_4$, NiFe$_2$O$_4$, CoFe$_2$O$_4$) [82–84]. In NPs of the same materials prepared with different methods an anomalous decrease in magnetisation has been measured [85, 86] . The magnetisation in diamagnetically substituted bulk ferrites show a similar decrease in the magnetisation with decreasing temperature [87, 88]. This anomalous temperature dependence has been proposed to originate from freezing of canted spin structures [18, 82, 84]. Canted spin structures are in general very complicated [89] and analytical calculations of the dynamics are usually not possible.

As discussed in the introduction the low symmetry of surface atoms on magnetic NPs can lead to magnetic frustration and non collinear (canted) spin structures. However, if canted spins were only a surface phenomenon the relative number of canted spins should increase with decreasing particle size and a number of studies have shown that this is not always the case [90–92]. Canted spins in the interior of particles and in bulk materials can be due to vacancies or substituted diamagnetic ions giving a low symmetry of the neighbouring spins [18].

We present analytical calculations of the temperature dependence of the magnetisation for a simple two dimensional ferrimagnetic structure with spin canting due to a vacancy in the interior of the particle. The modelled spin structure is the two dimensional lattice of spins on two sublattices A and B shown in Figure 3.1. The spins in the A-sublattice are represented with bold arrows and the remaining arrows are spins on the B-sublattice. The A-B interaction and B-B interaction are both AFM but the A-B interaction is assumed stronger than the B-B
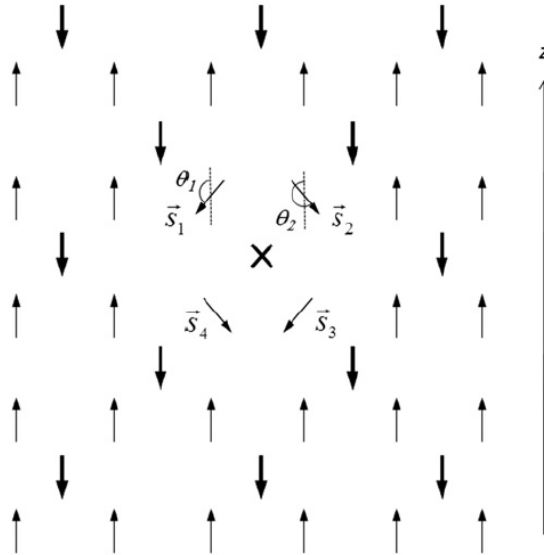
Figure 3.1: A simple two dimensional ferrimagnetic structure. The bold arrows represent A-site spins and the remaining arrows B-site spins. The × represents a missing A-site spin. The missing A-site spin leads to canting of the nearest neighbours to the vacant site. The drawing is from Paper [1]

interaction leading to a ferrimagnetic configuration with spins in the A sublattice antiparallel to the spins in the B-sublattice in the defect free structure. A missing A-site spin represented with a × in Figure 3.1 results in canting of the 4 nearest neighbours on the B-sublattice. For symmetry reasons the canting angles of the four canted spins are assumed to be pairwise identical so the canted structure can be described by the two angles θ_1 and θ_2 defined in Figure 3.1. For simplicity we only consider canting of the nearest neighbours to the missing A-site spin and assume the remaining spins to be collinear. The spins are considered as classical spins, and neglecting magnetic anisotropy the magnetic energy of the structure is [18, 93]

$$E\left(\theta_1, \theta_2\right) = a\left(\cos\theta_1 + \cos\theta_2\right) + b\cos(\theta_1 - \theta_2), \tag{3.1}$$

where

$$a = 4\lambda_{\mathrm{BB}} - 2\lambda_{\mathrm{AB}} + 2\lambda_{\mathrm{L}} - 2\mu B \tag{3.2}$$

and

$$b = 4\lambda_{\mathrm{BB}}. \tag{3.3}$$

Here λ_{BB} is the nearest neighbour B-B exchange coupling, λ_{AB} is the nearest neighbour A-B exchange coupling and λ_{L} is the exchange coupling between a B-site spin and more distant ions. The magnetic moment of B-site spins is μ and the magnetic field B is applied in the z-direction. λ_{BB} is positive and there is thus an energy cost associated with having the B-site spins parallel. λ_{AB} is also positive and the minus in the λ_{AB} term in (3.2) is because the B-site spins are pointing in the negative z-direction. Both the A-B and B-B exchange are thus AFM.

The minima and maxima of (3.1) can be found by differentiating with respect to θ_1 and θ_2. The minima and maxima are found to be [18] the collinear states with $\theta_1 = 0°$ or $180°$ and $\theta_2 = 0°$ or $180°$, and for $-2 > a/b > 2$ also the canted states with $\cos\theta_1 = \cos\theta_2 = \cos\theta_c = -a/2b$. The minimum is the canted state with energy

$$E(\theta_c, -\theta_c) = E(-\theta_c, \theta_c) = -b - \frac{a^2}{2b} \tag{3.4}$$

48

and the maxima are the collinear states with energies

$$E(0°, 0°) = 2a + b$$
$$E(180°, 180°) = -2a + b$$
$$E(0°, 180°) = -b$$
$$E(0°, 180°) = -b. \tag{3.5}$$

For an arbitrary θ_1 the values of θ_2 that minimizes the energy is given by (see Paper [1])

$$\tan\theta_2 = \frac{b\sin\theta_1}{a + b\cos\theta_1}. \tag{3.6}$$

Using this expression the energy can be found as function of θ_1 (see Paper [1]):

$$E(\theta_1) = a\cos\theta_1 - \sqrt{a^2 + b^2 + ab\cos\theta_1}. \tag{3.7}$$

The magnetic energy of the four canted spins as function of θ_1 (3.7) is plotted in the left panel of Figure 3.2 for $b/k_B = 200$ K and a/b in the range from 1.1 to 1.9. At zero temperature the system will be in an energy minimum and the total magnetic moment of the four canted spins will me $M_0 = 4\mu\cos\theta_c = -2\mu a/b$. At higher temperatures the spins directions will fluctuate and if the thermal energy is high enough the spins may overcome the energy barrier at $(\theta_1, \theta_2) = (180°, 180°)$. If $1.7 \leq a/b < 2$ the energy barrier is less than 10 K and the transverse relaxation can take place at low temperatures. The average of the z-component of the magnetic moment is $\langle M^z(T)\rangle = 2\mu\langle\cos\theta_1 + \cos\theta_2\rangle$, where $\cos\theta_2$ can be found from (3.6) and $\langle\rangle$ denotes thermal average. The thermal average magnetic moment can be calculated using Boltzmann statistics:

$$\langle M^z(t)\rangle = 2\mu\frac{\int\exp(-E(\theta_1/k_B)(\cos\theta_1 + \cos\theta_2)\sin\theta_1 d\theta_1}{\int\exp(-E(\theta_1/k_B)\sin\theta_1 d\theta_1}. \tag{3.8}$$

Numerically calculated values of $\langle M^z(t)\rangle$ are displayed in the right panel of Figure 3.2 for $b/k_B = 200$ K and values of a/b between 1.1 and 1.9 and between -1.1 and -1.9. At low temperatures the magnetic moment (and hence the magnetisation) of the canted spin structure increases or decreases significantly with decreasing temperatures.

Treating a system consisting of four spins as classical is of course a rough approximation and to accurately predict the temperature dependence of the magnetisation in the canted spin structure a quantum mechanical model should be employed. This was done in Paper [1] for spin $S = \frac{1}{2}$ and spin $S = 1$ giving results in qualitative agreement with the classical model.

The model presented here of a simple two dimensional ferrimagnetic structure with a cation vacancy shows that the magnetisation of canted spin structures can have a sharp increase or decrease at low temperatures due to transverse relaxation of the canted spins.

Of course most realistic canted spin structures are much more complicated than the two dimensional structure in Figure 3.1. Magnetic structures exist where a strong anisotropy confines the magnetic moments to be within a certain plane (e.g. AFM hematite above the Morin temperature) but for most realistic systems the model should be extended to three dimensions and a magnetic anisotropy should be added to the model. Even though the model is simple it shows at least qualitatively that transverse relaxation of canted spins can significantly influence the temperature dependence of the magnetisation in canted spin structures at low temperatures.

The relative number of canted spins and the canting angles in materials can be measured with Mössbauer spectroscopy and varies significantly between materials and preparation methods. The change in magnetisation at low temperatures shown in Figure 3.2 (right) is on the order of 10% and if a large number of defects like the one shown in Figure 3.1 exists the change in the total magnetisation will be on the same order as many of the experimental observations (see Paper [2]). The model discussed here concerns canted spins due to a cation vacancy in the interior of a ferrimagnetic structure but it is reasonable to assume that similar considerations do applies to canted spins on the surface of AFM NPs, and in the following section we will present measurements of the magnetisation of AFM goethite NPs that we interpret to be in accordance with the model of freezing of canted spins at low temperatures.
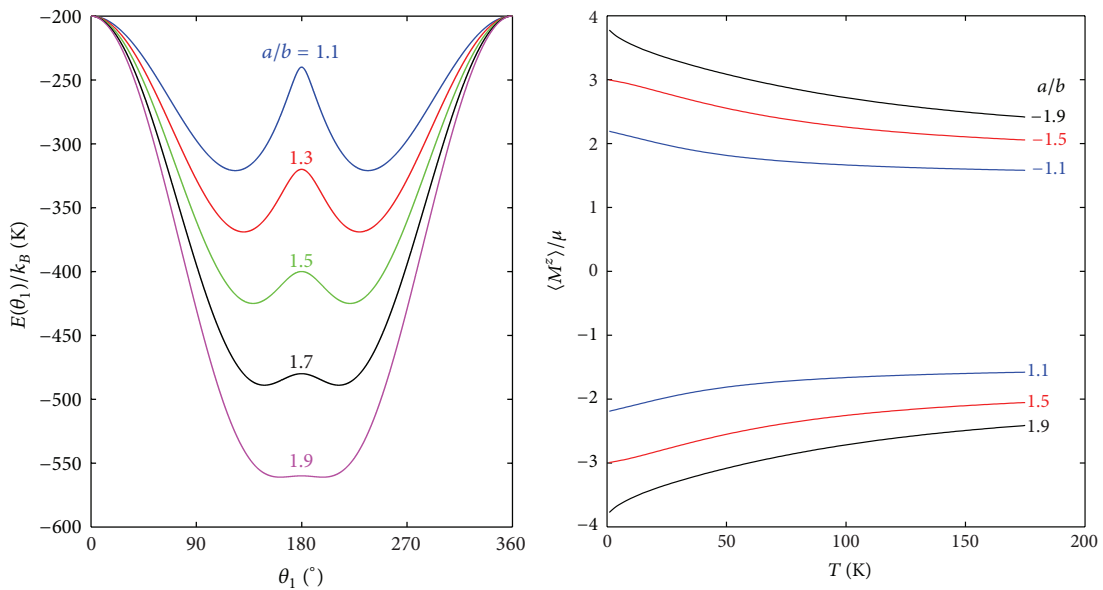
Figure 3.2: Left: The energy of the four canted spins in Figure 3.1 calculated from Equation (3.7) with $b/k_B = 200$ K and a/b of the indicated values. Figure from Paper [1]. Right: Magnetisation of the canted spin structure in Figure 3.1 calculated numerically from Equation (3.8) with $b/k_B = 200$ K and a/b of the indicated values. Figure from Paper [2].

3.2 Magnetic properties of ultra-small goethite nanoparticles

Goethite (α-FeOOH) is one of the most common AFM minerals on Earth. Particles of goethite commonly consists of nanocrystalline grains with low angle grain boundaries [94]. Because of interactions between the grains inside the particles it is difficult to determine the intrinsic magnetic properties of individual goethite crystals.

In Paper [3] we investigate the magnetic properties of ultra-small goethite particles (5.7 nm) that consist of only one or very few grains. This means that inter-grain interactions are less important than in most studied goethite samples. We further separate the particles by ball-milling with NaCl NPs to even further reduce the inter-grain and inter-particle interactions. The samples are investigated with magnetisation measurements, Mössbauer spectroscopy and inelastic neutron scattering. We find that the ultra-small size of the particles allows us to investigate the intrinsic magnetic properties of the individual grains. We find a significant upturn in the magnetisation at low temperatures in the field cooled and zero field cooled magnetisation curves and in AC magnetisation measurements. We interpret this as an effect of freezing of canted spins on the surface or in the interior of the particles as discussed in the previous section. This section will present the magnetisation measurements also presented in Paper [3] but first we will briefly mention the other main results of the paper.

Mössbauer spectra of goethite particles typically consist of asymmetrically broadened sextets and not a superparamagnetic doublet. Some authors have identified the asymmetrically broadened sextets as originating from fluctuations in interacting grains [11,94] but other explanations also exist [95–97]. We find the Mössbauer spectra of both samples to collapse to a doublet at a temperature of around 200 K and we interpret this as a signature of the samples undergoing fast SPM relaxation because of the reduced inter grain interactions. The collapse happens at a lower temperature for the ball-milled sample showing that the inter-grain and inter-particle interactions have been reduced by the ball milling.

The inelastic NS data which to our knowledge are the first published inelastic NS results on goethite NPs shows a sharp excitation peak which we interpret as excitations of the uniform mode ($q = 0$ spin waves) in non-interacting particles. For particles that are not dominated by interactions between grains measurement of the energy of the uniform mode by inelastic neutron scattering provides a unique way of determining the magnetic anisotropy. There has been some debate about the size of the magnetic anisotropy in goethite [95, 98–100]. We find an anisotropy constant of approximately $10^5 \mathrm{J/m^3}$ with both inelastic NS and Mössbauer spectroscopy.

3.2.1   Sample characterisation

A sample of goethite nanopowder labeled F2506 (Blend 07PSL-204) was obtained from Nano-Chemonics Inc. This sample is referred to as G1. To decrease the inter-particle interaction part of the G1 sample was mixed with NaCl nanoparticles at a weight ratio of one part G1 to 3 parts NaCl and ball milled for 48 hours at low intensity in an agate mill. The NaCl nanoparticles were prepared by ball-milling in a WC mill at high intensity (200 rpm). The ball-milled sample is referred to as GBM. Both samples were characterised with XRD and TEM and used for inelastic NS and Mössbauer experiments. The GBM sample was used for magnetisation measurements. For the XRD and TEM measurements the salt was washed out of the GBM sample.

X-ray diffraction

X-ray powder diffraction patterns were collected for the G1 sample and for the washed GBM sample at the Panalytical powder diffractometer at DTU-Cen. Rietveld refinements were performedunsing initial parameters for the refinement of the *Pnma* structure of goethite from [101]. Voigtian profiles were used in the refinements and the background was modelled with Chebyshew polynomials.

The XRD data and the refined models are shown in Figure 3.3 for both samples. For the G1 sample the peak position correspond well to the expected positions of the goethite reflections and the refined model represents the data relatively well even though there is a high background due to fluorescence from the Fe atoms in goethite. There are no signs of other phases than *Pnma* goethite in the sample. For the washed GBM sample the background is very irregular and there is a sharp peak at $q = 2.85 \text{ Å}^{-1}$ not belonging to the goethite structure. The unidentified impurity was included as a single peak in the model but still the agreement between calculated and observed diffraction pattern is not as satisfactory as for the G1 sample. The large irregular background seen in the diffraction pattern of the GBM sample may aside from fluorescence be ascribed to amorphous NaCl residue or perhaps something introduced by the ball-milling. Importantly the Mössbauer spectra of the sample confirmed that the chemical state of iron was not affected by the ball-milling (see Paper [3]).

The refined lattice parameters from the G1 XRD data are $a = 9.954(2)$ Å, $b = 3.0248(5)$ Å and $c = 4.618(1)$ Å. Using the Voigtian peak shape and assuming the Gaussian width to be determined by the instrumental resolution and the Lorentzian width to be only due to finite particle size the average particle diameter for the G1 sample was determined to be 5.9 ± 0.8 nm. The peak positions in the XRD data of the washed GBM sample corresponded to the goethite structure, and the peak broadening was similar in size to the broadening observed for the G1 particles indicating that the ball-milled particles are structurally unaltered and that the crystallite size have also not been changed significantly.

Transmission electron microscopy

TEM images of the G1 and the washed GBM samples were recorded on the FEI Tecnai T20 G2 microscope at DTU-CEN. Bright field and dark field images were recorded. Bright field images of G1 show that the sample consist of μm sized aggregates of particles with dimensions of around 3-5 nm as determined from particles at the rim of the aggregates. The lattice fringes show that neighbouring particles share some crystallographic alignment, but this only persist over very
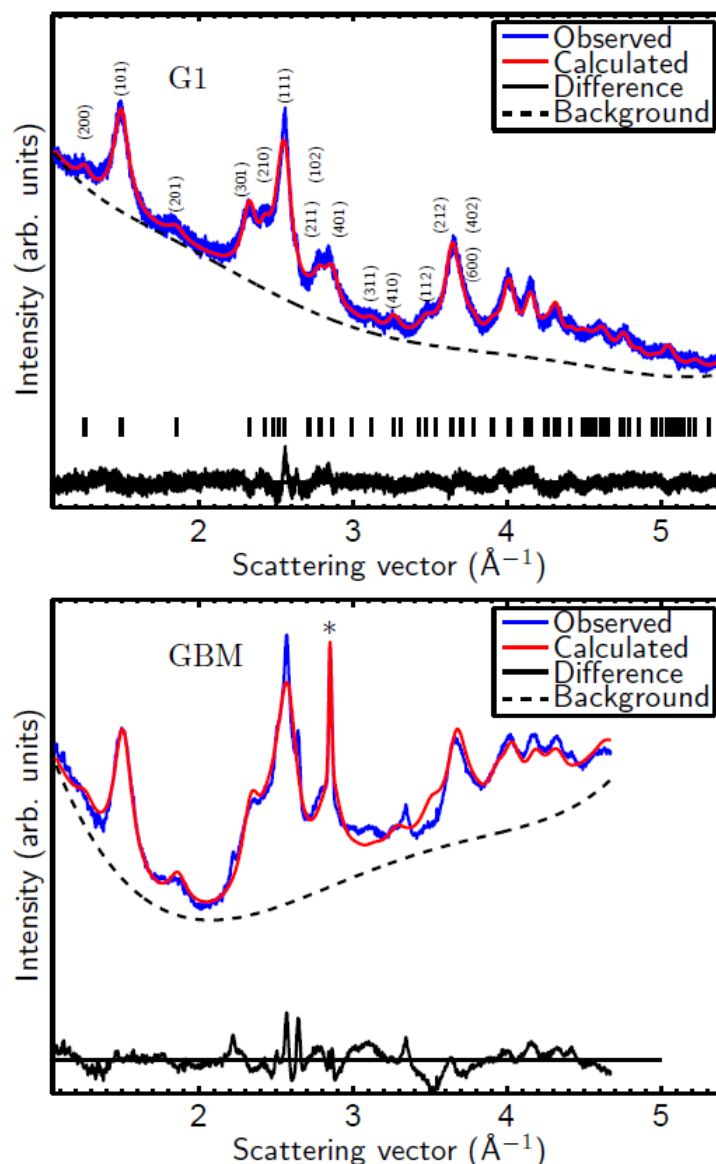
Figure 3.3: X-ray powder diffraction data for the G1 sample (top) and the washed GBM sample (bottom). The observed data is shown together with the calculated (refined) model. Also shown is the background and the difference between observed and calculated data. The most prominent reflections with $q < 4$ Å^{-1} are indexed in the top figure. The $*$ in the bottom figure indicates the unknown impurity peak. Figure from Paper [3].

few particles. An example bright field image of G1 is displayed in Figure 3.4 (a). The dark field images (see Fig. 3.4 (a)) confirms this tendency for alignment between neighbouring particles. The particle size for the G1 sample was determined by measuring 60 particles in the dark field images giving the size histogram in Figure 3.4 (c). The volume weighted particle size measured in this way is 5.4±1.7 nm in agreement with the value determined with XRD. Dark field images of the washed GBM sample (Fig. 3.4 (d)) are similar to dark field images of G1, confirming that the ball-milling has not significantly altered the morphology or size of the particles.

3.2.2 Magnetisation measurements

AC and DC magnetisation measurements were performed at Department of Chemistry, University of Copenhagen. Samples for AC and DC magnetisation measurements were prepared by mixing GBM with eicosane in a capsule of gelatine. The mixture was heated to approxi-
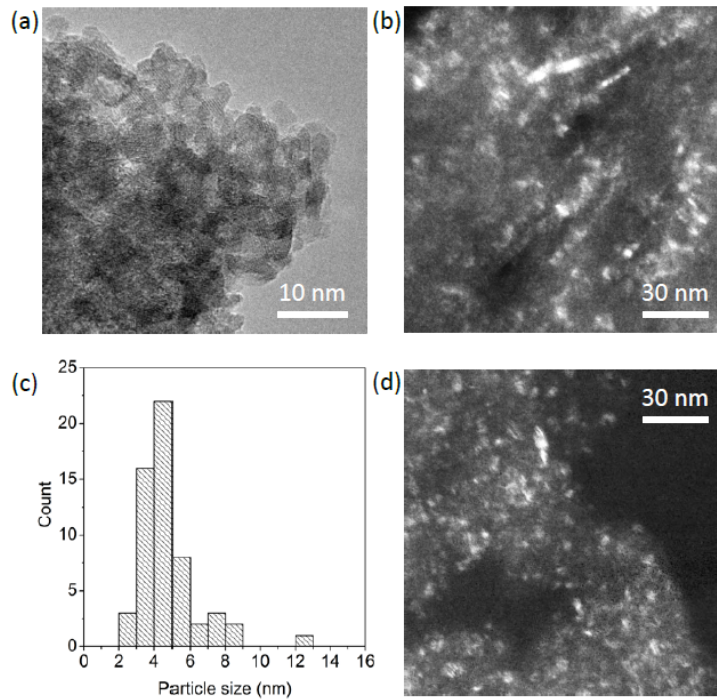
Figure 3.4: TEM images of ultra-small goethite nanoparticles. (a) Bright field image of G1. (b) Dark field image of G1. (c) Size distribution of G1 determined from dark field images. (d) Dark field image of GBM. Figure from Paper [3].

mately 40°C where eicosane becomes a liquid. GBM and eicosane is then mixed and when the eicosane wax solidifies it fixates the sample particles in the original (random) orientation. For the DC measurements 33.06 mg of GBM was mixed with 28.65 mg eicosane and for the AC measurements a larger sample with 139.4 mg GBM was prepared. In the DC magnetisation data the diamagnetic contributions from NaCl, eicosane and gelatine was subtracted using the mass susceptibilities (in 10^{-9}m^3/kg) of -6.4, -10.8 and -6.3 respectively.

Field cooled an zero field cooled magnetisation

FC and ZFC magnetisation curves was measured in temperatures between 4.2 K and 300 K in applied fields of $\mu_0 H = 2.0$ mT and 4.8 T. For the FC measurements the cooling field was the same as the applied field in the measurement. The FC and ZFC data are displayed in Figure 3.5.

In the ZFC measurement at the small applied field of $\mu_0 H =2.0$ mT there is a peak in the magnetisation at around 130 K. A peak in the ZFC data at the position of the SPM blocking temperature is expected for particles undergoing SPM relaxation, however, the blocking temperature determined from Mössbauer spectroscopy was about 160 K and because of the very different times scales of the two techniques the peak is expected to be at approximately 30 K in the ZFC magnetisation data. Pankhurst et al [102] found a similar peak in the ZFC data of goethite NPs which they attribute to 'cluster ordering' of magnetically interacting particles. For temperatures above approximately 150 K the FC and ZFC curves coincide, indicating that all particles have reached their SPM blocking temperature. At low temperatures there is a sharp increase in the measured magnetic moment with decreasing temperature in both the FC and ZFC curves. The increase in the moment from 30 K to 4.2 K is of similar sizes, namely $3.3 \cdot 10^{-3}$ Am^2 per kg goethite in the ZFC measurement and $3.0 \cdot 10^{-3}$ Am^2 per kg goethite in the FC measurement.

In the strong applied field of $\mu_0 H = 4.8$ T there is no peak in the ZFC measurement and the two curves nearly coincide in the whole temperature interval. Like in the 2.0 mT measurements

there is a sharp increase in the moment at low temperatures. Here the increase from 30 K to 4.2 K is approximately 5.8 Am^2 per kg goethite.
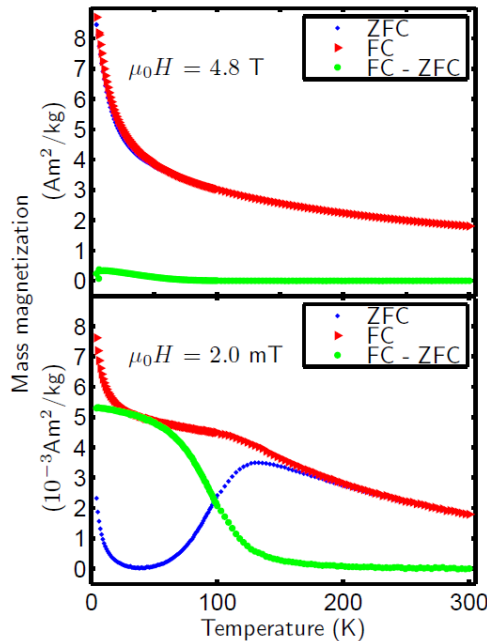

Figure 3.5: Field cooled and Zero field cooled magnetisation of the GBM sample in applied fields of 4.8 T (top) and 2.0 mT (bottom). The magnetisation is given per kg of goethite in the samples Figure from **Paper** [**3**].

AC susceptibility

The AC susceptibility was measured in the same temperature range as the DC measurements and with a driving field of $\mu_0 H$=0.38 mT. Both the in-phase susceptibility χ' and the out-of-phase susceptibility χ'' was measured with AC frequencies between 1 Hz and 1 kHz. χ' (see Fig, 3.6) shows a frequency dependent peak with a position that changes from about 150 K at 1 Hz to about 170 K at 1000 Hz. It was attempted to determine KV and τ_0 from the frequency dependence of the peak position using a method described in [79]. However, the method returned unrealistic values indicating that the SPM relaxation is not in accordance with the Néel-Brown law (1.3) probably due to inter-grain and inter-particle interactions. An increase in χ' is seen in the same temperature range as the increase in the DC magnetisation. A similar anomalous temperature dependence of the AC susceptibility of goethite particles have been measured by Pankhurst et al. [102]. In the measurement of χ'' the signal was very low and there was no upturn in the susceptibility at low temperatures.

3.3 Conclusions on spin canting and goethite

We have shown that a simple model of spin canting around a cation vacancy in a two dimensional system can lead to either an increase or a decrease of the magnetisation at low temperatures. The model may be too simple to accurately describe the magnetisation of realistic canted structures which are bound to be complicated and, except for a few cases with strong planar anisotropy, three dimensional. As discussed in Papers [1, 2] the measured anomalous temperature dependence of ferrimagnetic NPs and diamagnetically substituted bulk ferrites are not only in qualitative accordance with the model, but can also be of the same size as the model predicts if the number of spins and canting angles are of the right size.
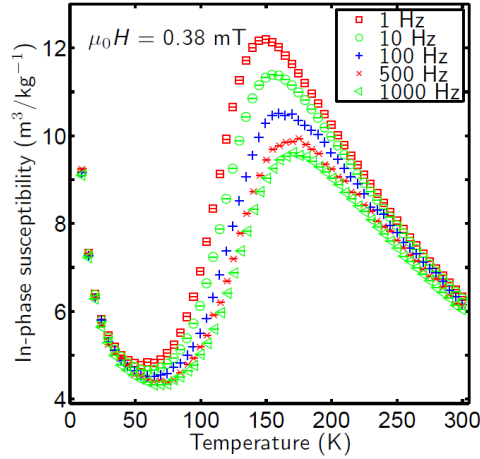
54

Figure 3.6: In phase AC susceptibility (χ') of the GBM sample in a driving field of $\mu_0 H = 0.38$ mT. Figure from **Paper** [**3**].

We believe that the simple two dimensional model gives an insight into how the temperature dependence of the magnetisation may be affected by canted spin structures in more complicated systems where it is not possible to calculate the magnetisation using an analytical model. Freezing of canted spins at low temperatures may give an increase or decrease of the magnetisation depending on the canting angle not only for canted spins in the interior of particles but also for canted spins at the surface of particles. Furthermore canted spins are not only important in ferrimagnetic structures and a similar temperature dependence of the magnetisation from canted spins in AFM particles is expected.

In the magnetisation data on goethite nanoparticles we see a significant increase in the DC and AC magnetisation at temperatures below 30 K. This upturn in the magnetisation is similar to the observations in ferrimagnetic NPs and diamagnetically substituted bulk ferrites discussed in section. 3.1 In the ultra-small goethite particles both canted spins on the particle surfaces and around defects in the interior of particles may be important and it likely that freezing of canted spins in goethite have a significant contribution to the magnetisation at low temperaturesm, and the measured increase in the magnetisation may be qualitatively explained by our model.

Spin orientation in NiO nanoparticles

Nickel oxide was one of the first AFM materials ever studied with NS in the pioneering work of Shull et. al. [50]. The magnetic structure of NiO NPs is not well understood, although NiO NPs can be very relevant to use e.g., with FM NPs in exchange coupled magnetic storage devices or nanocomposite magnetic materials. A few studies deal theoretically with the magnetic structure of NiO NPs [103], but the structure has not been resolved experimentally.

The large surface contribution the the magnetic anisotropy may lead to a change in spin orientation in NiO NPs compared to bulk NiO. In thin NiO films, a spin reorientation transition (SRT), in which the NiO spin orientation changes from within the film to perpendicular to the film, is observed. This transition happens below a certain critical film thickness ($\approx 3 - 10$ monolayers), but depends not only on the thickness of the NiO film but also on the support and on temperature [104–107]. Even though the thin-film systems are quite different from magnetic NPs something similar to the SRT in films might happen in NPs of NiO. Not only the size, but also the shape of the particles may influence the anisotropy, and lead to different spin orientations.

Here we investigate the effect of particle size on the spin orientation in plate shaped NiO NPs with thickness down to 2.0 nm using polarised neutron powder diffraction. Initial attempts to determine the spin orientation using unpolarised neutron diffraction were hampered by an overlap of the nuclear and magnetic scattering because of the finite particle size. We therfore turned to the technique of XYZ polarisation analysis. This allow us to reliably measure the intensity of the magnetic diffraction peaks in order to determine the spin orientation with respect to the AFM ordering vector in the particles.

The size and morphology of the particles are investigated with TEM and XRD, revealing that the NiO NPs are plate-shaped, with {111} planes of the NiO structure parallel to the plane of the particles. Previous investigations on similar samples (see ref. [108]) suggested that the AFM modulation vector is perpendicular to the particle plane. Our combined TEM and NS experiments confirm this observation, and this enables us to determine the spin orientation with respect to the particle plane directly from the intensity of the magnetic peaks.

4.1   Previous studies on plate shaped NiO nanoparticles

There has been a number of investigations of plate shaped NiO nanoparticles going back as far as the 1950ies and especially after the interest in nanotechnology started in the 1990ies. The reason for the focus on plate shaped particles is probably that it is easy to produce high purity samples with a reasonably narrow size distribution from the thermal decomposition of $Ni(OH)_2$ to NiO. However, the morphology of the particles, with one dimension much shorter than the other two, might be important for the magnetic properties. It could have a significant effect on the magnetic anisotropy of the particles and thus influence the magnetic structure. Plate-shaped NiO nanoparticles have been investigated with magnetisation techniques [24, 109–112], neutron scattering [19, 26] and Mössbauer spectroscopy [19, 24, 112], revealing that the particles undergo

SPM relaxation and that they carry a magnetic moment. The magnetic moment is found to be proportional to $N^{1/3}$, consistent with a uncompensated moment from random occupation of surface sites [112, 113]. The Neél temperature of the NPs are found to be reduced with respect to the bulk value of 524 K. For a sample of plate shaped NiO particles with diameter of about 12 nm and thickness of 2 nm $T_N \approx 460$ K was found [19]. A similar value can be expected for the particles to be investigated here.

An unexpected high magnetisation in plate-shaped NiO NPs lead some authors to propose a multi-sublattice model for the magnetic structure of NiO NPs, where the simple model of two AFM sublattices is replaced with up to 8 magnetic sublattices depending on particle size [103, 114,115]. Other authors maintain the two sublattice model, and explain the large uncompensated moment as a consequence of the sensitivity of magnetisation measurements to large magnetic moments or to interactions between the particles [112]. I will assume the NPs to have the simpler magnetic structure with two AFM sublattices like for bulk NiO [116, 117].

The orbital magnetic moment gives a significant contribution to the total moment of the Ni^{2+} ions. In NiO NPs similar to the ones investigated here the Ni^{2+} magnetic moment was determined from inelastic neutron scattering to $\mu = 2.19\mu_B$ [26], in good agreement with measurements on bulk NiO crystals with magnetic X-ray scattering [116, 117].

4.2 Crystal and magnetic structure of NiO

Nickel(II) oxide, NiO, crystallises in the cubic NaCl structure with space group $Fm\bar{3}m$ and a room temperature lattice constant of $a = 4.177$ Å [118]. At a Néel temperature of $T_N = 523$ K [119] the Fe^{2+} spins in NiO orders antiferromagnetically. The AFM order is with the AFM modulation along a body diagonal of the cubic structure, $\langle 111 \rangle$, and with the spins aligned within the corresponding $\{111\}$ planes (ref. [120]). A small in-plane anisotropy defines the easy axes of sublattice magnetization as the $\langle 11\bar{2} \rangle$ directions [121–124].

Below T_N there is a rhombohedral distortion of the lattice, corresponding to a slight contraction along one of the body diagonals. However, the departure of the rhombohedral angle from 90° is very small, varying from 0 at T_N to 0.075° at 0 K (extrapolated) [125] and I will therefore continue to describe the system in terms of the more symmetric cubic unit cell.

4.2.1 Structure factors of NiO

The AFM unit cell is a cube of sidelength $2a$ containing 8 of the chemical unit cells and with 32 magnetic atoms in the basis (see Appendix A.1). The larger magnetic unit cell was used to calculate both the nuclear and magnetic structure factors, but the index is with respect to the chemical cell. The first nuclear reflections are the forms $\{111\}$ and $\{200\}$ with multiplicities of 8 and 6 respectively. The structure factors (2.19) for these reflections are

$$F_{N,111} = 32\left(b_{Ni} - b_O\right), \tag{4.1}$$

$$F_{N,200} = 32\left(b_{Ni} + b_O\right), \tag{4.2}$$

where $b_{Ni} = 10.3(1)$ fm and $b_O = 5.805(4)$ fm [56] are the scattering lengths of Ni and O. Letting the AFM modulation vector be in the [111] direction the first few allowed magnetic reflections are $\left\{\frac{1}{2}\frac{1}{2}\frac{1}{2}\right\}$, $\left\{\frac{1}{2}\frac{1}{2}\frac{\bar{3}}{2}\right\}$ and $\left\{\frac{\bar{1}}{2}\frac{3}{2}\frac{3}{2}\right\}$, with multiplicities of 2, 6, and 6 respectively. The magnetic structure factors (2.27) are

$$F_M(\mathbf{q}) = 32M_\perp(\mathbf{q}), \tag{4.3}$$

which depends on the spin orientation relative to the scattering vector. All of the allowed nuclear and magnetic reflections in the q-range 0 - 4 Å^{-1} are given in Table 4.1.

$\{hkl\}$	$q(\text{Å})^{-1}$	j	Allowed reflections	Type
$\left\{\frac{1}{2}\frac{1}{2}\frac{1}{2}\right\}$	1.303	2	$\left(\frac{1}{2}\frac{1}{2}\frac{1}{2}\right)$, $\left(\frac{\bar{1}}{2}\frac{\bar{1}}{2}\frac{\bar{1}}{2}\right)$	M
$\left\{\frac{1}{2}\frac{1}{2}\frac{\bar{3}}{2}\right\}$	2.495	6	$\left(\frac{1}{2}\frac{1}{2}\frac{\bar{3}}{2}\right)$, $\left(\frac{1}{2}\frac{\bar{3}}{2}\frac{1}{2}\right)$, $\left(\frac{\bar{3}}{2}\frac{1}{2}\frac{1}{2}\right)$, $\left(\frac{\bar{1}}{2}\frac{\bar{1}}{2}\frac{3}{2}\right)$, $\left(\frac{\bar{1}}{2}\frac{3}{2}\frac{\bar{1}}{2}\right)$, $\left(\frac{3}{2}\frac{\bar{1}}{2}\frac{\bar{1}}{2}\right)$	M
$\{111\}$	2.605	8	(111), $(\bar{1}11)$, $(1\bar{1}1)$, $(11\bar{1})$,$(\bar{1}\bar{1}\bar{1})$,$(1\bar{1}\bar{1})$,$(\bar{1}1\bar{1})$, $(\bar{1}\bar{1}1)$	N
$\{200\}$	3.009	6	(200), (020), (002), $(\bar{2}00)$, $(0\bar{2}0)$,$(00\bar{2})$	N
$\left\{\frac{\bar{1}}{2}\frac{3}{2}\frac{3}{2}\right\}$	3.278	6	$\left(\frac{\bar{1}}{2}\frac{3}{2}\frac{3}{2}\right)$, $\left(\frac{3}{2}\frac{\bar{1}}{2}\frac{3}{2}\right)$, $\left(\frac{3}{2}\frac{3}{2}\frac{\bar{1}}{2}\right)$, $\left(\frac{1}{2}\frac{\bar{3}}{2}\frac{\bar{3}}{2}\right)$, $\left(\frac{\bar{3}}{2}\frac{1}{2}\frac{\bar{3}}{2}\right)$, $\left(\frac{\bar{3}}{2}\frac{\bar{3}}{2}\frac{1}{2}\right)$	M
$\left\{\frac{3}{2}\frac{3}{2}\frac{3}{2}\right\}$	3.908	2	$\left(\frac{3}{2}\frac{3}{2}\frac{3}{2}\right)$, $\left(\frac{\bar{3}}{2}\frac{\bar{3}}{2}\frac{\bar{3}}{2}\right)$	M

Table 4.1: Allowed reflections for NiO with scattering vectors up to 4 Å^{-1}. The reflections with integer hkl are nuclear (N) and the half integer valued ones are magnetic (M). The multiplicity of a reflection is j.

4.2.2 Obtaining the in-plane moment from the $\left\{\frac{1}{2}\frac{1}{2}\frac{1}{2}\right\}$ cross section

For the $\left\{\frac{1}{2}\frac{1}{2}\frac{1}{2}\right\}$ reflection only planes perpendicular to the direction of the AFM propagation contribute to the structure factor (see Table 4.1) and the scattering vector is thus parallel to the AFM propagation vector. This means that $M_\perp(\mathbf{q})$ is the magnetisation in the $\{111\}$ planes in which the spins are ferromagnetically aligned. This in-plane magnetisation can be found from the measured cross section of the $\left\{\frac{1}{2}\frac{1}{2}\frac{1}{2}\right\}$ peak (see (2.26)):

$$\frac{d\sigma}{d\Omega}_{\left\{\frac{1}{2}\frac{1}{2}\frac{1}{2}\right\}} = 2\left(\frac{\gamma r_0}{2}\right)^2 \frac{N(2\pi)^3}{V_0} g^2 f^2(q)\,(32M_\perp)^2\, L_\theta e^{-2W(q)}, \tag{4.4}$$

where L_θ is the Lorentz factor (2.30), and the factor of 2 is the multiplicity. In experiments the intensity is often not measured in absolute units, and it is therefore not possible to obtain the cross section (4.4) and calculate $M_\perp$ directly. however, one can normalise the intensity of the magnetic peak to that of a measured nuclear reflection to get rid of the unknown scale factors (noticeably the incident flux). The cross section of the nuclear $\{111\}$ reflection is (see (2.22))

$$\frac{d\sigma}{d\Omega}_{\{111\}} = 8\frac{N(2\pi)^3}{V_0}\left[32\left(b_{\text{Ni}} - b_{\text{O}}\right)\right]^2 e^{-2W(q)} L_\theta, \tag{4.5}$$

where the factor of 8 is the multiplicity. We normalise the intensity of the $\left\{\frac{1}{2}\frac{1}{2}\frac{1}{2}\right\}$ reflection to that of the $\{111\}$ reflection obtaining

$$\frac{I_{\left\{\frac{1}{2}\frac{1}{2}\frac{1}{2}\right\}}}{I_{\{111\}}} = \frac{\left[32M_\perp\left(\frac{\gamma r_0}{2}\right)f\left(q_{\left\{\frac{1}{2}\frac{1}{2}\frac{1}{2}\right\}}\right)\right]^2 L_{\theta_{\left\{\frac{1}{2}\frac{1}{2}\frac{1}{2}\right\}}}}{4\left[32(b_{\text{Ni}} - b_{\text{O}})\right]^2 L_{\theta_{\{111\}}}}, \tag{4.6}$$

where $I_{\left\{\frac{1}{2}\frac{1}{2}\frac{1}{2}\right\}}$ and $I_{\{111\}}$ are the measured intensities. The Debye-Waller factors have been disregarded. For measurements at low temperatures (4 K), where only the zero point fluctuations of the atoms contribute this gives an error of less than 1%. L_θ can be determined straight away from the measured Bragg angles, and the form factor can be calculated, e.g. using the analytical approximations in [55] and it is thus possible to calculate $M_\perp$ from:

$$M_\perp^2\left(\mathbf{q}_{\left\{\frac{1}{2}\frac{1}{2}\frac{1}{2}\right\}}\right) = \frac{I_{\left\{\frac{1}{2}\frac{1}{2}\frac{1}{2}\right\}}}{I_{\{111\}}} \frac{4\left(b_{\text{Ni}} - b_{\text{O}}\right)^2 L_{\theta_{\{111\}}}}{\left(\frac{\gamma r_0}{2}\right)^2 f^2\left(q_{\left\{\frac{1}{2}\frac{1}{2}\frac{1}{2}\right\}}\right) L_{\theta_{\left\{\frac{1}{2}\frac{1}{2}\frac{1}{2}\right\}}}}. \tag{4.7}$$

If the size of the total magnetic moment, μ_{Ni} is known the spin angle with respect to the scattering vector is then

$$\sin^2(\alpha) = M_\perp^2 \left(q_{\left\{ \frac{1}{2} \frac{1}{2} \frac{1}{2} \right\}} \right) / \mu_{\text{Ni}}^2, \tag{4.8}$$

where α is the angle between the sublattice spin and the $\frac{1}{2}\frac{1}{2}\frac{1}{2}$ scattering vector (i.e. the [111] direction). There is nothing special about the $\{111\}$ reflection and the normalisation could just as well have been with respect to any other nuclear reflection, e.g. the $\{200\}$ reflection.

4.2.3 Obtaining the spin angle from the relative magnetic intensities

By measurement of magnetic reflections with scattering vectors in different directions it is possible to obtain information about the AFM spin direction. Interpretation of the intensity of the $\left\{ \frac{1}{2} \frac{1}{2} \frac{\overline{3}}{2} \right\}$ reflection is more complicated than for the $\left\{ \frac{1}{2} \frac{1}{2} \frac{1}{2} \right\}$ reflection because it contains contributions from scattering vectors that makes different angles with the spin direction in the (111) plane. All the $\left\{ \frac{1}{2} \frac{1}{2} \frac{\overline{3}}{2} \right\}$ scattering vectors make an angle of 79.975° with [111] and they thus see the same out-of-plane magnetic moment $(M(\mathbf{q}) \cdot \sin^2(79.975° - \alpha))$. In the (111) plane they make 120° angles with respect to one another. The difference in the structure factor between the six $\left\{ \frac{1}{2} \frac{1}{2} \frac{\overline{3}}{2} \right\}$ reflections is contained in the different $M_\perp(\mathbf{q})$, and the total cross section for the $\left\{ \frac{1}{2} \frac{1}{2} \frac{\overline{3}}{2} \right\}$ reflection will be

$$\frac{d\sigma}{d\Omega}_{\left\{ \frac{1}{2} \frac{1}{2} \frac{\overline{3}}{2} \right\}} = \left(\frac{\gamma r_0}{2} \right)^2 \frac{N(2\pi)^3}{V_0} g^2 f^2(q) \sum_1^6 (32\mu_{\text{Ni}} \sin(\gamma_i))^2 \, L_\theta e^{-2W(q)}, \tag{4.9}$$

where the sum is over the 6 allowed reflections of the form $\left\{ \frac{1}{2} \frac{1}{2} \frac{\overline{3}}{2} \right\}$, and γ_i is the spin angle with respect to the i'th of these scattering vectors. If the spin component in the (111) plane is assumed to be randomly aligned along the three $\langle 11\overline{2} \rangle$ axes the in-plane spin orientation can be averaged out, arriving at an expression for the sum in (4.9) that depends only on α:

$$\left\langle \sum_i^6 \sin^2(\gamma_i) \right\rangle_\beta = 2 \left[3 - 3\cos^2(79.975°) + \sin^2(\alpha) \left(3\cos^2(79.975°) - \frac{3}{2}\sin^2(79.975°) \right) \right], \tag{4.10}$$

where $\langle \rangle_\beta$ denotes the average over the in-plane angle. Now α can be found from the ratio of the measured intensities of the two magnetic reflections. Using (4.4) and (4.9) we arrive at:

$$\sin^2(\alpha) = \frac{\dfrac{I_{\left\{ \frac{1}{2} \frac{1}{2} \frac{1}{2} \right\}}}{I_{\left\{ \frac{1}{2} \frac{1}{2} \frac{\overline{3}}{2} \right\}}} (3 - 3\cos^2(79.975°))}{\mathcal{F} - \dfrac{I_{\left\{ \frac{1}{2} \frac{1}{2} \frac{1}{2} \right\}}}{I_{\left\{ \frac{1}{2} \frac{1}{2} \frac{\overline{3}}{2} \right\}}} \left(3\cos^2(79.975°) - \frac{3}{2}\sin^2(79.975°) \right)}, \tag{4.11}$$

where, once again, the Debye-Waller factors have been ignored and

$$\mathcal{F} = \frac{L_{\theta\left\{ \frac{1}{2} \frac{1}{2} \frac{1}{2} \right\}} f^2 \left(q_{\left\{ \frac{1}{2} \frac{1}{2} \frac{1}{2} \right\}} \right)}{L_{\theta\left\{ \frac{1}{2} \frac{1}{2} \frac{\overline{3}}{2} \right\}} f^2 \left(q_{\left\{ \frac{1}{2} \frac{1}{2} \frac{\overline{3}}{2} \right\}} \right)}. \tag{4.12}$$

The presence of the form factor in $\mathcal{F}$ is the reason that it is only almost possible to obtain α without knowledge about the size of the magnetic moment of the Ni^{2+} ions. The form factor depends on the g factor through (2.29), but the precise value of g is not important. The value $g = 2.19$ [26] have been used here, but using the spin-only value of $g = 2$ would only introduce an error of 1-2% in $f(q)$.
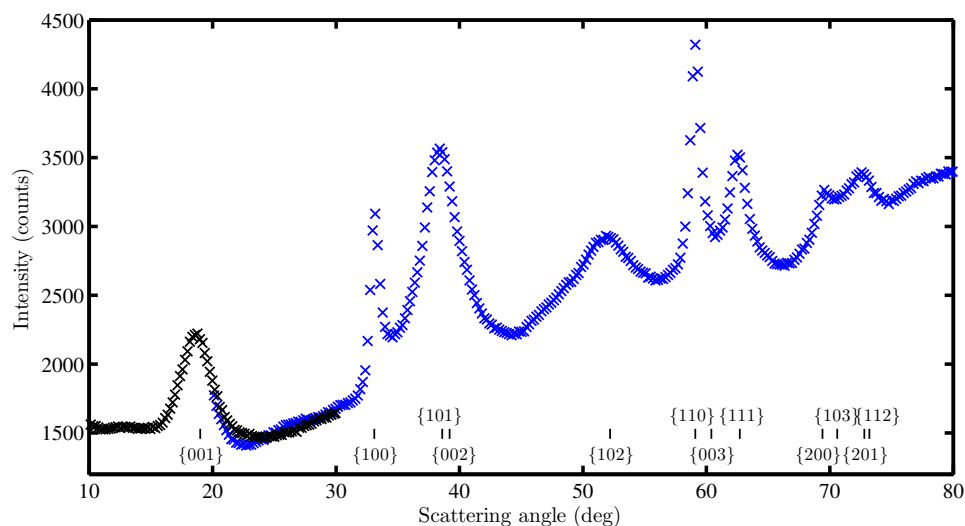
Figure 4.1: XRD pattern of the Ni(OH)$_2$ precursor. The low-angle part of the pattern (black) containing the {001} peak was measured separately. The indexing is with respect to the $P\bar{3}m1$ structure of Ni(OH)$_2$.

4.3 Production and characterisation of NiO nanoparticles

4.3.1 Ni(OH)$_2$ precursor

Samples of plate shaped NiO NPs of 4 different sizes were produced by thermal decomposition of plate shaped nanoparticles of Ni(OH)$_2$. The method is know to produce plate shaped NiO nanoparticles with a thickness that depends on the annealing temperature (see e.g. [24, 109–112]). The Ni(OH)$_2$ precursor is produced by chemical precipitation in aqueous solutions of NaOH and Ni(NO$_3$)$_2$·6H$_2$O as described in [110]. An XRD pattern of the Ni(OH)$_2$ precursor is shown in Figure 4.1. The peak positions are consistent with the hexagonal ($P\bar{3}m1$) crystal structure of Ni(OH)$_2$ [126] and there are no signs of other (impurity) phases in the sample. The relatively narrow {100} and {110} reflections and the much broader {001} reflection confirms that the particles are much shorter in the direction of the hexagonal [111] direction than in the perpendicular directions. The average particle dimensions are estimated from peak broadening using (2.31). The thickness of the particles are found from the broadening of the {001} peak, and assuming the particles to be cylindrical discs the particle diameter can be found from the broadening of the {100} and {110} peaks. In this way, after fitting the XRD data with Lorentzian line shapes, we find an average particle thickness of 3.39 ±0.02 nm and diameter of 12.1 ± 0.8 nm.

4.3.2 Conversion of Ni(OH)$_2$ to NiO

The Ni(OH)$_2$ powder was annealed in air for three hours at at temperatures between 250°C and 600°C. When the temperature was above approximately 230°C the colour of the powder changed from green to black indicating the conversion to NiO. The particle size increases with increasing conversion temperature because of sintering of the particles. The four samples were produced at heating temperatures of 250°C, 300°C, 350°C, and 600°C respectively. These samples will be named NiO250, NiO300, NiO350, and NiO600 respectively. Additionally a reference sample of bulk NiO powder labeled 'nickel (II) oxide puratronic Ⓡ, 99.998%' was bought from Alfa Aesar.

4.3.3 XRD Characterisation of NiO nanoparticles

All NiO samples were characterised with XRD, confirming that the samples are NiO with no detectable amounts of Ni(OH)$_2$ remaining. Sample XRD patterns of the samples NiO250 and
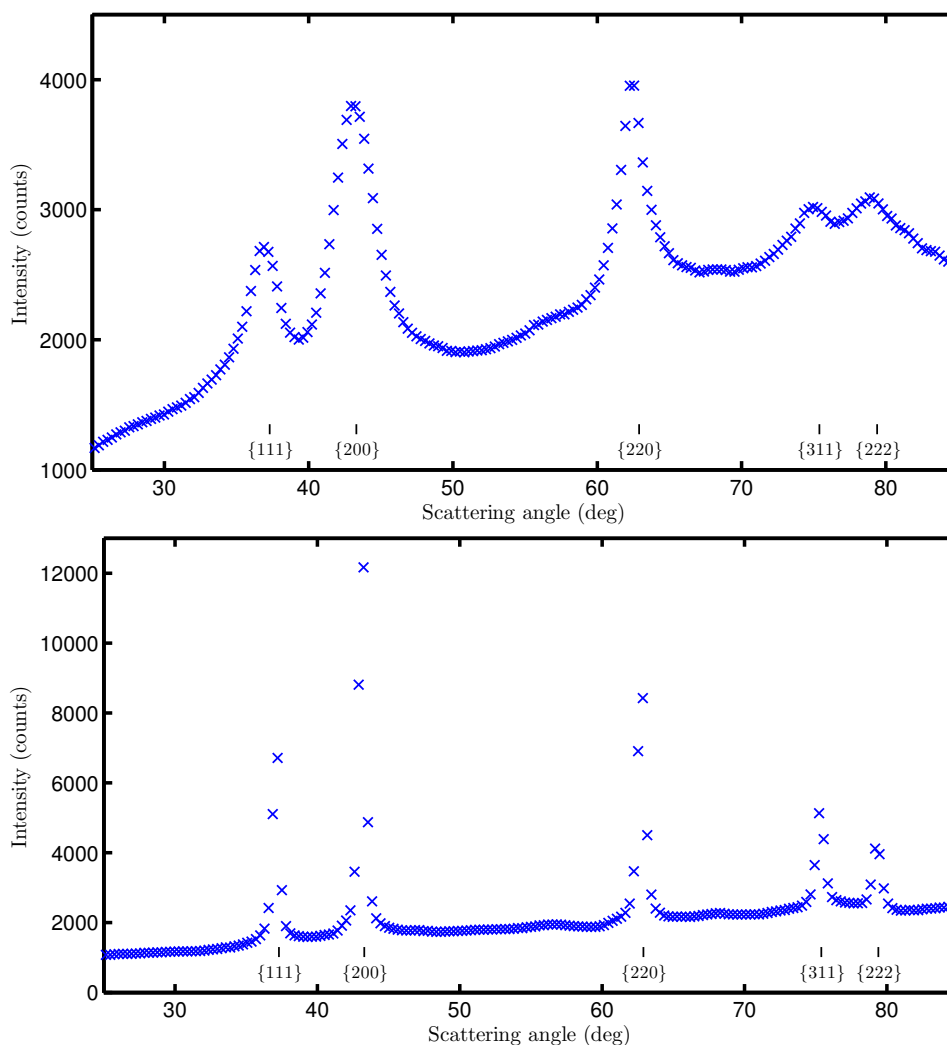
Figure 4.2: XRD pattern of the NiO250 (top) and NiO600 (bottom) samples. The indexing is with respect to the cubic $Fm\bar{3}m$ structure of NiO.

NiO600 are displayed in Figure 4.2. The line broadening in the XRD patterns decrease with increasing annealing temperature, confirming that the temperature controls the particle size. After the conversion to NiO the line broadening does not show the same variation between different reflections as seen in the spectrum in Figure 4.1. This is because the conversion to the high-symmetry cubic structure means that each reflection has contributions that corresponds to different directions with respect to the particle plane. If the particle plane is the (111) plane the real particle thickness is much smaller than what one would get from the broadening of the {111} peak, because the {111} peak contains contributions from all of the 8 {111} type reflections. Determining the platelet dimensions from XRD data is thus not as straight forward as for the less symmetric structure of $Ni(OH)_2$.

From the broadening of the {111} and {200} peaks the average particle sizes could be estimated. The two peaks gives very similar sizes and we will take the average of the two as our XRD particle size. The measured values for the four NP samples are 3.3 ± 0.2 nm, 4.9 ± 0.6 nm, 7.2 ± 0.7 nm and 28.3 ± 0.22 nm.

For the bulk NiO sample the line widths are very close to the instrumental resolution indicating that the particle size is larger than 200 nm.

	NiO250	NiO300	NiO350
t	1.99 ± 0.09 nm	2.21 ± 0.06 nm	3.29 ± 0.10 nm
t^V	2.5 ± 0.6 nm	2.5 ± 0.4 nm	3.7 ± 0.5 nm
D	8.8 nm	8.8 nm	13.0 nm

Table 4.2: Average particle thickness t measured from TEM images. The volume weighted thickness t^V is also given. The given uncertainty is the uncertainty on the mean. The widht of the size distribution is approximately an order of magnitude larger than the uncertainty on the average.

4.3.4 TEM characterisation of NiO nanoparticles

TEM images of all NiO nanoparticle samples were taken with magnification up to 400 kX. For each sample 50-100 images were recorded and sample pictures are given in Figure 4.3. The images confirm that the NiO nanoparticles have retained the plate-shape of the $Ni(OH)_2$ precursor. In high resolution images (not shown) it was possible to measure the spacing between lattice fringes parallel to the particle plane. These spacings are consistent with the 2.4 Å d-spacing of the {111} planes of the NiO structure and the plane of the particles are thus coincident with these planes. We might as well define the [111] direction to be the direction of the normal to the particle plane in order to avoid confusion. The particles do not show any appreciable degree of preferred orientation. This is important for the the neutron diffraction experiments.

The particles have a tendency to lie flat on the TEM grid and it is therefore difficult to measure the thickness of the particles. In images of NiO250, NiO300 and NiO350 it was possible to find a number of upright particles. The thickness of the particles that are seen edge on can easily be measured, and this was done for about 40 particles for each sample. For the NiO600 sample all particles were found to lie flat and it was thus not possible to measure the particle

Plate shaped NiO particle

thickness. It is worth noting that this method may underestimate the particle thickness because smaller particles have a larger tendency to be upright, as can be seen from the absence of upright particles in the images of NiO600. Even though the particles lie flat on the TEM grid the low contrast of the thin particles and the tendency for the particles to aggregate makes it almost impossible to distinguish individual particles lying down, and it is therefore not possible to measure the diameter of the particles. The measured average particle thicknesses $t = d_{<111>}$ are given in Table 4.3.4. Also given are the volume-weighted (t^3-weighted) average thickness t^V, which is the number that can be directly compared to sizes found with XRD and NPD.
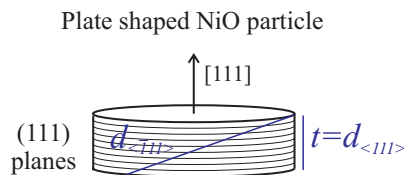
4.4 Determining spin orientation with XYZ-polarisation analysis

4.4.1 Unpolarised neutron diffraction experiments

As described earlier in this chapter the spin orientation in the plate shaped NiO NPs can be found with neutron diffraction. The data from Ref. [108] was not of a sufficient quality to determine the spin angle, and we therefore set out to perform neutron powder diffraction experiments on a new set of plate shaped NiO nanoparticles of different sizes.

We first performed an experiment at the DMC instrument at PSI in Switzerland, using long counting times to obtain better statistics than in the previous work. The data from the DMC
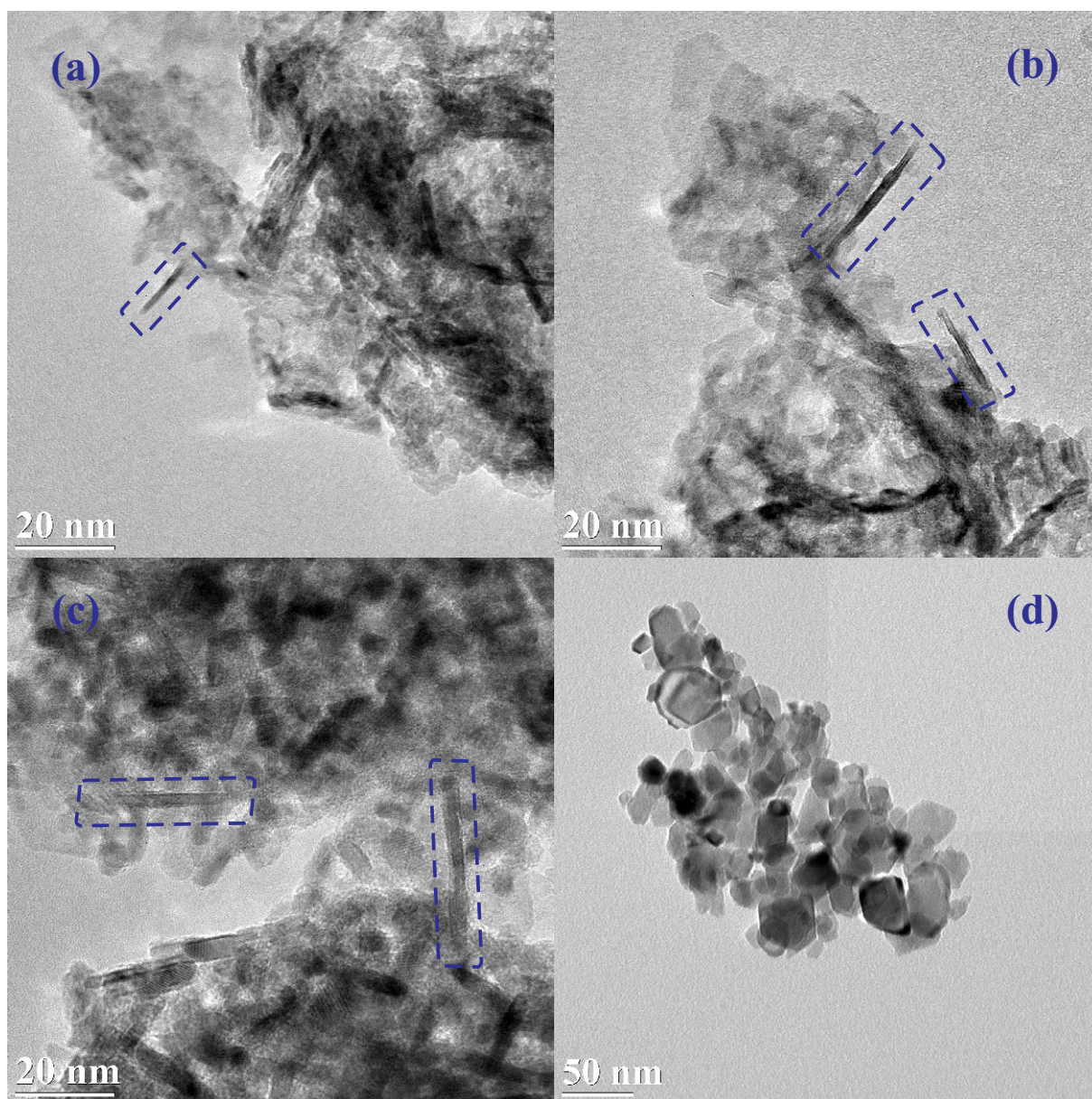
Figure 4.3: TEM images of the samples NiO250 (a), NiO300 (b), NiO350 (c) and NiO600 (d). Images (a)-(c) are taken with 195 kX magnification and image (d) with 115 kX magnification. Particles seen edge on, like the ones highlighted in images (a)-(c) were used to measure the average particle thickness.

experiment is displayed in Figure 4.4. This new data was a significant improvement of the previous data, however, even with counting times of about a whole day the signal was not easy to distinguish from the background for the smallest particles. Especially the magnetic $\left\{\frac{1}{2}\frac{1}{2}\frac{1}{2}\right\}$ peak is difficult to determine because the finite size broadening in the [111] direction makes the peak amplitude small, and because of the strong scattering signal at low q that, for the smallest particles, extends to the position of the $\left\{\frac{1}{2}\frac{1}{2}\frac{1}{2}\right\}$ peak. The low q signal falls of as q^{-4}, indicating that it is small angle scattering from the surfaces of the particles. These difficulties made a precise determination of $M\sin(\alpha)$ impossible.

We performed a similar experiment at the D1B instrument at ILL in Grenoble, where the high flux of the ILL reactor would enable us to get even better statistics than at DMC. Furthermore the detector at D1B has a larger angular range than DMC and D1B operates at a lower wavelength, enabling us to measure more Bragg peaks (with $q > 4\text{Å}^{-1}$). This could enable us to refine a simple model to the data in order to extract the desired information. The data from D1B gave us better statistics, but obviously the problems with small angle scattering, and overlapping peaks seen in the DMC data was still there. Furthermore systematic errors of the instrument that became significant with the large number of counts essentially meant that the data was less useful than the DMC data.

Even if it was possible to improve on the very good unpolarised diffraction data from DMC it would be difficult to accurately measure the intensity of the $\left\{\frac{1}{2}\frac{1}{2}\frac{1}{2}\right\}$ peak, because of the small angle signal, and because of the large peak overlap it would also be very difficult to measure the intensity of the peaks that are needed for normalisation. In particular the intensity of the $\left\{\frac{1}{2}\frac{1}{2}\frac{\bar{3}}{2}\right\}$, which is needed to determine α without assuming precise knowledge of the magnetic moment seems almost impossible to measure with unpolarised neutrons for the smallest particles. Fortunately we were allocated beam time at the D7 instrument, which has the capability of XYZ-polarisation analysis, enabling us to separate the desired magnetic cross section from SI and nuclear contributions. The remainder of this chapter describes the D7 experiment.
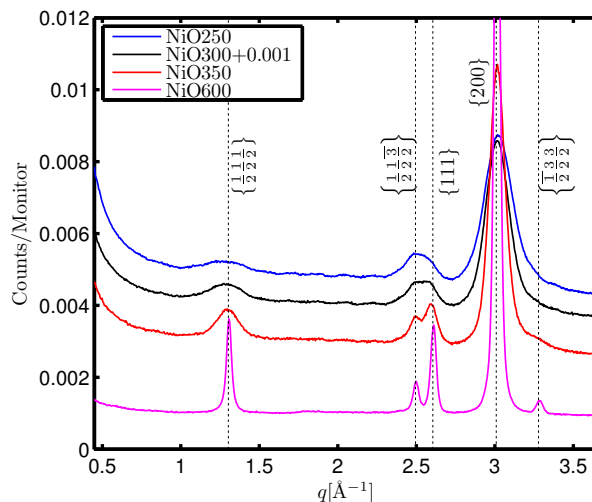

Figure 4.4: Neutron powder diffraction data on plate shaped NiO nanoparticles measured at DMC in 2011. The measurements were performed at a temperature of 2 K. The measurement times were about 12 hours for the smallest particles (NiO250) and a few hours for the largest (NiO600). The scattering at low q is small angle scattering from the surface of the particles. It was not possible to obtain the integrated intensity of the $\left\{\frac{1}{2}\frac{1}{2}\frac{1}{2}\right\}$ peak and a nuclear peak with good enough precision to obtain the spin orientation with the method described in section 4.2.2.

4.4.2 The XYZ polarisation analysis experiment on D7

To determine the spin orientation in the 5 samples of NiO particles an XYZ-polarisation analysis experiment was performed on the D7 instrument at ILL (the instrument is described in section 2.2.5). All samples were loaded in hollow-cylinder aluminium sample holders. They were loaded in a helium atmosphere to get a thermal exchange gas at low temperatures. The holders were sealed with indium. The sample masses were 2-3 g. All measurements were performed at a temperature of 1.5 K with a wavelength of $\lambda = 3.1$ Å. The first day of the experiment was used for setting up the instrument, and for calibration measurements. Before turning to the results of the experiment the calibration procedures will be explained.

Cadmium and empty can measurements (background subtraction)

To obtain the scattering intensity of the sample the background contribution to the intensity needs to be subtracted. The background comes from scattering from the sample holder, from air, from the cryostat, from various other parts of the instrument, and even sources of radiation outside the instrument. The background can be divided into a contribution from neutrons that have passed through the sample (scattering from the sample holder) and a contribution from neutrons that have not. The relationship between the measured and 'real' (i.e. background subtracted) intensity is then:

$$I_{\text{measured}} = I_{\text{real}}T + B_1T + B_2, \tag{4.13}$$

where T is the transmission of the sample, B_1 is the background from neutrons that have passed through the sample, and B_2 is the background from neutrons that have not passed through the sample. Two measurements are now performed to determine B_1 and B_2. First the empty sample container (empty can) is measured. This signal will be $I_{\text{EC}} = B_1 + B_2$. Next the sample can is filled with a piece of cadmium the same size as the sample. Cadmium absorbs neutrons very well and it can be assumed that the intensity of the cadmium measurement will only contain contributions from the neutrons that does not pass through the sample position, i.e. $I_{\text{Cd}} = B_2$. Because of the low number of counts in the background measurements it is necessary to measure for several hours to get significant statistics. The transmission of each sample was measured in a separate setup. The sample holder was placed in the beam in front of a small pinhole in front of a neutron monitor. The number of counts in 200 s was measured for the empty can, the can filled with the sample and the can with cadmium in place of the sample. The transmission of the sample is then simply

$$T = \frac{N_{\text{sample}} - N_{\text{Cd}}}{N_{\text{EC}} - N_{\text{Cd}}}, \tag{4.14}$$

where N_{sample}, N_{Cd} and N_{EC} are the number of counts during the 200 s. The transmission coefficients of our samples were between 0.92 and 0.96. Now the background subtraction can be performed:

$$I_{\text{real}} = \frac{I_{\text{measured}} - I_{\text{Cd}}}{T} - (I_{\text{EC}} - I_{\text{Cd}}). \tag{4.15}$$

The subtraction of the scattering from the sample can is sensible to small variations in the thickness of the can, and if it is to work perfectly it is required that the same sample holder is used for calibration and experiment. This was not done in our experiment, and therefore aluminium peaks are present in our data. The can used for the EC measurement were used for the other calibrations (cadmium, amorphous silica, and vanadium).

Amorphous silica measurement

A rod of amorphous silica was measured in order to determine the flipping ratio, so the data correction described in section 2.2.3 could be performed. The contributions to the cross sections from the isotopes of Si and O that has a nuclear spin is negligible, and the scattering

from amorphous silica can be assumed to be entirely nuclear coherent scattering. Hence the correction is performed so that the amorphous silica gives no SF scattering. Because the silica is amorphous it scatters in all directions, and the correction can thus be performed for all detectors simultaneously. Flipping ratios of $R \approx 30$ was measured in all channels (all detectors, all three polarisation directions), corresponding to a polarisation of $p = 0.94$. The rod of amorphous silica, a 20 mm cylinder inserted into one of the aluminium sample holders, was measured at 150 K for 7 hours to obtain sufficient statistics in the NSF channels.

Vanadium measurement

Vanadium is a strong incoherent scatterer and because the incoherent scattering is isotropic vanadium is used to calibrate for the different efficiencies of the detectors. Furthermore the normalisation with respect to the vanadium scattering gives the possibility to obtain the cross sections in absolute units. The vanadium sample is measured at 150 K to avoid inelastic contributions from phonons. A known mass of vanadium is measured (23.4 g in our case) and with knowledge of the molar density of vanadium the number of vanadium atoms in the beam is a known quantity. The cross section of vanadium is 5.08 barns per atom [56] and the measured intensity from vanadium (after background subtraction) then corresponds to $5.08/4\pi$ barns per steradian times the number of vanadium atoms. Now, when a sample is measured, the intensity is normalised to the intensity of vanadium giving the cross section in absolute units (barns per steradian). With knowledge of the sample mass, and molar mass of the sample (74.69 g/mol for NiO) the cross section can be given in barns per steradian per formula unit (barn/sr/f.u.). This unit will be used for the cross section in the following

4.4.3 Results from the D7 experiment

Separation of magnetic and nuclear cross-sections

Before analysing the data of the NiO NPs we take a look at the diffraction pattern of the bulk sample obtained at D7. The total scattering (i.e. nuclear + magnetic + SI) diffraction pattern of the bulk sample is given in Figure 4.5, showing the two nuclear and three magnetic NiO peaks as well as two peaks from the aluminium sample holder. The subtraction of the empty can measurements from the measurements of the sample does not remove the aluminium signal completely, probably because of a slight variation in the thickness of walls of the individual sample holders. A well defined signal from aluminium was preferred over a small but unknown contribution due to imperfect subtraction and it was therefore decided not to perform the empty-can correction. The peaks, which are rather broad because of the poor resolution of D7, are fitted very well with Gaussian profiles plus a flat background. The fitted peak widths from the bulk sample are considered the instrumental resolution and will be used in the analysis of the nanoparticle data.

The six measured cross sections (2.55) have been corrected for imperfect polarisation by the procedure described in section 2.2.3, and the magnetic, nuclear and SI cross sections have been calculated as described in section 2.2.2. For the bulk sample the resulting patterns are displayed in Figure 4.6 and reveals a successful separation of the three cross sections. Apart from the diffraction peaks the nuclear cross section contains a flat baseline, which can be attributed to II scattering from Ni (0.41 barns/sr/atom [56]). The magnetic cross section contains the three expected peaks and no background. The SI scattering is close to zero as expected for a dry bulk sample of NiO. The correction for imperfect polarisation can never be done perfectly, and there will therefore always be some leakage between the different cross sections. This is the reason for the small features in the SI scattering at the positions of some of the Bragg peaks. The smallness of these artifacts in the data shows that the separation of the cross sections works well. Also shown in Figure 4.6 is the SF and NSF (and average) contributions to the magnetic scattering. In most of the measured q-range the NSF and SF signals are identical, indicating that the scattering from the sample is isotropic, and thus ruling out any significant degree of preferred
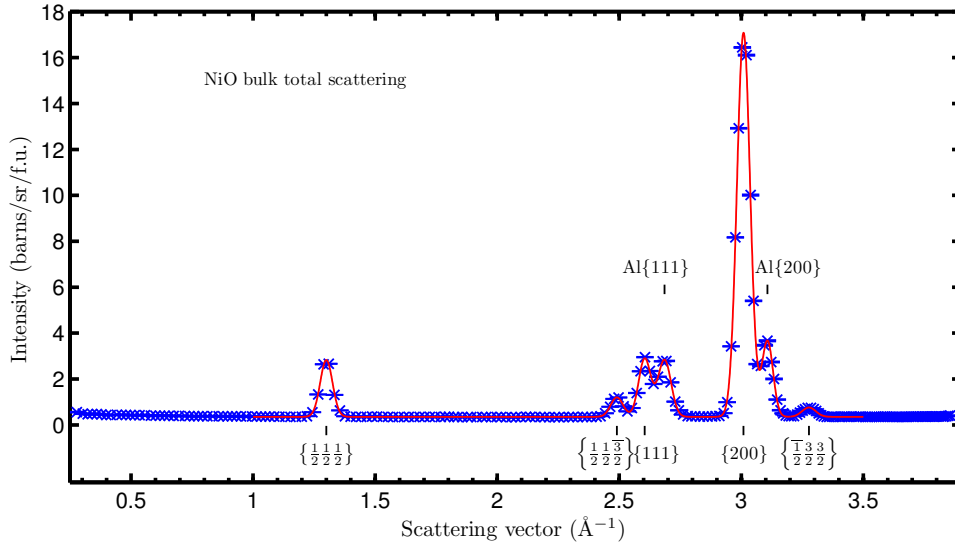
Figure 4.5: Diffraction pattern of bulk NiO measured on D7. This diffraction pattern is the total scattering, containing the nuclear, magnetic and SI scattering. The instrumental resolution is extracted from Gaussian fits to this data.
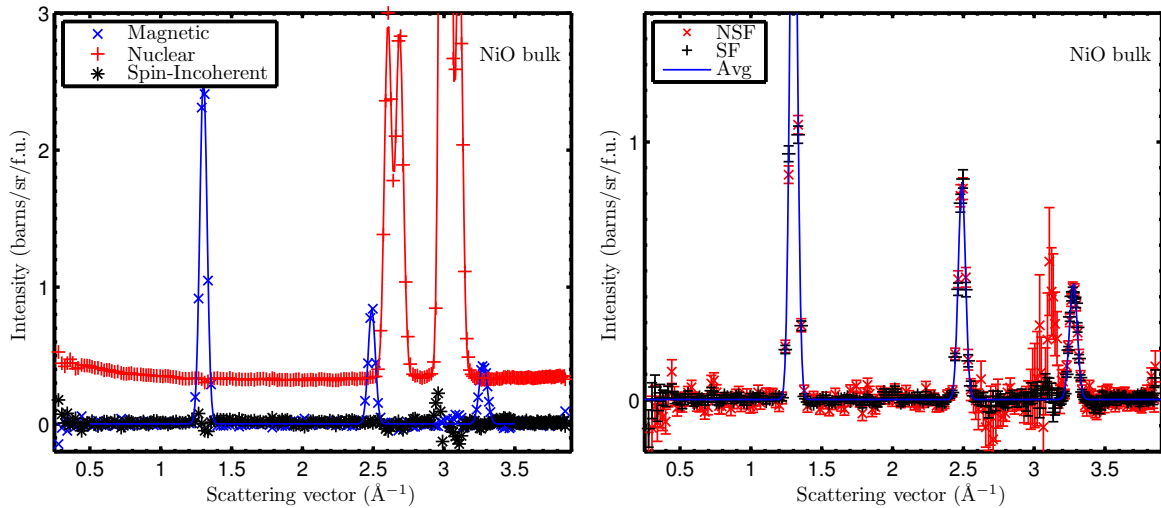

Figure 4.6: Left: The diffraction patterns of bulk NiO separated into magnetic, nuclear and spin-incoherent contributions. Right: The SF and NSF components of the magnetic scattering from bulk NiO. The full line is a fit to the average mangetic cross section.

magnetic orientation in the powder. The irregular spike in the NSF signal at the position of the strong nuclear {200} peak can be ascribed to leakage of a small amount of the nuclear signal into the magnetic SF channel. Importantly the separation works very well in the vicinity of the two important magnetic peaks. For the four NP samples the separation of the cross sections also works well. Apart from the large peak broadening due to the finite particle size, the most striking difference between the cross sections of the bulk sample in Fig 4.6 and those of the NP samples shown in Figure 4.7 is a very large SI signal and a large upturn in the nuclear signal at low q. If the SI scattering is assumed to be entirely due to hydrogen in water adsorbed at the surface of the particles, the SI signal at low q can be used to estimate the amount of water in the samples. The SI cross section of hydrogen is 6.39 barns/sr/atom [56] and the SI levels of about 0.4, 1.6, 0.39 and 0.39 barns/sr/f.u. for the four samples translate to about 0.03, 0.13,
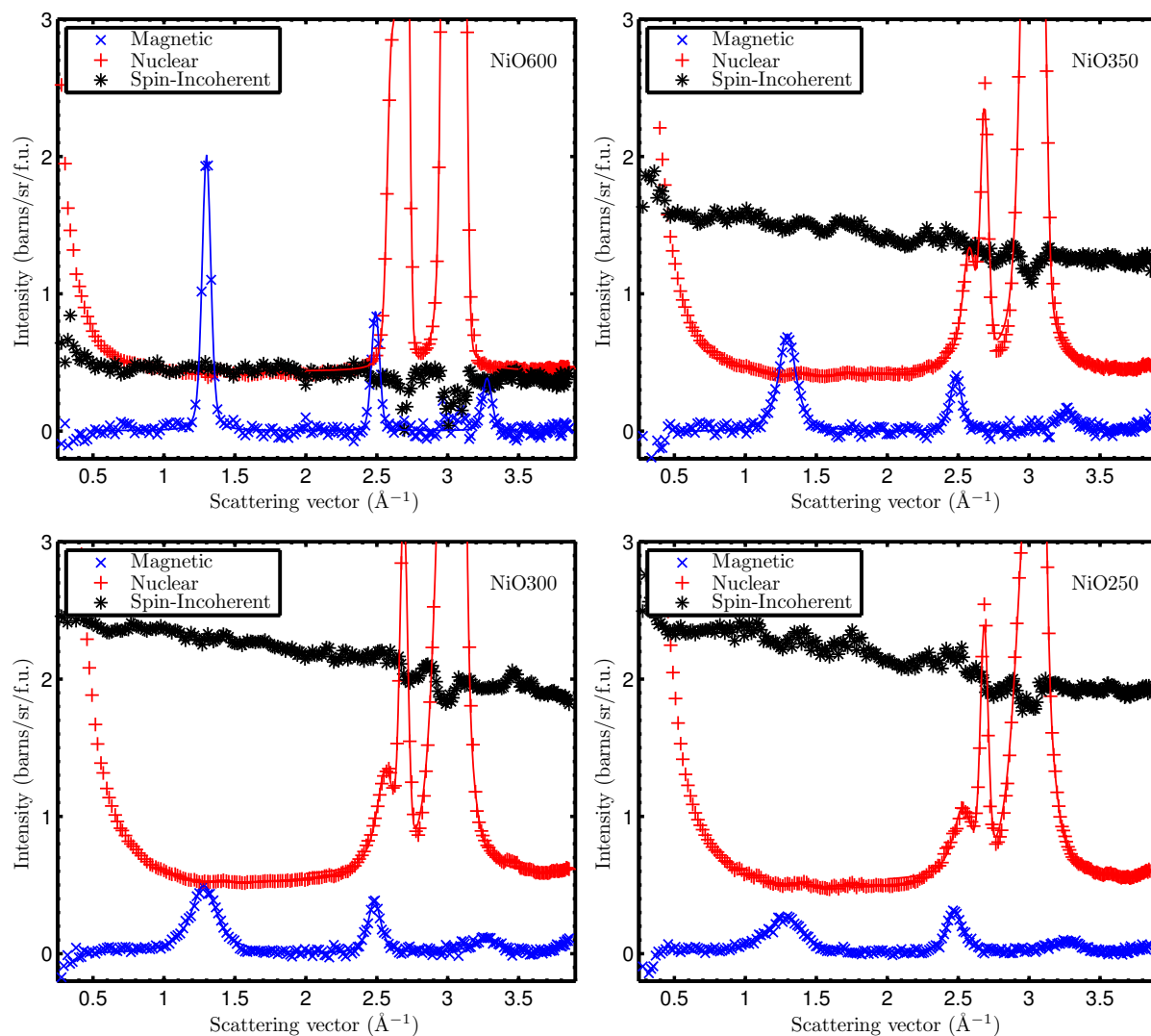
Figure 4.7: Polarisation analysed neutron powder diffraction patterns on the four samples of plate shaped NiO nanoparticles. The separation of the data into the magnetic, nuclear and spin-incoherent cross-sections have been performed. The full lines are the fits described in the text.

0.20, and 0.20 H_2O molecules per formula unit NiO for the samples NiO600, NiO350, NiO300 and NiO250 respectively. The reason for the decay in the SI signal as a function of q is probably the increased probability of (undetected) inelastic incoherent scattering from the hydrogen as function of q. The large SI scattering and the q^{-4} small angle scattering was also seen in the unpolarised data and was very problematic for the data analysis, but with the clear separation of the SI, nuclear, and magnetic signals the q^{-4} small angle scattering no longer overlaps with the $\left\{ \frac{1}{2} \frac{1}{2} \frac{1}{2} \right\}$ peak, just as the magnetic and nuclear Bragg peaks no longer overlap, and the very large SI background have been removed from the diffraction pattern altogether. Obtaining the peak intensities, which was near impossible from the unpolarised data, is now almost trivial for the well isolated magnetic peaks. The nuclear data was fitted with two Voigtian profiles to account for the nuclear Bragg peaks from the NiO NPs plus two Gaussians to account for the Al peaks from the sample container. The Gaussian widths of the Voigts as well as the Gaussians were fixed to the instrumental resolution as determined from the Gaussian fit to the bulk data. A flat background was added to the fit, which was performed on the q range between 2Å^{-1} and 3.8Å^{-1}. The magnetic signal was fitted with three Voigts, also with Gaussian widths fixed to the bulk value, plus a flat background which was very close to zero. The fits are included in Figures 4.6 and 4.7. The intensities of the peaks are obtained by numerical integration of

the Voigt functions. The errors on the intensities are estimated by a Monte Carlo method. In general the fits represent the data well. The magnetic peaks are fitted very well, whereas the fits of the nuclear peaks are a bit more difficult because they overlap. Most significantly the {200} peak does not seem to be perfectly represented by the peak, and this may give rise to a significant error on the {200} intensity. The measured magnetic cross sections for all five samples are shown in Figure 4.8. The particle sizes estimated from the Lorentzian widths of the {111} peak using (2.32) are 4.4 nm, 5.0 nm, 7.2 nm and 26.4 nm, in good agreement with the values found with XRD (see section 4.3.3), except for the NiO250 sample which comes out a bit larger. The particle sizes determined from the {200} peak, 7.6 nm, 4.9 nm, 11.1 nm and 36.7 nm are in general larger, probably reflecting that the fit does not represent this peak as well.
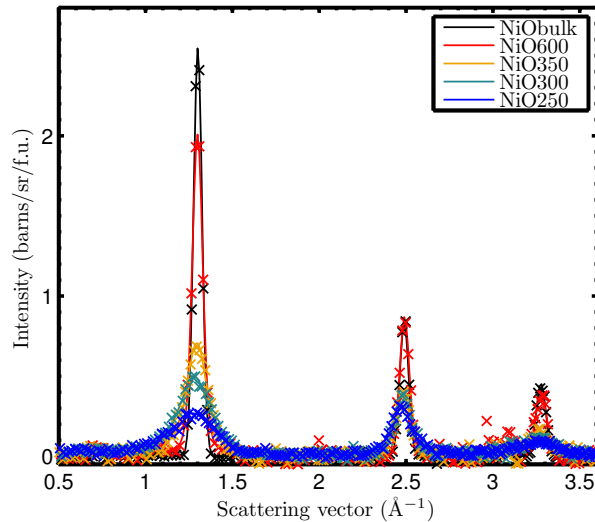
Figure 4.8: Magnetic cross sections of the five NiO samples measured at D7.

Direction of AFM modulation

To determine if the AFM correlation is in the direction normal to the particle plane, as proposed in previous studies (ref. [108]), we determine the magnetic correlation length in the direction of AFM modulation from the Lorentzian broadening of the $\left\{\frac{1}{2}\frac{1}{2}\frac{1}{2}\right\}$ peak using Equation (2.32), and compare them to the particle thickness determined with TEM. The magnetic correlation lengths determined from the $\left\{\frac{1}{2}\frac{1}{2}\frac{1}{2}\right\}$ peak are given in Table 4.3 together with the volume weighted thickness measured with TEM. If we assume [111] to be normal to the particle plane, then the remaining $\langle 111\rangle$ scattering vectors make an angle of 70.5° to the particle plane. The particle size in the [111] direction, $d_{<111>}$, is then the particle thickness, and the particle size in any of the other $\langle 111\rangle$ directions, say $[\bar{1}11]$, is $d_{[\bar{1}11]} = d_{<111>}/\cos(70.5°)$. The calculated $d_{[\bar{1}11]}$ is given in 4.3 for comparison. The measured values of $d_{\left\{\frac{1}{2}\frac{1}{2}\frac{1}{2}\right\},\mathrm{NPD}}$ are relatively close to the particle thickness, $d^V_{[111],\mathrm{TEM}}$, but in general a bit larger. The particle size in the $[\bar{1}11]$ direction is, however, much larger and with the assumption that the particles are single domain this makes it reasonable to assume that the antiferromagnetic modulation direction is perpendicular to the particle plane rather than in any one of the other $\langle 111\rangle$ directions.

This is an important result, because this means that the scattering vector for the $\left\{\frac{1}{2}\frac{1}{2}\frac{1}{2}\right\}$ reflection is normal to the particle plane (see Fig. 4.9), and the spin direction with respect to the normal of the particle plane can therefore be determined from the intensity of the $\left\{\frac{1}{2}\frac{1}{2}\frac{1}{2}\right\}$ peak, using the magnetic structure factor. The plate shape of the particles thus imposes a reduced symmetry on the cubic structure that enables us to determine the AFM spin direction with respect to the particle plane and not just the spin direction with respect to **q**.

70

	NiO250	NiO300	NiO350	NiO600
$d_{\left\{\frac{1}{2}\frac{1}{2}\frac{1}{2}\right\},\mathrm{NPD}}$ (nm)	2.26 ± 0.08	3.11 ± 0.07	5.3 ± 0.2	28 ± 2
$d^{V}_{[111],\mathrm{TEM}}$ (nm)	2.5 ± 0.6 nm	2.5 ± 0.4 nm	3.7 ± 0.5 nm	
$d^{V}_{[\bar{1}11],\mathrm{TEM}}$ (nm)	8 ± 2 nm	7.4 ± 1.2 nm	11 ± 2 nm	

Table 4.3: Comparison of the magnetic correlation length determined from the width of the $\left\{\frac{1}{2}\frac{1}{2}\frac{1}{2}\right\}$ peak with the particle thickness in the [111] direction measured with TEM. The particle thickness in the $[\bar{1}11]$ direction is also given for comparison.
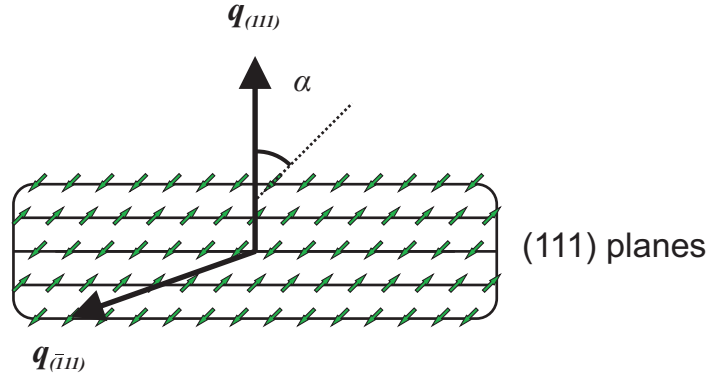
Figure 4.9: Illustration of the relationship between the spin angle with respect to the scattering vector $\mathbf{q}_{<111>}$. α is at the same time the angle to the surface normal and to $\mathbf{q}_{\langle 111 \rangle}$. The $\mathbf{q}_{\langle \bar{1}11 \rangle}$ scattering is indicated as well. If the AFM modulation was in this direction the magnetic correlation length would be larger than measured.

Determining the in-plane magnetic moment from the $\left\{\frac{1}{2}\frac{1}{2}\frac{1}{2}\right\}$ peak

To determine the in-plane magnetic moment we normalise the intensity of the $\left\{\frac{1}{2}\frac{1}{2}\frac{1}{2}\right\}$ peak to the intensity of one of the nuclear peaks as described in section 4.2.2. $M_{\perp}(\mathbf{q})$ is the magnetic moment in the (111) plane, and is displayed in Figure 4.10 as a function of particle size. There are small differences in the measured in plane moment for the different particle sizes, but the differences are small and the variation is not very systematic. There is a small, but systematic difference between the magnetic moment determined from normalisation to the {111} peak compared to normalisation to the {200} peak. This may be ascribed to a systematic error in the fitting process. The average in-plane magnetic moment is 2.0 μ_{B} for the {111} normalisation and 2.2 μ_{B} for the {200} normalisation. Assuming a total magnetic moment of 2.19 μ_{B} α can be determined to either 66° or 90° depending on the normalisation.

Obtaining the spin angle from the relative magnetic intensities

Because the magnetic peaks are well isolated from one another they can be fitted better than the nuclear peaks, and we should be able to obtain a more reliable value for the spin angle, and without any knowledge of the size of the magnetic moment. The spin angle α calculated from the relative intensities of the $\left\{\frac{1}{2}\frac{1}{2}\frac{1}{2}\right\}$ and $\left\{\frac{1}{2}\frac{3}{2}\frac{3}{2}\right\}$ peaks using (4.11) is displayed in Figure 4.11. For the smallest particles (NiO250) $\alpha \approx 60°$ corresponding to an out of plane angle of 30°. For the other particle sizes including bulk the spin angle is $\alpha \approx 75°$, corresponding to an out of plane angle of 15°.

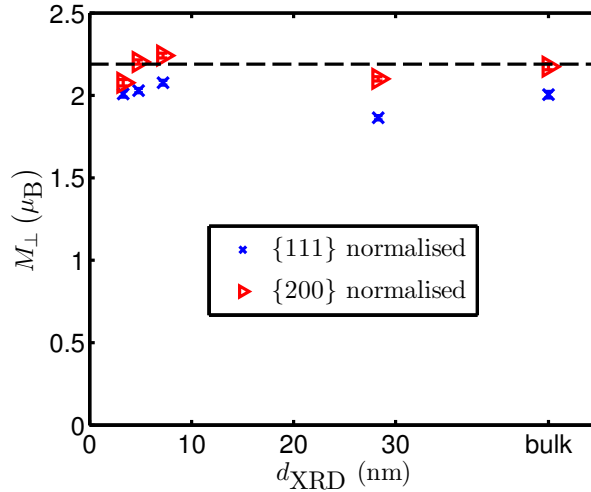**Figure 4.10:** In-plane magnetic moment calculated from the intensity of the $\left\{\frac{1}{2}\frac{1}{2}\frac{1}{2}\right\}$ peak versus d_{XRD}. The blue crosses were obtained by normalisation to the $\{111\}$ peak and the red triangles by normalising to the $\{200\}$ peak. The size of the bulk sample is assigned an arbitrary value. The dashed line at $M_\perp = 2.19\mu_{\mathrm{B}}$.
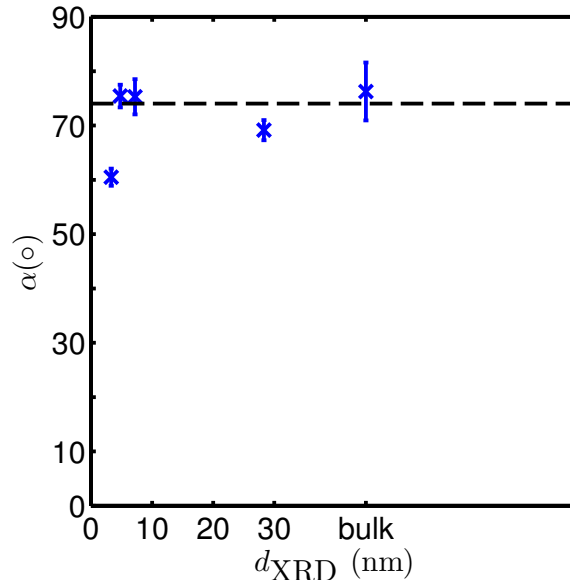

Figure 4.11: Spin angle with respect to particle normal determined from the relative intensities of the $\left\{\frac{1}{2}\frac{1}{2}\frac{1}{2}\right\}$ and $\left\{\frac{1}{2}\frac{\overline{3}}{2}\frac{\overline{3}}{2}\right\}$ peaks. For all but the smallest sample (NiO250) α is roughly constant around 70-75° with particle size, around 70-75°. For the NiO250 sample $\alpha \approx 60°$ corresponding to an out of plane angle of 30°. The size of the bulk sample is assigned an arbitrary value. The dashed line is the average of α for the samples NiO300, NiO350, NiO600 and bulk.

4.5 Discussion

We have performed a XYZ-polarisation analysis experiment on NiO nanoparticles, successfully demonstrating that the technique can be used for separating the nuclear, magnetic and SI contributions. Because XYZ-polarisation analysis can be done at a multidetector instrument we were able to obtain separate magnetic and nuclear powder diffraction patterns over a q-range from 0.28 Å^{-1} to 3.86 Å^{-1}. The separated diffraction patterns from the XYZ polarisation analysis experiment was a vast improvement of the existing data from unpolarised NPD which suffered from overlap between the magnetic peaks and the nuclear signal rendering an analysis

of the magnetic structure of the smallest particles extremely difficult. With the magnetic and nuclear signal separated the intensities of the magnetic peaks can be determined and the data analysis can proceed to produce information about the magnetic structure.

From comparison of the magnetic correlation length in the direction of AFM propagation with the particle thickness measured with TEM we determine that the direction of AFM propagation is normal to the particle plane. This $\left\{\frac{1}{2}\frac{1}{2}\frac{1}{2}\right\}$ magnetic correlation length is somewhat larger than the measured particle thickness, but this is likely due to an overrepresentation of the smallest particles in the determination of the thickness with TEM. Furthermore the particle size in the $\langle 111 \rangle$ directions not perpendicular to the particle plane is 2-3 times larger than the magnetic correlation length and these directions thus seems very unlikely to be the directions of AFM modulation.

We determine the magnetic moment in the (111) plane of the particle from the intensity of the $\left\{\frac{1}{2}\frac{1}{2}\frac{1}{2}\right\}$ peak normalised to either the nuclear {100} or {200} peak. We obtain an in-plane magnetic moment of 2.0 μ_{B} when normalising to the {100} peak and 2.2 μ_{B} when normalising to the {200} peak. The difference between these two values is likely due to a systematic error in the fitting of the nuclear peaks. If a total magnetic moment of 2.19 μ_{B} is assumed for the Ni^{2+} ions [26] the measured in-plane moments correspond to spin orientations in the (111) plane and 23° out of the plane.

The spin angle α was determined, without assumptions about the size of the magnetic moment, directly from the relative intensities of magnetic peaks which were well determined because the magnetic peaks are isolated. With this approach we find an out-of-plane angle of 15° for all but the smallest particles, including the bulk NiO sample. For the smallest particles ($t = 2.0$ nm) we obtain an out-of-plane angle of 30°.

The in-plane magnetic moment determined by normalising the magnetic intensity to either of the nuclear peaks does not change significantly with particle size whereas α is different in the smallest particles compared to the rest, as determined from the relative magnetic intensities. If the magnetic moment of the Ni^{2+} ions is assumed to be independent of particle size these two results contradict each other and this may be due to systematic errors, most likely in the determination of the intensities of the nuclear peaks. It is possible that the magnetic moment changes with particle size so that the in-plane moment remains constant but the out of plane component grows significantly for the smallest particles, but this seems unlikely. It should be noted that it is intrinsicly difficult to measure small differences in the orientation of $M_{\perp}(\mathbf{q})$ for a magnetic moment that is close to perpendicular to $\mathbf{q}$ (i.e. where $\sin \alpha \approx 90°$) and the results are therefore sensitive to small systematic errors. This is true for the results in both Figure 4.10 and 4.11.

In conclusion we measure a magnetic moment oriented close to the (111) plane for plate shaped NiO NPs with thikcnesses larger than 2.2 nm (including bulk). The spin angle to the (111) plane in these particles is about 15°. The magnetic structure in bulk NiO is usually found to be within the (111) plane [120–124] and it is thus surprising that we find a (small) out of plane spin angle in the bulk sample. The small out of plane angle may be ascribed to small systematic errors which can easily give a significant change in the measured spin angle (the difference between $\sin 90°$ and $\sin 75°$ is only 3.5%). For the NiO250 sample, wich is the sample with the smallest particles ($t = 2.0$ nm), the measured out of plane spin angle is 30° and this is significant. The out of plane spin orientation in very thin particles is similar to the spin reorientation transition observed in thin NiO films [104, 105].

Magnetic structure in aggregated and hydrothermally grown hematite nanoparticles

In this chapter we study the effect on the magnetic properties of aggregation and crystal growth of magnetic NPs. Nanoparticles in nature or in industrial applications are often not in an isolated but in an agglomerated form and it is important to know how the interactions between the agglomerated particles affect the magnetic properties. As previously discussed inter-particle interactions can significantly affect both the magnetic structure and the dynamics in magnetic NPs. Here we prepare hematite NPs in aqueous suspension in different states of aggregation by a hydrothermal treatment and by adding salt ions to the suspension. We follow the development in particle and aggregate size with DLS, XRD and TEM and the magnetic properties with Mössbauer spectroscopy. The purpose of these investigations is a controlled study of how the magnetic structure in hematite NPs depends on aggregation and growth of the particles. In particular we wish to determine whether the Morin transition, which is normally absent in particles smaller than ≈ 20 nm, can be recovered by assembling ≈ 9 nm hematite particles into larger aggregated structures.

Before continuing with the discussion of hematite NPs the magnetic structure of hematite is reviewed. This will be relevant for both the discussion of hematite NPs in this chapter and for Chapter 6 about the spin orientation in hemo-ilmenite.

5.1 Magnetic structure of hematite

Hematite (α-Fe$_2$O$_3$) is a naturally occurring mineral and the most stable of the iron oxides. It crystallises in the corundum structure (space group $R\bar{3}c$). Using the hexagonal unit cell the room temperature lattice parameters are $a = b = 5.038$ Å and $c = 13.722$ Å [127]. The magnetic structure of hematite (see Fig. 5.1) is AFM below a Néel temperature of $T_N = 955$ K [127]. The direction of AFM modulation is along the c-axis with parallel alignment of spins within the ab planes of the hexagonal structure. Between T_N and $T_M \approx 264$ K Fe^{+3} spins in the same planes of the hexagonal structure are parallel, and spins on adjacent planes are antiparallel apart from a small canting of about $0.065°$ [127]. In this state of so-called canted antiferromagnetism (CAF), the spins imperfect AFM alignment leads to a weak ferromagnetism in hematite. In the CAF state the spins are usually assumed to be confined within the basal plane of the hexagonal structure by a strong out of plane anisotropy. The much smaller in-plane anisotropy places the spins preferably perpendicular to the six fold axes and with the canting also in the basal plane.

While the spins in the CAF state are usually assumed to be aligned within the basal plane [50, 127], symmetry does allow for an out of plane component, but theory predicts it to be small [128]. Most experiments are consistent with the spins in, or very close to the basal plane in the CAF
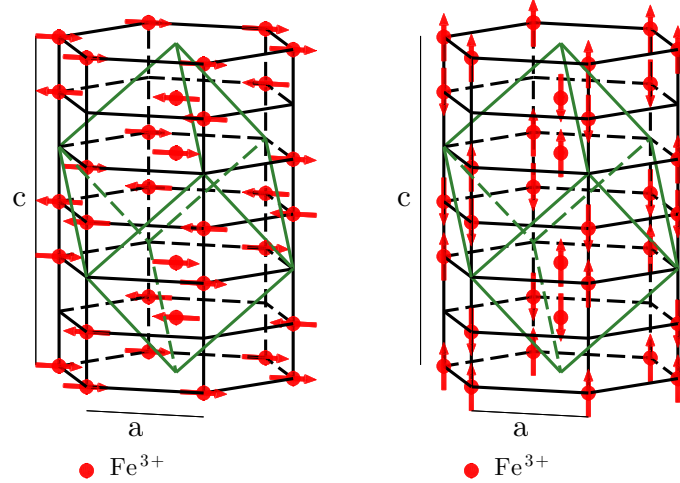
Figure 5.1: Crystal and magnetic structure of hematite. Only the Fe^{3+} cations and not the intermediate O^{2-} anions are shown. The rhombohedral unit cell is shown in green. Left: Magnetic structure in the CAF state for $T_M < T < T_N$ (the canting is not shown) . Right: Magnetic structure below T_M. The drawing is (modified) from **Paper** [7].

state [50,129]. However, measurements of large out of plane moments have been reported in bulk hematite samples. Tobler et al. measured an out of plane angle of 3.9° [130] with Mössbauer spectroscopy, and with NPD Parise et. al have measured an out of plane angle as large as 20° in a synthetic hematite sample.

At a temperature $T_M \approx 264$ K [20,21], known as the Morin temperature, hematite undergoes a spin-flop transition in which the spin orientation changes from close to the basal plane to along the hexagonal c-axis, maintaining the AFM alignment between adjacent planes.

The magnetic structure and dynamics of hematite can be understood from the exchange and anisotropy energy of the structure. The exchange energy per unit volume responsible for the AFM ordering can be written [127,131]

$$F_e = J\mathbf{M}_A \cdot \mathbf{M}_B - \mathbf{D} \cdot (\mathbf{M}_A \times \mathbf{M}_B),$$ (5.1)

where $J < 0$ is the exchange constant, $\mathbf{M}_A$ and $\mathbf{M}_B$ are the sublattice magnetisations and $\mathbf{D}$ is the so-called Dzyaloshinsky-vector, which is a constant vector that in hematite is in the [001] direction. The first term in the expression (5.1) takes the familiar form of the Heisenberg interaction (1.1) and the second term is the so-called Dzyaloshinski-Moriya (DM) interaction. The result of the DM interaction is a small canting of the AFM sublattices away from antiparallel alignment resulting in a small net magnetisation in hematite. Dzyaloshinsky was the first to realise that the symmetry of the system allows for a canting of the sublattice magnetisations [128] and Moriya was the one that explained the microscopic origin of the interaction as a combination of superexchange and spin-orbit coupling. [132] The magnetic anisotropy of hematite has a strong uniaxial component in the [001] direction and a weak component in the basal plane. In general the magnetocrystalline anisotropy in the basal plane should reflect the six fold symmetry of the hexagonal structure. It turns out, however, that there is another contribution, due to stress, to the basal plane anisotropy which is uniaxial. This component may be large, and it is argued that it is dominant in hematite nanoparticles [131] and it will therefore suffice to treat the basal plane anisotropy as uniaxial. The magnetic anisotropy in hematite (nanoparticles) per unit volume can then be expressed [131]

$$F_{UB} = -K_1 \cos^2 \theta + K_{Bu} \sin^2 \theta \sin^2 \phi,$$ (5.2)

76

where θ is the (polar) angle between $l = M_A - M_A$ and the [001] direction and ϕ is the (azimuthal) angle between l and an the easy direction in the basal plane. The out of plane anisotropy constant K_1 is much larger than K_{Bu} and the magnetic sublattices are thus relatively free to rotate in the basal plane. The Morin transition can be understood as a change of sign of K_1 at T_M with K_1 negative for $T > T_M$ and positive for $T < T_M$.

5.2   Hematite nanoparticles and aggregation

Hematite nanoparticles have been the subject of numerous studies focusing in particular on the dynamics [131, 131, 133, 134]. Some investigations have dealt with the effects of interactions by comparing experiments on particles that are treated in different ways. These studies confirm that SPM relaxation in the particles tends to be suppressed by inter-particle interactions [23, 25, 27]. It has also been observed that the spin direction in hematite NPs can be affected by inter-particle exchange interactions between hematite particles [28] or between hematite and nickel oxide particles [**4**]. The spin orientation in hematite can be found from the quadrupole splitting through the formula [28, 127]

$$\epsilon = \epsilon_0 \left(3\cos^2\theta - 1 \right)/2, \tag{5.3}$$

where $\epsilon_0 = 0.20$ mm/s and θ is the angle of the spin to the EFG which in hematite is in the [001] direction. Above T_M the spins are in the basal plane and $\epsilon = -0.10$ mm/s and below T_M the spins are along [001] and $\epsilon = 0.20$ mm/s. The Morin temperature is known to be significantly lowered for particles smaller than 1 μm and the MT is absent at temperatures down to 4.2 K in particles smaller than 20 nm [22]. It is not known, however, how the MT is affected by aggregation of particles and a recovery of the MT by assembling smaller particles to larger structures would indicate a collective magnetic structure extending over several particles.

5.2.1   Oriented attachment and mesocrystals

Particles in a suspension undergoing Brownian motions may aggregate because of the van der Waals forces between the particles and the precise attachment of the particles may be random or oriented in a specific way. A recent study [135] have shown that Coulomb interactions between surface atoms of particles in close proximity may lead to oriented attachment. If the particles attach with (partial) crystallographic alignment the process is known as oriented attachment (OA). Aggregation of many nanoparticles into larger structures, known as mesocrystals [136,137] that subsequently fuse into single crystals is an important mechanism for crystal growth and may also be a viable route to build functional nanostructured materials. [136] The driving mechanism behind the OA is minimisation of the surface energies by attaching particles by high energy surfaces. If the particles are magnetic the magnetic interactions may also play a role for the OA. Certainly the dipole interactions between ferri- or ferromagnetic particles can be important as have been seen in several studies where chains of magnetic structures are formed either by the magnetic attraction between the particles or by the aid of an applied magnetic field. Despite its short range exchange interaction may also play a role in the attachment between AFM NPs. In fact Frandsen et al. estimate the exchange interaction between the (111) facets of hematite particles to be on the same order as the surface energy and the exchange energy may therefore be the reason for the observed tendency for hematite to attach by the (001) facets even though it is not the surface of highest energy [138]. In 20 nm hematite particles Hansen et al. measured a magnetisation similar to that produced by the weak ferromagnetism in bulk CAF hematite [23] and any magnetisation from uncompensated moments is therefore expected to be small. The magnetic dipole moment of the particles is thus not likely to play a role in the assembly.

If AFM particles are epitaxially aligned and in very close proximity the magnetic order may continue over several particles. This has been observed in hematite NPs that were found to attach preferentially in the (001) direction of their hexagonal crystal structure forming oriented

aggregates of a size of 3 particles on average. The magnetic correlation length was measured with NPD and it was found that the magnetic order did continue across the particle interfaces [138].

In the following we will study the aggregation and growth of individual hematite particles subjected to different hydrothermal treatments and determine how the aggregation and growth affects the magnetic structure, in particular if the MT is recovered.

5.2.2 Sample preparation

As prepared sample

Monodisperse hematite particles in aqueous suspension was produced by a gel-sol method similar to that described by Sugimoto et al. [139]. The particles are suspended in HNO_3 ($pH \approx 3.9$) and the electrostatic charging of the particles means that the suspension is stable with a zeta-potential $\zeta >50$ mV. Characterisation of this as-prepared suspension with XRD and DLS, to be discussed below, gives an average particle diameter $d_{XRD} = 9.3$ nm and a hydrodynamic diameter (volume distribution) $d_H = 11.8 \pm 5.2$, where $\pm$ refers to the standard of the volume distribution and not the uncertainty on the peak position.

TEM images of the as-prepared sample presented in Figure 5.2 shows rather well dispersed particles as well as some collections of particles that may be an effect of the drying of the suspension on the grid. On closer inspection the dispersed particles typically looks like small aggregates of 2-5 particles leading to an irregular often slightly elongated shape that can be described as pseudo-elipsoide. Because the particles are not spherical their size is not well represented by a single number and the dimensions of the particles were therefore measured in two directions. The particle size in the longest direction and in the direction perpendicular to the longest direction were measured for 45 particles giving an average particle length of 14 ± 2 nm and a particle width of 8 ± 2 nm, where ± 2 denotes the standard deviation of the average. Assuming an elipsoide particle shape the corresponding volume weighted particle length and width are 15 nm and 9 nm. The particle edges are soft and irregular shaped and no crystal facets are seen. High resolution TEM and X-ray investigations on hematite NPs prepared with a similar method shows particles that are elongated in the hexagonal [001] direction and form chains of on average three particles with aligned [001] axes [138, 140].
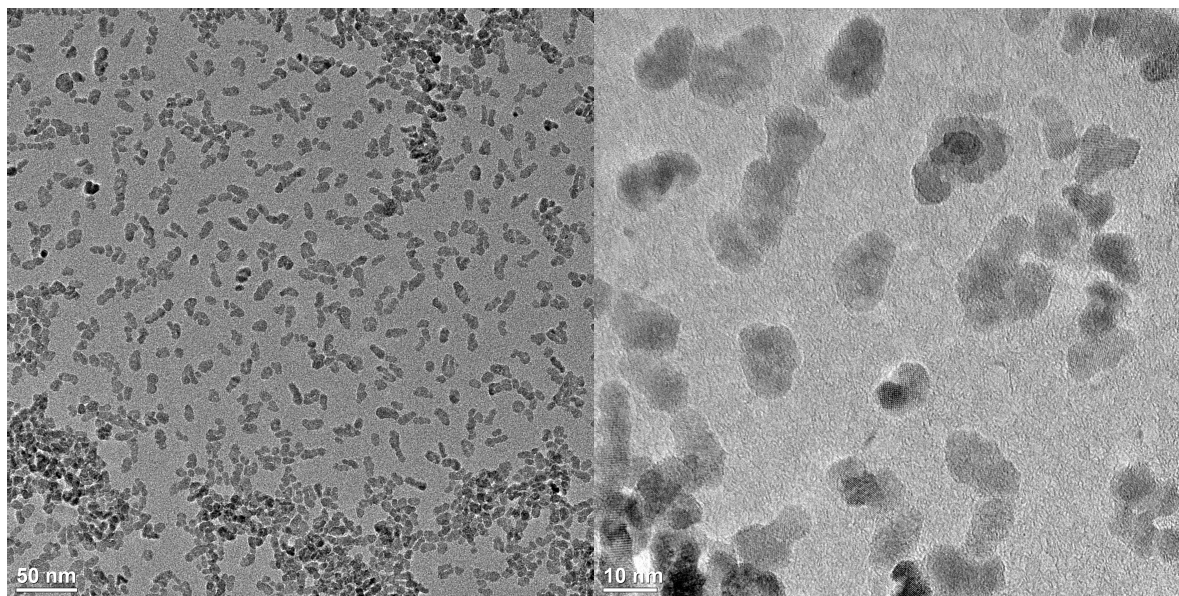

Figure 5.2: TEM micrographs of the as prepared sample.

Hydrothermal treatment

Hydrothermal treatment of hematite NPs in aqueous suspension and addition of NaCl ions to
the suspension have been shown to be an effective way of inducing aggregation. The aggregation
depends on the concentration of particles in the suspension, the pH value, the ionic strength
(the concentration of ionic charges) and also on the particle size [141]. To prepare samples
of hematite NPs with different degrees of aggregation the as-prepared sample was heated for
10 days in autoclaves at temperatures of 100°C, 120°C, and 140°C. The ionic strength of the
suspension was controlled by adding NaCl to a concentration between 0.5 mM and 25 mM.
Higher concentrations (50 mM) of NaCl resulted in immediate sedimentation. The effect of
adding NaCl is a neutralisation of the charge on the particles by the salt salt ions.

After the hydrothermal treatment the suspensions were measured with DLS. Samples for
Mössbauer spectroscopy was prepared by freezing of the particle suspensions in liquid N_2. Be-
cause of the relative low concentration of particles in the suspension the Mössbauer absorption of
the samples was quite low (1-3%) and to obtain significant statistics the samples were typically
measured for 48-72 hours. TEM samples were prepared by allowing a drop of the suspension to
dry on TEM grid and TEM images of the samples were obtained at the TECNAI microscope at
DTU-Cen. The sample with 25 mM NaCl before hydrothermal treatment was further selected
for high resolution TEM imaging performed by Thomas Willum Hansen. XRD measurements
were only performed for the as prepared sample and the 25 mM NaCl sample aged at 140°C.
The XRD samples were prepared by drying the suspension on a silicium XRD sample holder.

5.3   Effect of ionic strength - aggregation

Dynamics light scattering
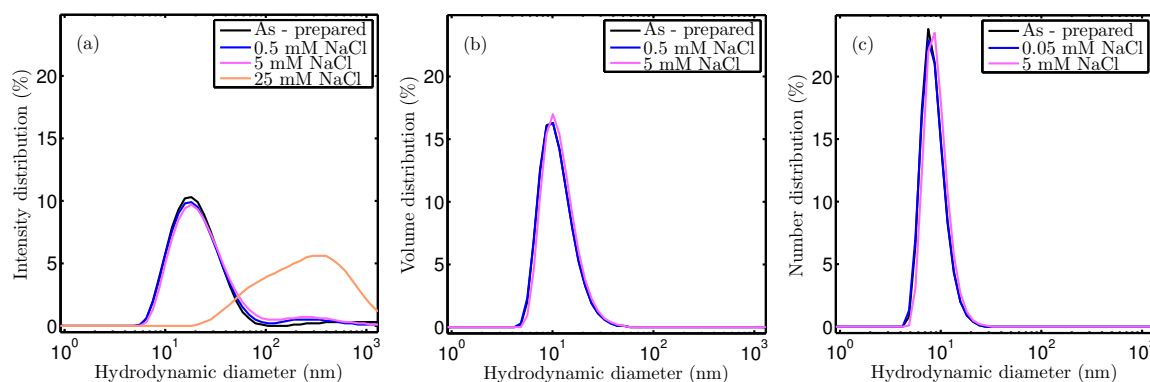
Figure 5.3: Particle size distributions measured with DLS before hydrothermal treatment. (a) Size
distribution by intensity. (b) Size distribution by volume. (c) Size distribution by numbers.

The particle size distributions (PSDs) measured with DLS before hydrothermal treatment is
shown in Figure 5.3 for the as prepared sample and three different concentrations of NaCl. Both
intensity, volume and number distributions of the particle size (hydrodynamics diameter) are
shown. The intensity PSD (Fig. 5.3 (a)) shows one well defined peak centered at $d_H = 22 \pm 12$
nm for the as prepared sample, where once again $\pm$ denotes the width of the distribution. The
hydrodynamic diameter of the as prepared sample from the volume distribution is $d_H = 11.8 \pm 5.2$
nm and from the number distribution it is $d_H = 8.8 \pm 2.6$.

The intensity PSDs for the samples with NaCl concentrations up to 5 mM are essentially
identical to that of the as prepared sample, however, addition of NaCl to a concentration of
25 mM have a profound effect on the hydrodynamic diameter. The intensity PSD of the 25
mM NaCl sample is centered at a much larger value and extends over more than an order of
magnitude giving a hydrodynamic diameter of $d_H = 352 \pm 338$ nm. This very high polydispersity

makes it impossible to convert the intensity PSD of the 25 mM NaCl sample to volume or number distributions.
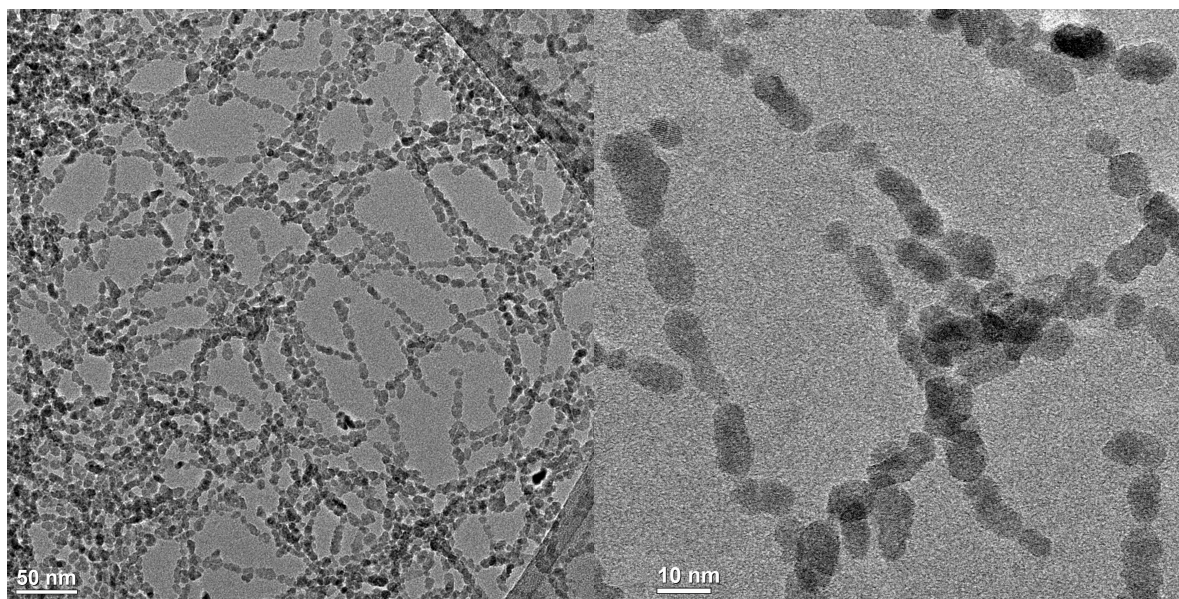
Transmission electron microscopy

Figure 5.4: TEM micrographs of the 25 mM NaCl sample before hydrothermal treatment.

TEM images of the sample in 5 mM NaCl solution (not shown) are very similar to those of the as prepared sample (shown in Fig. 5.2) showing no effect of the change in ionic strength in the suspension, in agreement with the DLS data. Figure 5.4 shows TEM images of the sample with 25 mM NaCl concentration.

In contrast to images of the particles with 0 and 5 mM NaCl the images in Figure 5.4 shows that the particles form long chains. The chains consist of particles similar to those observed in the as prepared sample. Some chains are several hundred nanometers long consisting of dozens of particles. The particles in the chains are not fused together and there may be solvent molecules between the particles. One could speculate that the chains might not be present in the aqueous suspension but be an effect of NaCl crystallisation during drying. However, DLS shows a large increase in the particle size in the 25 mM NaCl sample which suggests that the chains are present in the suspension.

The attachment tends to be with the long axes of the particles aligned and this could indicate that the attachment is crystallographically oriented. From the already mentioned previous studies it seems likely that the alignment of the chains is along the [001] direction. To test this hypothesis high resolution TEM images were taken by Thomas Willum Hansen at the FEI Titan E Cell 80 300ST microscope at DTU-Cen. Examples of the high resolution images of the 25 mM NaCl sample are shown in Figure 5.5. The most prominent lattice fringes in the presented images are the ones parallel to the elongated particle which is also shown in the zoom-in to the right in the figure. The periodicity of the fringes is 2.5 Å corresponding to the d-spacing of the (110) planes in hematite. Since the (110) planes are perpendicular to the (001) planes this confirms that the particles are elongated in the [001] direction. Furthermore the alignment of the lattice planes continue from one particle to the next even though there is a gap between the particles as seen in the zoom-in image in Figure 5.5. The elongated particle in the lower panel of Figure 5.5 has two sets of visible lattice planes, one parallel and one perpendicular to the long axis of the particle with respective periodicities of 2.5 Å and 4.6 Å as confirmed by the Fourier transform also shown in the Figure. The 2.5 Å is once again the (110) d-spacing and the 4.6 Å corresponds well to the (003) d-spacing which is usually not an allowed reflection. It is not

clear why the (003) lattice planes are seen, but they have been seen in other studies of hematite
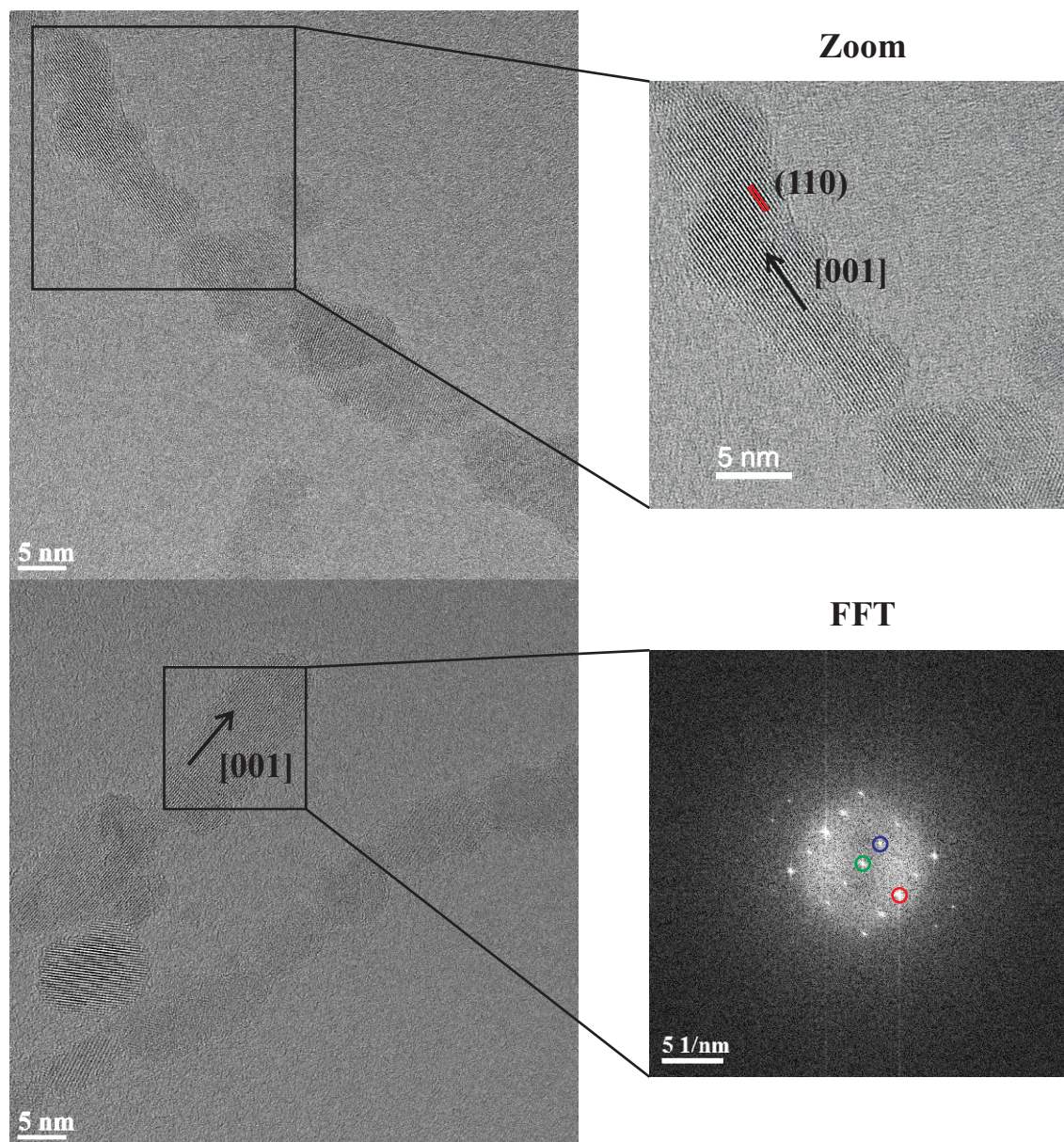nanoparticles [142], and it confirms that the particles are elongated in the [001] direction.

Figure 5.5: High resolution TEM micrographs of the 25 mM NaCl sample before hydrothermal
treatment obtained at the FEI Titan E Cell 80 300ST microscope at DTU-Cen by Thomas Willum
Hansen. Top: Image of a chain of hematite particles with lattice planes of neighboring particles aligned.
A zoom-in on the part of the image enclosed in a square is given to the left. The spacing between the
lattice fringes correspond to the (110) d-spacing. Bottom: The particle enclosed in the square have two
sets of perpendicular lattice fringes corresponding to the (110) and (003) d-spacings of the hematite
structure as confirmed by the Fourier transform shown to the left. The distance between the central
spot (green) and the red spot 3.91 nm^{-1} and the distance between the central spot and the blue spot is
2.15 nm^{-1}. The corresponding d-spacings are 2.56 Å and 4.65 Å roughly corresponding to the (110)
and (003) d-spacings of hematite.
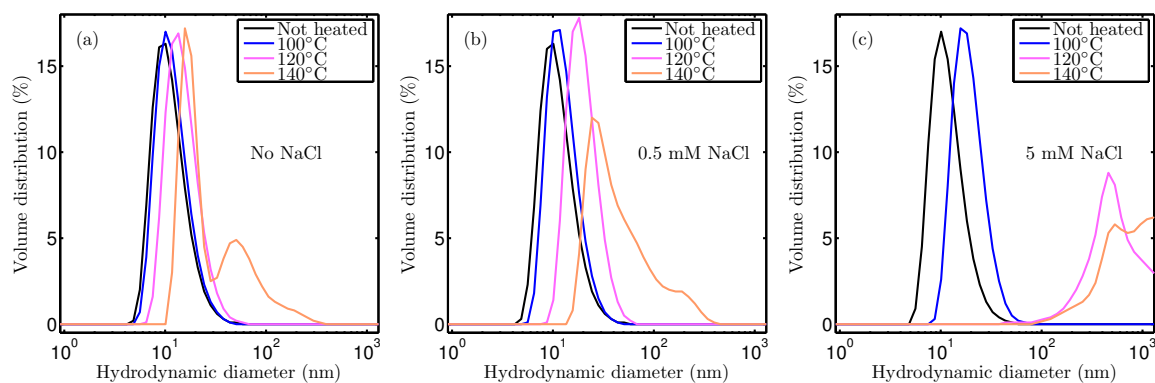
Figure 5.6: Particle size distributions as function of autoclaving temperature measured with DLS. (a) No NaCl. (b) 0.5 mM NaCl . (c) 5 mM NaCl.

5.4 Effect of hydrothermal treatment - crystal growth

Dynamic light scattering

The effect of increasing autoclaving temperature on particle size was investigated with DLS resulting in the volume PSDs shown in Figure 5.6(a) for the samples without NaCl, with 0.5 mM NaCl 5.6 (b) and 5 mM NaCl 5.6(c). For the sample without NaCl (Fig 5.6 (a)) the hydrothermal treatment at 100°C has the effect of shifting the PSD from $d_H = 11.8 \pm 5.2$ nm to $d_H = 12.5 \pm 5.2$ nm. When the autoclaving temperature is increased to 120°C the PSD changes more significantly to $d_H = 15.7 \pm 6.3$ nm. For the sample autoclaved at 140°C d_H is shifted to even higher sizes and the PSD becomes much broader. The PSD is bimodal with two distributions centered about 18 nm and 73 nm. It may be noted that 97% of the scattering is comming from the particles giving rise to the peak at 73 nm in the volume distribution.

From PSDs of the samples with 0.5 mM and 5 mM NaCl shown in Figure 5.6 (b) and (c) it is clear that increasing addition of NaCl enhances the effect of the hydrothermal treatment, leading to larger hydrodynamic diameters: With 0.5 mM NaCl the PSDs of the samples heated at 100°C and 120°C are shifted towards larger d_H (13.2 ± 5.2 nm and 20.5 ± 7.4 nm)and the PSD of the 140°C sample is even more polydisperse than the corresponding sample without NaCl also shifted to higher sizes ($d_H = 58 \pm 54$ nm).

For the 5 mM NaCl sample the PSDs of the sample heated at 100°C is further shifted to 19.9 ± 7.5 nm and the PSD of the samples heated at 120°C and 140°C are both very broad, ranging over sizes from hundreds to thousands of nanometers.

For the sample with 25 mM NaCl the PSD was already very polydisperse before the hydrothermal treatment as shown in Figure 5.3 and after heating at 140°C the particles or aggregates were so large that a large fraction of them sedimented during the DLS measurements.

As discussed in section 2.5 determining PSDs with DLS for very polydisperse samples can be problematic and the exact shape of the PSDs should probably not be given too much significance. However, the PSD can be considered an indication of the ever increasing particle size with autoclaving temperature.

Transmission electron microscopy

TEM images of the samples heated at 140°C are shown in Figure 5.7 for the sample without NaCl and the sample with 25 mM NaCl.

From the images in Figure 5.7 (a) and (b) it can be seen that the sizes and shapes of individual particles have changed with the heating. Contrary to the particles in Figure 5.2 (a) and (b) the particles after the hydrothermal treatment have sharp edges resembling crystal facets. The particle size has increased so that some particles are larger than 30 nm while particles smaller than 10 nm still exist. After the hydrothermal treatment most particles are

collected in aggregates of more than 20 particles while a few particles are still isolated. These
large aggregates could be an effect of the drying, however, DLS shows that there are also large
aggregates in the suspension. The aggregates are not as pronounced linear chains as in the
images of the 25 mM NaCl sample before heating (Fig. 5.2 (c-d)) but there are shorter twisted
chain like structures. For the sample without NaCl heated at 140°C the particle sizes were
measured in the same way as for the as prepared sample giving average particle dimensions of
18 ± 6 nm $\times 14 \pm 4$ nm corresponding to volume weighted average dimensions of 23×17 nm.

For the 25 mM NaCl sample heated at 140°C the particles (Fig. 5.7 (c-d)) the effect of the
hydrothermal treatment have been increased by the NaCl resulting in more large particles with
more particles larger than 30 nm and more pronounced faceting of the particles. The aggregates
look more random than in the sample without NaCl and there are almost no isolated particles.
There is no sign of the long linear chains of particles seen in the sample before the hydrothermal
treatment.
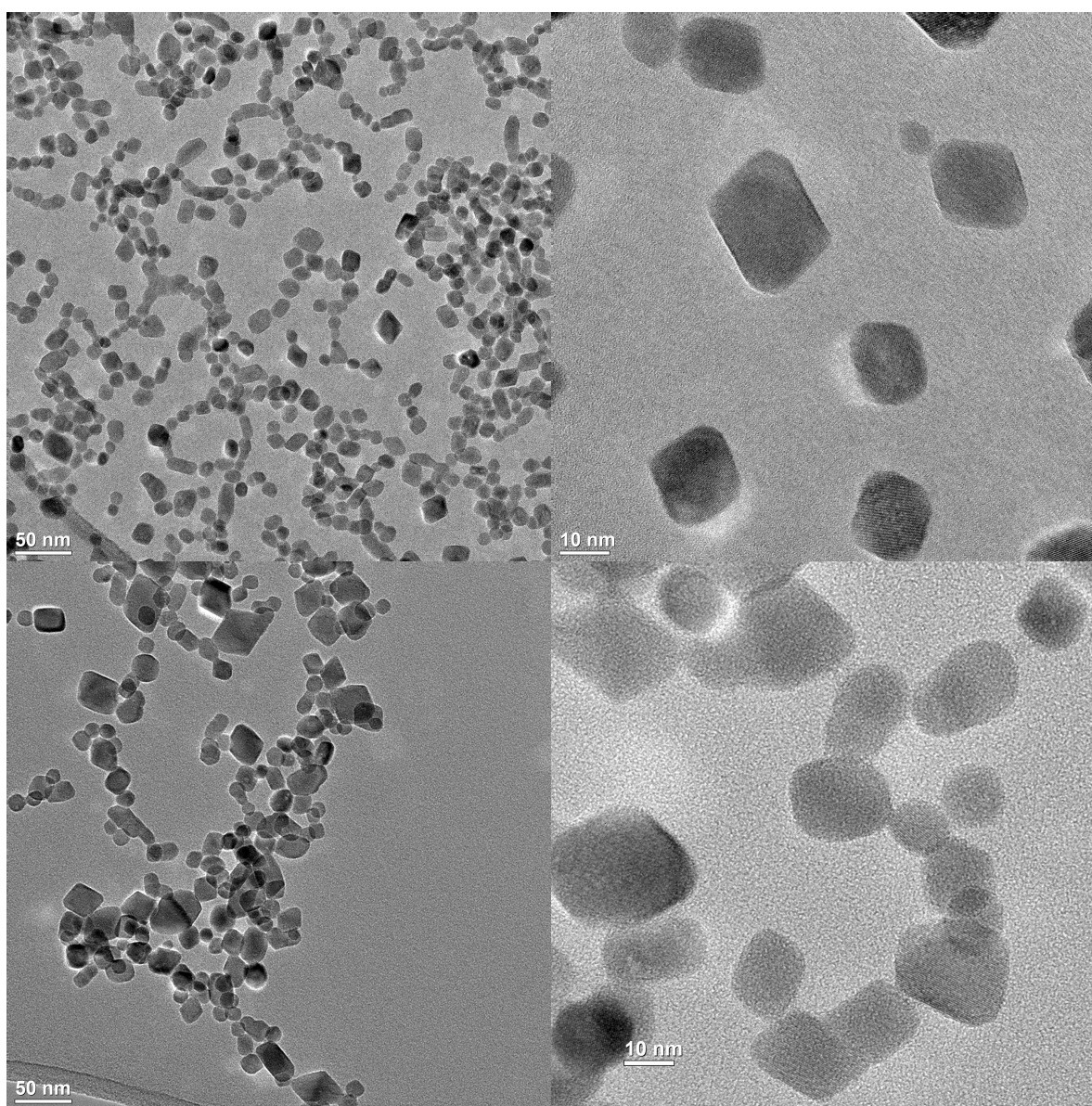
Figure 5.7: TEM micrographs of samples after hydrothermal treatment at 140°C. Top: Sample
without NaCl. Bottom: Sample with 25 mM NaCl.
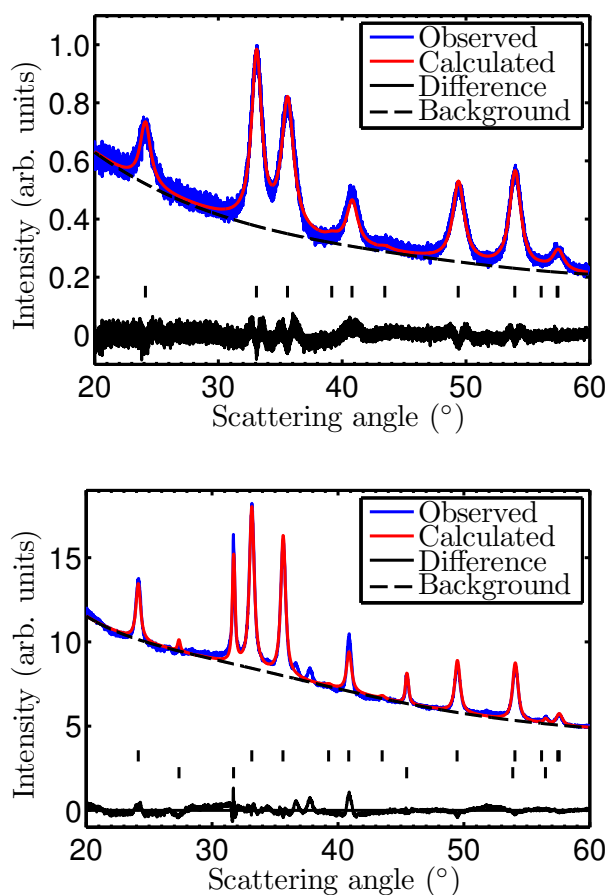
Figure 5.8: X-ray diffraction patterns of the as prepared sample (top) and the 25 mM NaCl sample after hydrothermal treatment at 140°C (bottom). The lower tick marks in the bottom figure correspond to the NaCl structure.

X-ray diffraction

The as prepared sample and the sample with 25 mM NaCl after hydrothermal treatment at 140°C was characterized with XRD. The diffraction patterns of the two samples are shown in Figure 5.8. Rietveld refinement of the $R\bar{3}c$ structure of hematite was performed using Voigtian lineshapes to extract the mean particle sizes.

The positions of the Bragg peaks in the diffraction pattern of the as prepared sample correspond well to the expected positions of diffraction peaks of the hematite structure. The refined model represents the data reasonably well. The disagreements between the calculated and observed pattern originates primarily in misfits of the profile function due to the assumption of purely Gaussian instrumental broadening and purely Lorentzian broadening from the sample. The refinement results in unit cell parameters of $a = 5.042$ Å and $c = 13.790$ Å and a mean particle size of 9.5 ± 0.3 nm. A refinement of a model with two particle size parameters was performed to obtain information about the particle size in the [001] direction and in the direction perpendicular to [001]. This results in particle sizes of 10.2 nm in the [001] direction and 8.2 nm perpendicular to [001]. However, these refined particle sizes depend delicately on changes in the refined model (e.g. changing the number of background parameters) and their precise values cannot be trusted, but the size in the [001] direction is consistently refined as larger than in the perpendicular direction.

In the diffraction pattern of the 25 mM NaCl sample after hydrothermal treatment the peaks have become considerably more narrow indicating an increased particle size. An extra phase was included in the refinement to account for the scattering from the NaCl in the sample. Overall the model represents the data well, but there are once again some misfit of the profile shape and
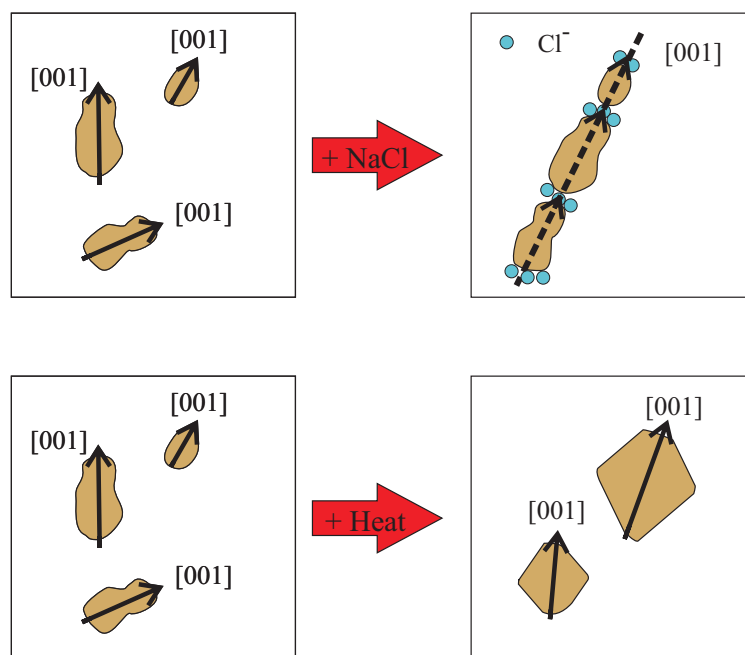
Figure 5.9: Model of aggregation and crystal growth. Top: oriented attachment assisted by Cl⁻ ions attached to (001) surfaces of the particles could lead to linear chains like observed in the TEM images of the sample with 25 mM NaCl before hydrothermal treatment (shown in Fig. 5.4). We cannot observe if any ions are sitting on the particles surfaces so the model is speculative. Bottom: Crystal growth during heating like observed in TEM images of the heated samples (see Fig. 5.7).

there are also two peaks at about 37° and 38° from an unidentified impurity. The refinement results in unit cell parameters of $a = 5.034$ Å and $c = 13.757$ Å and a mean particle size of 23.4 ± 0.3 nm. A model with two Lorentzian parameters was also refined to this data giving particles sizes of 23 nm both parallel and perpendicular to [001].

5.4.1 Discussion of aggregation and crystal growth

Our observations of the as-prepared sample is consistent with observations in previous studies [138, 140] that hematite particles in aqueous suspension are elongated in the [001] direction typically consisting of 2-5 pseudo spherical particles.

With DLS we see that the hydrodynamic diameter is unaltered by addition of NaCl up to concentrations of 5 mM, but with a concentration of 25 mM NaCl the hydrodynamic diameter increases dramatically and the PSD becomes very broad.

With TEM we have seen that the addition of NaCl to a suspension of hematite particles may lead to the formation of linear chains of these elongated particles. These structures are similar to the mesocrystals discussed in the literature [136, 137] and seen in suspensions of goethite NPs [137], and the particles in the chains are crystallographically aligned even though they are not fused together. One could speculate that the Cl⁻ ions attach to the particles preferentially on certain crystallographic surfaces and facilitate the OA of the particles. As sketched in Figure 5.9 Cl⁻ ions adsorbed on the (001) surfaces could lead to the formation of linear chains like seen in the TEM images 5.4. Another possibility is that the exchange interaction between surface atoms on neighbouring particles may be responsible for the preferential attachment of the particles in the [001] direction.

DLS shows that the hydrothermal treatment results in an increase in hydrodynamic diameter and that the NaCl concentration in the suspension enhances the effect of the hydrothermal treatment on d_H. TEM images show that the effect of the hydrothermal treatment is growth of the individual particles and a change of shape from pseudo spherical to faceted. The parti-

cle growth may be ascribed to both particle migration and coalescence and atomic migration between particles (Ostwald ripening). The faceting is presumably because the thermal energy makes the atoms more mobile and their random motion leads to the shape of the nanocrystals converging towards their equilibrium shape, with the faces with highest surface energies least exposed. The addition of increasing amounts of NaCl enhances the effect of the hydrothermal treatment, presumably because the change in ionic strength brings the particles closer together, facilitating sintering of the particles. Only a limited analysis of the TEM images have been performed at the present time. Measuring the size distribution of the particles with TEM for all would give a quantitative measure of the particle growth.

X-ray diffraction patterns confirm that the crystalline particle size increases from 9.5 ± 0.3 nm in the as-prepared sample to 23.4 ± 0.3 nm for the sample with 25 mM NaCl heated at 140°C in good agreement with the TEM data. The XRD data further shows that the particles in the as-prepared sample are elongated in the [001] direction whereas the particles have the same size in the [001] direction and perpendicular to [001] in the sample with 25 mM NaCl heated at 140°C. This is also in accordance with the observations with TEM. It would be desirable to obtain XRD patterns of all sample, but this was not possible because the available amount of sample was not sufficient. It would have been particular interesting to have XRD data from the sample showing the linear aggregates. The correlation length in the [001] direction could then be determined, giving information of the coherence of the aggregates.
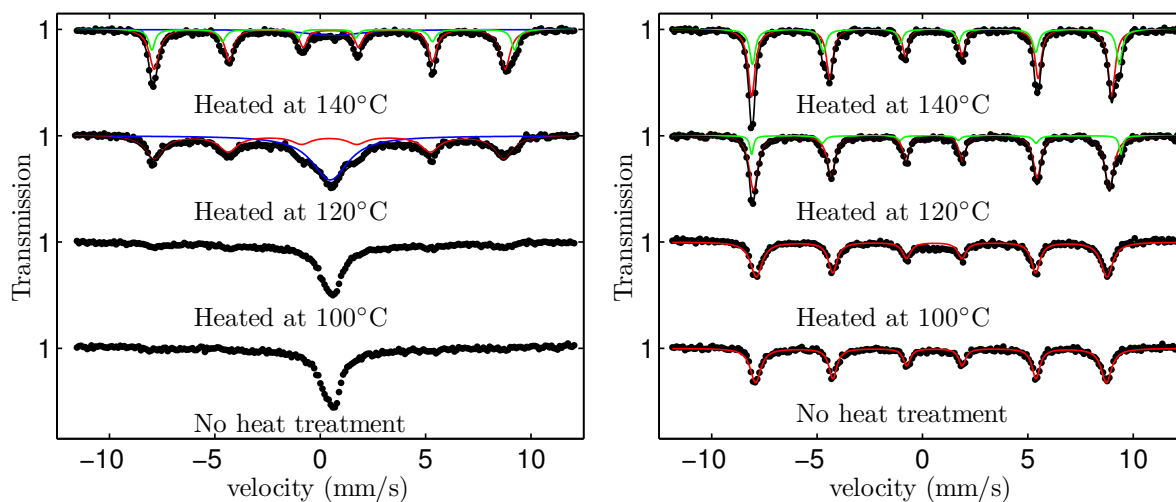
5.5 Magnetic properties

Figure 5.10: Mössbauer spectra of the samples without NaCl heated at the indicated temperature. The superparamagnetic doublet is plotted in blue, and sextet 1 and 2 are plotted in red and green respectively. Left: Measurement at 80 K. Right: Measurement at 20 K.

Mössbauer spectra of the samples without NaCl obtained at 20 K and 80 K are shown in Figure 5.10. The 80 K spectrum of the as-prepared sample consists of a single feature which we attribute to particles undergoing SPM relaxation. The line is a doublet with lines so close together that it is effectively a singlet. There is little change in the Mössbauer spectrum after hydrothermal treatment at 100°C, but there are indications of the appearance of a magnetically split sextet In the sample heated at 120°C the sextet component have become clearly visible and there is an asymmetry between lines 1 and 6 with line 1 being more narrow and with a larger amplitude than line 6. The asymmetry of is due to the presence of more than one quadrupole splitting in the sample, which can be an effect of different spin angles and thus could be a sign that the MT have been recovered in part of the sample.

The magnetically split component is fitted with Lorentzian lines with area ratio 1:2:3:3:2:1 between the six lines and the SPM doublet is fitted with a single Lorentzian. In the 80 K spectrum of the sample heated at 140°C the sextet is dominant, with the relative area of the SPM doublet reduced to 14% of the spectral area and the lines in the sextet have become very assymetric. The magnetically split component now clearly consists of two magnetically split components and is therefore fitted with two sextets. Sextet 1 has a quadrupole splitting of -0.03 mm/s and sextet 2 has a quadrupole splitting of 0.14 mm/s and they comprise relative ares of 65% and 21% of the spectrum. The quadrupole splitting of the sextets are in between the values of -0.10 mm/s and 0.20 mm/s expected for hematite above and below the MT but we interpret the two sextets as representing parts of the sample having a magnetic structure resembling that of hematite above and below the MT respectively. The departure from the expected quadrupole splitting can be due to a distribution of spin angles in the sample or it can be a consequence of the crudeness of the fitted model.

The spectra of the samples without NaCl obtained at 20 K are all magnetically split and it can be concluded that the SPM blocking temperature is above 20 K. The 20 K spectra of the as-prepared sample and the sample heated at 100° C are fitted with a single sextet. The 20 spectra of the samples heated at 120° C and 140° C are both split into two sextets and are fitted accordingly. The fits returns relative areas of sextet 1 of 88% and 70% and the realtive area of sextet 2 as 12% and 30% in the two samples, confirming the observation from the 20 K data that after the hydrothermal treatment there is a fraction of the particles in the sample that undergoes MT and further that this fraction increases with increased heating. The relative spectral areas of sextets 1 and 2 in the sample heated at 140°C determined from the 80 K spectrum is in fair agreement with the result from the 20 K indicating that the particles undergoing MT at 20 K all have a Morin temperature above 80 K. For the samples without NaCl the hyperfine parameters of the sextet components and the relative spectral areas of the components are given in Table 5.1.

Mössbauer spectra of the samples with 25 mM NaCl NaCl obtained at 20 K and 80 K are shown in Figure 5.11. The 80 K spectrum of the sample with 25 mM NaCl not subjected to hydrothermal treatment is dominated by a doublet due to SPM relaxation but unlike the spectrum of the as-prepared sample there is a visible sextet component to the spectrum. The 80 K spectrum of the sample with 25 mM NaCl heated at 100°C shows a more distinct sextet component which is fitted in the same way as described above, obtaining a relative spectral area of 50%. For the sample with 25 mM NaCl heated at 140°C the 80 K spectrum has no significant doublet component, and the sextet is split into two components with relative spectral ares of 77% and 23%.

The 20 K spectra of the samples with 25 mM NaCl have no doublet component. The spectrum of the 25 mM NaCl sample not subjected to hydrothermal treatment consists of a single sextet with hyperfine parameters corresponding to hematite above the MT. The spectrum is not much affected by the hydrothermal treatment at 100°C, but there is a slight increase in the quadrupole split that might indicate that a small proportion of the sample has reached its Morin temperature. At 140 °C the spectrum is split into two sextets with relative spectral areas of 30% and 70% in reasonable agreement with the result obatained at 80 K. The hyperfine parameters parameters of the sextet components and the relative spectral areas of the fit components for the samples with 25 mM NaCl are given in Table 5.2.

5.5.1 Discussion of magnetic properties

In summary the effect of the hydrothermal treatment on the 80 K Mössbauer spectra is the appearance of a sextet component to the spectrum, which for the as-prepared sample consists of a SPM doublet. The doublet component is reduced to 14% of the spectral area in the sample heated at 140°C and furthermore the hyperfine sextet is split into two components with different quadrupole splitting. We regard this splitting as evidence that there is (partial) MT in the sample.

	80 K data								
	Sextet 1				Sextet 2				Doub
Heating	B_{hf}	δ	ϵ	$A(\%)$	B_{hf}	δ	ϵ	$A(\%)$	$A(\%)$
120°C	51.4	0.42	0.00	52					48
140°C	51.6	0.48	-0.03	65	53.4	0.48	0.14	21	14
	20 K data								
	Sextet 1				Sextet 2				Doub
Heating	B_{hf}	δ	ϵ	A (%)	B_{hf}	δ	ϵ	A (%)	A (%)
No	51.6	0.49	-0.08	100					
100°C	51.6	0.50	-0.06	100					
120°C	52.4	0.49	-0.06	88	54.4	0.49	0.17	12	
140°C	53.0	0.49	-0.06	70	54.0	0.49	0.15	30	

Table 5.1: Hyperfine parameters for the sextet fits to the Mössbauer spectra in Figure 5.10. Hyperfine field, B_{hf}, is given in Tesla, isomer shift, δ, and quadrupole split, ϵ, in mm/s. The SPM doublets are fitted with single Lorentzians. The relative spectral area, A, of the components are also given.
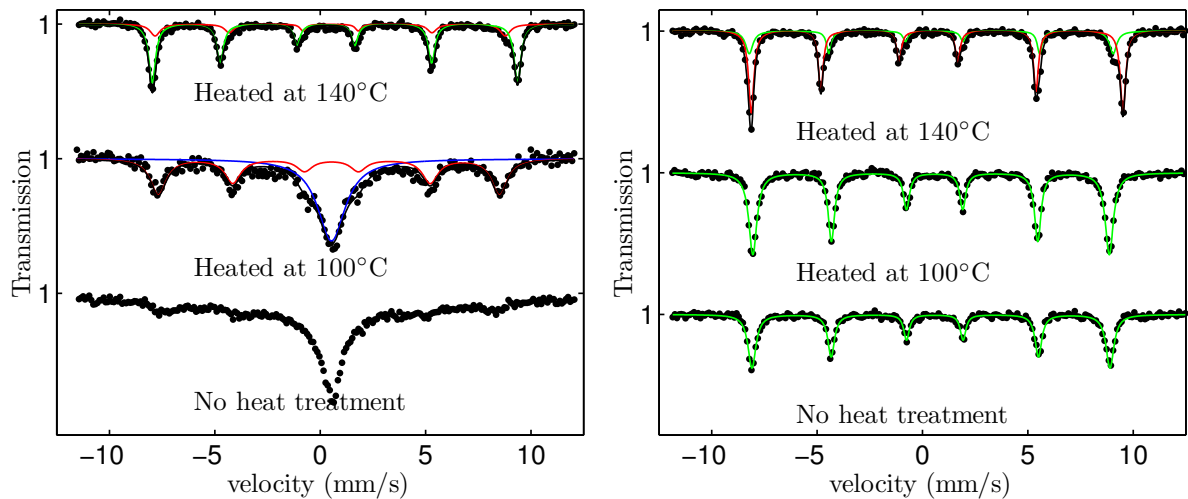
Figure 5.11: Mössbauer spectra of the samples with 25 mM NaCl NaCl heated at the indicated temperature. The superparamagnetic doublet is plotted in blue, and sextet 1 and 2 are plotted in red and green respectively. Left: Measurement at 80 K. Right: Measurement at 20 K.

	80 K data								
	Sextet 1				Sextet 2				Doub
Heating	B_{hf}	δ	ϵ	A (%)	B_{hf}	δ	ϵ	A (%)	A(%)
100°C	50.2	0.47	-0.06	50					50
140°C	51.5	0.48	-0.01	23	53.8	0.48	0.21	77	
	20 K data								
	Sextet 1				Sextet 2				Doub
Heating	B_{hf}	δ	ϵ	A (%)	B_{hf}	δ	ϵ	A (%)	A (%)
No	52.7	0.494	-0.09	100					
100°C	52.5	0.49	-0.08	100					
140°C	53.5	0.49	-0.08	28	54.7	0.49	0.21	72	

Table 5.2: Hyperfine parameters for the sextet fits to the Mössbauer spectra in Figure 5.11. Hyperfine field, B_{hf}, is given in Tesla, isomer shift, δ, and quadrupole split, ϵ, in mm/s. The SPM doublets are fitted with single Lorentzians. The relative spectral area, A, of the components are also given.

In the 20 K spectra the particles are below their SPM blocking temperature and the spectra are well defined sextets. The sextet splits into two components for the sample heated at 120°C and 140°C. For the sample heated at 140°C the relative spectral areas of the two sextets are approximately the same as in the 80 K spectra confirming that about 70% of the sample has a magneitc structure similar to that of hematite above T_M and about 30 % of the sample have a structure corresponding to hematite below T_M.

The addition of NaCl increases the effect of the hydrothermal treatment on the MT so that more than 70 % of the sample undergoes MT after hydrothermal treatment at 140°C. Another effect of addition of NaCl is a partial suppression of the SPM relaxation, as can be seen in the 80 K data. The SPM relaxation is completely dominant in the as-prepared sample and the sample without NaCl heated at 100°C, but in the corresponding samples with 25 mM NaCl a weak doublet appears in the unheated sample and in the sample with 25 mM NaCl heated at 100°C the sextet component has a spectral area of 50%. Samples with lower concentrations of NaCl than 0.25 mM gave an effect on the Mössbauer spectra similar to the 25 mM NaCl sample, but less pronounced.

The measured hyperfine fields are in general a bit lower than what would be expected for bulk hematite [127]. This could be an effect of collective magnetic excitations. The hyperfine field is expected to be 0.8 T larger for hematite below the MT than above [130] and we do see a larger b_{hf} in the sextets representing hematite below T_M, however, the shift in hyperfine field is larger than the expected 0.8 T. The measured isomer shifts correspond well to what should be expected for hematite at the relevant temperatures [43] except for the 80 K measurement of the sample without NaCl heated at 120°C which comes out a bit low. The measured quadrupole splitting was in general not as expected for hematite above or below T_M, but somewhere in between. Especially the sextet associated with hematite above the MT showed a quadrupole splitting different from the expected -0.10 mm/s. This might be due to an altered spin angle,

or a distribution of spin angles in the samples.

5.6 Conclusions

The characterisation of aggregation and crystal growth shows that addition of NaCl to a suspension of hematite particles can lead to oriented attachment of particles in long linear chains. Neighbouring particles in the chains are crystallographically aligned. The aggregation of particles into linear chains could be associated with preferential attachment of Cl⁻ ions on the (001) surfaces of the particles, or exchange interaction between surface atoms of neighbouring particles could be responsible for the attachment in this particular direction. Conceivably the Cl⁻ ions on the surface of particles could mediate the exchange interaction.

The hydrothermal treatment leads to growth of the single particles. The growth of the individual particles leads to a recovery of the MT in a fraction of the particles that increases with autoclaving temperature. Since the MT is only recovered in samples subjected to hydrothermal treatment it is probably an effect of the growth of single particles and not of magnetic order extended over several particles in the mesocrystal-like aggregates. TEM measurements confirms that the particles that show MT have a significant fraction of particles with sizes larger than 20 nm.

While addition of NaCl does not in itself induce MT it does increase the effect of the hydrothermal treatment, leading to a higher proportion of the sample undergoing MT. The NaCl ions may facilitate particle growth by reducing the ionic strength and thus allowing the particles to come closer together or possible by formation of mesocrystals which fuse together to form larger single crystals. While the addition of NaCl does not in itself introduce a MT it does have the effect of partially suppressing the SPM relaxation. This could be ascribed to particle growth as discussed above, or to increased inter-particle interactions between the particles in the suspension with an increased ionic strength.uce a MT it does have the effect of partiall suppresing the SPM relaxation. This could be ascribed to particle growth as discussed above, or to increased inter-particle interactions between the particles in the suspension with an increased ionic strength.

More information about the magnetic properties could be obtained by measuring Mössbauer spectra at more temperatures to determine the Morin temperatures and superparamagnetic blocking temperatures of the particles as function of particle growth and aggregation. This would require a significant amount of time, as each spectrum of the particles in suspension takes 2-3 days to record. It might, however, be possible to produce more concentrated samples with similar characteristics. Of course the samples are likely to have a complicated distribution of Morin- and blocking temperatures because of the broad particle (and aggregate) size distribution, and thoroughly understanding the spectra might require complicated modelling of the spectra. In the present work the particle sizes have only been determined with TEM for two of the samples and this should of course be done for all samples. This would help understanding the effect of hydrothermal treatment and NaCl concentration better, and make a more quantitative comparison of the magnetic properties as function of particle size possible.

Spin orientation in hemo-ilmenite

In this chapter the spin orientation in the rock mineral hemo-ilmenite is studied with uniaxial polarisation analysis to elucidate the origin of its unusual magnetic properties. Hemo-ilmenite, consisting of hematite in a host of ilmenite is common in different areas on the Earth, such as Scandinavia and North America, and has been identified as important for anomalies in the magnetic field of the Earth [143,144] and perhaps even on the planet Mars [145]. Natural hemo-ilmenite samples have shown a high coercivity, and a large natural remanent magnetisation (NRM), that is stable over geological timescales. The NRM is far to large to be explained by the combined properties of CAF hematite and ilmenite, which is paramagnetic at room temperature. Hemo-ilmenite samples formed by slow cooling of magma billions of years ago have fine exsolution structures with intergrown lamellae of hematite and ilmenite with a thickness down to a few nm, and the unusual magnetic properties have been proposed to originate from uncompensated spins in the contact layers between these lamellae [144,146]. The material have received considerable scientific attention because of its peculiar magnetic properties and because of its importance for geomagnetism. Furthermore, intermediate compositions of solid solution hematite-ilmenite $0.5 < x < 0.85$ are magnetic semiconductors [147,148], and a detailed understanding of the interactions between the two phases may lead to discoveries that could be important for future devices in the field of spin-tronics [149–151].

Here we investigate the orientation of hematite spins in a natural single crystal sample of hemo-ilmenite from South Rogaland, Norway. The spin orientation, and in particular the orientation of the hematite spins in the basal plane of the hexagonal structure when a saturating magnetic field is applied can reveal whether the magnetisation is dominated by the contribution from the canted hematite moments, lamellar moments or a combination thereof. The uniaxial polarisation analysis experiment in applied fields up to 2.5 T was performed at the IN12 experiment at ILL. The results of the IN12 experiment presented here are also the subject of **Paper [5]**.

6.1 Hemoilmenite - A natural mineral intergrowth

While hematite is CAF below 955 K ilmenite is paramagnetic at temperatures down to a Néel Temperature of 58 K [152] where it orders antiferromagnetically. The crystal structure of ilmenite is $R\bar{3}$, which is identical to that of hematite, except that the layers of Fe^{3+} are replaced by alternating layers of Ti^{4+} and Fe^{2+}. In the AFM state of ilmenite the Fe^{2+} spins are aligned along the c-axis, with spins in adjacent layers antiparallel. The crystal and magnetic structure of ilmenite is displayed in Figure 6.1 together with the structure of hematite above T_M.

The Morin transition is known to be suppressed when small amounts ($\approx 1\%$) of Ti are substituted into the hematite structure [20, 21] and the expected magnetic structure of the hematite is the one shown to the left in Figure 6.1 at all temperatures below T_N. However, as discussed in section 5.1 there might be an out of plane component of the hematite spins. In
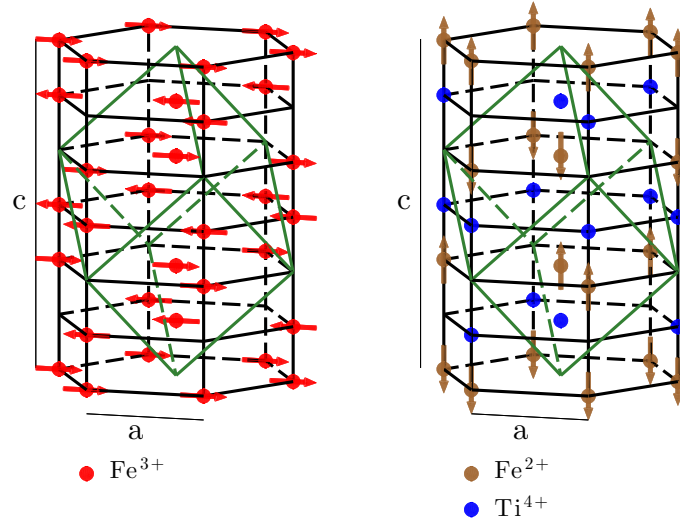
Figure 6.1: Left: Crystal and magnetic structure of hematite in the CAF state. Right: Crystal and magnetic structure of ilmenite below $T_N = 58$ K. Above 58 K ilmenite is paramagnetic. The rhombohedral unit cell is shown in green. The drawing is (modified) from **Paper** [5].

particular an out of plane angle of 30° have been measured in a natural hemo-ilmenite sample with fine scale exsolution structures [153].

The lattice parameters of ilmenite in the hexagonal unit cell are $a = b = 5.088$ Å and $c = 14.085$Å [154, 155], which is close to the lattice parameters of hematite, and this means that the two phases can grow epitaxially together. In natural samples that slowly cooled billions of years ago [156] complex exsolution structures have been found, with several generations of exsolution lamellae of sizes ranging from a few unit cells to several microns [157]. The lamellae are flat in the [001] direction extended in the (001) basal planes of the hexagonal structure.

The NRM of hemo-ilmenite samples have been measured to be on the order of 10^{-3}Am^2/kg [158], which is too large to be explained by the combination of paramagnetic ilmenite and CAF hematite. The coercivities and demagnetisation temperatures of the samples are similar to the values for hematite [146]. The large NRM is believed to be connected to the exsolution structure of the samples. In particular a theory known as lamellar magnetism explains the NRM as origination from uncompensated magnetic layers at the interfaces between lamellae [144, 146, 159–161]. An alternative explanations for the large magnetisation could be an enhanced canting angle in hematite, possibly associated with strain in the lamellae, but it would have to be a rather dramatic change in the canting angle. Magnetic impurities could of course also be though as possible explanations of the NRM, especially in a natural sample. However, the unusual magnetic properties also exist in samples where no ferromagnetic impurities are found. The cation ordering during exsolution have been modeled with Monte Carlo simulations [146, 159], confirming the lamellar magnetism hypothesis as a possible explanation for the NRM. Magnetisation measurements, shows shifts of the hysteresis loop (exchange bias) when samples with the pristine NRM still intact are cooled below the ordering temperature of ilmenite, confirming that the magnetic moment responsible for the NRM are indeed situated on the interfaces between the two phases [162, 163].

6.2 Sample characterisation

A sample of hemo-ilmenite from South Rogaland, Norway, was provided by Suzanne McEnroe. The sample, referred to as Pramsknuten 5-1T was cut from a larger piece, and selected for experiments because electron backscatter diffraction (EBSD) revealed that the sample was a single crystal of hemo-ilmenite [158]. The sample is rectangular with dimensions of about $12 \times$

8mm and has a mass of 1.977 g. The EBSD investigations determined the orientation of the crystal with respect to the sample faces, which is important for further experiments.

6.2.1 Composition and impurities

Because the sample is of natural origin it cannot be expected to be very pure. The sample composition as well as the presence of impurity phases was investigated with X-ray fluorescence (XRF) and EBSD [158, 164]. The XRF data gives an average composition of 16.18% hematite structure and 83.82% ilmenite structure (percentage of end members). If the sample was pure this means that the sample composition would be xFeTiO$_3$-(1-x)Fe$_2$O$_3$, with $x = 0.8382$ [158, 164]. However, the XRF measurements revealed a significant impurity of MgTiO$_3$ (18.7% of end member) as well as smaller impurities of MnTiO$_3$, ZnTiO$_3$ and NiTiO$_3$ (less than 1% of end member) in the ilmenite phase. In the hematite phase small impurities of Al$_2$O$_3$, Cr$_2$O$_3$ and V$_2$O$_3$ (less than 1% of end member) were found. The data from the XRF measurements is an average over several samples from the same prospect, but the results from EBSD are in reasonable agreement. Most importantly no ferromagnetic impurities were found. Our sample will be considered to be 0.84FeTiO$_3$-0.16Fe$_2$O$_3$, and the impurities will not be included in the discussion.

6.2.2 Single crystal sample

The crystalline quality of the sample was studied at the MORPHEUS two axis spectrometer at PSI with a neutron wavelength of 4.72 Å. The result of this experiment was the mapping of the nuclear (003) ilmenite and magnetic (003) hematite peaks displayed in Figure 6.2. Both (003) peaks have 'shoulders', indicating that the sample consists of two crystallites oriented at an angle of approximately 0.6° with respect to each other. This small misorientation of the two crystallites in the sample is within the mosaicity that can be expected for single crystals, and for the purpose of our investigation the sample can be considered a single crystal.
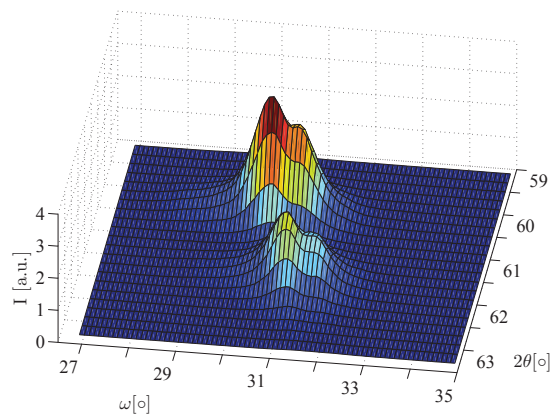
Figure 6.2: Mapping of the (003) peaks at the MORPHEUS spectrometer. 2θ is the scattering angle, and ω is the rotation angle of the sample. The peak at $2\theta \approx 60°$ is the nuclear ilmenite reflection and the peak at $2\theta \approx 62°$ is the magnetic hematite reflection. The figure is from **Paper [5]**.

6.2.3 Magnetic properties

The NRM of the sample was measured before the sample had been subjected to any applied magnetic fields to be $2.613 \cdot 10^{-3}$ Am^2/kg, and to be oriented close to the basal plane (6.1° out of plane angle) and close to one of the basal plane crystallographic axes [158]. The saturation magnetisation and coercivity of the sample can be estimated to 0.43 Am^2/kg and 60 mT from measurements of other pieces from the same slab [165]. The mass percentage of hematite

(ignoring impurities) is approximately 17% and this means that there is about 0.33 g hematite in the sample. CAF hematite has a saturation magnetisation of 0.404 Am^2/kg [127] and the magnetisation of the sample from the weak ferromangetism of CAF hematite can thus only amount to about 0.067 Am^2/kg, or about 16% of the measured saturation magnetisation.

6.3 Determining the spin direction

The response of the magnetic moments to an applied field can give information about the configuration of the atomic spins. In particular the response of the hematite spins to a saturating field applied in the basal plane can determine whether or not the lamellar magnetism hypothesis is a plausible explanation for the spin structure in the lamellar system. Here we perform a uniaxial polarisation analysis experiment on the hemo-ilmenite sample in applied fields up to 2.5 T to directly measure the response of any lamellar moments to a magnetic field applied in the basal plane.
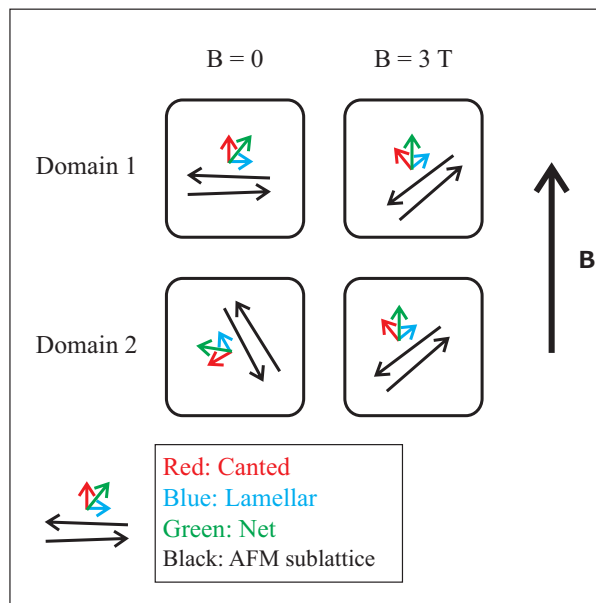
Figure 6.3: Orientation of the hematite spins in the basal plane in zero field and in a 3 T applied field. The net magnetic moment is the sum of the CAF moment which is perpendicular to the AFM sublattice directions and the lamellar moment which is parallel to the AFM sublattice. In zero field the spins are randomly oriented as represented by the two 'domains' to the left. In an applied field the net magnetic moment will respond to the applied field by rotating from its initial random orientation towards the direction of the field becoming parallel to the field at saturation (here assumed to be below 3 T). The average spin orientation is no longer random but depends on the relative proportions of CAF and lamellar moments. The average (in-plane) angle between the hematite spins and the applied field is exactly what we determine in the polarisation analysis experiment. The figure is from **Paper [5]**.

Let us assume for simplicity that the Fe^{3+} spins of hematite are in the basal plane. Then the low in-plane anisotropy would make the spins relatively free to rotate and any net moment would be expected to align with the applied field when the field is large enough. A sketch of how the hematite spins are expected to rotate when a magnetic field is applied is given in Figure 6.3. The net magnetic moment is believed to be a (vector) sum of a moment from the canting, which is (nearly) perpendicular to the AFM sublattice directions, and a lamellar moment, which is expected to be parallel to the AFM sublattice directions.

In the uniaxial polarisation analysis experiment we measured the magnetic (003) hematite reflection. In this way we see the total in-plane spin (and only that). Because we measure a magnetic peak the cross section for elastic scattering for neutrons polarised in the $z-$direction

(2.41) can be obtained from the scattering amplitudes (2.46), and it follow immediately that

$$\frac{d\sigma}{d\Omega}^{\text{NSF}} = KM_{\perp,z}^2,$$ (6.1)

where K is a constant, and likewise

$$\frac{d\sigma}{d\Omega}^{\text{SF}} = KM_{\perp,y}^2,$$ (6.2)

where K is the same constant. Her we have just repeated the rule of uniaxial polarisation analysis that moments parallel to the polarisation gives rise to NSF scattering only, whereas moments perpendicular to the polarisation direction gives rise to SF scattering only. From the ratio of the SF to the NSF cross section we can calculate the angle α between the in-plane magnetisation $\mathbf{M}_\perp$ and the polarisation:

$$\frac{\frac{d\sigma}{d\Omega}^{\text{SF}}}{\frac{d\sigma}{d\Omega}^{\text{NSF}}} = \frac{M_\perp^2 \cos^2\alpha}{M_\perp^2 \sin^2\alpha} = \tan^2\alpha.$$ (6.3)

The geometry of the experiment is depicted in Figure 6.4. The magnetic field is applied in the polarisation direction (the z-direction) and the angle α measured in the experiment is thus the average spin angle to the applied field. The average spin-angle is essentially the average direction of the AFM sublattices, since the canting is only a slight perturbation. The average saturation angle (see Fig. 6.3) would thus be close to $90°$ if the net moment were due to the CAF moment alone and close to $0°$ if it was only due to lamellar moments. In this way the measured saturation value of α can be used to asses the validity of the lamellar magnetism hypothesis.
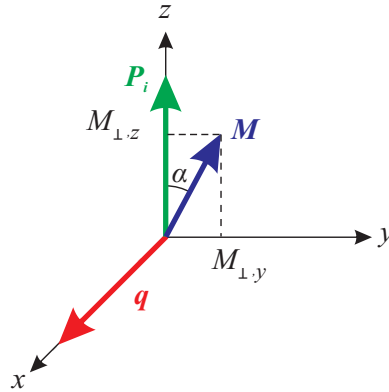
Figure 6.4: Geometry in the the uniaxial polarisation analysis experiment on IN12. $\mathbf{P}_i$ is the incident polarisation, $\mathbf{q}$ is the scattering vector, and $M_\perp$ is the (sublattice) magnetisation perpendicular to $\mathbf{q}$. The magnetic field is applied in the z-direction, and the angle α is thus the spin angle with respect to the applied field. The figure is (modified) from **Paper [5]**.

6.4 The uniaxial polarisation analysis experiment at IN12

The spin orientation in the hemo-ilmenite sample was investigated with uniaxial polarisation analysis at the IN12 triple axis spectrometer at ILL (see section 2.2.4) in August 2010. In our experiment the monochromator and analyser were oriented for elastic scattering with a constant wavelength of $\lambda = 4.05$ Å. The used collimation sequence was guide-open-polariser-40'-sample-40'-analyser-60'-detector. Where the angular divergence is given in minutes of arc ('). This collimation gives sufficient resolution to resolve the hematite and ilmenite (003) reflections at $q = 1.34$ Å^{-1} and $q = 1.37$ Å^{-1}. The sample environment was a cryomagnet, capable of applying

vertical magnetic fields from -0.75 to 2.5 T and a temperature in the range 2-290 K at the sample position.

The sample was glued to a custom made aluminium holder with the $\mathbf{c}^*$- and $\mathbf{a}^*$-axes roughly vertical, based on the crystal orientation from EBSD measurements [158]. The initial sample alignment 'by' eye was correct to within a few degrees, good enough to perform the final alignment in the beam by tilting the cryostat about 1.2° and rotating the sample about the sample stick, verifying the alignment using the nuclear ilmenite (003) and hematite $(10\bar{2})$ peaks. In this way, with $\mathbf{a}^*$ and $\mathbf{c}^*$ axes in the (horizontal) scattering plane, all reflections $(hk0)$ can be measured by rotating the sample. The reciprocal lattice of the sample was defined using the lattice parameters of ilmenite, and the by the reflections used for alignment, and the scans were performed using these reciprocal lattice units (r.l.u.).

The experiment on IN12 was preceded by an experiment on the TASP instrument at PSI in 2006, which is the topic of my master's thesis [166]. The TASP experiment was similar to the one later performed at IN12, but largely unsuccessful due to problems with the instrument. The IN12 experiment, and the data analysis was done in close collaboration with Morten Sales, and a lot of details that will not be discussed here can be found in his Master's thesis [167].

6.5 Results

To determine the in-plane spin angle,α, of the hematite spins all we need is to measure the NSF and SF cross sections of the magnetic (003) hematite reflection and use (6.3). The measured peaks were fitted with a procedure described in [167], using Gaussian line shapes for the ilmenite peaks and Voigtian line shapes for the hematite peaks because of Lorentzian finite size broadening. Before analysing the data, the measured NSF and SF cross sections needs to be corrected for imperfect polarisation by the procedure described in section 2.2.3.

6.5.1 Data correction

An example of an uncorrected measurement of the two (003) peaks is shown in Figure 6.5. The nonzero SF intensity at the position of the nuclear ilmenite reflection is due to the imperfect polarisation of the beam. The correction was performed using the flipping ratio determined from the fitted NSF and SF intensity of the ilmenite peak using (2.65) and the data was corrected using (2.64). In Figure 6.6 the same data has been corrected with $R = 43$, corresponding to polarisation of $p = 0.95$. The very small remaining SF intensity at the ilmenite (003) position can be ascribed to an imperfect fit of the ilmenite peak with a Gaussian profile. The correction was performed in the same way for each measurement of the (003) peaks. The measured polarisation only varied slightly with applied field and temperature and was always in the range 0.94-0.96.

6.5.2 Magnetic ordering of ilmenite

The magnetic ordering of the ilmenite phase was investigated by measurement of the magnetic $\left(10\frac{\bar{1}}{2}\right)$ ilmenite peak. Because the AFM sublattice direction in ilmenite is along the c-axis, which is perpendicular to the polarisation direction the magnetic ordering of the ilmenite only gives rise to SF scattering. The amplitude of the $\left(10\frac{\bar{1}}{2}\right)$ SF peak is shown as a function of temperature in Figure 6.7. The data was fitted to a power law, yielding a Neél temperature of $T_{\mathrm{N}} = 41.3$ K and a critical exponent of $\beta = 0.22$. The slightly lower Neél temperature than the 58 K usually reported for ilmenite [152] is likely due to impurities in the ilmenite.

6.5.3 In plane spin orientation

The magnetic (003) hematite reflection was measured at 8 temperatures from 2 K to 288 K, and in a range of applied fields from -0.5 to +2.5 T. The values of α calculated from the measured intensities using (6.3) are shown as a function of temperature and field in Figure 6.8. At all
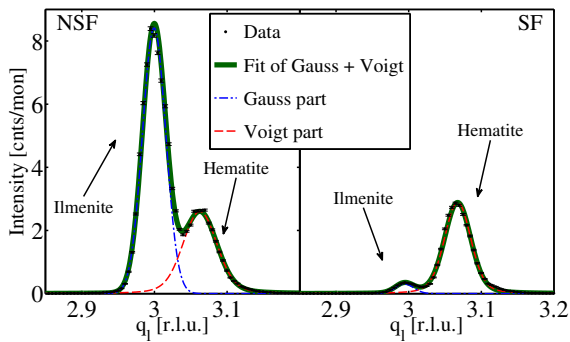
Figure 6.5: Measurement of the nuclear (003) ilmenite peak and magnetic (003) hematite peak at 65 K and an applied field of 0.25 T. The nonzero SF intensity at the position of the nuclear ilmenite peak is because of the imperfect polarisation. Figure from **Paper [5]**
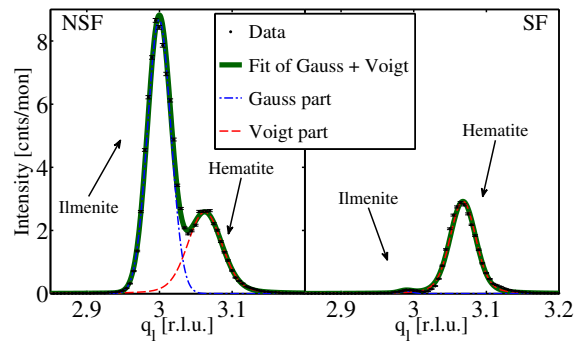
Figure 6.6: Corrected measurement of the nuclear (003) ilmenite peak and magnetic (003) hematite peak at 65 K and an applied field of 0.25 T. In this measurement the flipping ratio was $R = 43$ corresponding to a polarisation of $p = 0.95$. Figure from **Paper [5]**
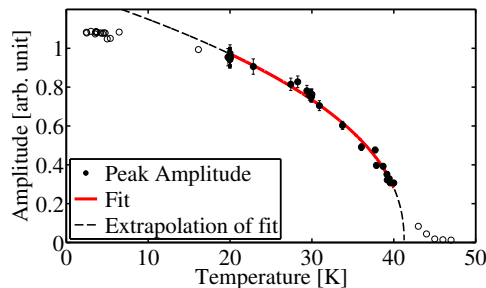
Figure 6.7: Ordering of ilmenite. The amplitude of the $\left(10\frac{\overline{1}}{2}\right)$ SF ilmenite peak shows the second order phase transition from paramagnetic to AFM. The filled points have been fitted to a power law, resulting in a transition temperature $T_N = 41.3$ K . Figure from **Paper [5]**.

temperatures the value of α at zero applied field (there is still a small guide field) is close to 45°, consistent with a random alignment of the spins in the basal plane. When a field is applied α increases with the field, reaching approximately 56° in a 2.5 T field for measurements at temperatures $T \geq 150$ K whereas it reaches only 50-53° in 2.5 T at the lower temperatures.

The sample becomes magnetically harder with decreasing temperature. In the data obtained at 288 K the value for α seems to be approaching saturation in the 2.5 T field, whereas this does not seem to be the case for the data at lower temperatures. At 2 K, 65 K and 288 K measurements were also performed in both negative and positive applied fields, to investigate the hysteresis of the sample. At 288 K there is no significant hysteresis in the sample, whereas there is a distinct hysteresis feature in the data obtained at 65 K. At 2 K, where the ilmenite is ordered the hysteresis has disappeared again. The ordering of the ilmenite does not seem to have much effect on the value of α in high fields, as the 35 K and 65 K data looks very similar, except for the hysteresis feature at lower fields in the 65 K data.

Unpolarised diffraction experiment to determine the saturation field

Because it is unclear whether the spin rotation is saturated in a 2.5 T field at 288 K, or would continue at larger fields, and because it seems clear that it is not saturated in 2.5 T at lower temperatures an unpolarised diffraction experiment in a higher magnetic field was performed at the RITA-II triple axis spectrometer at PSI. The experiment was similar to the one performed at IN12, except that unpolarised neutrons were used. The sample was aligned in the same way as in the IN12 experiment and positioned inside a cryomagnet capable of applying magnetic fields
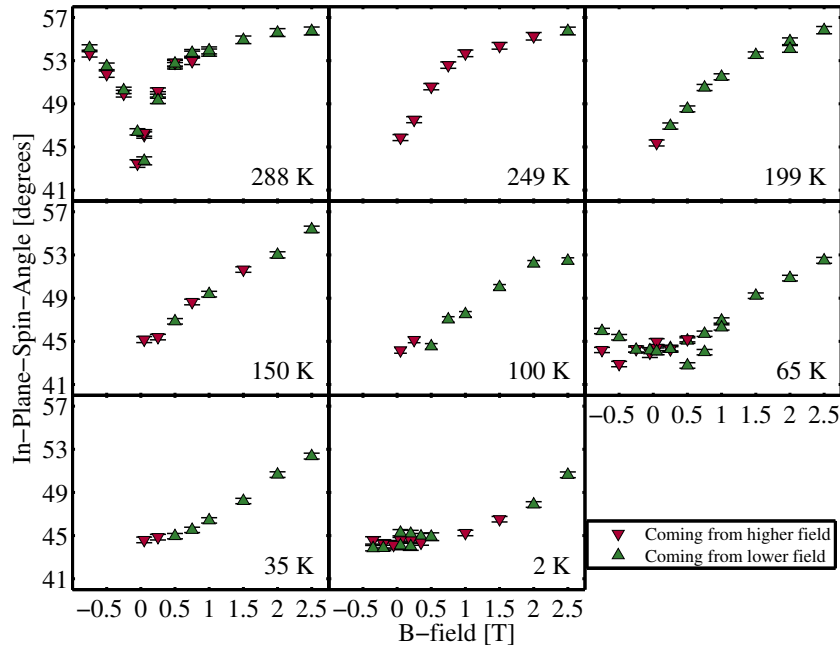
Figure 6.8: In-plane spin angle, α as function of applied field for different temperatures. Figure from **Paper [5]**.

up to 11 T. With unpolarised neutrons, and a magnetic field applied in the basal plane, it would not be possible to obtain the saturation field from measurements of the magnetic (003) peak, because the rotation of the spins would be perpendicular to **q**. In stead the (101) magnetic hematite peak was measured. For this reflection a rotation of the spins in the basal plane will change the projection of the magnetic moment perpendicular to **q** ($\mathbf{M}_\perp^2$), and hence the intensity. The intensity of the (101) reflection was measured at 2K and 150 K in magnetic fields from 0 to 11 T, with measurements in both increasing and decreasing fields. In the 150 K data the (191) intensity decreases from zero field to approximately 2.5 T and then increases when the field is further increased to 11 T. This is consistent with a saturation of the rotation of the net moment (like shown in Fig. 6.3) at approximately 2.5 T, followed by a rotation of the AFM sublattices away from antiparallel (normal AFM susceptibility). When the field is decreased again there is a significant hysteresis. The situation is similar for the 2 K measurements, but the saturation is not reached before approximately 5 T.

The results from the unpolarised experiment can be used to make conclusions about the data from the polarised experiment on IN12. Importantly we can conclude that for temperatures above 150 K the measured value of $\alpha \approx 56°$ at 2.5 T is the saturation value. At the lower temperatures the sample is more magnetically hard, and does not reach saturation in the applied 2.5 T field.

6.6 Discussion

We set out to measure the orientation in the basal plane of the hematite spins in a natural sample of hemo-ilmenite. This was achieved with the method of uniaxial polarisation analysis on the IN12 instrument at ILL. The objective of the experiment was, in particular, to determine whether the magnetic moments responsible for the NRM of the sample could be identified as uncompensated moments on the lamellar interfaces, or have some other origin.

The canted moment is normally to small to explain the size of the NRM found in this and other samples, but it is not inconceivable that strain could change the DM interaction, possibly leading to an increased canting. While the size of the strain in the system has not been measured
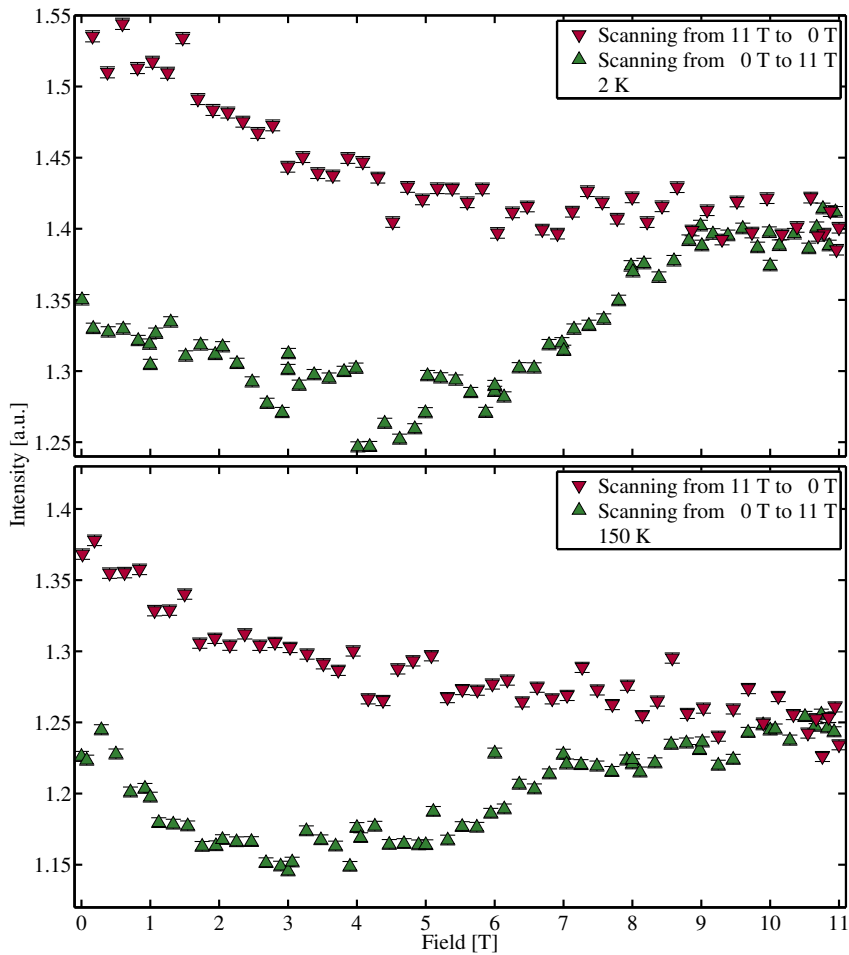
Figure 6.9: Unpolarised neutron scattering intensity of the (101) magnetic hematite peak as function of applied field measured at temperatures of 2 K (top) and 150 K (bottom). The measurements were performed at the RITA-II instrument, PSI. Figure from **Paper** [**5**].

it is reasonable to assume that there is significant strain in samples consisting of intergrowths of materials with slightly different lattice parameters.

The expected response of the hematite spins to an applied field are depicted in Figure 6.3 for a model with combined CAF and lamellar magnetic moments. If the net magnetisation of the sample was due to canting only, the average spin angle to the applied field would be close to $\alpha = 90°$ at saturation, where the net moment is aligned with the field. Uncompensated spins on the surface of lamellae are expected to align with the applied field and if the magnetisation of the sample was solely due to these magnetic moments α would be expected to saturate at an angle of 0°.

In zero field we find $\alpha \approx 45°$ at all temperatures, corresponding to the expected random average spin orientation. When a magnetic field is applied in the basal plane the average moment turns away from the field reaching a saturation of $\alpha \approx 56°$ at temperatures above 150 K. The measurement on the RITA-II instrument at PSI confirmed that the spin rotation is saturated in the 2.5 T field. At lower temperatures the moment does not saturate in the 2.5 T field. This magnetic hardening of the material might be related to increased pinning of domain walls in hematite at low temperatures. There is no significant hysteresis in the system at 288 K and not at 2 K either (below the ordering temperature of ilmenite). There is a small but distinct hysteresis in the measurement at 65 K.

The saturation angle of $\alpha \approx 56°$ is consistent with a model with some CAF spins aligning (nearly) perpendicular to the field and some uncompensated moments aligning parallel to the

field. If all the moments were either perpendicular or parallel to the applied field $\alpha \approx 56°$ would correspond to approximately 62% of the moments being CAF and 38% being lamellar moments. This calculation is certainly too simple to be quantatively usefull, but it illustrates that not only canting, but also lamellar moments are important in the system. Our results thus strongly supports the theory of lamellar magnetism as the origin of the NRM. In samples with more fine scale exsolutions than in the one investigated here the proportion of lamellar moments might be higher.

However, while our experiment confirms that a significant proportion of the hematite spins align parallel to the applied field at saturation we cannot determine whether these spins are uncompensated magnetised layers at the interfaces between lamellae as proposed in the lamellar magnetism hypothesis, randomly placed spins at the lamellar interfaces, or are dispersed in the volume of the lamellae. The measurements of exchange bias indicates that the spins reside on the surface of the lamellae [162, 163]. The lamellar moments might be uncompensated spins randomly distributed on the surface of the hematite lamellae, similar to the mechanism that is believed to be responsible for the magnetisation in NPs of for example NiO [112, 113]. The uncompensated moment in hematite NPs is, however, assumed to be small [131], and the NRM is in all likelihood a consequence of the lamellar structure.

Conclusions and outlook

7.1 Conclusions

The magnetic properties of antiferromagnetic NPs and related systems have been studied with a range of experimental techniques. The focus have been on the magnetic structure, and how it is affected by the finite size of very small antiferromagnetic particles and by aggregation of the particles.

- **Canted spin structures and goethite**

In addition to the experimental work a theoretical model for a simple two-dimensional canted spin structure was developed. This classical model, which is in qualitative agreement with a quantum mechanical model, shows that freezing of the canted spin at low temperatures can either increase or decrease the magnetisation depending on the canting angle. The model can explain observations of anomalous temperature dependence in a range of studies of ferrimagnetic nanoparticles and also in bulk systems with substituted diamagnetic ions. Furthermore, our magnetisation measurements on 5.7 nm goethite particles show an upturn in the magnetisation at low temperatures, which can be explained by freezing of canted spins like described in the model.

The simple two-dimensional spin structure is too simple to expect qualitative agreement with experiment. A realistic model would have to be three-dimensional, but that might make an analytical solution impossible. Furthermore, the model could be refined by adding magnetic anisotropy. A qualitative model of the temperature dependence of the magnetisation of canted spin structures at the surface of antiferromagnetic particles would be desirable, but might be problematic because of the complicated spin structures.

- **Spin orientation in NiO nanoparticles**

The spin orientation in plate shaped NiO particles was studied as a function of particle size with XYZ polarisation analysis for particles with plate thickness from 2.0 nm to hundreds of nanometers (bulk sample). This technique enabled us to separate the magnetic, nuclear, and spin incoherent parts of the scattering, resulting in a vast improvement of earlier data from unpolarised neutron diffraction. We determine the direction of antiferromagnetic modulation to be in the direction normal to the particle plane, as proposed in previous studies. We find a spin orientation close to the (001) planes of the particles in the bulk sample and in the nanoparticle samples with plate thickness down to 2.2 nm. In the smallest particles, with thickness 2.0 nm, we find a significant out of plane angle of 30°.

It would be interesting to investigate the spin orientation in NiO nanoparticles of different shapes, e.g., spherical particles, to see if the out of plane spin component found in small plate shaped particles are due to the low symmetry of the particle shape. Furthermore, if even thinner NiO nanoparticle could be produced it would be interesting to see if the spin orientation

is rotated even more out of the plane, approaching the 90° spin orientation seen in thin films. Measuring a change in the spin angle when the spin is almost perpendicular to the scattering vector is intrinsicly difficult because $\sin(\alpha)$ only changes slightly with α when α is close to 90° and any such experiment is therefore sensitive to systematic errors. XYZ-polarisation analysis is a powerful method to investigate magnetic nanoparticles because of the ability to separate the magnetic signal from the spin incoherent background from water adsorbed on the particles and from nuclear scattering which may have overlapping peak due to the finite size broadening in nanoparticles.

- **Magnetic structure in hematite particles as function of aggregation and growth**

The magnetic properties of hematite nanoparticles in aqueous suspension were studied as function of particle growth and aggregation. In a NaCl concentration of 25 mM the particles in formed long linear chains with crystallographic alignment of neighbouring particles. The possibility to control the aggregation of nanocrystals to mesoscopic structures, for example by changing concentration of salts (e.g. NaCl) in the suspension, could potentially be used to produce functionalised structures for applications. Our studies have shown that this is a viable route for controlling particle attachment into linear chains. The hydrothermal treatment resulted in growth of the individual particles and the effect of NaCl in combination with hydrothermal treatment was an increased particle growth. The magnetic structure of the particles were followed by Mössbauer spectroscopy, showing that the hydrothermal treatment resulted in recovery of the Morin transition in a fraction of the sample, which can be understood on the basis growth of individual particles. The addition of NaCl further had the effect of partially suppressing the superparamagnetic relaxation seen in the Mössbauer spectra. This is likely because of increased inter-particle interactions because the increased ionic strength allows the particles to get closer together.

    The work presented here on aggregation of hematite particles and their corresponding change in magnetic properties is an initial study that opens many possibilities for further research. The characterisation of the magnetic properties presented here was far from exhausting, and a more thorough modelling of the Mössbauer data could elucidate the magnetic properties further. With temperature series of Mössbauer spectra it should be possible to determine the Morin temperatures and the superparamagnetic blocking temperatures of the samples and correlate this to the size and shapes of aggregates and individual particles. Further experimentation with different NaCl concentrations, different salts, and different temperatures and times of the hydrothermal treatment would be necessary to reliably control the aggregation process, and study the kinetics of first aggregation and then coalescence of the particles.

- **Spin orientation in hematite-ilmenite**

The spin orientation in a natural sample of hemo-ilmenite, consisting of hematite lamellae with thickness down to a few nm exsolved in ilmenite, was studied by uniaxial neutron polarisation analysis to determine the origin of the natural remanent magnetisation. We find an average angle of the hemaite spins in the basal plane of the hexagonal structure with respect to the (vertical) polarisation axis to be 45° in zero field, corresponding to a random average spin orientation. At a saturating magnetic field of 2.5 T applied in the polarisation direction we find an average spin angle of 56°. This corresponds roughly to 62% of the hematite spins being canted antiferromagnetic moments aligning perpendicular to the field and 38% of the spins being uncompensated magnetic moments aligning parallel to the field. This result strongly supports the theory of lamellar magnetism in which the natural remanent magnetism is explained as originating form uncompensated spins in contact layers between lamellae.

    In summary the thesis have demonstrated methods for investigation of spin structures in nanoparticles. Especially the increase or decrease in the magnetisation in canted spin structures is a phenomenon that can be theoretically explained by our classical model and can explain

many experimental observations of anomalous temperature dependence in nanoparticles, and in bulk systems with defects. Moreover, analysis of neutron polarisation in spin polarised neutron diffraction have been demonstrated on antiferromagnetic nanoparticles to provide experimental data that is a vast improvement compared to the more frequently applied unpolarised neutron diffraction, demonstrating that XYZ-polarisation analysis is an effective method for determining the magnetic structure of antiferromagnetic nanoparticles.

List of Papers

[1] Henrik Jacobsen, Kim Lefmann, Erik Brok, Cathrine Frandsen, and Steen Mørup. Temperature dependence of the magnetization of canted spin structures. *Journal of Magnetism and Magnetic Materials*, 324(19):3218–3222, September 2012.

[2] Steen Mørup, Erik Brok, and Cathrine Frandsen. Spin Structures in Magnetic Nanoparticles. *Journal of Nanomaterials*, 2013.

[3] E Brok, C Frandsen, D E Madsen, H Jacobsen, J O Birk, K Lefmann, J Bendix, C Boothroyd, A A Berhe, G Simeoni, and S Mørup. Magnetic properties of ultra-small goethite nanoparticles. *Submitted manuscript*, pages 1–20, 2013.

[4] C. Frandsen, K. Lefmann, B. Lebech, C. R. H. Bahl, E. Brok, S. N. Ancoña, L. Theil Kuhn, L. Keller, T. Kasama, L. C. Gontard, and S. Morup. Spin reorientation in α-Fe2O3 nanoparticles induced by interparticle exchange interactions in α-Fe2O3/NiO nanocomposites. *Physical Review B*, 84(21):214435, December 2011.

[5] Erik Brok, Morten Sales, Kim Lefmann, Luise Theil Kuhn, Wolfgang F Schmidt, Bertrand Roessli, Peter Robinson, Suzanne A McEnroe, and Richard J Harrison. Spin Orientation in Naturally Nano-Structured Hemo-Ilmenite – Investigated by Polarized Neutron Scattering. *Manuscript*, 2013.

[6] Steen Mørup, Helge K Rasmussen, Erik Brok, Lukas Keller, and Cathrine Frandsen. Influence of cation disorder on the magnetic properties of ball-milled ilmenite (FeTiO3). *Materials Chemistry and Physics*, 136:184–189, 2012.

[7] Erik Brok, Cathrine Frandsen, Kim Lefmann, Suzanne McEnroe, Peter Robinson, and Richard Harrison. Spin orientation in titanium substituted hematite. *Manuscript*, 2013.

References

[8] S. Mørup, M. F. Hansen, and C. Frandsen, in *Comprehensive Nanoscience and Technology*, 1 ed., edited by G. Andrews, G. Scholes, and G. Wiederrecht (Elsevier B.V., Philadelphia, USA, 2011), pp. 437–491.

[9] F. Bødker and S. Mørup, Europhysics Letters **52**, 217 (2000).

[10] W. F. J. Brown, Physical Review **130**, 1677 (1963).

[11] S. Mørup, Journal of Magnetism and Magnetic Materials **37**, 39 (1983).

[12] S. Mørup and H. Topsøe, Applied Physics **11**, 63 (1976).

[13] S. Mørup and B. R. Hansen, Physical Review B **72**, 024418 (2005).

[14] L. Berger, Y. Labaye, M. Tamine, and J. Coey, Physical Review B **77**, 104431 (2008).

[15] J. Coey, Physical Review Letters **27**, 1140 (1971).

[16] A. H. Morrish and K. Haneda, Journal of Magnetism and Magnetic Materials **35**, 105 (1983).

[17] R. H. Kodama, Journal of Magnetism and Magnetic Materials **200**, (1999).

[18] S. Mørup, Journal of Magnetism and Magnetic Materials **266**, 110 (2003).

[19] S. Klausen *et al.*, Physica Status Solidi (a) **189**, 1039 (2002).

[20] F. J. Morin, Physical Review **78**, 819 (1950).

[21] P. J. Besser, A. H. Morrish, and C. W. Searle, Physical Review **153**, 632 (1967).

[22] N. Yamamoto, Journal of the Physical Society of Japan **24**, 23 (1968).

[23] M. Hansen, C. B. Koch, and S. Mørup, Physical Review B **62**, 1124 (2000).

[24] F. Bødker, M. F. Hansen, C. B. Koch, and S. Mørup, Journal of Magnetism and Magnetic Materials **221**, 32 (2000).

[25] C. Frandsen and S. Mørup, Journal of Magnetism and Magnetic Materials **266**, 36 (2003).

[26] C. R. H. Bahl *et al.*, Journal of Physics: Condensed Matter **18**, 11203 (2006).

[27] L. Theil Kuhn *et al.*, Physical Review B **74**, 184406 (2006).

[28] C. Frandsen and S. Mørup, Physical Review Letters **94**, 027202 (2005).

[29] M. Colombo *et al.*, Chemical Society reviews **41**, 4306 (2012).

[30] N. A. Frey, S. Peng, K. Cheng, and S. Sun, Chemical Society reviews **38**, 2532 (2009).

[31] I. Hilger, R. Hergt, and W. A. Kaiser, Journal of Magnetism and Magnetic Materials **293**, 314 (2005).

[32] *Inorganic nanoparticles: Synthesis, Applications, and perspectives*, edited by C. Altavilla and E. Ciliberto (CRC Press, United States, 2010), No. Richter, pp. 33–68.

[33] D. Weller *et al.*, IEEE Transactions on Magnetics **37**, 2185 (2001).

[34] R. Skomski and J. Coey, Physical Review B **48**, 15812 (1993).

[35] H. Zeng *et al.*, Nature **420**, 395 (2002).

[36] G. Hadjipanayis and A. Gabay, IEEE Spectrum 36 (2011).

[37] N. Jones, Nature **472**, 22 (2011).

[38] C. Chappert, A. Fert, and F. N. Van Dau, Nature materials **6**, 813 (2007).

[39] S. A. Wolf *et al.*, Science **294**, 1488 (2001).

[40] V. Skumryev *et al.*, Nature **423**, 19 (2003).

[41] C. Frandsen *et al.*, Physical Review B **70**, 134416 (2004).

[42] L. Néel, C. R. Acad Sci Paris **252**, 4075 (1961).

[43] S. Mørup, *Mössbauer spectroscopy and its applications in materials science* (Technical University of Denmark, Kgs Lyngby, Denmark, 2004).

[44] G. L. Squires, *Thermal Neutron Scattering* (Cambridge University Press, Cambridge, 1978).

[45] G. Shirane, S. M. Shapiro, and J. M. Tranquada, *Neutron Scattering With a Triple-Axis Spectrometer* (Cambridge University Press, Cambridge, 2002).

[46] K. Lefmann, *Neutron Scattering : Theory , Instrumentation , and Simulation* (Niels Bohr Institute, University of Copenhagen, 2100 CPH, 2011).

[47] O. Halpern and M. H. Johnson, Physical Review **55**, 898 (1938).

[48] J. Chadwick, Nature **129**, 312 (1932).

[49] C. G. Shull and J. S. Smart, Physical Review **76**, 1256 (1949).

[50] C. G. Shull, W. A. Strauser, and E. O. Wollan, Physical Review **83**, 333 (1951).

[51] C. G. Shull, *Early deveopment of neutron scattering*, Nobel lecture,www.nobelprize.org, 1994.

[52] R. L. Liboff, *Introductory Quantum Mechanics* (Addison Wesley, San Francisco, 2003).

[53] C. Kittel, *Introduction to solid state physics* (John Wiley and Sons, Inc., Hoboken, NJ, 2005).

[54] J. R. Stewart *et al.*, Journal of Applied Crystallography **42**, 69 (2008).

[55] E. J. Lisher and J. B. Forsyth, Acta Crystallographica Section A **27**, 545 (1971).

[56] *Neutron Data Booklet*, edited by A.-J. Dianoux and G. Lander (Institut Laue-Langevin, Grenoble, 2003).

[57] R. E. Watson and A. J. Freeman, Acta Crystallographica **14**, 27 (1961).

[58] F. C. Blake, Reviews of Modern Physics **5**, 169 (1933).

[59] P. Scherrer, Nachrichten von der Gesellschaft der Wissenschaften zu Göttingen, Mathematisch-Physikalische Klasse 98 (1933).

[60] J. I. Langford and A. J. C. Wilson, Journal of Applied Crystallography **11**, 102 (1978).

[61] J. I. Langford and D. Louër, Journal of Applied Crystallography **15**, 20 (1982).

[62] R. Moon, T. Riste, and W. Koehler, Physical Review **181**, 920 (1969).

[63] O. Schärpf and H. Capellmann, Physica Status Solidi (a) **359**, 359 (1993).

[64] A. R. Wildes, Neutron News **17**, 17 (2006).

[65] Home page of the IN12 instrument.

[66] B. Roessli and P. Böni, in *Scattering: Scattering and inverse scattering in pure and applied sciences*, edited by R. Pike and P. Sabatier (Academic Press, San Diego, USA, 2002), Chap. 2.8.5, pp. 1242–1263.

[67] Home page of the D7 instrument.

[68] O. Schärpf, Physica B: Condensed Matter **156-157**, 639 (1989).

[69] O. Schärpf, Physica B **174**, 514 (1991).

[70] H. M. Rietveld, Acta Crystallographica **22**, 151 (1967).

[71] H. M. Rietveld, Journal of Applied Crystallography **2**, 65 (1969).

[72] R. J. Hill and C. J. Howard, AAEC (now ANSTO) Report M112, Lucas Heights Research Laboratory, NSW, Australia, 1986.

[73] D. B. Williams and C. B. Carter, *Transmission Electron Microscopy* (Springer Science + Business Media Inc, New York, 1996).

[74] *Dynamic Light Scattering: Applications of Photon Correlation Spectroscopy*, edited by R. Pecora (Plenum Press, New York, 1985).

[75] C. E. Barnett, Journal of Physical Chemistry **46**, 69 (1941).

[76] R. L. Mössbauer, Zeitschrift für Physik **151**, 124 (1958).

[77] R. L. Mössbauer, Die Naturwissenschaften **45**, 538 (1958).

[78] R. L. Mössbauer, *Recoilless nuclear resonance absorption of gamma radiation*, Nobel lecture, `www.nobelprize.org`, 1961.

[79] D. E. Madsen, M. F. Hansen, J. Bendix, and S. Mørup, Nanotechnology **19**, 315712 (2008).

[80] E. Tronc *et al.*, Journal of Magnetism and Magnetic Materials **221**, 63 (2000).

[81] T. N. Shendruk, R. D. Desautels, B. W. Southern, and J. van Lierop, Nanotechnology **18**, 455704 (2007).

[82] R. Aquino *et al.*, Physical Review B **72**, 184435 (2005).

[83] K. Mandal, S. Mitra, and P. A. Kumar, Europhysics Letters **75**, 618 (2006).

[84] D. Peddis *et al.*, Nanotechnology **21**, 125705 (2010).

[85] B. Martínez *et al.*, Physical Review Letters **80**, 181 (1998).

[86] C. Chinnasamy *et al.*, Physical Review B **63**, 184108 (2001).

[87] G. Gavoille, J. Hubsch, and I. Mirebeau, Journal of Magnetism and Magnetic Materials **171**, 291 (1997).

[88] T. A. Anhø j *et al.*, Journal of Magnetism and Magnetic Materials **260**, 115 (2003).

[89] R. Kodama, A. Berkowitz, E. McNiff, and S. Foner, Physical review letters **77**, 394 (1996).

[90] C. J. Serna *et al.*, Solid State Communications **118**, 437 (2001).

[91] S. Chkoundali *et al.*, Journal of Physics: Condensed Matter **16**, 4357 (2004).

[92] A. G. Roca *et al.*, Journal of Applied Physics **105**, 114309 (2009).

[93] P. G. Bercoff and H. R. Bertorello, Journal of Magnetism and Magnetic Materials **213**, 56 (2000).

[94] D. E. Madsen *et al.*, Journal of Physics. Condensed Matter **21**, 016007 (2009).

[95] Q. A. Pankhurst and R. J. Pollard, Journal of Physics. Condensed Matter **2**, 7329 (1990).

[96] S. Bocquet and S. J. Kennedy, Journal of Magnetism and Magnetic Materials **109**, 260 (1992).

[97] S. Bocquet, R. J. Pollard, and J. D. Cashion, Physical Review B **46**, 11657 (1992).

[98] R. J. Pollard, Q. A. Pankhurst, and P. Zientek, Journal of Magnetism and Magnetic Materials **104-107**, 1557 (1992).

[99] J. Coey *et al.*, Journal of Physics. Condensed Matter **7**, 759 (1995).

[100] F. Martin-Hernandez and M. M. García-Hernández, Geophysical Journal International **181**, 756 (2010).

[101] A. Szytula *et al.*, Physica Status Solidi **429**, 429 (1968).

[102] Q. A. Pankhurst *et al.*, Physical Review B **85**, 174437 (2012).

[103] R. Kodama, S. Makhlouf, and A. Berkowitz, Physical Review Letters **79**, 1393 (1997).

[104] K. Baberschke and M. Farle, Journal of Applied Physics **81**, 5038 (1997).

[105] P. P and K. Baberschke, Journal of Physics: Condensed Matter **11**, 9495 (1999).

[106] D. Deng, X. Jin, and R. Tao, Physical Review B **69**, 172403 (2004).

[107] J. Li *et al.*, Physical Review B **84**, 012406 (2011).

[108] C. R. H. Bahl, Ph.D. thesis, 2006.

[109] J. T. Richardson and W. O. Milligan, Physical Review **102**, 1289 (1956).

[110] S. a. Makhlouf, F. T. Parker, F. E. Spada, and a. E. Berkowitz, Journal of Applied Physics **81**, 5561 (1997).

[111] Y. Ichiyanagi, Physica B: Condensed Matter **329-333**, 862 (2003).

[112] C. R. H. Bahl *et al.*, Journal of physics. Condensed matter : an Institute of Physics journal **18**, 4161 (2006).

[113] J. T. Richardson *et al.*, Journal of Applied Physics **70**, 6977 (1991).

[114] A. E. Berkowitz *et al.*, Journal of Magnetism and Magnetic Materials **196-197**, 591 (1999).

[115] V. V. Pishko *et al.*, Journal of Applied Physics **93**, 7382 (2003).

[116] W. Neubeck *et al.*, Journal of Applied Physics **85**, 4847 (1999).

[117] V. Fernandez *et al.*, Physical Review B **57**, 7870 (1998).

[118] F. Fiévet, P. Germi, F. de Bergevin, and M. Figlarz, Journal of Applied Crystallography **12**, 387 (1979).

[119] J. R. Tomlinson, L. Domash, R. G. Hay, and C. W. Montgomery, Journal of the American Chemical Society **77**, 909 (1955).

[120] W. L. Roth, Physical Review **110**, 1333 (1958).

[121] W. L. Roth and G. A. Slack, Journal of Applied Physics **31**, S352 (1960).

[122] M. T. Hutchings and E. J. Samuelsen, Physical Review B **6**, 3447 (1972).

REFERENCES

[123] J. Baruchel, M. Schenker, K. Kurosawa, and S. Saito, Philosophical Magazine B **43**, 853 (1981).

[124] E. Ressouche, N. Kernavanois, L.-P. Regnault, and J.-Y. Henry, Physica B: Condensed Matter **385-386**, 394 (2006).

[125] L. C. Bartel and B. Morosin, Physical Review B **3**, 1039 (1971).

[126] C. Greaves and M. A. Thomas, Acta Crystallographica B **42**, 51 (1986).

[127] A. H. Morrish, *Canted Antiferromagnetism: Hematite* (World Scientific, Singapore, 1994).

[128] I. Dzyaloshinsky, Journal of Physics and Chemistry of Solids **4**, 241 (1958).

[129] P. J. Flanders, Journal of Applied Physics **43**, 2430 (1972).

[130] L. Tobler, W. Kündig, and I. Savic, Hyperfine Interactions **10**, 1017 (1981).

[131] F. Bødker and S. Mørup, Europhysics Letters **217**, 217 (2000).

[132] T. Moriya, Physical Review **120**, 91 (1960).

[133] S. Klausen *et al.*, Journal of Magnetism and Magnetic Materials **266**, 68 (2003).

[134] S. Klausen *et al.*, Physical Review B **70**, 214411 (2004).

[135] D. Li *et al.*, Science (New York, N.Y.) **336**, 1014 (2012).

[136] M. Niederberger and H. Cölfen, Physical Chemisty Chemical Physics **8**, 3271 (2006).

[137] V. M. Yuwono, N. D. Burrows, J. A. Solitis, and R. L. Penn, Journal of the American Chemical Society **132**, 2163 (2010).

[138] C. Frandsen *et al.*, Physical Review B **72**, 214406 (2005).

[139] T. Sugimoto, Y. Wang, H. Itoh, and A. Muramatsu, Colloids and Surfaces A **134**, 265 (1998).

[140] B. Gilbert, C. Frandsen, E. Maxey, and D. Sherman, Physical Review B **79**, 035108 (2009).

[141] Y. T. He, J. Wan, and T. Tokunaga, Journal of Nanoparticle Research **10**, 321 (2008).

[142] C. Frandsen *et al.*, Submitted manuscript (2013).

[143] S. A. McEnroe *et al.*, Journal of Physics: Conference Series **17**, 154 (2005).

[144] S. A. McEnroe, P. Robinson, and P. T. Panish, American Mineralogist **86**, 1447 (2001).

[145] S. A. McEnroe *et al.*, Geophysical Research Letters **31**, L19601 (2004).

[146] P. Robinson, R. J. Harrison, S. A. McEnroe, and R. B. Hargreaves, Nature **418**, 517 (2002).

[147] Y. Ishikawa and S.-I. Akimoto, Journal of the Physical Society of Japan **12**, 1083 (1957).

[148] Y. Ishikawa, Journal of the Physical Society of Japan **13**, 37 (1958).

[149] W. H. Butler, A. Bandyopadhyay, and R. Srinivasan, Journal of Applied Physics **93**, 7882 (2003).

[150] H. Hojo, K. Fujita, K. Tanaka, and K. Hirao, Applied Physics Letters **89**, 082509 (2006).

[151] T. Fujii *et al.*, Solid State Ionics **172**, 289 (2004).

[152] H. Kato *et al.*, Solid State Communications **45**, 669 (1983).

[153] R. J. Harrison, S. A. McEnroe, P. Robinson, and C. J. Howard, American Mineralogist **95**, 974 (2010).

[154] D. H. Lindsley, Carnegie Inst. Washington Year Book **64**, 144 (1965).

[155] R. M. Cornell and U. Schwertmann, *The Iron Oxides* (Wiley, Weinheim, 2003).

[156] U. Schärer, E. Wilmart, and J. C. Duchesne, Earth and Planetary Science Letters **139**, 335 (1996).

[157] S. A. McEnroe, R. J. Harrison, P. Robinson, and F. Langenhorst, Geophysical Journal International **151**, 890 (2002).

[158] P. Robinson *et al.*, Geophysical Journal International **165**, 17 (2006).

[159] P. Robinson, R. J. Harrison, S. A. McEnroe, and R. B. Hargreaves, American Mineralogist **89**, 725 (2004).

[160] P. Robinson, Fabian K, M. S. A., and F. Heidelbach, Geophysical Journal International **192**, 514 (2013).

[161] S. a. McEnroe *et al.*, Journal of Geophysical Research **112**, B10103 (2007).

[162] K. Fabian, S. A. McEnroe, P. Robinson, and V. P. Shcherbakov, Earth and Planetary Science Letters **268**, 339 (2008).

[163] S. A. McEnroe *et al.*, Nature nanotechnology **2**, 631 (2007).

[164] J. C. Duchesne, Mineralium Deposita **34**, 182 (1999).

[165] S. McEnroe, Personal communication, 2013.

[166] E. Brok, Master's thesis, University of Copenhagen, 2009.

[167] M. Sales, Master's thesis, University of Copenhagen, 2012.

Appendix

A.1   Atoms in the unit cell of NiO

atom#	x	y	z	spin	atom#	x	y	z	spin
1	0	0	0	+	17	0	0	0.5	-
2	0.5	0	0	-	18	0.5	0	0.5	+
3	0.25	0.25	0	-	19	0.25	0.25	0.5	+
4	0.75	0.25	0	+	20	0.75	0.25	0.5	-
5	0	0.5	0	-	21	0	0.5	0.5	+
6	0.5	0.5	0	+	22	0.5	0.5	0.5	-
7	0.25	0.75	0	+	23	0.25	0.75	0.5	-
8	0.75	0.75	0	-	24	0.75	0.75	0.5	+
9	0	0.25	0.25	-	25	0	0.25	0.75	+
10	0	0.75	0.25	+	26	0	0.75	0.75	-
11	0.25	0	0.25	-	27	0.25	0	0.75	+
12	0.25	0.5	0.25	+	28	0.25	0.5	0.75	-
13	0.5	0.25	0.25	+	29	0.5	0.25	0.75	-
14	0.5	0.75	0.25	-	30	0.5	0.75	0.75	+
15	0.75	0	0.25	+	31	0.75	0	0.75	-
16	0.75	0.5	0.25	-	32	0.75	0.5	0.75	+

Table A.1: The 32 atoms in the magnetic unit cell.

Part II

Part II - Papers

Temperature dependence of the magnetization of canted spin structures

Henrik Jacobsen [a], Kim Lefmann [a], Erik Brok [b,c], Cathrine Frandsen [b,*], Steen Mørup [b]

[a] *Nano-Science Center, Niels Bohr Institute, University of Copenhagen, DK-2100 Copenhagen Ø, Denmark*
[b] *Department of Physics, Technical University of Denmark, DK-2800 Kongens Lyngby, Denmark*
[c] *Center for Electron Nanoscopy, Technical University of Denmark, DK-2800 Kongens Lyngby, Denmark*

ARTICLE INFO

ABSTRACT

Numerous studies of the low-temperature saturation magnetization of ferrimagnetic nanoparticles and diamagnetically substituted ferrites have shown an anomalous temperature dependence. It has been suggested that this is related to freezing of canted magnetic structures. We present models for the temperature dependence of the magnetization of a simple canted spin structure in which relaxation can take place at finite temperatures between spin configurations with different canting angles. We show that the saturation magnetization may either decrease or increase with decreasing temperature, depending on the ratio of the exchange coupling constants. This is in agreement with experimental observations.

1. Introduction

Ferrite nanoparticles as well as bulk ferrites are of great interest both from a fundamental point of view and because of their many technological applications [1]. The temperature dependence of the saturation magnetization of bulk ferrites usually follows the well-known Bloch $T^{3/2}$ law within the spin wave regime at low temperatures, while nanoparticles may show a linear decrease of the magnetization with increasing temperature at low temperature, because of quantization of the spin wave spectrum, and the thermal excitations being dominated by excitations of the uniform mode [2,3]. However, in several studies of ferrimagnetic nanoparticles and diamagnetically substituted ferrites an anomalous temperature dependence of the saturation magnetization has been observed at temperatures well below 100 K. In studies of chemically prepared nanoparticles of maghemite (γ-Fe_2O_3) [4–7], copper ferrite [8,9], manganese ferrite [9,10], nickel ferrite [11] and cobalt ferrite [12], the saturation magnetization was found to increase significantly with decreasing temperature, but in other cases, e.g. in ball-milled nickel ferrite [13,14] and in maghemite nanoparticles prepared by a vaporization–condensation process [15] the saturation magnetization showed an anomalous decrease with decreasing temperature. A similar decrease of the saturation magnetization with decreasing temperature has been observed in diamagnetically substituted ferrites, such as $Mg_{1.55}Fe_{0.9}Ti_{0.55}O_4$ [16] and $Mn_{0.25}Zn_{0.75}Fe_2O_4$ [17].

It is well established that ferrimagnetic nanoparticles [18,19] as well as diamagnetically substituted ferrites [17,20,21] often have non-collinear (canted) spin structures. Several authors have suggested that the anomalous temperature dependence of the saturation magnetization at low temperatures is related to freezing of magnetic fluctuations in canted spin structures, but no detailed model explaining the data quantitatively has been published. It may seem contradictory that freezing of canted spins can explain both an increase and a decrease of the magnetization with decreasing temperature.

In diamagnetically substituted ferrites the canting may be localized around substituted diamagnetic ions [20,21]. In nanoparticles it is often assumed that the canted spins are located in a surface layer with a spin glass-like structure. In accordance with this model, several studies have shown that the relative number of canted spins in nanoparticles increases with decreasing particle size. However, other studies have shown a large variation of the relative number of canted spins in particles with similar size [22], and it has been shown that nickel ferrite nanoparticles with diameter less than 5 nm [23] and 6.4 nm magnetite particles [24] can be prepared in a way such that they show essentially no spin canting. Thus, spin canting is not an always existing surface phenomenon in nanoparticles, but rather seems to be related to the presence of spins in low-symmetry environments at the surface and in the interior of the particles.

In this paper we present a simple model for magnetic dynamics in canted spin structures that can explain both an anomalous increase and decrease of the low temperature magnetization with decreasing temperature. The spin structures around surfaces and defects in ferrimagnetic materials can be very complex [25], and in

general, analytical calculations are not feasible. In order to illustrate the magnetic properties of canted spin structures we therefore consider a very simple case, which may qualitatively be used to illustrate the temperature dependence of the magnetization of canted spin structures in ferrites. We consider a two-dimensional lattice with magnetic ions in A and B sites, illustrated in Fig. 1. The bold arrows are A-site spins and the other arrows are B-site spins. The cross represents a missing A-site spin. The A–B and the B–B exchange couplings are assumed to be antiferromagnetic and the A–B coupling is assumed stronger than the B–B coupling such that all B-site spins are parallel, but antiparallel to the A-site spins in the defect-free structure. Because of the antiferromagnetic B–B exchange coupling and the missing A-site ion, the four spins around the A-site vacancy in Fig. 1 may be canted with canting angles that depend on the exchange coupling constants and the applied magnetic field [26]. The canting angles can be larger than 90°, as illustrated in the figure.

2. Classical model

First, we use a classical model to calculate the temperature dependence of the average magnetization of the two-dimensional canted spin structure in Fig. 1. Neglecting the magnetic anisotropy and the canting of next nearest spins, and assuming for symmetry reasons that the angles between the spins and the z-direction are pairwise identical we find in the classical model [20,21,26]

$$E(\theta_1,\theta_2) = a(\cos\theta_1 + \cos\theta_2) + b\cos(\theta_1 - \theta_2) \quad (1)$$

where

$$a = 4\lambda_{BB} - 2\lambda_{AB} + 2\lambda_L - 2\mu B \quad (2)$$

and

$$b = 4\lambda_{BB} \quad (3)$$

Here λ_{BB} (>0) is the B–B exchange parameter for nearest neighbor B–B coupling, λ_{AB} is the exchange parameter for nearest neighbor A–B coupling and λ_L is the exchange parameter for the exchange interaction between a B-site ion and all more distant ions. μ is the magnetic moment of a B-site ion and B is the applied magnetic field, defining the z-direction.
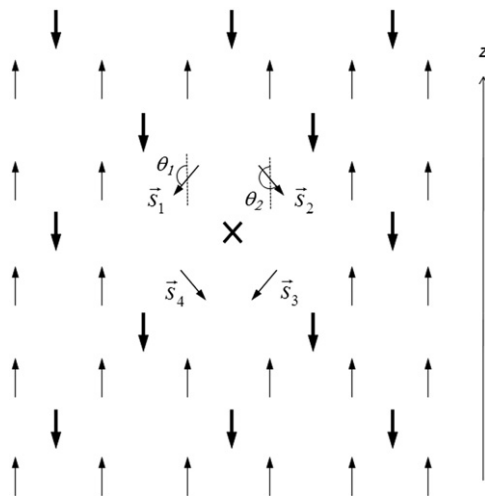
Fig. 1. Schematic illustration of a canted two-dimensional spin structure. The bold arrows correspond to A-site spins and the other arrows correspond to B-site spins. The cross represents a missing A-site spin.

In order to find the energy minima and maxima, we differentiate Eq. (1) with respect to θ_1 and θ_2 and find minima for [26]

$$\sin\theta_1 = -\sin\theta_2 \quad (4)$$

and

$$\cos\theta_1 = \cos\theta_2 = -\frac{a}{2b} \quad (5)$$

with energy $E_{min} = -b - a^2/2b$.

There are maxima at $\theta_1 = \theta_2 = 0°$ with energy $E(0°,0°) = 2a + b$, at $\theta_1 = \theta_2 = 180°$ with $E(180°,180°) = -2a + b$, and at $(\theta_1,\theta_2) = (0°,180°)$ or $(180°,0°)$ with energy $E(0°,180°) = E(180°,0°) = -b$ [26].

For an arbitrary value of θ_1 one can find the value of θ_2, which minimizes the energy

$$tg\theta_2 = \frac{b\sin\theta_1}{a + b\cos\theta_1} \quad (6)$$

Therefore, in general, the angles θ_1 and θ_2 are quite different. Using the relation

$$\cos\theta_2 = \pm\frac{1}{\sqrt{tg^2\theta_2 + 1}} = \pm\frac{a + b\cos\theta_1}{\sqrt{a^2 + b^2 + 2ab\cos\theta_1}} \quad (7)$$

and inserting (7) in Eq. (1) we find

$$E(\theta_1) = a\cos\theta_1 \pm \sqrt{a^2 + b^2 + 2ab\cos\theta_1}, \quad (8)$$

where the sign of the last term in Eq. (8) is the sign of $\cos\theta_2$.

Thus, the energy can be calculated as a function of θ_1 and, as an example, Fig. 2 shows the energy as a function of the canting angle for $b/k_B = 200$ K, where k_B is Boltzmann's constant, and values of a/b between 1.1 and 1.9 ($\cos\theta_2$ is negative in this case). At temperature $T = 0$ K, the system is found in an energy minimum and the total magnetic moment of the four canted spins is $M_0 = -2\mu a/b$. At higher temperatures, the spin directions fluctuate and eventually overcome the energy barrier at $(\theta_1,\theta_2) = (180°,180°)$. The average value of the z component of the magnetic moment is then given by $\langle M^z(T)\rangle = 2\mu\langle\cos\theta_1 + \cos\theta_2\rangle$, where $\cos\theta_2$ is given by Eq. (7). By use of Boltzmann statistics we can calculate the thermal average of the z component of the magnetic moment

$$\langle M^z(T)\rangle = 2\mu\frac{\int\exp(-E(\theta_1)/kT)(\cos\theta_1 + \cos\theta_2)\sin\theta_1 d\theta_1}{\int\exp(-E(\theta_1)/kT)\sin\theta_1 d\theta_1} \quad (9)$$

As illustrated in Fig. 3, at low temperatures the thermal average of the magnetic moment decreases rapidly with decreasing temperature
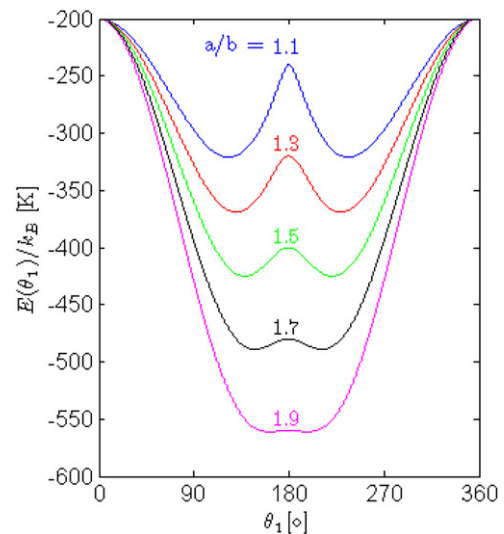

Fig. 2. The energy of the canted spin structure, shown in Fig. 1, as a function of the angle θ_1 for values of a/b in the range from 1.1 to 1.9. The calculations were carried out using a classical model (Eq. (8)) with $b/k_B = 200$ K.
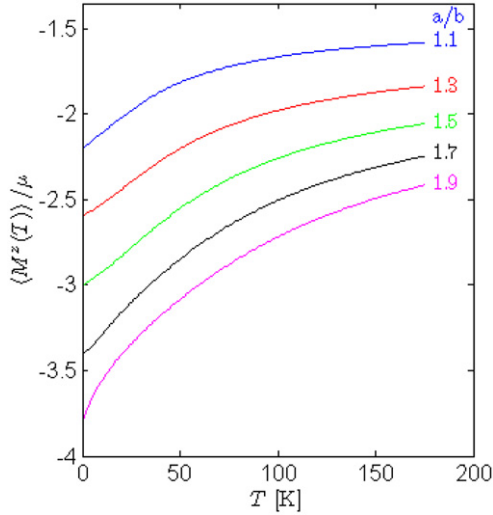
Fig. 3. Temperature dependence of the thermal average of the magnetic moment of the canted spin structure, shown in Fig. 1. The data were calculated using the classical model (Eq. (9)) with $b/k_B = 200$ K and values of a/b in the range from 1.1 to 1.9.

for all values of a/b between 1.1 and 1.9. If the sign of a/b is negative, the temperature dependence of the magnetization is reversed.

3. Quantum mechanical model

The use of a classical model for a system with only four spins is a rough approximation and it is more realistic to perform a quantum mechanical calculation of the states of the four canted spins, treating the rest of the magnetic system in a mean field approach. The Hamiltonian of the four canted spins is then given by

$$\hat{H} = \frac{a}{2}\sum_{i=1}^{4} \vec{s}_i \cdot \hat{z} + \frac{b}{4}\sum_{i=1}^{4} \vec{s}_i \cdot \vec{s}_{i+1} \tag{10}$$

where $\hat{z}$ is a unit vector in the z-direction, $\vec{s}_i$ is the spin of one ion, and we define $\vec{s}_5 = \vec{s}_1$. a and b are the same as in Eq. (1). The first term can be interpreted as the interaction of the four canted spins with an effective magnetic field in the z-direction, and the second term represents the (antiferromagnetic) interaction between the four spins.

In the jth eigenstate of $\hat{H}$, the z component of the total magnetic moment of the four spins can be written as $M_j^z = g\mu_B S_j^z$, where g is the gyromagnetic ratio, μ_B is the Bohr magneton and $S_j^z = \sum_{i=1}^{4} s_i^z(j)$. The temperature dependence of the thermal average of the z component of the total magnetic moment, $\langle M^z(T) \rangle$ can be computed using Boltzmann statistics

$$\langle M^z(T) \rangle = \frac{\sum_j M_j^z \exp(-E_j/k_B T)}{\sum_j \exp(-E_j/k_B T)} \tag{11}$$

where E_j is the jth eigenvalue of $\hat{H}$, and the sum runs over all eigenstates of $\hat{H}$. To find the eigenvalues, we first note that the two terms in Eq. (10) commute. This means that the eigenvalues of $\hat{H}$ are given by

$$E_j = E_j^a + E_j^b \tag{12}$$

where $E_j^a = (a/2)S_j^z$ is the jth eigenvalue of the first term of Eq. (10), $\hat{H}^a$, and E_j^b is the jth eigenvalue of the second term, $\hat{H}^b$.

To calculate the values of E_j^b, we rewrite the second term of Eq. (10) to

$$\hat{H}^b = \frac{b}{4}\sum_{i=1}^{4} \left(s_i^z s_{i+1}^z + \frac{1}{2}(s_i^+ s_{i+1}^- + s_i^- s_{i+1}^+) \right) \tag{13}$$

where s_i^+ and s_i^- are the raising and lowering operators of the ith spin, respectively. It is now possible for a complete set of states to calculate the eigenvalues and insert these values into Eq. (11) to find $\langle M^z(T) \rangle$. We have done this for a spin-one system (having a total of 81 states). For a spin-one system, the values of E_j are shown in Fig. 4 for $a/b = 1.6$ and $a/b = 1.9$ and $b/k_B = 200$K. The temperature dependence of $\langle M^z(T) \rangle$ is shown in Fig. 5 for $b/k_B = 200$ K and values of a/b between 1.1 and 1.9. We note that at the lowest temperatures, $\langle M^z(T) \rangle$ in some cases increases with decreasing temperature, while it in other cases decreases.

To explain the temperature dependence of $\langle M^z(T) \rangle$, we again consider the cases $a/b = 1.9$ and $a/b = 1.6$. At low temperatures, only the ground state is populated, so that the total spin $S^z = -3$ for both values of a/b(see the insets in Fig. 4). As the temperature increases, the system will fluctuate between the ground state and the lowest lying excited states. For $a/b = 1.6$, the lowest excited state has $S^z = -2$, and the total magnetization will increase with increasing temperature. For $a/b = 1.9$, the lowest excited state has $S^z = -4$ and the total magnetization will decrease with increasing temperature. As the temperature is further increased, more excited states become accessible, and the resulting magnetization increases with increasing temperature due to population of states with larger values of the total spin. For $a/b = 1.5$ the lowest states with $S^z = -2$ and $S^z = -3$ have exactly the same energy, and therefore $\langle S^z \rangle = -2.5$ at $T = 0$ K.

If the sign of a/b is negative, so is the sign of S^z, and, therefore, for $a/b = -1.9$ the magnetization increases with increasing temperature, while it decreases for $a/b = -1.6$.
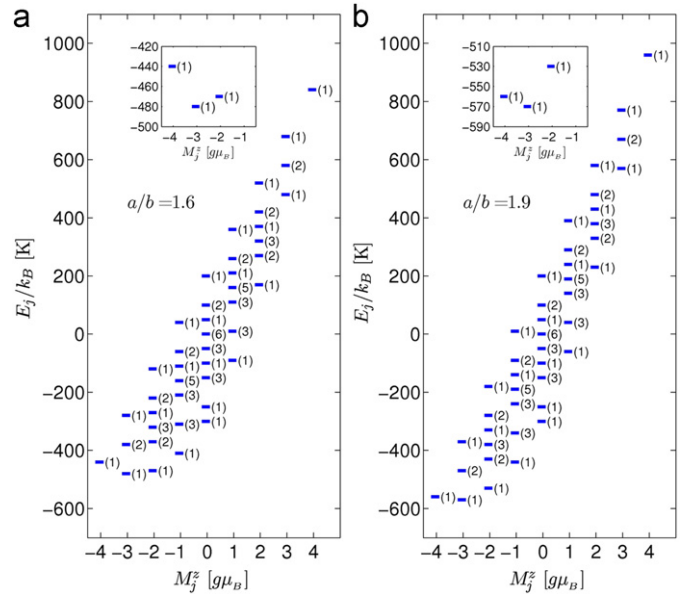

Fig. 4. Energy levels for a spin-one system for $b/k_B = 200$ K, calculated from a quantum mechanical model for the canted spin structure shown in Fig. 1. The numbers in parentheses indicate the degeneration of the energy levels. In (a), $a/b = 1.6$ and the first excited state has $S^z = -2$, which means the average magnetic moment increases when the temperature increases, while in (b), $a/b = 1.9$ and the first excited state has $S^z = -4$ such that the average magnetic moment decreases with increasing temperature. The insets show magnified views of the lowest energy levels.
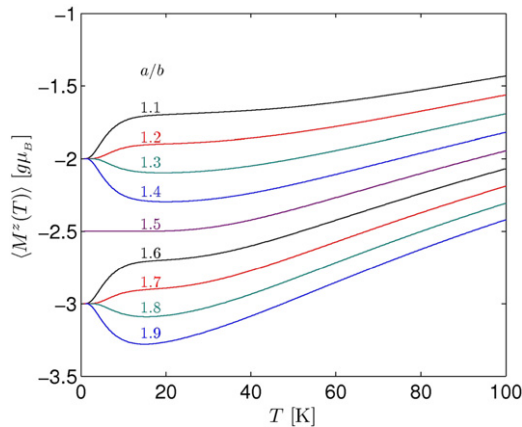
Fig. 5. The thermal average of the *z* component of the magnetic moment of the canted spin structure in Fig. 1 as a function of temperature. The data were calculated using the quantum mechanical model with $b/k_B = 200$ K and values of a/b between 1.1 and 1.9.

We have also carried out calculations for a system with $s = \frac{1}{2}$ and found results for the temperature dependence of the magnetization that are qualitatively similar to those for the $s = 1$ system.

4. Discussion

It should be emphasized that the canted two-dimensional spin structure, illustrated in Fig. 1 and with magnetic energy given by Eq. (1) or Eq. (10), is a very simple model, and in reality, the canted spin structures will usually be much more complex. In more exact models, a finite magnetic anisotropy should be included, the calculations should be performed for three-dimensional structures, and spin structures with lower symmetry should also be considered, but this would preclude derivation of simple analytical solutions. However, in spite of the simplicity of the present model, it illustrates at least qualitatively how relaxation between canted states can influence the temperature dependence of the magnetization.

The mechanism behind the temperature dependence of the average magnetic moment is the same in the classical and quantum mechanical calculations: fluctuations between the lowest energy configurations of the spins can, depending on the value and sign of a/b, either increase or decrease the magnetization with increasing temperature. The difference is that in the classical picture, the lowest energy states have exactly the same energy, while in the quantum mechanical calculations they are in general different. In the quantum mechanical model, the change in magnetization at low temperatures can be seen as a consequence of quantization of the magnetic moment of small spin clusters. This gives rise to the more complicated behavior of the magnetization at very low temperatures.

It is interesting to compare the theoretical results for the change in the thermal average of the magnetic moment at low temperatures with experimental values. In experimental studies, the average canting angles and in some cases the relative numbers of canted spins can conveniently be estimated by Mössbauer spectroscopy at low temperature and with large magnetic fields applied parallel to the gamma ray direction. In an ideal ferrimagnet, the relative intensities of lines 2 and 5 in the magnetically split six-line components vanish, when the material is magnetized parallel to the gamma ray direction, but in canted spin structures these lines have a non-zero intensity, which allows estimates of the relative number of canted spins as well as the average canting angles [17–19]. For example, in a study of nanoparticles of maghemite (γ-Fe$_2$O$_3$) with different particle size [27], it was found that the

average canting angle increased from 9° for 10 nm particles to 37° in 2.7 nm particles. In another study of maghemite nanoparticles and tin-doped maghemite [28] it was found that the A-site spins in the spinel lattice had negligible canting, whereas around half of the Fe^{3+} ions in the B-sites were canted with canting angles larger than 40°. In studies of maghemite particles with particle size around 3.5 nm, prepared by laser pyrolysis of iron pentacarbonyl, it was found that essentially all Fe^{3+} ions were canted [22]. Nanoparticles of NiFe$_2$O$_4$, prepared by ball milling, have shown that the average canting angle increases with the milling time [14]. After a milling time of 30 h an average canting angle of 34° was found. A study of CoFe$_2$O$_4$ particles with particle size between 2.8 and 6.7 nm, prepared by an auto-combustion technique, showed average canting angles around 40° [29].

In several studies of nanoparticles and diamagnetically substituted ferrites with canted spin structures, it has been found that the relative intensity of lines 2 and 5 decreases with increasing temperature and the hyperfine field of the canted spins decreases [4,17,28]. This can be explained by relaxation between canted spin configurations with different canting angles in accordance with the model presented in this paper.

The size of the low-temperature anomalies of the magnetization varies considerably and has been found to depend both on particle size, composition and the preparation method. In chemically prepared maghemite nanoparticles with particle size in the range 2.7–7.1 nm, an increase of the magnetization with decreasing temperature below 100 K was observed [4,5]. The largest effect was found in the 2.7 nm particles, for which an increase in the saturation magnetization up to around 50% was found, whereas the larger particles showed an increase of only a few percent. In another study of 7 nm maghemite particles, an increase by around 30% was found below 50 K [30]. In CuFe$_2$O$_4$ nanoparticles an increase of around 10% has been measured at temperatures below 50 K [8,9]. A similar effect was observed in nanoparticles of MnFe$_2$O$_4$ [8]. In 3 nm CoFe$_2$O$_4$ particles, prepared by an autocombustion technique, the saturation magnetization was found to increase by around 20% below 50 K [12]. An increase of the saturation magnetization of up to 15% was found for 2.5 nm NiFe$_2$O$_4$ particles in a SiO$_2$ matrix [11]. However, in NiFe$_2$O$_4$ nanoparticles, prepared by ball-milling, a 3% decrease was found below 40 K. [13]. A similar tendency was observed in another study of ball milled nanocrystalline NiFe$_2$O$_4$ [14]. In the diamagnetically substituted bulk ferrites, Mg$_{1.55}$Fe$_{0.9}$Ti$_{0.55}$O$_4$ [16] and Mn$_{0.25}$Zn$_{0.75}$Fe$_2$O$_4$ [17] the saturation magnetization was found to decrease by around 10% below 50 K. Thus, the size and the sign of the anomalous change in saturation magnetization seem to depend on both composition, particle size and preparation conditions.

The change in the average magnetic moment of the four canted spins at very low temperatures, shown in Figs. 3 and 5, is on the order of 10%. The total average magnetic moment of a material is the sum of contributions from the canted spins and spins without canting. If a large fraction of the spins are canted, the change in saturation magnetization in the simple canted spin configuration, shown in Fig. 1, is on the same order of magnitude as many of the experimental observations. We note that there may also be other contributions to the low-temperature magnetization in large applied fields, which need to be considered. For example, paramagnetic impurity ions and superparamagnetic particles with a very small magnetic moment give negligible contributions to the magnetization in large applied fields at high temperatures, but at low temperatures they may become almost magnetically saturated and can therefore contribute to the increase of the magnetization at low temperatures. This may explain some of the observations of a very large increase of the magnetization at low temperatures.

5. Conclusions

We have shown that at very low temperatures, the average magnetic moment of a simple, canted spin configuration may either increase or decrease with temperature, depending on the values of the exchange coupling constants and the applied magnetic field. The simple model can explain, at least qualitatively, the anomalous temperature dependence of the low-temperature magnetization, which has been measured in several studies of nanoparticles and diamagnetically substituted ferrites.

Acknowledgments

References

[1] S. Mørup, M.F. Hansen, C. Frandsen, in: D. Andrews, G. Scholes, G. Wiederrecht. (Eds.), Comprehensive Nanoscience and Technology, 1, Elsevier, 2011, pp. 437–491.
[2] S. Mørup, B.R. Hansen, Physical Review B 72 (2005) 024418.
[3] S. Mørup, C. Frandsen, M.F. Hansen, Beilstein Journal of Nanotechnology 1 (2010) 48.
[4] E. Tronc, A. Ezzir, R. Cherkaoui, C. Chanéac, M. Noqués, H. Kachkachi, D. Fiorani, A.M. Testa, J.M. Grenèche, J.P. Jolivet, Journal of Magnetism and Magnetic Materials 221 (2000) 63.
[5] H. Kachkachi, A. Ezzir, M. Nogués, E. Tronc, European Physical Journal B 14 (2000) 681.
[6] T.N. Shendruk, R.D. Desautels, B.W. Southern, J. van Lierop, Nanotechnology 18 (2007) 455704.
[7] F.T. Parker, M.W. Foster, D.T. Margulies, A.E. Berkowitz, Physical Review B 47 (1993) 7885.
[8] R. Aquino, J. Depeyrot, M.H. Sousa, F.A. Tourinho, E. Dubois, R. Perzynski, Physical Review B 72 (2005) 184435.
[9] C.R. Alves, R. Aquino, J. Depeyrot, T.A.P. Cotta, M.H. Sousa, F.A. Tourinho, H.R. Rechenberg, G.F. Goya, Journal of Applied Physics 99 (2006) 08M905.
[10] F.G. Silva, R. Aquino, V. Dupuis, J. Depeyrot, F.A. Tourinho, R. Perzynski, Journal of Physics: Conference Series 200 (2010) 072035.
[11] K. Mandal, M. Subarna, P.A. Kumar, EPL 75 (2006) 618.
[12] D. Peddis, C. Cannas, G. Piccaluga, E. Agostinelli, D. Fiorani, Nanotechnology 21 (2010) 125705.
[13] R.H. Kodama, A.E. Berkowitz, E.J. McNiff Jr., S. Foner, Physical Review Letters 77 (1996) 394.
[14] C.N. Chinnasamy, A. Narayanasamy, N. Ponpandian, K. Chatttopadhyay, K. Shinnod, B. Jeyadevan, K. Nakatsuka, T. Furubayashi, I. Nakatani, Physical Review B 63 (2001) 184108.
[15] B. Martinez, X. Obradors, L. Balcells, A. Rouanet, C. Monty, Physical Review Letters 80 (1997) 181.
[16] G. Gavoille, J. Hubsch, I. Mirebeau, Journal of Magnetism and Magnetic Materials 171 (1997) 291.
[17] T.A. Anhøj, B. Bilenberg, B. Thomsen, C.D. Damsgaard, H.K. Rasmussen, C.S. Jacobsen, J. Mygind, S. Mørup, Journal of Magnetism and Magnetic Materials 260 (2003) 115.
[18] J.M.D. Coey, Physical Review Letters 27 (1971) 1140.
[19] A.H. Morrish, K. Haneda, Journal of Magnetism and Magnetic Materials 35 (1983) 105.
[20] C.E. Patton, Y. Liu, Journal of Physics C: Solid State Physics 16 (1983) 5995.
[21] P.G. Bercoff, H.R. Bertorello, Journal of Magnetism and Magnetic Materials 213 (2000) 56.
[22] C.J. Serna, F. Bødker, S. Mørup, M.P. Morales, F. Sandiumenge, S. Veintemillas-Verdaguer, Solid State Communications 118 (2001) 437.
[23] S. Chkoundali, S. Ammer, N. Jouini, F. Fiévet, P. Molinié, M. Danot, F. Villain, J.-M. Grenèche, Journal of Physics: Condensed Matter 16 (2004) 4357.
[24] A.G. Roca, D. Niznansky, J. Poltierova-Vejpravova, B. Bittova, M.A. González-Fernández, C.J. Serna, M.P. Morales, Journal of Applied Physics 105 (2009) 114309.
[25] A.E. Berkowitz, R.H. Kodama, S.A. Makhlouf, F.T. Parker, F.E. Spada, E.J. McNiff Jr., S. Foner, Journal of Magnetism and Magnetic Materials 196-197 (1999) 591.
[26] S. Mørup, Journal of Magnetism and Magnetic Materials 266 (2003) 110.
[27] E. Tronc, P. Prené, J.P. Jolivet, J.L. Dormann, J.M. Grenèche, Hyperfine Interactions 112 (1998) 97.
[28] Ö. Helgason, H.K. Rasmussen, S. Mørup, Journal of Magnetism and Magnetic Materials 302 (2006) 413.
[29] D. Peddis, M.V. Mansilla, S. Mørup, C. Cannas, A. Musino, G. Piccaluga, F. D'Orazio, F. Lucari, D. Fiorani, Journal of Physical Chemistry B 112 (2008) 8507.
[30] R.D. Desautels, E. Skoropata, J. van Lierop, Journal of Applied Physics 103 (2008) 07D512.

Review Article

Spin Structures in Magnetic Nanoparticles

Steen Mørup,[1] Erik Brok,[1,2] and Cathrine Frandsen[1]

[1] *Department of Physics, Technical University of Denmark, 2800 Kongens Lyngby, Denmark*
[2] *Center for Electron Nanoscopy, Technical University of Denmark, 2800 Kongens Lyngby, Denmark*

Correspondence should be addressed to Cathrine Frandsen; fraca@fysik.dtu.dk

Spin structures in nanoparticles of ferrimagnetic materials may deviate locally in a nontrivial way from ideal collinear spin structures. For instance, magnetic frustration due to the reduced numbers of magnetic neighbors at the particle surface or around defects in the interior can lead to spin canting and hence a reduced magnetization. Moreover, relaxation between almost degenerate canted spin states can lead to anomalous temperature dependences of the magnetization at low temperatures. In ensembles of nanoparticles, interparticle exchange interactions can also result in spin reorientation. Here, we give a short review of anomalous spin structures in nanoparticles.

1. Introduction

The magnetic properties of nanoparticles differ in many respects from those of the corresponding bulk materials [1]. In very small magnetic particles, the magnetization direction is not fixed but fluctuates at finite temperatures, and the magnetization may spontaneously be reversed (superparamagnetic relaxation) above the blocking temperature [2, 3]. At low temperatures, the spin wave excitations are dominated by the uniform mode ($q = 0$ spin waves), resulting in a linear temperature dependence of the magnetization in contrast to the Bloch $T^{3/2}$ law valid for bulk materials [4]. In several studies, it has been found that the saturation magnetization of nanoparticles of ferrimagnetic materials is smaller than the bulk value. This can in many cases be explained by spin canting, that is, noncollinear spin structures. The reduced number of magnetic neighbor ions around surface atoms can lead to magnetic frustration, which results in canted spin structures in materials with otherwise collinear spin structures [5, 6]. Near the surface, the low local symmetry can result in a large contribution to the local magnetic anisotropy, which also can influence the spin orientations. Both in nanoparticles and in bulk materials, defects in the interior, such as diamagnetic substitution or cation vacancies, can also lead to noncollinearity [7]. In materials with spin canting there may be different canted states that are separated by

very low energy barriers [7]. Therefore, magnetic fluctuations can take place at very low temperatures. Freezing of the spins can result in an anomalous temperature dependence of the magnetization at low temperatures. Moreover, exchange interaction between surface atoms of neighboring particles can have a profound influence on the magnetic properties because this can affect both the superparamagnetic relaxation [8–10] and the spin structure [9, 11]. For many applications of magnetic nanoparticles, a large saturation magnetization is desirable, and it is therefore important to control and minimize spin canting. In this paper, we present a short review on spin structures in magnetic nanoparticles.

2. Theoretical Models for Spin Canting

Canted spin structures at surfaces and around defects in the interior of a material are in general very complex, and analytical calculations of the magnetic properties may therefore not be feasible, but the spin structures can be elucidated by use of computer simulations. Kodama et al. [12] have performed computer simulations of the spin structure of 2.5 nm nanoparticles of the inverse spinel $NiFe_2O_4$. In the simulations, the magnetic anisotropy was neglected and it was assumed that the interior of the particles was defect-free. Therefore, there is only spin canting near the surface. Figure 1 shows a calculated spin structure for a (111) plane
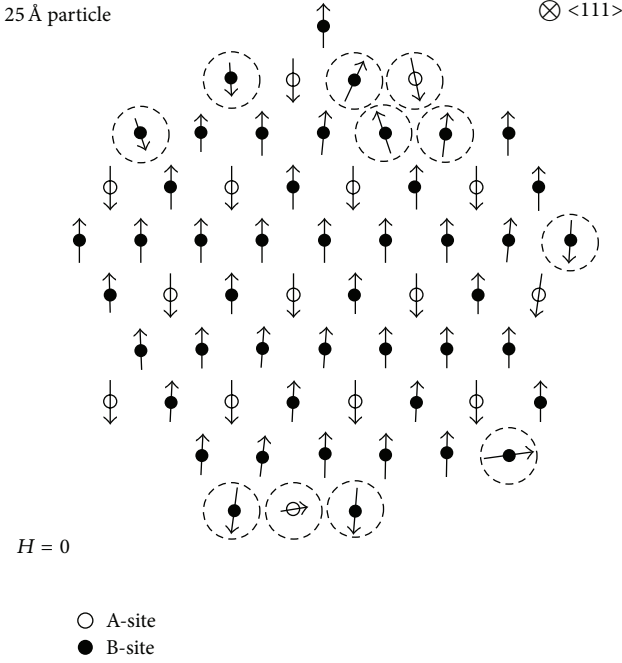
25 Å particle $\otimes$ <111>

$H = 0$

○ A-site
● B-site

Figure 1: Calculated spin structures for a (111) cross-section of a 2.5 nm NiFe$_2$O$_4$ particle. Reproduced with permission from Kodama et al. [12].
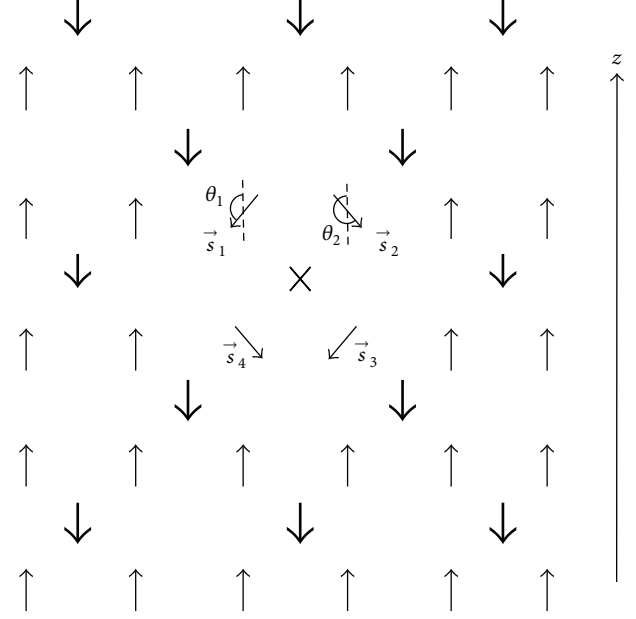

Figure 2: Schematic illustration of a canted two-dimensional spin structure. The bold arrows correspond to A-site spins and the other arrows correspond to B-site spins. The cross represents a missing A-site spin. Reproduced with permission from Jacobsen et al. [14].

of a 2.5 nm NiFe$_2$O$_4$ particle. Highly misoriented spins are indicated by dashed circles. It is noteworthy that some of the surface spins are completely reversed. The simulations also showed that different canted states commonly are separated by very low energy barriers. If surface anisotropy is included in the model, more surface spins will be strongly canted [13].

In very simple cases, analytical calculations of spin structures around defects and at surfaces can be performed. Although simple, these calculations show at least qualitatively that the magnetization may increase or decrease in an anomalous way at low temperatures. Figure 2 shows a simple two-dimensional canted spin structure, which allows obtaining analytical solutions for the spin directions and the temperature dependence of the magnetization by use of a classical model [7, 14]. In the model, spins at A-sites and B-sites are antiparallel in the defect-free structure. The bold arrows in Figure 2 represent A-site spins and the remaining arrows represent B-site spins. The cross represents a missing A-site spin, which can give rise to magnetic frustration and canting of neighboring B-site spins. In the calculations, the magnetic anisotropy and canting of next nearest spins are neglected. For symmetry reasons, the angles between the spins and the z-direction are assumed to be pairwise identical. The magnetic energy can then be written [7, 14]:

$$E\left(\theta_1, \theta_2\right) = a\left(\cos\theta_1 + \cos\theta_2\right) + b\cos\left(\theta_1 - \theta_2\right), \quad (1)$$

where θ_1 and θ_2 are defined in the figure, $a = 4\lambda_{BB} - 2\lambda_{AB} + 2\lambda_L - 2\mu B$, and $b = 4\lambda_{BB}$. Here, λ_{BB} is the exchange parameter for nearest neighbor B-B coupling, λ_{AB} is the exchange parameter for nearest neighbor A-B coupling, and λ_L is the exchange parameter for the exchange interaction between a

B-site ion and all more distant ions. μ is the magnetic moment of a B-site ion, and B is the applied magnetic field, defining the z-direction.

By differentiating (1), one can find the spin orientations, which give minimum energy. Calculations have been performed for $b/k_B = 200$ K (k_B is Boltzmann's constant) and values of a/b between 1.1 and 1.9 [14]. Energy minima are found for $\sin\theta_1 = -\sin\theta_2$ and $\cos\theta_1 = \cos\theta_2 = -a/2b$ with energy $E_{\min} = -b - a^2/2b$. They are separated by maxima at $\theta_1 = \theta_2 = 180°$ with $E(180°, 180°) = -2a + b$. A more comprehensive discussion of the energy maxima and minima in simple canted spin structures is given in [7].

For arbitrary values of θ_1, the values of θ_2, which minimize the energy, are given by [14]

$$tg\theta_2 = \frac{b\sin\theta_1}{a + b\cos\theta_1}, \quad (2)$$

and the magnetic energy as a function of the angle θ_1 is given by [14]

$$E\left(\theta_1\right) = a\cos\theta_1 - \sqrt{a^2 + b^2 + 2ab\cos\theta_1}. \quad (3)$$

Figure 3 shows the magnetic energy as a function of θ_1 for values of a/b between 1.1 and 1.9. At very low temperatures, the system is found in an energy minimum, but at higher temperatures, the spin may perform transverse relaxation, that is, fluctuations of the spin directions across the energy barrier at $\theta_1 = 180°$. For $1.7 \leq a/b < 2.0$, the height of the energy barrier is less than 10 K, and transverse relaxation may therefore take place at very low temperatures.

In general, the average value of the z component of the magnetic moment is given by $\langle M^z(T) \rangle = 2\mu\langle\cos\theta_1 + \cos\theta_2\rangle$,
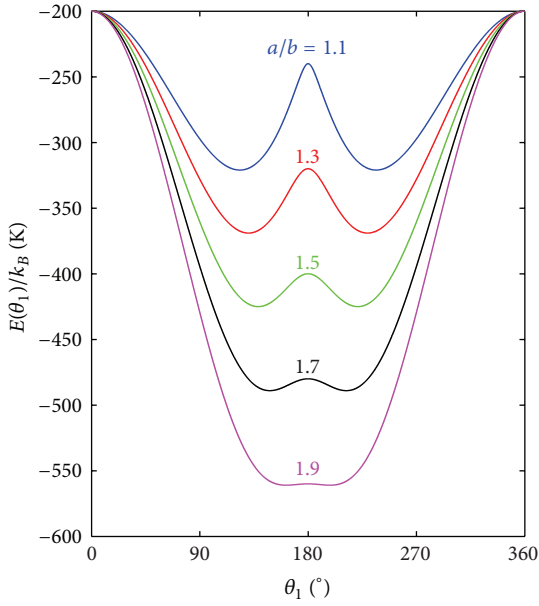
FIGURE 3: The energy of the canted spin structure, shown in Figure 2, as a function of the angle θ_1 for the indicated values of a/b. The calculations were carried out using (3) with $b/k_B = 200$ K. Reproduced with permission from Jacobsen et al. [14].
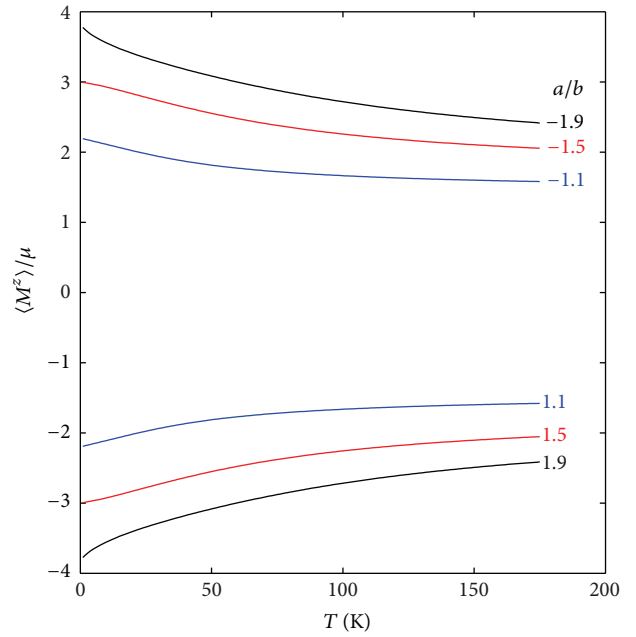

FIGURE 4: Temperature dependence of the thermal average of the canted spin structure, shown in Figure 2. The calculations were carried out using Boltzmann statistics for $b/k_B = 200$ K and the indicated values of a/b. Reproduced with permission from Jacobsen et al. [14].

where μ is the magnetic moment of a single atom. The temperature dependence of $\langle M^z(T) \rangle$ for values of a/b between 1.1 and 1.9 and between -1.1 and -1.9 calculated by use of Boltzmann statistics is shown in Figure 4. At low temperatures, the thermal average of the magnetic moment increases or decreases rapidly with decreasing temperature. Several experimental studies of ferrimagnetic nanoparticles have shown anomalous temperature dependencies of the magnetization at low temperatures that are in accordance with this model [12, 17–24]. A quantum mechanical calculation gives results that are qualitatively similar to those of the classical model [14].

3. Experimental Studies of Spin Canting

Mössbauer spectroscopy in large applied magnetic fields is a very useful method to investigate spin canting in ferrimagnetic materials [5, 6]. The magnetic hyperfine splitting in Mössbauer spectra is proportional to the total magnetic field at the nucleus, B_{tot}, which has contributions from the hyperfine field, B_{hf}, and the applied field, B_{app}, and can be found from the relationship

$$B_{\text{hf}}^2 = B_{\text{tot}}^2 + B_{\text{app}}^2 - 2B_{\text{tot}}B_{\text{app}} \cos \theta, \tag{4}$$

where θ is the angle between the direction of the total magnetic field at the nucleus and the gamma ray direction. The relative areas of the six lines of a ^{57}Fe Mössbauer spectrum of a magnetic material depend on the angle θ as the relative areas are given by $3:p:1:1:p:3$, where

$$p = \frac{4 \sin^2 \theta}{2 - \sin^2 \theta}. \tag{5}$$

In polycrystalline ferrimagnetic materials in zero applied field with random orientation of the crystallites, the orientations of the sublattice magnetization directions are random, and the relative areas are then $3:2:1:1:2:3$. If a large magnetic field is applied parallel to the gamma ray direction, the sublattice magnetization directions of a collinear ferrimagnetic material will be parallel and antiparallel to this direction, resulting in zero intensity of lines 2 and 5. However, in nanoparticles of ferrimagnetic materials, these two lines usually have nonzero intensity because of spin canting. In several publications, it has been suggested that this spin canting is located at the surface, because the reduced number of magnetic neighbor ions at the surface can result in magnetic frustration. However, in other studies it has been found that the canting does not vary with particle size in a regular way [25–27]. This strongly suggests that canting is not only a surface effect but also commonly occurs around defects in the interior of the particles [25–27].

As an example, Figure 5 shows a Mössbauer spectrum of magnetic Dynabeads, consisting of 1 μm porous polymer beads containing 7.7 nm maghemite (γ-Fe$_2$O$_3$) particles in the pores. Such beads are used, for example, for preparation and handling of biological materials, and a large saturation magnetization of the maghemite particles is essential for the performance. The saturation magnetization of the maghemite particles in the beads was 336 kA m^{-1} [28], which is about 10% less than the bulk value. The Mössbauer spectrum, shown in Figure 5, was obtained at 6.0 K with a magnetic field of 6.0 T applied parallel to the gamma ray direction. The spectrum
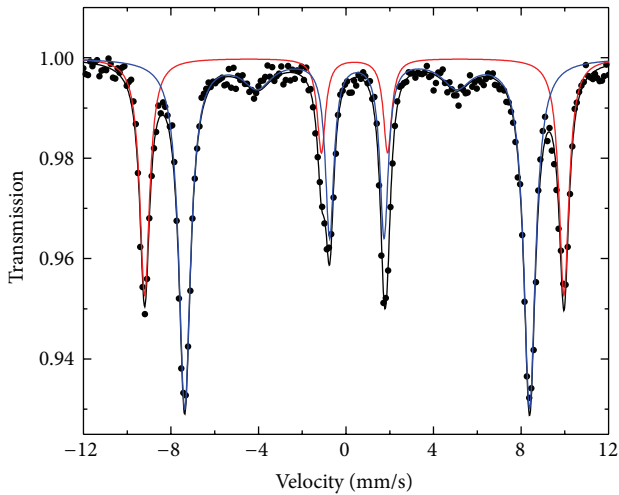
Figure 5: Mössbauer spectrum of $1\,\mu$m magnetic Dynabeads, containing 7 nm maghemite (γ-Fe_2O_3) nanoparticles. The spectrum was obtained at 6 K with a magnetic field of 6 T applied parallel to the gamma ray direction. The red and blue fit lines represent Fe^{3+} in A- and B-sites, respectively.

was fitted with two sextets, corresponding to iron in the A-sites (red fit lines) with a total field of 59.4 T and B-sites (blue fit lines) with a total field of 48.9 T. The intensity of lines 2 and 5 of the A-site component is negligible, whereas the relative areas of lines 2 and 5 for the B-site component were $p \approx 0.55$, corresponding to an average canting angle, $\theta \approx 29°$ for the B-site spins. These results show that there is essentially no canting in A-sites but some canting in B-sites. The canting can affect all B-site ions or be restricted to a fraction of B-site spins with large canting angles, but the data can explain at least qualitatively the reduced value of the saturation magnetization compared to the bulk value.

A study of the temperature dependence of the spin structure has been made for 7 nm maghemite particles [15]. The Mössbauer spectra of the sample, shown in **Figure 6**, were obtained at the indicated temperatures with a magnetic field of 4 T applied parallel to the gamma ray direction. At low temperatures, lines 2 and 5 have nonzero intensity indicating the presence of spin canting. The best fits of the spectra were obtained with three sextets, two of which had zero intensity of lines 2 and 5, corresponding to iron in the tetrahedral A-and the octahedral B-sites of the spinel structure with a perfect collinear ferrimagnetic structure. The third sextet with nonzero intensity of lines 2 and 5 had an isomer shift indicating that it was mainly due to iron in the octahedral B-sites. Thus, the data indicate that the canting only affects a fraction of the B-site spins, whereas the remaining B-site spins and the A-site spins are essentially not affected by the canting. Sextets 1 and 2 had relatively narrow lines at all temperatures, but sextet 3 showed a substantial line broadening and a decreasing relative area of lines 2 and 5 with increasing temperature. Similar results have been found in studies of 2.7 nm and 4.6 nm maghemite particles [29]. This temperature dependence can be explained by transverse relaxation between canted states, characterized by canting
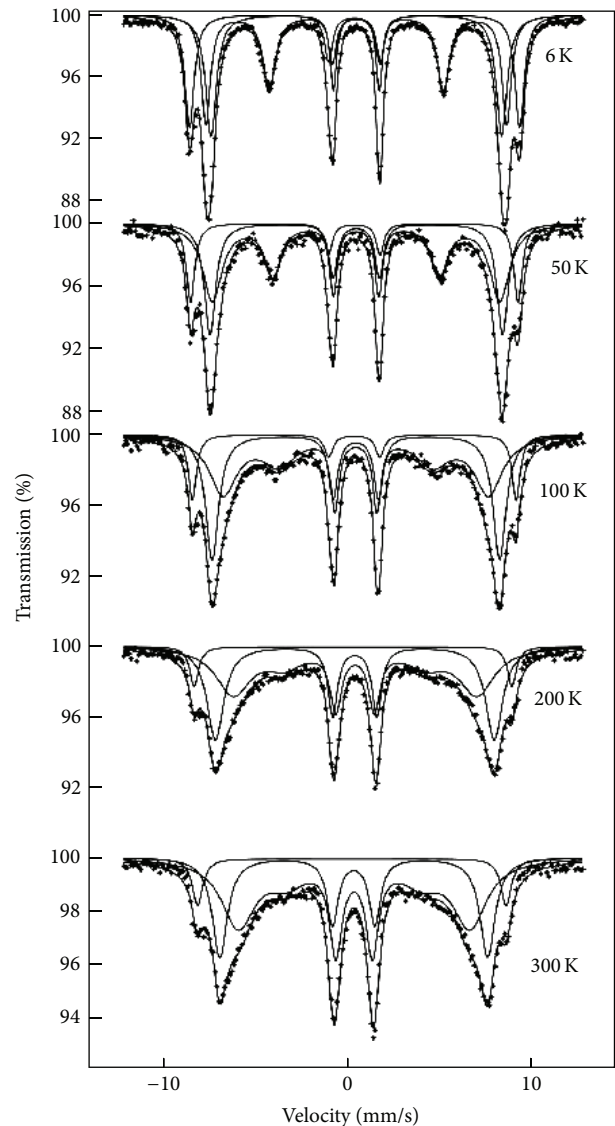
Figure 6: Mössbauer spectra of 7.7 nm maghemite (γ-Fe_2O_3) particles. The spectra were obtained at the indicated temperatures with a magnetic field of 4 T applied parallel to the gamma ray direction. Reproduced with permission from Helgason et al. [15].

angles θ_c and $-\theta_c$. At very low temperatures, the spins are fixed in one of two energy minima (curves plotted in **Figure 3** for the simple canted structure shown in **Figure 2**). When the temperature is increased, relaxation takes place between the two minima and this results in line broadening, and for very fast relaxation, the nucleus only experiences the average field that is parallel (or antiparallel) to the applied field and the gamma ray direction. Similar data have been found in studies of diamagnetically substituted bulk ferrimagnets such as $Mn_{0.25}Zn_{0.75}Fe_2O_4$ [30] and $Li_{1.125}Ti_{1.25}Fe_{0.625}O_4$ [31].

When the transverse relaxation is fast, the magnitude of the average hyperfine field will be given by $B_0 \langle \cos \theta \rangle$. The fits of the spectra in **Figure 6** show that the relative intensity of lines 2 and 5 of sextet 3 does not disappear completely even
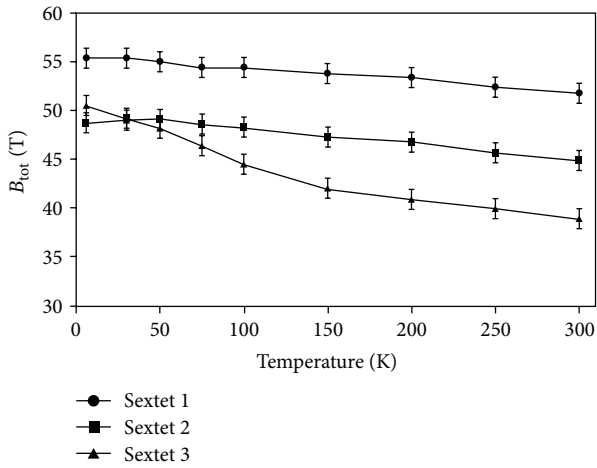
FIGURE 7: Temperature dependence of the total magnetic field at the nuclei, obtained from fits of the spectra shown in Figure 6. Reproduced with permission from Helgason et al. [15].

at 300 K indicating relaxation times of the same order of magnitude as the time scale of Mössbauer spectroscopy. The temperature dependence of the magnetic hyperfine fields of the three sextets is shown in Figure 7. For sextets 1 and 2, the hyperfine fields decrease by a few percent when heating up to 300 K. This is similar to the behavior of bulk maghemite. However, the hyperfine field of sextet 3 decreases much faster with increasing temperature, in accordance with the model for transverse relaxation of the canted spins and the overall temperature dependence of the particle magnetization.

4. Spin Reorientation due to Interparticle Interactions

Magnetic interactions between nanoparticles can have a large influence on the magnetic properties. Magnetic dipole interactions between ferromagnetic or ferrimagnetic nanoparticles can significantly affect the superparamagnetic relaxation time [10]. Nanoparticles of antiferromagnetic particles usually have a finite magnetic moment because of uncompensated spins, but this moment is typically so small that the dipole interactions are insignificant [8]. However, if antiferromagnetic nanoparticles are in close proximity, the superparamagnetic relaxation can be suppressed because of exchange interactions between surface atoms of neighboring particles [8, 10]. Such exchange interactions can in some cases also have a strong influence on the spin structure [9, 11, 16]. This can conveniently be investigated by Mössbauer spectroscopy studies. In hematite (α-Fe$_2$O$_3$) nanoparticles, the magnitude and the sign of the quadrupole shift depend on the angle θ_0 between the [001] direction of the hexagonal structure and the magnetic hyperfine field. The quadrupole shift is given by [11]

$$\varepsilon = \frac{\varepsilon_0 \left(3\cos^2\theta_0 - 1 \right)}{2}, \tag{6}$$

where $\varepsilon_0 = 0.20$ mm/s. In bulk hematite, $\theta_0 = 0°$ below the Morin transition temperature at $T \approx 263$ K, whereas $\theta_0 = 90°$ above this temperature, such that $\varepsilon = -0.10$ mm/s. However, in noninteracting hematite nanoparticles with dimensions below ~20 nm, $\theta_0 = 90°$ at all temperatures, but interparticle interactions can change the spin orientation [11]. In a recent study of α-Fe$_2$O$_3$/NiO nanocomposites [16], it was found that interactions between the hematite and nickel oxide nanoparticles can have a very strong influence on the spin orientation in the hematite nanoparticles. Figure 8(a) shows Mössbauer spectra of noninteracting 8 nm hematite particles, and Figure 8(b) shows Mössbauer spectra of hematite nanoparticles from the same batch, but interacting with NiO nanoparticles. At the lowest temperatures, the difference in quadrupole shift of the hematite nanoparticles in the two samples is easily measurable. Fitting the spectra of noninteracting hematite nanoparticles (Figure 8(a)) provides a spin angle of $\theta_0 = 90°$ for all particles. The spectra of the hematite nanoparticles interacting with NiO (Figure 8(b)) were well fitted with two sextets. The quadrupole shifts of the two sextets as a function of temperature are shown in Figure 9. For sextet 1, the quadrupole shift is around + 0.16 mm/s corresponding to $\theta_0 = 21°$, whereas sextet 2 has a quadrupole shift of 0.08 mm/s corresponding to $\theta_0 = 39°$. This clearly shows that the spin angle deviates significantly from that of noninteracting particles where $\theta_0 = 90°$, but we note that the bimodal distribution of spin angles ($\theta_0 = 21°$, $\theta_0 = 39°$) may be a consequence of the fitting procedure using only two sextets. With increasing temperature, the quadrupole shifts of both sextets decrease; that is, the spin angle θ_0 increases. Neutron diffraction studies of the samples confirmed the Mössbauer data and furthermore found that the spin angle is the same within each particle (i.e., no domain formation) [16].

The data can be at least qualitatively understood by considering the interaction between the two particles shown in Figure 10. The magnetic energy of the two particles may be written as

$$E\left(\theta_p, \theta_q\right) = K_p V_p \sin^2\theta_p + K_q V_q \sin^2\theta_q$$
$$- J_{\text{eff}} M_p M_q \cos\left(\alpha - \theta_p - \theta_q\right). \tag{7}$$

The first two terms represent the anisotropy energies of particles p and q, respectively, where K_p and K_q are the anisotropy constants, V_p and V_q the volumes, and θ_p and θ_q the angles between the sublattice magnetizations and the easy axes of the particles. The last term comes from the effective exchange interaction between the particles p and q where J_{eff} is the exchange coupling constant between the sublattice magnetizations, M_p and M_q, of the particles p and q, and α denotes the angle between the easy axes $\vec{e}_p$ and $\vec{e}_q$. Because of the exchange interaction at the interface, the sublattice magnetization directions $\vec{M}_p$ and $\vec{M}_q$ are rotated by the angles θ_p and θ_q, respectively. For an arbitrary value of θ_p the minimum energy is found for

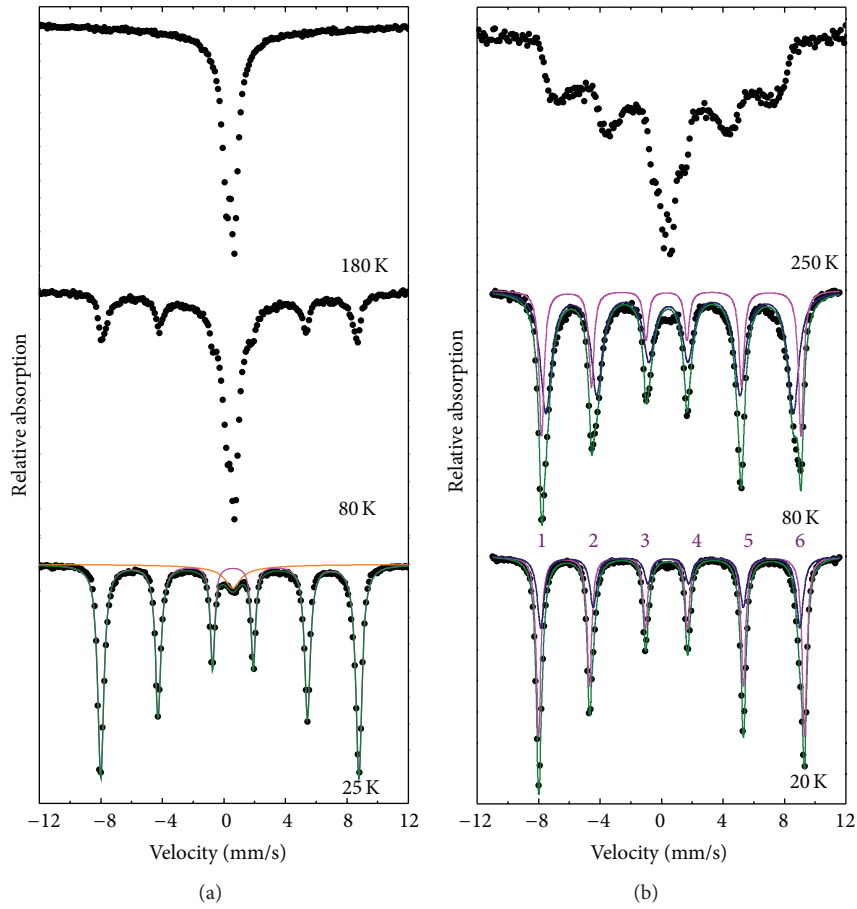$$\sin 2\theta_q = \frac{K_p V_p}{K_q V_q} \sin 2\theta_p. \tag{8}$$

(a)

(b)

FIGURE 8: Mössbauer spectra of 8 nm hematite (α-Fe$_2$O$_3$) nanoparticles obtained at the indicated temperatures. (a) Noninteracting hematite particles coated with oleic acid and in aqueous suspension. (b) Hematite particles mixed with NiO. The spectra of the α-Fe$_2$O$_3$/NiO nanocomposite were fitted with two sextets, as shown in panel (b). Reproduced with permission from Frandsen et al. [16].
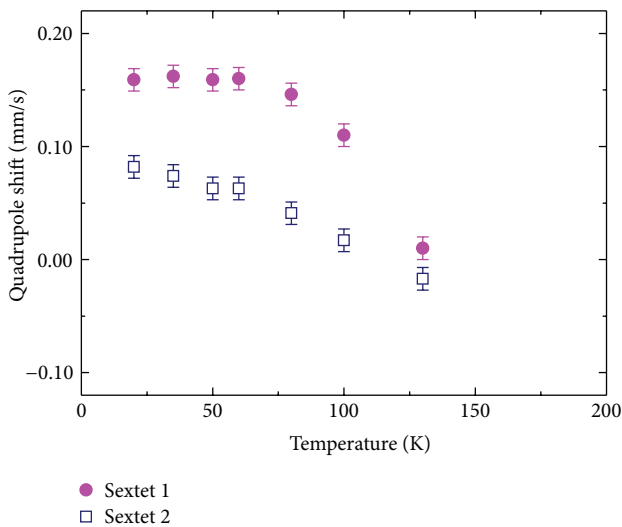

● Sextet 1
□ Sextet 2

FIGURE 9: Temperature dependence of the quadrupole shift of the two sextet components shown in Figure 8(b). Reproduced with permission from Frandsen et al. [16].

To illustrate the effects of interactions, we here consider the simple case where $K_p V_p = K_q V_q \equiv KV$ for which one can find an analytical solution for the rotation angle $\theta_p = \theta_q \equiv \theta_r$

$$\cot 2\theta_r = \frac{KV}{E_{\text{int}} \sin \alpha} + \cot \alpha, \tag{9}$$

where $E_{\text{int}} = J_{\text{eff}} M_p M_q$. If the easy axes of the two particles are parallel ($\alpha = 0°$), one finds that $\theta_r = 0°$ irrespective of the strength of the interaction energy. However, a large interaction energy compared to the anisotropy in combination with a large value of the angle α results in a large rotation angle, θ_r, at low temperatures. At higher temperatures, the sublattice magnetization directions perform fast fluctuations around the directions corresponding to the energy minima [1, 8, 10]. Therefore, M_p and M_q should be replaced by the thermal averages $\langle M_p \rangle$ and $\langle M_q \rangle$ such that the interaction energy is given by $E_{\text{int}} = J_{\text{eff}} \langle M_p \rangle \langle M_q \rangle$. With increasing temperature, $\langle M_p \rangle$ and $\langle M_q \rangle$ decrease leading to an increase of $\cot 2\theta_r$, that is, a decrease of the spin rotation angle. Such a mechanism
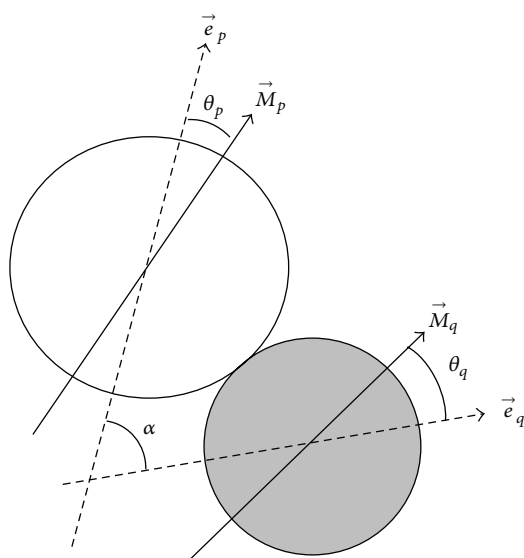
FIGURE 10: Schematic illustration of two interacting nanoparticles with easy axes $\vec{e}_p$ and $\vec{e}_q$ and sublattice magnetization directions $\vec{M}_p$ and $\vec{M}_q$. α is the angle between the two easy axes, and θ_p and θ_q denote the angles between the easy axes and the sublattice magnetization of the two particles. Reproduced with permission from Frandsen et al. [16].

can qualitatively explain the temperature dependence of the reorientation angle.

Also, in samples of interacting hematite particles, a spin reorientation has been observed, but the effect is smaller than that in the α-Fe$_2$O$_3$/NiO nanocomposite [11].

5. Conclusions

Theoretical and experimental studies of magnetic nanoparticles show that the spin structures often differ from those of perfect bulk materials. The low symmetry around surface atoms and around defects in the interior of the particles can lead to localized spin canting, and also thermal fluctuations between almost degenerate spin states may take place even at low temperature. This can lead to anomalous magnetization behaviors of nanoparticles. Furthermore, exchange interactions between surface atoms of neighboring nanoparticles in close proximity can result in reorientation of the sublattice magnetization directions in the whole particles.

Conflict of Interests

The authors declare no conflict financial of interests.

Acknowledgment

References

[1] S. Mørup, M. F. Hansen, and C. Frandsen, "Magnetic nanoparticles," in *Comprehensive Nanoscience and Technology*, D. Andrews, G. Scholes, and G. Wiederrecht, Eds., vol. 1, pp. 437–491, Elsevier, 2011.

[2] L. Néel, "Théorie du traînage magnétique des ferromagnétiques en grains fins avec applications aux terres cuites," *Annales Geophysique*, vol. 5, pp. 99–136, 1949.

[3] W. F. Brown, "Thermal fluctuations of a single-domain particle," *Physical Review*, vol. 130, p. 1677, 1963.

[4] S. Mørup, C. Frandsen, and M. F. Hansen, "Uniform excitations in magnetic nanoparticles," *Beilstein Journal of Nanotechnology*, vol. 1, pp. 48–54, 2010.

[5] J. M. D. Coey, "Noncollinear spin arrangement in ultrafine ferrimagnetic crystallites," *Physical Review Letters*, vol. 27, pp. 1140–1142, 1971.

[6] A. H. Morrish and K. Haneda, "Surface magnetic properties of fine particles," *Journal of Magnetism and Magnetic Materials*, vol. 35, p. 105, 1983.

[7] S. Mørup, "Spin-canting and transverse relaxation at surfaces and in the interior of ferrimagnetic particles," *Journal of Magnetism and Magnetic Materials*, vol. 266, p. 110, 2003.

[8] M. F. Hansen, C. Bender Koch, and S. Mørup, "Magnetic dynamics of weakly and strongly interacting hematite nanoparticles," *Physical Review B*, vol. 62, p. 1124, 2000.

[9] C. Frandsen and S. Mørup, "Inter-particle interactions in composites of antiferromagnetic nanoparticles," *Journal of Magnetism and Magnetic Materials*, vol. 266, p. 36, 2003.

[10] S. Mørup, M. F. Hansen, and C. Frandsen, "Magnetic interactions between nanoparticles," *Beilstein Journal of Nanotechnology*, vol. 1, p. 182, 2010.

[11] C. Frandsen and S. Mørup, "Spin rotation in α-Fe$_2$O$_3$ nanoparticles by interparticle interactions," *Physical Review Letters*, vol. 94, Article ID 027202, 2005.

[12] R. H. Kodama, A. E. Berkowitz, E. J. McNiff Jr., and S. Foner, "Surface spin disorder in NiFe$_2$O$_4$ nanoparticles," *Physical Review Letters*, vol. 77, no. 2, pp. 394–397, 1996.

[13] R. H. Kodama and A. E. Berkowitz, "Atomic-scale magnetic modeling of oxide nanoparticles," *Physical Review B*, vol. 59, p. 6321, 1999.

[14] H. Jacobsen, K. Lefmann, E. Brok, C. Frandsen, and S. Mørup, "Temperature dependence of the magnetization of canted spin structures," *Journal of Magnetism and Magnetic Materials*, vol. 324, p. 3218, 2012.

[15] Ö. Helgason, H. K. Rasmussen, and S. Mørup, "Spin-canting and transverse relaxation in maghemite nanoparticles and in tin-doped maghemite," *Journal of Magnetism and Magnetic Materials*, vol. 302, p. 413, 2006.

[16] C. Frandsen, K. Lefmann, B. Lebech et al., "Spin reorientation in α-Fe$_2$O$_3$ nanoparticles induced by interparticle exchange interactions in α-Fe$_2$O$_3$/NiO nanocomposites," *Physical Review B*, vol. 84, Article ID 214435, 2011.

[17] E. Tronc, A. Ezzir, R. Cherkaoui et al., "Surface-related properties of γ-Fe$_2$O$_3$ nanoparticles," *Journal of Magnetism and Magnetic Materials*, vol. 221, p. 63, 2000.

[18] H. Kachkachi, A. Ezzir, M. Nogués, and E. Tronc, "Surface effects in nanoparticles: application to maghemite γ-Fe$_2$O$_3$," *The European Physical Journal B*, vol. 14, p. 681, 2000.

[19] T. N. Shendruk, R. D. Desautels, B. W. Southern, and J. van Lierop, "The effect of surface spin disorder on the magnetism

of γ-Fe$_2$O$_3$ nanoparticle dispersions," *Nanotechnology*, vol. 18, no. 45, Article ID 455704, 2007.

[20] F. T. Parker, M. W. Foster, D. T. Margulies, and A. E. Berkowitz, "Spin canting, surface magnetization, and finite-size effects in γ-Fe$_2$O$_3$ particles," *Physical Review B*, vol. 47, no. 13, pp. 7885–7891, 1993.

[21] K. Mandal, S. Mitra, and P. A. Kumar, "Deviation from Bloch T3/2 law in ferrite nanoparticles," *Europhysics Letters*, vol. 75, no. 4, pp. 618–623, 2006.

[22] D. Peddis, C. Cannas, G. Piccaluga, E. Agostinelli, and D. Fiorani, "Spin-glass-like freezing and enhanced magnetization in ultra-small CoF$_2$O$_4$ nanoparticles," *Nanotechnology*, vol. 21, no. 12, Article ID 125705, 2010.

[23] C. N. Chinnasamy, A. Narayanasamy, N. Ponpandian et al., "Mixed spinel structure in nanocrystalline NiFe$_2$O$_4$," *Physical Review B*, vol. 63, no. 18, Article ID 184108, 2001.

[24] B. Martinez, X. Obradors, L. Balcells, A. Rouanet, and C. Monty, "Low temperature surface spin-glass transition in γ-Fe$_2$O$_3$ nanoparticles," *Physical Review Letters*, vol. 80, p. 181, 1997.

[25] C. J. Serna, F. Bødker, S. Mørup, M. P. Morales, F. Sandiumenge, and S. Veintemillas-Verdaguer, "Spin frustration in maghemite nanoparticles," *Solid State Communications*, vol. 118, no. 9, pp. 437–440, 2001.

[26] S. Chkoundali, S. Ammer, N. Jouini et al., "Nickel ferrite nanoparticles: elaboration in polyol medium via hydrolysis, and magnetic properties," *Journal of Physics: Condensed Matter*, vol. 16, p. 4357, 2004.

[27] A. G. Roca, D. Niznansky, J. Poltierova-Vejpravova et al., "Magnetite nanoparticles with no surface spin canting," *Journal of Applied Physics*, vol. 105, no. 11, Article ID 114309, 2009.

[28] G. Fonnum, C. Johansson, A. Molteberg, S. Mørup, and E. Aksnes, "Characterisation of Dynabeads (R) by magnetization measurements and Mössbauer spectroscopy," *Journal of Magnetism and Magnetic Materials*, vol. 293, p. 41, 2005.

[29] E. Tronc, P. Prené, J. P. Jolivet, J. L. Dormann, and G. M. Grenèche, "Spin canting in γ-Fe$_2$O$_3$ nanoparticles," *Hyperfine Interactions*, vol. 112, p. 97, 1998.

[30] T. A. Anhøj, B. Bilenberg, B. Thomsen et al., "Spin canting and magnetic relaxation phenomena in Mn$_{0.25}$Zn$_{0.75}$Fe$_2$O$_4$," *Journal of Magnetism and Magnetic Materials*, vol. 260, p. 115, 2003.

[31] J. L. Dormann, M. El Harfaoui, M. Noguès, and J. Jove, "Relaxation of the transverse spin component in randomly canted Li-Ti ferrite below T$_N$," *Journal of Physics C*, vol. 20, p. L161, 1987.

Magnetic properties of ultra-small goethite nanoparticles

E. Brok,[1,2] C. Frandsen,[1] D.E. Madsen,[1*] H. Jacobsen,[3] J. O. Birk,[3] K. Lefmann,[3] J. Bendix,[4] K. S. Pedersen,[4] C. Boothroyd,[5] A.A. Berhe,[6] G.G. Simeoni,[7] and S. Mørup[1]

[1]*Department of Physics, Technical University of Denmark, DK-2800 Kgs. Lyngby, Denmark*

[2]*Center for Electron Nanoscopy, Technical University of Denmark, DK-2800 Kgs. Lyngby, Denmark*

[3]*Nano-Science Center, Niels Bohr Institute, University of Copenhagen, DK-2100 Copenhagen Ø, Denmark*

[4]*Department of Chemistry, University of Copenhagen, DK-2100 Copenhagen Ø, Denmark*

[5]*Ernst Ruska-Centrum und Peter Grünberg Institut, Forschungszentrum Jülich, D-52425 Jülich, Germany*

[6]*Life and Environmental Sciences Group, University of California, Merced, CA 95343, USA*

[7]*Forschungsneutronenquelle Heinz Maier-Leibnitz FRM II, Technische Universität München, D-85747 Garching, Germany*

Abstract

Goethite (α-FeOOH) is a common nanocrystalline antiferromagnetic mineral. However, it is typically difficult to study the properties of isolated single-crystalline goethite nanoparticles, because goethite has a strong tendency to form particles of aggregated nanograins often with low-angle grain boundaries. This nanocrystallinity leads to complex magnetic properties that are dominated by magnetic fluctuations in interacting grains. Here we present a study of the magnetic properties of 5.7 nm particles of goethite by use of magnetization measurements, inelastic neutron scattering and Mössbauer spectroscopy. The "ultra-small" size of these particles allows for more direct elucidation of the particles' intrinsic magnetic properties. We find from ac and dc magnetization measurements a significant upturn of the magnetization at very low temperatures most likely due to freezing of spins in canted spin structures. From hysteresis curves we estimate the saturation magnetization from uncompensated magnetic moments to be $\sigma_s = 0.044$ Am^2 kg^{-1} at

room temperature. Inelastic neutron scattering measurements show a strong signal from excitations of the uniform mode ($q = 0$ spin waves) at temperatures of 100- 250 K and Mössbauer spectroscopy studies show that the magnetic fluctuations are dominated by "classical" superparamagnetic relaxation at temperatures above ~170 K. From the temperature dependence of the hyperfine fields and the excitation energy of the uniform mode we estimate a magnetic anisotropy constant of around 1.0×10^5 Jm^{-3}.

1. Introduction

Goethite (α-FeOOH) is a common mineral on Earth [1] and it has also recently been found on Mars [2]. The crystal structure of goethite is orthorhombic with space group *Pnma*. It is antiferromagnetic with a Néel temperature around 400 K [3,4]. Goethite usually forms rod-shaped nanoparticles, which often lack long-range crystalline order, because the particles consist of many grains, typically around 3-7 nm in size, with low-angle grain boundaries [5-7], both when found in nature and when laboratory synthesized. The complex influence of the nanocrystallinity on the magnetic properties of goethite is apparent in Mössbauer spectroscopy studies [5] and the magnetic properties have been the subject of many such studies [4, 5, 8-13].

Usually, Mössbauer spectra of non-interacting magnetic nanoparticles show a superposition of a doublet due to particles with fast superparamagnetic relaxation and a sextet due to particles with slow relaxation. The relative areas of the two components depend on temperature because of the temperature dependence of the superparamagnetic relaxation time. However, inter-particle interactions can have a significant influence on the magnetic dynamics and result in magnetically split Mössbauer spectra with asymmetrically broadened lines at temperatures where non-interacting particles show a quadrupole doublet because of fast superparamagnetic relaxation [14, 15].

Using a mean field model for interacting particles, the magnetic energy, E_p, of a nanoparticle p may be written as a sum of a uniaxial anisotropy term E_p^a and an exchange interaction term, E_p^{int} [14-18]

$$E_p = E_p^a + E_p^{\text{int}} = KV_p\sin^2\theta_p - J_{\text{eff}}^p \vec{M}_p \cdot \langle \vec{M}_p \rangle \tag{1}$$

where V_p is the particle volume, K is the magnetic anisotropy constant, θ_p is the angle between the sublattice magnetization vector and the easy magnetization direction, $\vec{M}_p$ is the sublattice magnetization, $\langle \overrightarrow{M_p} \rangle$ is the average value of the sublattice magnetizations of neighbouring particles and J_{eff}^p is the effective interparticle exchange coupling constant (with dimensions Jm^2A^{-2}). $J_{\text{eff}}^p \langle \vec{M}_p \rangle$ can be considered as an effective interaction field acting on $\vec{M}_p$.

Almost all Mössbauer studies of goethite particles have shown spectra, which consist of sextets with asymmetrically broadened lines, typical for interacting nanoparticles that are influenced by relaxation effects. This is the case even for quite large goethite particles (e.g., rods which are around 100 nm wide and 1000 nm long [10]). The magnetic anisotropy constant is relatively large ($K \approx 5 \times 10^4$ Jm^{-3} [5]) and therefore one might expect that relaxation effects should be negligible at room temperature for particles of this size. However, within the rod-shaped nanoparticles there are usually many defects such as low-angle grain boundaries, dislocations and interstitial water and/or OH^- [5-8,19, 20] that may lead to a reduced magnetic coupling between the grains [5]. Because of the many defects, the magnetic dynamics is dominated by fluctuations of the sublattice magnetization directions in small interacting grains within the particles. In a mean field model, the magnetic energy, E_g, of such a grain g may be written as a sum of a uniaxial anisotropy term, E_g^a, and an exchange interaction term, E_g^{int},

$$E_g = E_g^a + E_g^{\text{int}} = KV_g\sin^2\theta_g - J_{\text{eff}}^g \overrightarrow{M_g} \cdot \langle \overrightarrow{M_g} \rangle \,, \tag{2}$$

where V_g is the grain volume, θ_g is the angle between the sublattice magnetization vector and the easy magnetization direction, $\overrightarrow{M_g}$ represents the sublattice magnetization vector of the grain, $\langle \overrightarrow{M_g} \rangle$ is the average sublattice magnetization of neighboring grains and J_{eff}^g is an effective exchange coupling constant representing the exchange interactions with neighboring grains such that $J_{\text{eff}}^g \langle \vec{M}_g \rangle$ can be considered as an effective interaction field acting on $\vec{M}_g$. This grain model can explain the asymmetric line broadening in the Mössbauer spectra of larger goethite particles [5].

There is usually a large tendency for oriented attachment or nearly oriented attachment of particles and grains in goethite samples [5-7, 19, 20]. Therefore, the interaction field can be considered

approximately parallel to the easy direction of magnetization. Eqs. (1) and (2) may therefore be written in the form [5]

$$E(\theta) \approx KV \sin^2 \theta - J_{\text{eff}} M_0^2(T) b(T) \cos \theta ,$$ (3)

where $M_0(T)$ is the sublattice magnetization and

$$b(T) = \frac{\left|\langle \vec{M}(T) \rangle\right|}{M_0(T)}$$ (4)

is the order parameter. In thermal equilibrium, the order parameter can be calculated by the use of Boltzmann statistics:

$$b(T) = \frac{\int_0^\pi \exp\left(-\frac{E(\theta)}{k_{\text{B}}T}\right) \sin \theta \cos \theta \, d\theta}{\int_0^\pi \exp\left(-\frac{E(\theta)}{k_{\text{B}}T}\right) \sin \theta \, d\theta}.$$ (5)

Eqs. (3) and (5) are a set of coupled equations, which can be numerically solved self-consistently to find the order parameter $b(T)$ [5, 17].

For interacting nanoparticles or grains the relative size of the two terms in Eq. (1) or Eq. (3) is important. If the interaction energy is predominant, there will only be one energy minimum, and the relaxation will then take place between states in this energy well and is expected to be fast [5]. The magnetic hyperfine splitting can therefore be considered to be proportional to $\left|\langle \vec{M}(T) \rangle\right| = M_0(T) b(T)$. If the anisotropy energy is predominant or comparable to the interaction energy, there will be two (non-equivalent) energy minima, which are separated by an energy barrier. In the absence of interactions, there are two equivalent minima and the magnetic dynamics is dominated by "classical" superparamagnetic relaxation with a relaxation time given by [21, 22]

$$\tau = \tau_0 \exp\left(\frac{KV}{k_{\text{B}}T}\right) ,$$ (6)

where τ_0 is on the order of 10^{-9}-10^{-13} s.

Classical superparamagnetic behaviour, i.e. reversals of the sublattice magnetization directions of a particle as a whole, is rarely observed in studies of goethite, because magnetic fluctuations within the exchange-coupled grains are predominant [5]. However, if the particles are sufficiently small and separated such that inter-particle interactions are negligible ($E_p^{\text{int}} \ll E_p^a$), the magnetic dynamics may be dominated by superparamagnetic relaxation of individual particles, and it may then be possible to estimate, for example, the magnetic anisotropy energy by use of Mössbauer spectroscopy and neutron scattering as it has been done in earlier studies of hematite (α-Fe$_2$O$_3$) nanoparticles [16, 23-25]. No previously published studies of goethite particles have included inelastic neutron scattering but recently, Pankhurst *et al*. suggested investigations by this technique to help understand the magnetic properties of goethite [26].

In this paper we present studies of a commercial sample of ultra-small goethite particles before and after low-energy ball-milling together with rock salt (NaCl) nanoparticles. The goethite nanoparticles have an average diameter of around 5.7 nm, but each particle is made up of a few smaller interacting grains (or clusters). We therefore have two types of magnetic interactions in the samples, namely interactions between particles and interactions between grains. The interactions between particles are weak, especially in the ball milled sample, and because the particles are very small the Mössbauer spectra are dominated by classical superparamagnetic relaxation at temperatures above ~170 K in contrast to larger goethite particles in which the magnetic dynamics was dominated by fluctuations in interacting grains. Due to the small particle size and weak inter-particle interaction, we have been able to study more directly the intrinsic magnetic properties of goethite particles by use of Mössbauer spectroscopy, magnetization measurements and inelastic neutron scattering..

2. Experimental details

A goethite powder sample was obtained from the company NanoChemonics Inc. The sample was sold as F-2506 (Blend 07PSL-204). In the following this sample is named G1. Part of G1 was ball-milled with NaCl nanoparticles (weight ratio 1:3) at low intensity (40 rpm) for 48 hours in an agate mill. NaCl nanoparticles, here termed "nano"-salt, were prepared by high-intensity (200 rpm) ball-milling in a WC ball-mill for 24 hours. This sample of goethite ball-milled with "nano"-salt is

named GBM and used as prepared for the neutron scattering, Mössbauer spectroscopy and magnetization measurements, but with the salt washed out for the XRD and TEM measurements.

X-ray diffraction (XRD) over an angular range of 15°-90° was performed, using a Panalytical diffractometer with a Cu anode (λ = 1.54 Å). Rietveld refinement of the orthorhombic *Pnma* structure of goethite was performed using the WINPOW program, a modified version of the LHMP1 program [27]. The least squares refinements were performed with Voigtian peak profiles and the background was modelled with Chebyshew polynomials. Initial structural and atomic parameters were taken from [28].

TEM bright and dark field images of the samples were taken using an FEI Technai T20 G2 microscope with a thermionic LaB_6 filament and an accelerating voltage of 200 kV.

[57]Fe Mössbauer spectroscopy was carried out using conventional constant acceleration spectrometers with sources of [57]Co in rhodium and calibration was carried out using a 12.5 μm foil of α-Fe at room temperature. Spectra obtained at temperatures down to 20 K were recorded in a close cycle helium refrigerator from APD Cryogenics. A spectrum obtained with an applied magnetic field of 6 T was recorded in a liquid helium cryostat with a superconducting coil.

Inelastic neutron scattering measurements were performed at the time-of-flight spectrometer TOFTOF at FRM-2, Munich [29]. A neutron wavelength of 7.0 Å was used, with a chopper speed of 12000 rpm, giving an energy resolution of the elastic line of 10 μeV. Data were taken in a temperature range of 10 K to 300 K using the two samples G1 and GBM. Both samples had a mass of about 2 g and were filled in hollow cylinder Al cans. The typical exposure time was 5 h (8 h) for the G1 (GBM) sample.

AC and DC magnetization measurements were performed with a Quantum Design MPMS-XL magnetometer using a SQUID detector. The sample for the DC magnetization measurements was comprised of 33.06 mg of GBM mixed with 28.65 mg of eicosane. The mixture was heated to

approximately 40°C where eicosane is a liquid. When the sample is cooled the eicosane becomes a solid wax, ensuring that the particles in the sample maintain the original (random) orientation. The sample was loaded in a capsule of gelatine. A sample with a larger amount of goethite (139.4 mg GBM) was prepared in a similar way for the AC measurements. Zero field cooled (ZFC) magnetization measurements were performed in a temperature range from 4.2 K to 300 K in applied fields $\mu_0 H$ = 2.0 mT and 4.8 T. After each ZFC measurement the sample was cooled to 4.2 K and a field cooled (FC) magnetization measurement was performed in the same way as the ZFC. To isolate the contribution to the magnetization coming from the goethite particles we have subtracted the diamagnetic contributions from NaCl, eicosane (wax) and gelatine (capsule) in the ZFC/FC and hysteresis measurements, using the corresponding mass susceptibilities (in 10^{-9} m^3/kg) of -6.4, -10.8 and -6.3, respectively. AC magnetization measurements were performed over the same temperature range with a driving field amplitude of 0.38 mT, at frequencies ranging from 1.0 to 1000 Hz.

The magnetization as a function of applied field (hysteresis loops) was measured in fields over the range between - 5 T and + 5 T at temperatures of 4.2 K and 300 K.

3. Results

3.1. Structural characterization

The XRD patterns of sample G1 and sample GBM (after the "nano"-salt has been washed away) are shown in Fig. 1, together with the refined models. For the G1 sample there are no signs of other phases in the sample than the *Pnma* goethite represented by the model. For GBM, there is, in addition to *Pnma* goethite, an unidentified impurity peak at q=2.85 Å^{-1} which we have included in the refined model. The large and non-uniform background can be ascribed to fluorescence from the Fe atoms in the sample, and probably also to amorphous NaCl residues in sample GBM. The unit cell parameters, a Lorentzian profile broadening parameter, an overall temperature factor, and background parameters were refined. The instrumental broadening was assumed to be Gaussian and was known from measurement of a Si-standard, while the sample broadening was assumed to be Lorentzian. The refined lattice parameters are a=9.954(2) Å, b=3.0248(5) Å, and c=4.618(1) Å, and the weighted-profile-residual (R_{WP}) is 1.69 for sample G1. Assuming the sample broadening is only due to the finite particle size the refinement results in an average particle diameter of 5.9 ± 0.8 nm for sample G1. XRD data of the ball-milled sample GBM, after the "nano"-salt was washed away, showed a very irregular background and XRD data of GBM could not be as satisfactorily refined

as G1. However, the refinement of data from GBM indicated similar line broadening (i.e., particle size) as for sample G1 and the peak positions were in correspondence with the goethite structure.

TEM bright field images show that the G1 sample consists of micrometer-sized aggregates of pseudo-spherical goethite nanoparticles with dimensions around 3 - 5 nm as determined from the morphology of particles at the rim of the aggregates (Fig. 2(a)). From the lattice fringes (Fig. 2(a)) we infer that neighbouring particles have some crystalline alignment, but this is not extending over more than a few particles. This crystalline alignment is confirmed by dark field images (Fig. 2(b)). From dark-field images of the G1 sample, we have measured the size of 57 particles (Fig. 2(c)), and calculated a volume-weighted average particle size to 5.4 ± 1.7 nm. This particle size is in agreement (within uncertainty) with that determined from the XRD data from sample G1. TEM dark field images of the ball-milled sample, GBM, after the "nano"-salt has been washed away, show that the low-energy ball-milling has not significantly altered size and morphology of the goethite nanoparticles (Fig. 2(d)). Thus XRD and TEM data show that the volume weighted particle size is around 5.7 nm. Assuming spherical particle shape, this corresponds to a particle volume close to 100 nm^3.

3.2. Magnetization measurements
3.2.1. ZFC/FC measurements

Figure 3 shows the ZFC/FC measurements for GBM. In the low applied field of μ_0H= 2.0 mT the magnetization curves in the temperature range from about 30 K to 300 K look as expected for nanoparticles undergoing superparamagnetic relaxation. The peak temperature in the ZFC curve is T_P = 130 K. This value depends on the distribution of superparamagnetic blocking temperatures in the sample, and in turn on the particle size distribution as well as the degree of inter-particle interactions [15]. Above a temperature of around 250 K the ZFC and FC curves coincide, indicating that all particles have reached their blocking temperature. An interesting feature in the measurements is the sharp increase of the magnetization below 30 K in both the ZFC and the FC measurements. The magnetization in the FC measurement increases by 3.3 $\times 10^{-3}$ Am^2 per kg goethite from 30 K to 4.2 K. The increase in the ZFC magnetization has nearly the same magnitude (3.0·10^{-3} Am^2/kg). A similar anomalous temperature dependence of the low-temperature magnetization has been observed in several studies of ferrite nanoparticles [30] and may be

explained by freezing of spins in canted spin structures [30]. For the measurements in a strong applied field of $\mu_0 H = 4.8$ T there is no peak in the ZFC curve and the ZFC and FC curves nearly coincide in the whole temperature range. There is an increase in the magnetization below 30 K qualitatively similar to the observations in the 2.0 mT measurements of around 5.4 Am^2/kg both in the ZFC and FC curves.

3.2.2. AC magnetization measurements

The in-phase AC susceptibility (χ') data for GBM are shown in Fig. 4. From the dependence of the peak positions as a function of frequency it was attempted to determine τ_0 and *KV* by plotting ln*(ω)* vs. the reciprocal peak temperature (ω is the angular frequency) and fitting a straight line. This method has been demonstrated, for example, in [31]. However the fit resulted in an unreasonable value of τ_0 (on the order of 10^{-26} s), indicating that the temperature dependence of the relaxation time is not in accordance with Eq. (6), presumably because of inter-particle and/or inter-grain interactions. The increase in magnetization at low temperatures seen in the ZFC/FC measurements is also seen in the in-phase AC-susceptibility and is largely independent on the frequency of the driving field. A similar increase in the AC magnetization of goethite nanoparticles at low temperatures has recently been observed by Pankhurst *et al*. [26]. We also measured the out-of-phase signal (χ''), but the signal was very weak. There was no increase in χ'' at low temperatures.

3.2.3. Hysteresis measurements

Hysteresis loops in fields up to $\mu_0 H = 5$ T were measured for the GBM sample at 4.2 K and 300 K. The 300 K hysteresis loop is shown in Figure 5. At 300 K there is no hysteresis within the experimental uncertainty (i.e. the remanence is less than about 0.003 Am^2/kg and the coercive field is less than a few mT). The hysteresis loop at 4.2 K is shown in the lower insert in Figure 5. There is only a very weak hysteresis, with a remanence of approximately 0.015 Am^2/kg and a coercive field of about 5 mT. For the 300 K data the branches of the hysteresis loop were well approximated by a straight line at fields higher than about 2 T. A straight line was fitted to the points at higher fields and subtracted from the hysteresis curve in order to see the response of the uncompensated magnetic moment as demonstrated in Refs. 26 and 32. This is shown in the upper insert in Figure 5, where the step in the magnetization corresponds to a saturation specific magnetization of $\sigma_s = 0.044$ Am^2 kg^{-1} of goethite in the sample. The magnetization saturates in an applied field of approximately

0.2 T. For the 4.2 K hysteresis measurement (lower insert in Fig. 5) the points at higher fields could not be fitted well with a straight line, indicating that there is some unsaturated moment. This may be related to the rise in magnetization at low temperatures seen in the ZFC/FC curves.

3.3. Neutron scattering

Inelastic neutron scattering data for G1 and GBM at 10-300 K are shown in Fig. 6 as intensity maps of the neutron momentum transfer, q, vs. the neutron energy transfer, ε. Around q-values of 1.258 Å^{-1} and 1.502 Å^{-1}, corresponding to the (002) and (101) diffraction peaks, inelastic signals are clearly seen up to a few meV at temperatures of 87-300 K. The magnetic and the chemical unit cells have the same size [3], and hence there are both structural and magnetic contributions to (002) and (101) diffraction peaks. The inelastic signal is, however, most likely of magnetic origin because there is an energy gap between the elastic line and the excitation at temperatures up to about 200 K which then collapses into the elastic line at a temperature of about 300 K. If the signal was originating from lattice dynamics, i.e. phonons, it might also be gapped because of the finite particle size, but the gap would then be expected to remain at temperatures up to the melting point of the sample. The broadening around $\varepsilon =0$ is expected to be due to superparamagnetic relaxation and the strong satellite peak around an energy transfer of 1.0-1.5 meV a signature of excitations of the uniform mode ($q=0$ spin waves) as seen in previous studies of antiferromagnetic (e.g., hematite) nanoparticles [16, 24]. Although the signals from the two magnetic q-values partially overlap, we perform a separate treatment of the intense $q=1.258$ Å^{-1} signal and assume that all inelastic signal has a magnetic origin.

Figure 7 shows the energy transfer at $q=1.258$ Å^{-1} at 100-300 K for samples G1 and GBM. The data for GBM have a low signal to noise ratio because the sample was diluted with NaCl. If all particles were identical and non-interacting, the energy dependence of the magnetic signal would consist of one quasi-elastic peak centered at $\varepsilon=0$ and two side peaks at energy $\pm\varepsilon_0$. The quasi-elastic peak would have a width and shape determined by the instrumental resolution and the superparamagnetic relaxation time, while the side peaks have an intrinsic broadening due to its damped harmonic oscillator (dho) nature [24]. However, in practice there will be additional broadening due to a distribution of uncompensated spins [33] and interparticle interactions [16] leading to a distribution of excitation energies.   In the data for samples G1 and GBM the side peaks are asymmetrically broadened and can be described as relatively sharp peaks at $\pm\varepsilon_0$ and broader peaks extending to higher energies. We suggest that a fraction of the particles have only weak interactions, giving rise

to the clear satellite peak at ε_0. The broader peaks at higher energies can be attributed to particles with stronger interparticle interactions and/or to magnetic fluctuations in interacting grains, because magnetic interactions result in an increase of the excitation energies [16]. The data are therefore fitted with one Voigtian profile to take account of the (quasi-)-elastic line plus two dho modes to fit the main peak at ε_0 and the scattering at higher energies, respectively. The fits are shown together with the data in Fig. 7. Even though the assumption of only two dho modes to fit the inelastic signal is quite simple, the fit reproduces the observed features reasonably well, including the clear asymmetry with tails extending towards higher energy values. We have used this method consistently in our data analysis for all data from the G1 and GBM samples, except that the inelastic signal is too small in the 10 K data to extract any reliable information. Figure 8 shows the temperature dependence of ε_0, i.e. the energy positions of the sharp peaks, which we attribute to uniform magnetic excitations of non-interacting particles. We found that for sample G1 ε_0 decreases from around 1.38 meV at 100 K to 1.06 meV at 250 K. Correspondingly, for the GBM sample ε_0 decreases from about 1.48 meV at 100 K to 1.03 (3) meV at 250 K. The solid lines in Figure 8 are fits of the data at temperatures below 300 K to the theoretical model developed by Würger [34] in which the temperature dependence of the excitation energy is given by

$$\varepsilon_0 = \varepsilon_0(T=0)\sqrt{1-\frac{k_\mathrm{B}T}{KV}} \qquad (k_\mathrm{B}T < KV). \tag{7}$$

The model represents the data well and yields the parameters $\varepsilon_0(T=0) \approx 1.55$ meV and $KV/k_\mathrm{B} \approx 467$ K for G1, and $\varepsilon_0(T=0) \approx 1.68$ meV and $KV/k_\mathrm{B} \approx 417$ K for GBM. With a particle volume of 100 nm^3 this corresponds to a magnetic anisotropy constant of $K \approx 0.6 \times 10^5$ Jm^{-3} for both samples. (In the calculations we have neglected the possible temperature dependence of K). The distinct ε_0-peak has almost disappeared at 300 K (sample G1, Fig. 7), indicating that there is a transition from coherent precession of the sublattice magnetization around an easy axis to incoherent motion, as expected when the thermal energy becomes comparable to the energy barrier [34].

For an isolated nanoparticle of a simple uniaxial antiferromagnetic material, the position of the satellite peak is given by [16, 35]

$$\varepsilon_0 = g\mu_B\left[\sqrt{B_A^2 + B_A B_E(2+\delta) + \frac{B_E^2\delta^2}{4}} - \frac{B_E\delta}{2}\right] \approx g\mu_B\left[\sqrt{2B_A B_E} - \frac{B_E\delta}{2}\right], \tag{8}$$

where $B_A = K/M_0$ is the anisotropy field, K is the magnetic anisotropy constant, M_0 is the sublattice magnetization and B_E is the exchange field. In goethite $B_E \approx 390$ T and $M_0 = 5.25 \times 10^5$ JT^{-1}m^{-3} [36]. δ is a measure of the uncompensated magnetic moment and is defined as $\Delta M/M_0$ where ΔMV is the difference between the magnetic moments of the two sublattices. For an antiferromagnetic nanoparticle with N magnetic ions the uncompensated magnetic moment is expected to be on the order of $N^{1/3}$ if the interior of the particle is free of defects, but surface sites are randomly occupied [15, 37, 38]. Using the saturation magnetization estimated from the magnetization measurements shown in Fig. 5 we find that δ is about 3.6×10^{-4}. The neutron data show that $\varepsilon_0 \approx 1.6$ meV at very low temperatures. Inserting $\varepsilon_0 = 1.6$ meV and $\delta = 3.6 \times 10^{-4}$ in Eq. (7) we find $K \approx 1.3 \times 10^5$ Jm^{-3}. This is same order of magnitude as the values estimated in earlier studies ($K = 6 \times 10^4$ Jm^{-3} [26], $K \approx 3 \times 10^5$ Jm^{-3} [39, 40] and $K > 6 \times 10^4$ Jm^{-3} [41]). The particles in GBM are much smaller than those used for earlier estimates of the magnetic anisotropy constant, and therefore the surface contribution to the magnetic anisotropy is expected to be larger [15, 42].

3.4. Mössbauer spectroscopy

Mössbauer spectra of the samples G1 and GBM, obtained at the indicated temperatures, are shown in Fig. 9 (a) and 9 (b), respectively. At the lowest temperatures the spectra are magnetically split with a magnetic hyperfine field is 49.5 T, an isomer shift of 0.49 mms^{-1} and a quadrupole shift of −0.13 mms^{-1}, which is in accordance with previous Mössbauer studies of goethite particles [4, 39]. There is no indication of impurity phases. Thus the ball-milling of GBM has not affected the chemical state of iron. At higher temperatures, the spectra of G1 and GBM show an asymmetric line broadening, indicating that the magnetic properties are influenced by magnetic fluctuations in interacting grains, as typically seen in goethite. However, already at temperatures of ~220 K and ~170 K the spectra of G1 and GBM collapse to doublets suggesting that the particles exhibit fast superparamagnetic relaxation. It has previously been suggested [12] that such a collapse of the magnetic splitting in Mössbauer spectra of goethite is not due to the onset of fast superparamagnetic relaxation, but a low Néel temperature. We have investigated this possibility by applying a magnetic field to G1 of 6 T at 260 K, i.e. above the temperature where the magnetic splitting has collapsed to a doublet. If the goethite was paramagnetic at this temperature, the spectrum should only show a slight line broadening compared to the zero-field spectrum. However, the spectrum in

Fig. 10 shows a substantial line broadening, corresponding to magnetic hyperfine fields up to around 40 T. This clearly shows that the collapse of the magnetic splitting is not due to a low Néel temperature, but due to fast superparamagnetic relaxation.

The distribution of anisotropy energies and interaction energies in a sample will result in a distribution of magnetic hyperfine fields at finite temperatures. In the superferromagnetism model [4, 17, 18], the values of the anisotropy energy, KV and the interaction energy parameter T_p^0 are free parameters for each quantile, where the quantile, f, is defined as

$$f = \int_0^{B_f(T)} p(B_{\mathrm{hf}}(T)) dB_{\mathrm{hf}} . \tag{9}$$

T_p^0 is defined as the ordering temperature for a sample with zero anisotropy ($KV = 0$) and is given by the expression [4, 5, 17]

$$T_p^0 = \frac{J_{\mathrm{eff}} M_0 (T_p^0)^2}{3k_{\mathrm{B}}} . \tag{10}$$

It has been found that the temperature dependence of quantiles in the hyperfine field distribution $p(B_{\mathrm{hf}}(T))$ in hematite nanoparticles gave values of the magnetic anisotropy energies, which were in accordance with those found for the non-interacting particles [17]. This strongly supports the validity of the model. The interaction energy, $E_i(T) = J_{\mathrm{eff}} M_0(T)^2 b(T)$ depends on temperature, because both $b(T)$ and $M_0^2(T)$ are temperature dependent. As an approximate measure of the interaction energy well below T_{p} we use the value $E_{\mathrm{int}} = 3k_{\mathrm{B}} T_p^0$.

In an earlier Mössbauer study of goethite with particle size on the order of 1800 nm^3 the anisotropy energy KV/k_{B} was found to increase from around 400 K for the 40% quantile to around 1400 K for the 80% quantile [5]. The interaction energy $E_{\mathrm{int}}/k_{\mathrm{B}}$ was on the order of 800 K for all quantiles in the same range. Thus, the interaction energy and the anisotropy energy were on the same order of magnitude in this sample. For a particle with volume of 1800 nm^3 and a magnetic anisotropy constant $K \geq 5 \times 10^4$ Jm^{-3} and $\tau_0 \approx 10^{-11}$ s the relaxation time at 300 K should be on the order of 0.03 s or longer, i.e. much longer than the time scale of Mössbauer spectroscopy. Therefore, the line shape in the Mössbauer spectra could not be explained by fluctuations of the sublattice magnetization in the particle as a whole, but by magnetic fluctuations in small grains within the particles.

For sample G1, the analysis of hyperfine field distributions was only performed at temperatures below 200 K, because the doublet becomes predominant at higher temperatures. The estimated values of KV and T_p^0 for sample G1, obtained from the superferromagnetism model, are shown in Fig. 11. Presumably, the magnetic hyperfine field distribution is influenced by both inter-grain interactions and inter-particle interactions. The total interaction $3T_p^0$ varies between ~400 and 600 K for all fractiles shown in Fig. 11, but a quantification of the two interaction energy contributions is not feasible by the superferromagnetism model. The anisotropy energy, KV, varies from around 200 K to around 1600 K with a value around 500 K for the 50% quantile, and the interaction energy was on the order of 450 K. If we assume that the volume V is the average volume of the particles (~100 nm^3) we find an anisotropy constant $K \approx 0.7 \times 10^5$ Jm^{-3} which is close to that estimated by other methods.

In sample GBM the magnetic hyperfine splitting has almost completely collapsed at a much lower temperature (around 170 K) than in the as-prepared sample, indicating that inter-particle interactions have been reduced by the milling. An analysis based on the superferromagnetism model was not made for sample GBM because the doublet is predominant at quite low temperatures. Instead we plotted the average hyperfine field as a function of temperature, see Fig. 12. In non-interacting magnetic nanoparticles at low temperatures this temperature dependence is given by [14, 15]

$$B_{\text{hf}}(T) \approx B_{\text{hf}}(0)\left[1 - \frac{k_{\text{B}}T}{2KV}\right]. \qquad (11)$$

A fit of the data to a straight line gave the value $K = 0.9 \times 10^5$ Jm^{-3}. However, if inter-particle interactions and magnetic fluctuations in grains are not negligible, this value may be overestimated.

4. Discussion.

Magnetic relaxation in non-interacting nanoparticles of most magnetic materials, such as, for example, α-Fe$_2$O$_3$, γ-Fe$_2$O$_3$, NiO and α-Fe, is usually dominated by "classical" superparamagnetic relaxation with a relaxation time given by Eq. (6) [15]. Mössbauer spectra then show a superposition of a sextet due to particles with relatively slow relaxation and a doublet due to particles with fast relaxation. The area ratio of the two components depends on temperature because

of the temperature dependence of the relaxation time. However, Mössbauer spectra of goethite nanoparticles commonly show an unusual behavior because the magnetic relaxation is dominated by fluctuations of the sublattice magnetization directions in strongly interacting grains within the particles, and this results in Mössbauer spectra consisting of sextets with asymmetrically broadened lines in a broad range of temperatures without the presence of a doublet [5]. The reason for the unusual behavior of goethite nanoparticles is that goethite usually is poorly crystalline and contains defects like dislocations and low-angle grain boundaries. The particles can therefore be described as consisting of grains that interact due to exchange coupling [5]. The present studies of ultra-small goethite particles have clearly shown that particles with dimensions below a critical size and weak inter-particle interactions show a magnetic relaxation that is dominated by "classical" superparamagnetic relaxation. Our studies also show that inter-particle interactions can be reduced by ball-milling together with nanosized NaCl particles. This reduction of the inter-particle interactions can be clearly seen from the temperature dependence of the Mössbauer spectra.

Inelastic neutron scattering has earlier revealed that uniform excitations are the predominant spin-wave excitations in α-Fe_2O_3 [16, 24] and NiO [43] below the superparamagnetic blocking temperature. The present neutron study shows that this is also the case for goethite. In the inelastic neutron data for both G1 and GBM, a relatively sharp peak at around $1.0 - 1.5$ meV was attributed to particles with negligible inter-particle interactions, whereas a broader component with higher energy was attributed to interacting particles and magnetic fluctuations in interacting grains. This can explain why the position of the sharp peak is not much affected by the ball milling. This interpretation is in accordance with earlier studies of α-Fe_2O_3 [16] and NiO [43] with varying inter-particle interactions. We have previously performed inelastic neutron scattering studies of larger goethite particles in which the magnetic fluctuations are dominated by fluctuations of the sublattice magnetization of interacting grains (unpublished). In these studies no sharp satellite peaks were observed. Instead the data showed very broad features, similar to the broad satellite peaks in Fig. 7. In inelastic neutron studies of 8 nm hematite particles [16] and disc shaped NiO nanoparticles [43] it was also found that inter-particle interactions result in broadening of the satellite peaks a a shift towards higher energies . This supports the interpretation of the broad components in the inelastic neutron scattering data for G1 and GBM.

The magnetic anisotropy of goethite has been the subject of much controversy. In early Mössbauer studies it was noticed that the magnetically split spectra had strongly asymmetric lines and the magnetic hyperfine splitting in relatively large goethite particles collapsed well below the Néel temperature [44, 45]. It was therefore concluded that the magnetic anisotropy constant was much smaller than that of α-Fe_2O_3 and was of the order of only 10^3 Jm^{-3} [45]. Later, Mössbauer studies of a single crystal of goethite in large applied magnetic fields indicated a much larger value, $K > 6 \times 10^4$ Jm^{-3} [41], whereas Mössbauer studies of the line shape of a polycrystalline sample in large applied fields indicated a value of 3×10^5 Jm^{-3} [39]. Magnetization measurements at 4.2 K revealed a spin flop transition at an applied field of 20 T, corresponding to a magnetic anisotropy constant of around 6×10^4 Jm^{-3} [36]. The present estimates of the magnetic anisotropy constant from inelastic neutron scattering data and Mössbauer data are of the order of 10^5 Jm^{-3}. In a recent study of hysteresis loops of goethite samples a much smaller value of only 210 Jm^{-3} at 5 K was estimated from the values of the coercivity [32]. We believe, however, that magnetization measurements on antiferromagnetic nanoparticles may give incorrect values of the anisotropy constants, because the magnetization is dominated by contributions from uncompensated magnetic moments, which may reverse their spin directions without a reversal of the sublattice magnetization directions of the whole particle.

In antiferromagnetic nanoparticles, it has been predicted that the initial susceptibility at low temperature and the magnetization should increase with temperature because of thermoinduced magnetization [46]. This has been observed in a study of akaganeite (β-FeOOH) nanoparticles [47]. In goethite nanoparticles, the magnetization at low temperatures is dominated by a large upturn of both the ac and dc magnetization with decreasing temperature, as one can see in Figs. 3 and 4. This was also observed in an earlier ac magnetization study of goethite particles [26]. We interpret this as a result of freezing of the magnetization of uncompensated spins and canted spin structures around defects and at the surface of the particles [30].

The ZFC magnetization curve of GBM (Fig. 3) shows a maximum at around 130 K. Such a peak may be explained as a result of blocking of superparamagnetic particles. However, the blocking temperature estimated from Mössbauer spectroscopy with a time scale on the order of 5×10^{-9} s is around 160 K, and for the ZFC measurement with a time scale of around 100 s one should therefore expect a much lower blocking temperature (around 30 K). Therefore, the peak at 130 K cannot be

explained by superparamagnetic blocking. Pankhurst *et al.* [26] found a similar peak in ZFC magnetization studies of goethite particles. They suggested that it is related to "cluster ordering" of magnetically interacting clusters or particles. Our estimates of the interaction energy from the Mössbauer data indicate values on the order of 150 K, i.e. close to the peak temperature in the ZFC measurement. This supports the interpretation in terms of "cluster ordering".

5. Conclusions

The present Mössbauer studies have shown that in ultra-small goethite particles the magnetic relaxation is dominated by "classical" superparamagnetic relaxation at temperatures above ~170 K, in contrast to larger goethite particles in which the relaxation commonly is dominated by magnetic fluctuations in interacting grains. We have estimated the value of the uncompensated magnetic moment from magnetization measurements. The temperature dependence of the magnetization shows a large anomalous upturn at very low temperatures. This can be explained by freezing of canted spin structures at the surface and around defects. Inelastic neutron scattering and Mössbauer spectroscopy both show that the value of the magnetic anisotropy constant is close to 10^5 Jm^{-3}. Previously, the value of the magnetic anisotropy constant for goethite has been much debated. The difficulty in determining K relies partly on difficulties in separating the magnetic anisotropy energy from the interaction energy in samples of interacting grains. In the present study of small particles with limited inter-grain and inter-particle interactions this problem has been reduced. The inelastic neutron scattering data show that for small particles not dominated by interaction effects, this technique can be very useful in determining K as the measurements single out (with a sharp inelastic signal) the excitation energy of the *q=0* modes at low temperatures.

References

1. U. Schwertmann and R.M. Cornell, *The Iron Oxides: Structure, Properties, Reactions, Occurrences and Uses,* Wiley-VCH., 2. edition, (2003).

2. R.V. Morris, G. Klingelhöfer, C. Schröder, D.S. Rodionov, A. Yen, D.W. Ming, P.A. de Souza Jr., I. Fleischer, T. Wdowiak, R. Gellert, B. Bernhardt, E.N. Evlanov, B. Zubkov, J. Foh, U. Bonnes, E. Kankeleit, P. Gütlich, F. Renz, S.W. Squyres and R.E. Arvidson, *J. Geophys. Res.-Planet*, E02S13 (2006).

3. J.B. Forsyth, I.G. Hadley and C.E. Johnson, *J. Phys. C (Proc. Phys. Soc.) Ser. 2,* **1**, 179 (1968).

4. S. Mørup, M.B. Madsen, J. Franck, J. Villadsen and C.J.W. Koch, *J. Magn. Magn. Mater.* **40**, 163 (1983).

5. D.E. Madsen, L. Cervera-Gontard, T. Kasama, R.E. Dunin-Borkowski, C.B. Koch, M.F. Hansen, C. Frandsen and S. Mørup, *J. Phys.: Condens. Matter* **21**, 016007 (2009).

6. D.J. Burleson and R.L. Penn, *Langmuir* **22**, 402 (2006).

7. R.L. Penn, J.J. Erbs and D.M. Gulliver, *J. Cryst. Growth* **293**, 1 (2006).

8. C.A. Barrero, J.D. Betancur, J.M. Greneche, G.F. Goya and T.S. Berquó, *Geophys. J. Int.* **164** 331 (2006).

9. D.E. Madsen, M.F. Hansen, C. Bender Koch and S. Mørup, *J. Phys.: Condens. Matter* **20**, 135215 (2008).

10. C.J.W. Koch, M.B. Madsen and S. Mørup, *Surf. Sci.* **156**, 249 (1985).

11. E. Murad, *Amer. Miner.* **67**, 1007 (1982).

12. S. Bocquet, R.J. Pollard and J.D. Cashion, *Phys. Rev. B* **46**, 11657 (1992).

13. T.S. Berquó, R.L. Imbernon, A. Blot, D.R. Franco, M.C.M. Toledo and C.S.M. Partiti, *Phys. Chem. Minerals* **34**, 287 (2007).

14. S. Mørup, D.E. Madsen, C. Frandsen, C.R.H. Bahl and M.F. Hansen *J. Phys.: Condens. Matter* **19** 213202 (2007).

15. S. Mørup, M.F. Hansen and C. Frandsen: in *Comprehensive Nanoscience and Technology, Vol. 1,* Eds. D. Andrews, G. Scholes and G. Wiederrecht, Elsevier 437-491 (2011).

16. L. Theil Kuhn, K. Lefmann, C.R.H. Bahl, S.N. Klausen, P.-A. Lindgård, C. Frandsen, D.E. Madsen and S. Mørup, *Phys. Rev. B* **74**, 184406-1-9 (2006).

17. M.F. Hansen, C. Bender Koch and S. Mørup, *Phys. Rev. B* **62**, 1124 (2000).

18. S. Mørup, C. Frandsen and M.F. Hansen, *Beilstein Journal of Nanotechnology*, **1**, 48 (2010).

19. J.F. Banfield, S.A. Welch, H. Zhang, T.T. Ebert and R.L. Penn, *Science* **289**, 751 (2000).

20. M. Nesterova, J. Moreau and J.F. Banfield, *Geochim. Cosmochim. Acta* **67**, 1177 (2003).

21. L. Néel, *Ann. Geophys*. **5**, 99 (1949).

22. W.F. Brown, *Phys. Rev.* **130,** 1677 (1963).

23. F. Bødker, M.F. Hansen, C. Bender Koch, K. Lefmann and S. Mørup, *Phys. Rev. B* **61** 6826 (2000).

24. M. F. Hansen, F. Bødker, S. Mørup, K. Lefmann, K.N. Clausen and P.-A. Lindgård, *Phys. Rev. Lett.* **79**, 4910 (1997).

25. S.N. Klausen, K. Lefmann, P.-A. Lindgård, L.T. Kuhn, C. Frandsen, S. Mørup, B. Roessli, and N. Cavadini, *Phys. Rev. B* **70**, 214411 (2004).

26. Q.A. Pankhurst, L.F. Barquín, J.S. Lord, A. Amato and U. Zimmermann, *Phys. Rev. B* **85**, 174437 (2012).

27. C. J. Howard, R J. Hill, AAEC (now ANSTO) Report M112, Lucas Heights Research Laboratory, 1986.

28. A. Szytula, A. Burewickz, Z. Dimitrij, S. Krasnick, H. Rzany, J. Todorovi, A. Wanic and W. Wolski. *Phys. Status Solidi*, **26**, 429 (1968).

29. T. Unruh, J. Neuhaus and W. Petry, *Nucl. Instr. Meth. A*, **580**, 1414 (2007).

30. H. Jacobsen, K. Lefmann, E. Brok, C. Frandsen and S. Mørup, *J. Magn. Magn. Mater.* **324**, 3218 (2012).

31. D. E. Madsen, M. F. Hansen, J. Bendix and S. Mørup, *Nanotechnology* **19,** 315712 (2008).

32. F. Martin-Hernandez and M.M. Garcia-Hernández, *Geophys. J. Int*. **181**, 756 (2010).

33. C.R.H. Bahl, J. Garde, K. Lefmann, T.B.S. Jensen, P.-A. Lindgård, D.E. Madsen and S. Mørup, *Eur. Phys. J B* **62** 53 (2008).

34. A. Würger, *Europhys. Lett.* **44**, 103 (1998).

35. C. Kittel, *Phys. Rev.* **82**, 565 (1951).

36. J.M.D. Coey, A. Barry, J.-M. Brotto, H. Rakoto, S. Brennan, W.N. Mussel, A. Collomb and D. Fruchard, *J. Phys.: Condens. Matter* **7**, 759 (1995).

37. L. Néel, *Comptes Rendus Hebdomadaires des Seances de L'academie des Sciences* **242**, 4075 (1961).

38. J.T. Richardson, D.I. Yiagas, B. Turk, K. Forster and M.W. Twigg, *J. Appl. Phys.* **70**, 6977 (1991).

39. Q.A. Pankhurst and R.J. Pollard, *J. Phys.: Condens. Matter* **2**, 7329 (1990).

40. Q.A. Pankhurst, *Hyperfine Interact*. **90**, 201 (1994).

41. A. Meagher, Q.A. Pankhurst and D.P.E. Dickson, *Hyperfine Interact.* **28**, 533 (1986).

42. F. Bødker and S. Mørup, *Europhys. Lett*. **52**, 217 (2000).

43. C.R.H. Bahl, K. Lefmann, L.T. Kuhn, N.B. Christensen, H. Várquez and S. Mørup, *J. Phys.: Condens. Matter*, **18**, 11203 (2006).

44. A.M. van der Kraan and J.J. van Loef, *Phys. Lett.* **20**, 614 (1966).

45. T. Shinjo, *J. Phys. Soc. Japan*, **21**, 917 (1966).

46. S. Mørup and C. Frandsen, *Phys. Rev. Lett.* **92**, 217201 (2004).

47. A. Urtiberea, F. Luis, A. Millán, E. Natividad, F. Palacio, E. Kampart and U. Zeitler, *Phys. Rev. B*, **83**, 214426 (2011).

Figure captions.

Figure 1.

X-ray diffraction patterns of samples G1 and GBM. The refined model, the background and the difference between model and experiment are displayed. The most prominent reflections up to $q = 4$ Å^{-1} have been indexed. The impurity peak (sample GBM) is marked by *.

Figure 2

TEM images. (a) High-resolution image from the rim of a G1 aggregate. (b) Dark-field image from a G1 aggregate. (c) Particle sizes measured from a dark-field image of the G1 sample. (d) Dark-field image of sample GBM, after the "nano"-salt has been washed away.

Figure 3.

ZFC/FC magnetization curves for the sample GBM obtained in an applied field of (top) 4.8 T and (bottom) 2.0 mT. The magnetization is given per kg of goethite in the sample.

Figure 4.

In-phase AC susceptibility $(\chi^{'})$ as a function of temperature for the GBM sample. The amplitude of the driving field was $\mu_0 H = 0.38$ mT.

Figure 5.

Hysteresis loop of the GBM sample at 300 K. The magnetization is given per kg of goethite in the sample. The upper insert shows the average of the positive and negative magnetization curves after subtraction of a linear function resulting from a fit to the high-field parts of the curves. The step in the curve corresponds to a moment of 0.033 Am^2/kg. The lower insert shows the hysteresis loop of the GBM sample at 4.2 K. The units on the inserts are the same as on the main figure.

Figure 6.

Inelastic neutron scattering data for samples G1 and GBM shown as intensity maps of neutron momentum transfer q and neutron energy transfer ε at the indicated temperatures.

Figure 7.

Neutron energy transfer data integrated over a narrow q-range at $q=1.258$ Å^{-1} of samples G1 and GBM at the indicated temperatures. Each data set is fitted with one Voigtian profile (Voigt) and two damped harmonic oscillator modes (dho1 and dho2) as described in the text.

Figure 8. The ε_0-values as a function of temperature obtained from fitting neutron data of samples G1 and GBM.

Figure 9.

Mössbauer spectra of G1 (a) and GBM (b) obtained at the indicated temperatures in zero applied field.

Figure 10.

Mössbauer spectra of G1 obtained at 260 K with and without an applied field of 6 T.

Figure 11.

Magnetic anisotropy energy (top) and interaction energy (bottom) for sample G1 in units of Kelvin as a function of the quantile.

Figure 12.

Magnetic hyperfine field of sample GBM as a function of temperature.
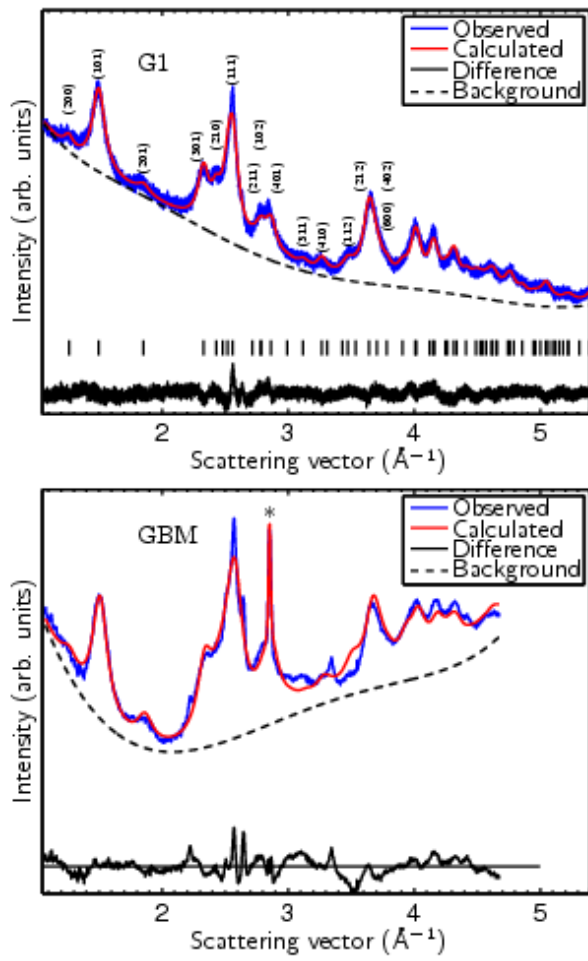
Figure 1

(a)

10 nm

(b)

30 nm

(c)

(d)

30 nm
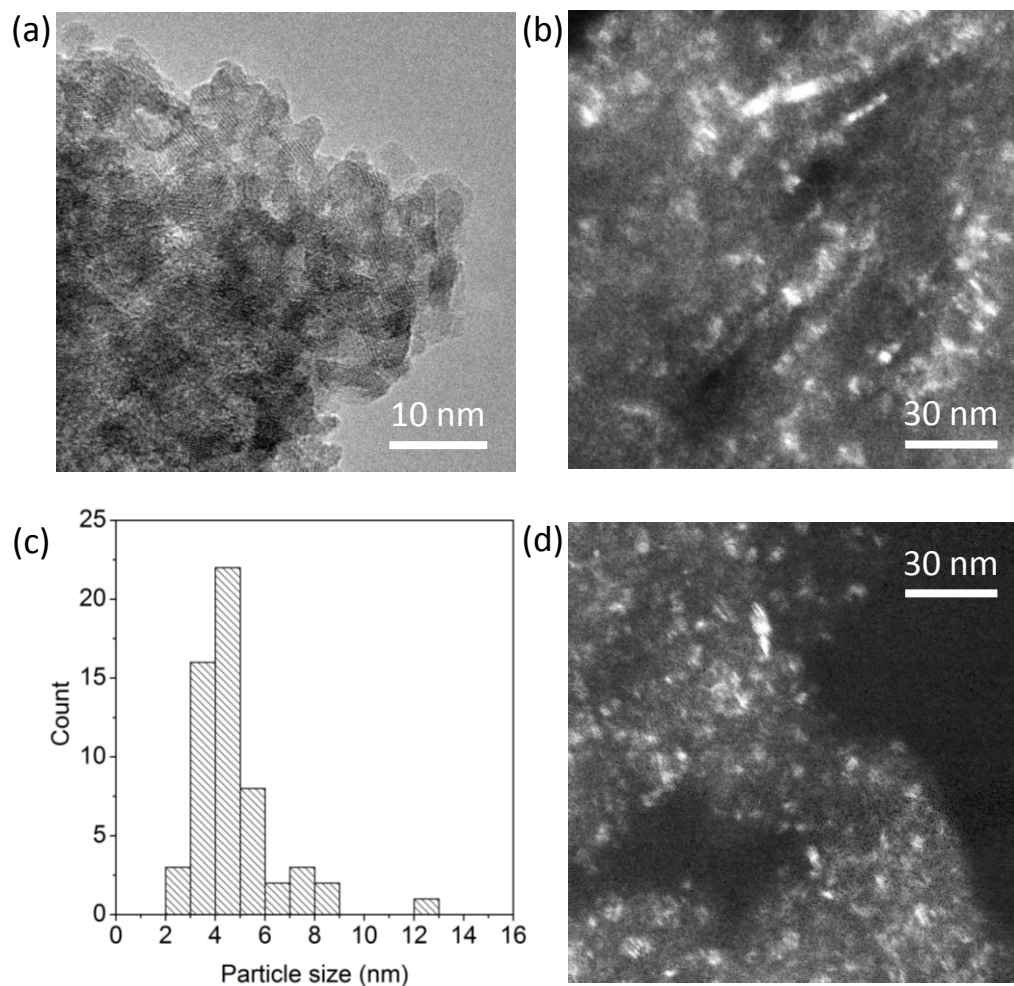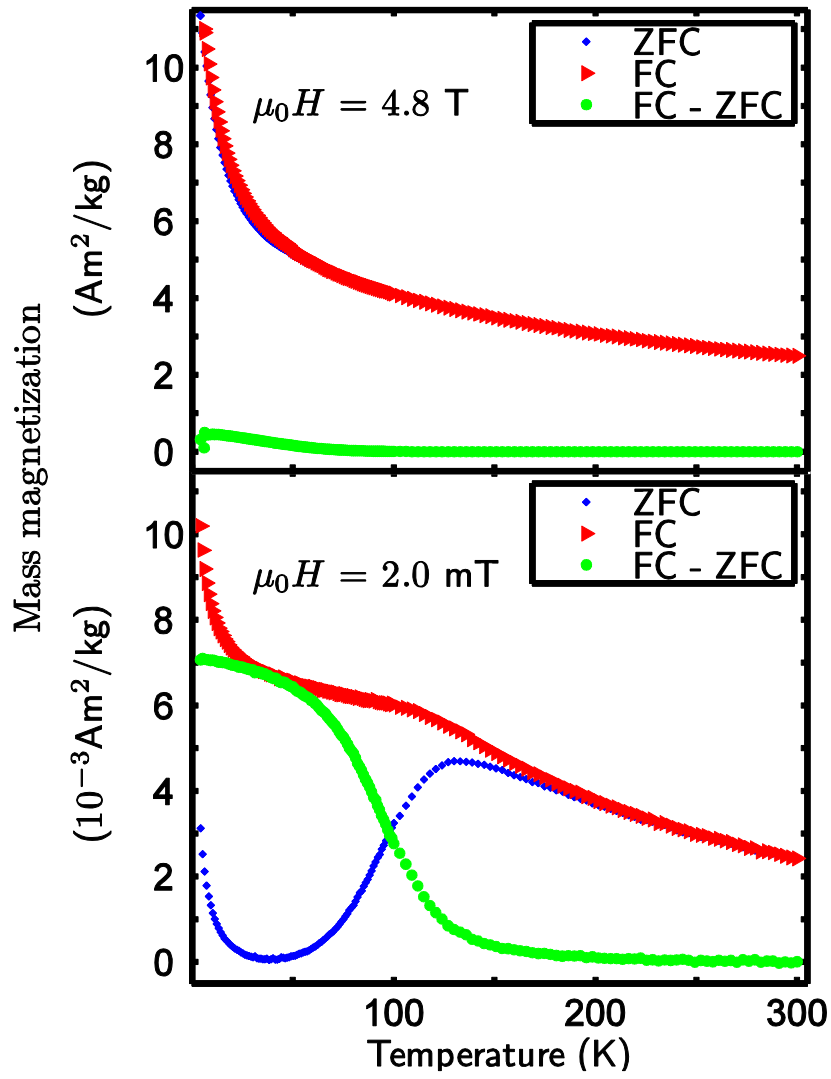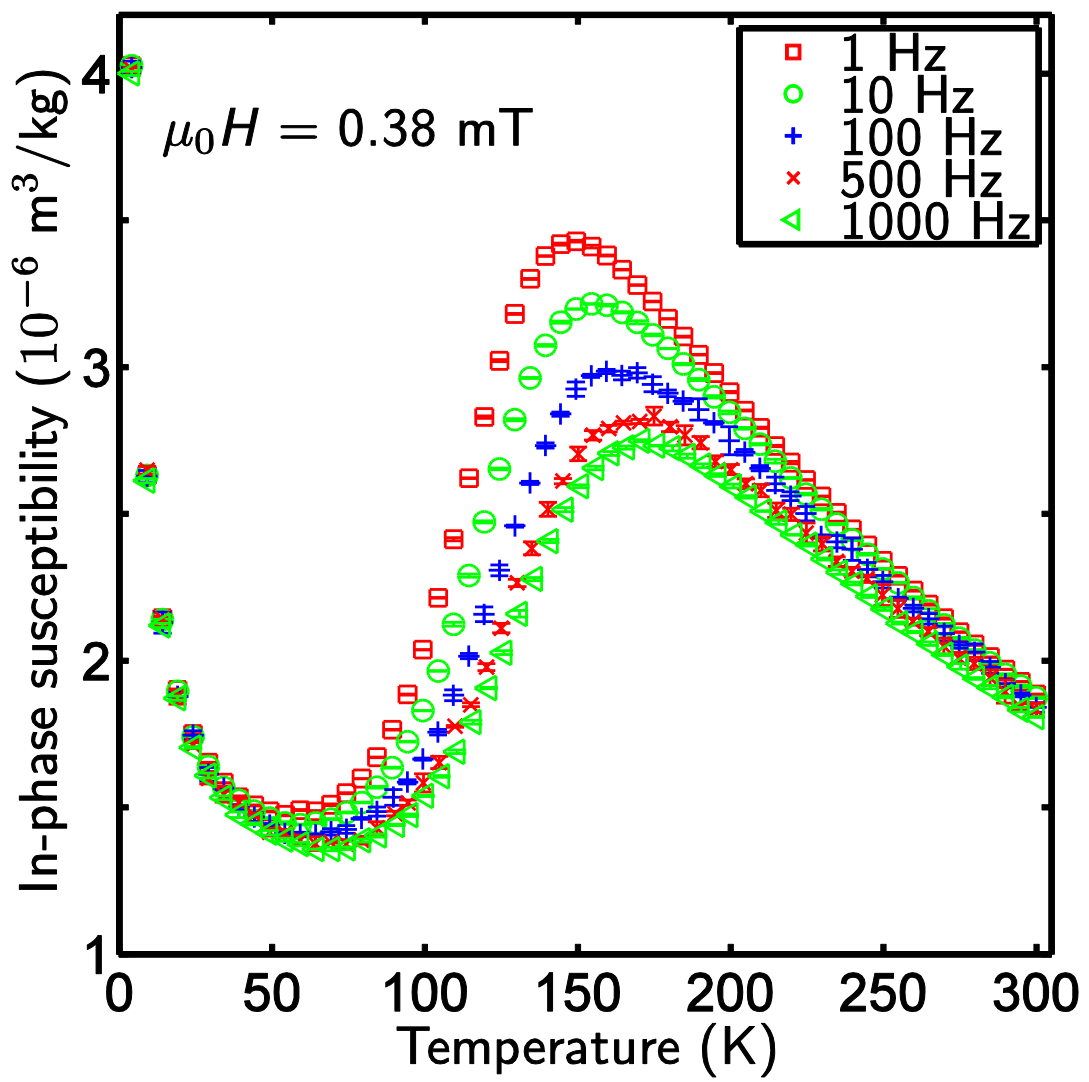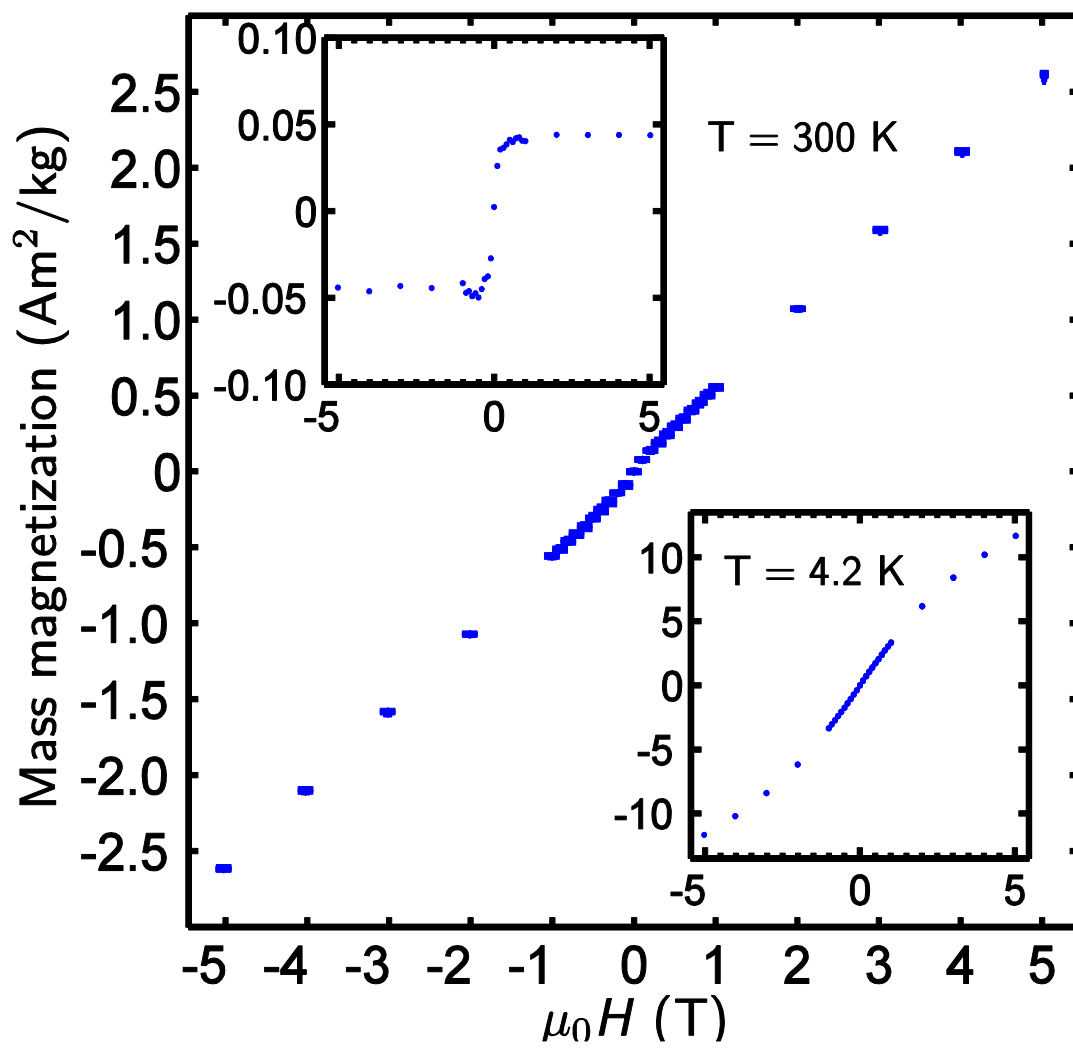
Figure 2

Figure 3
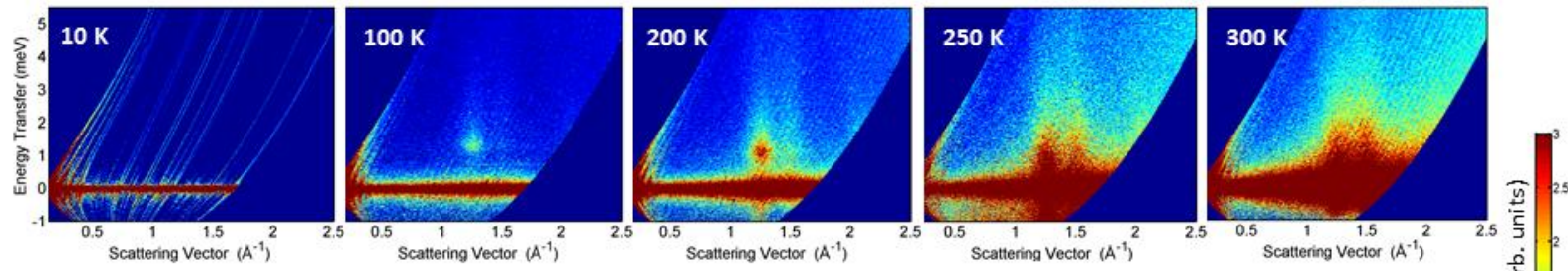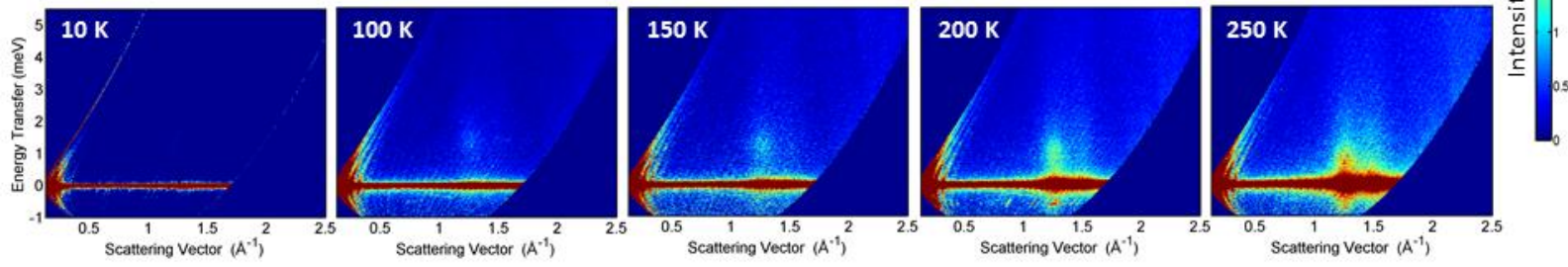
Figure 4
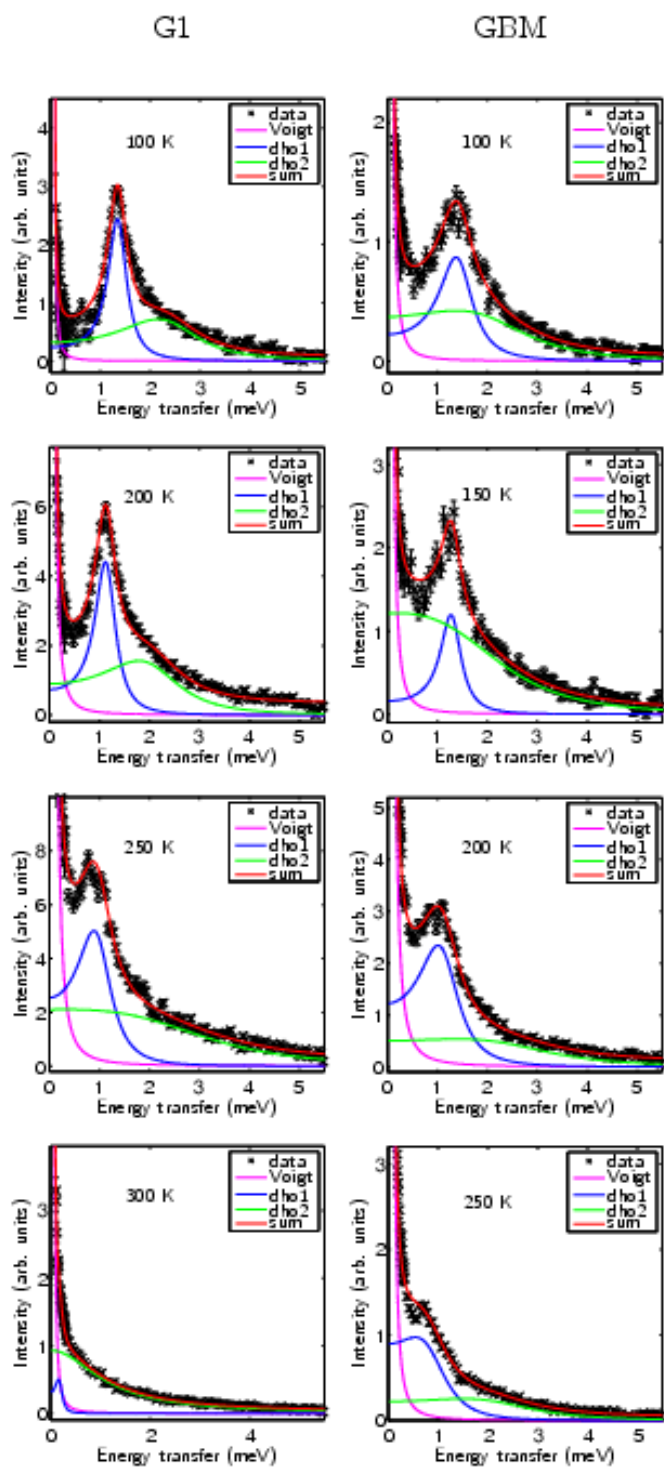
Figure 5
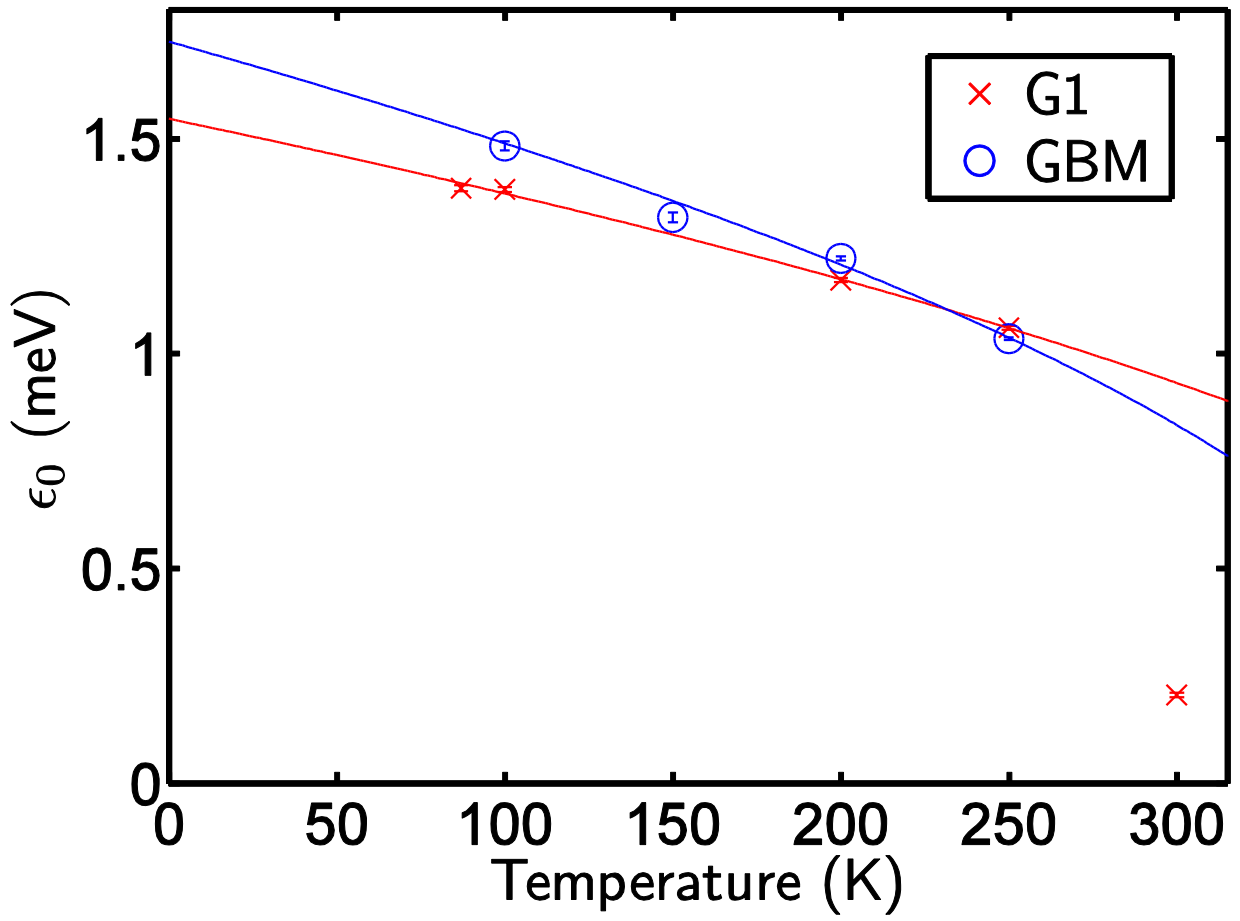
Figure 6
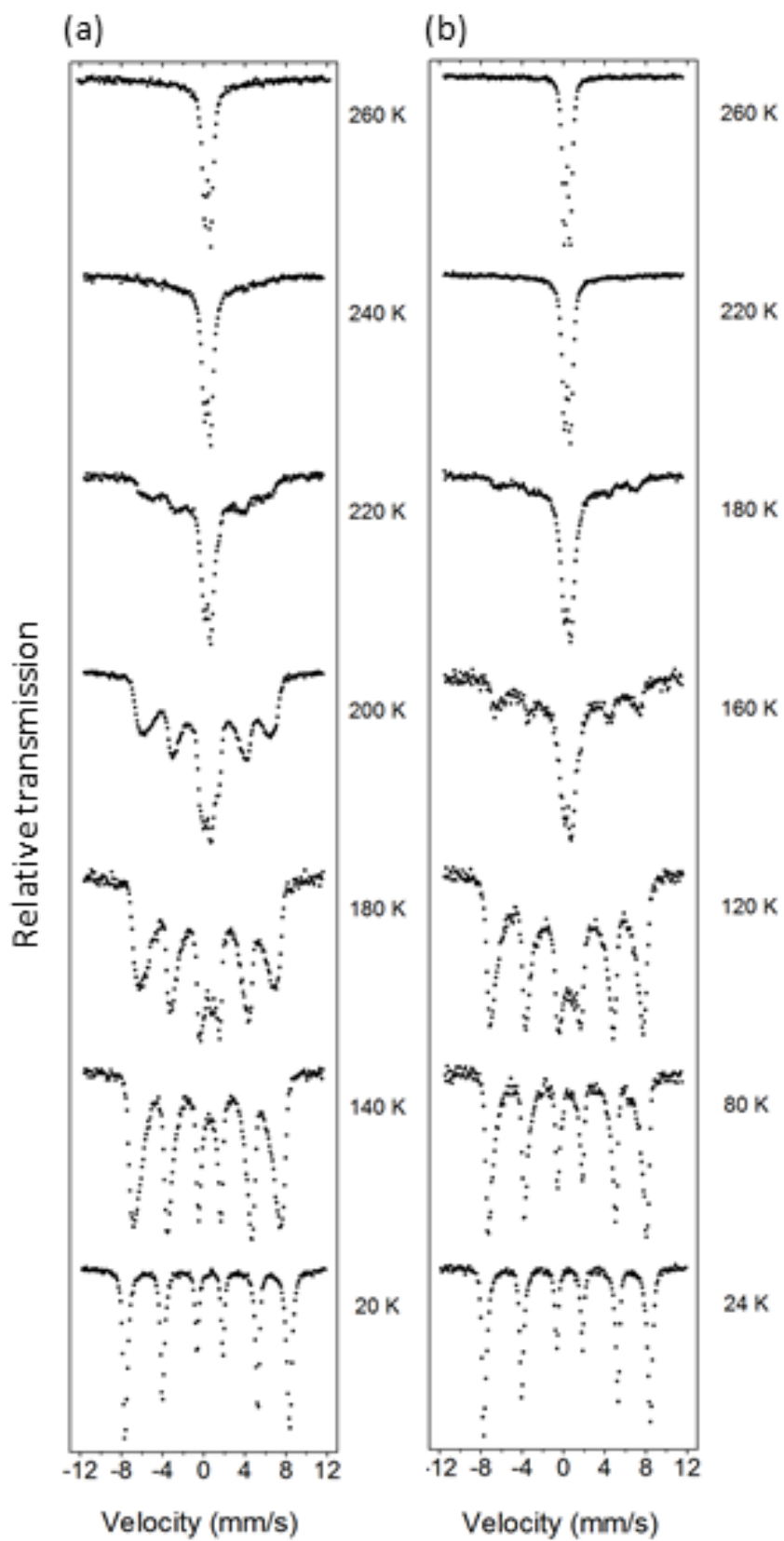
Figure 7
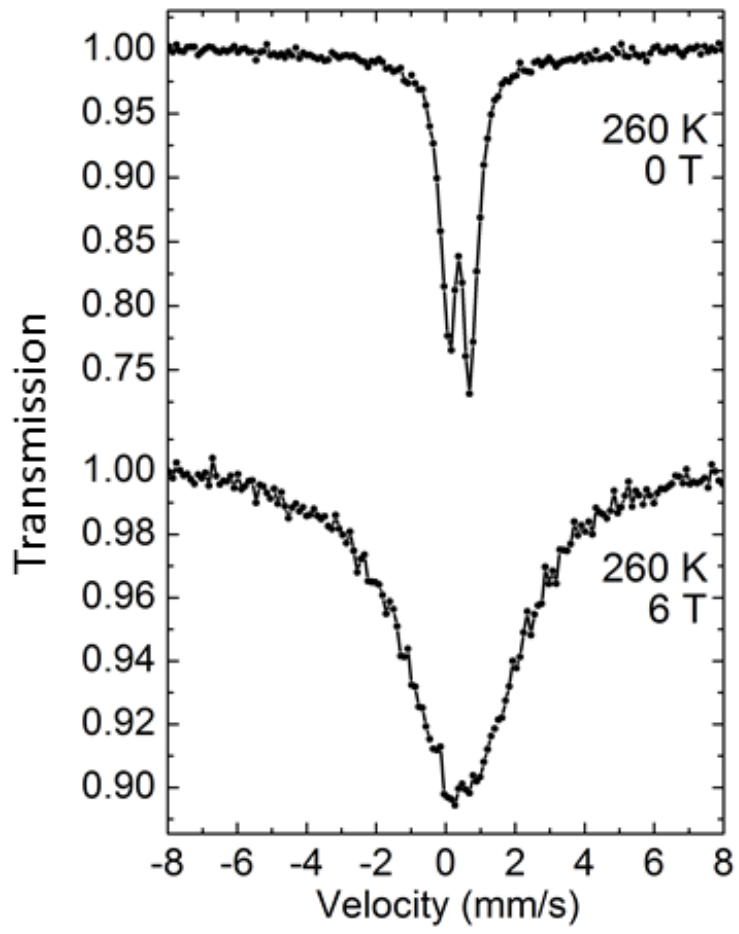
Figure 8
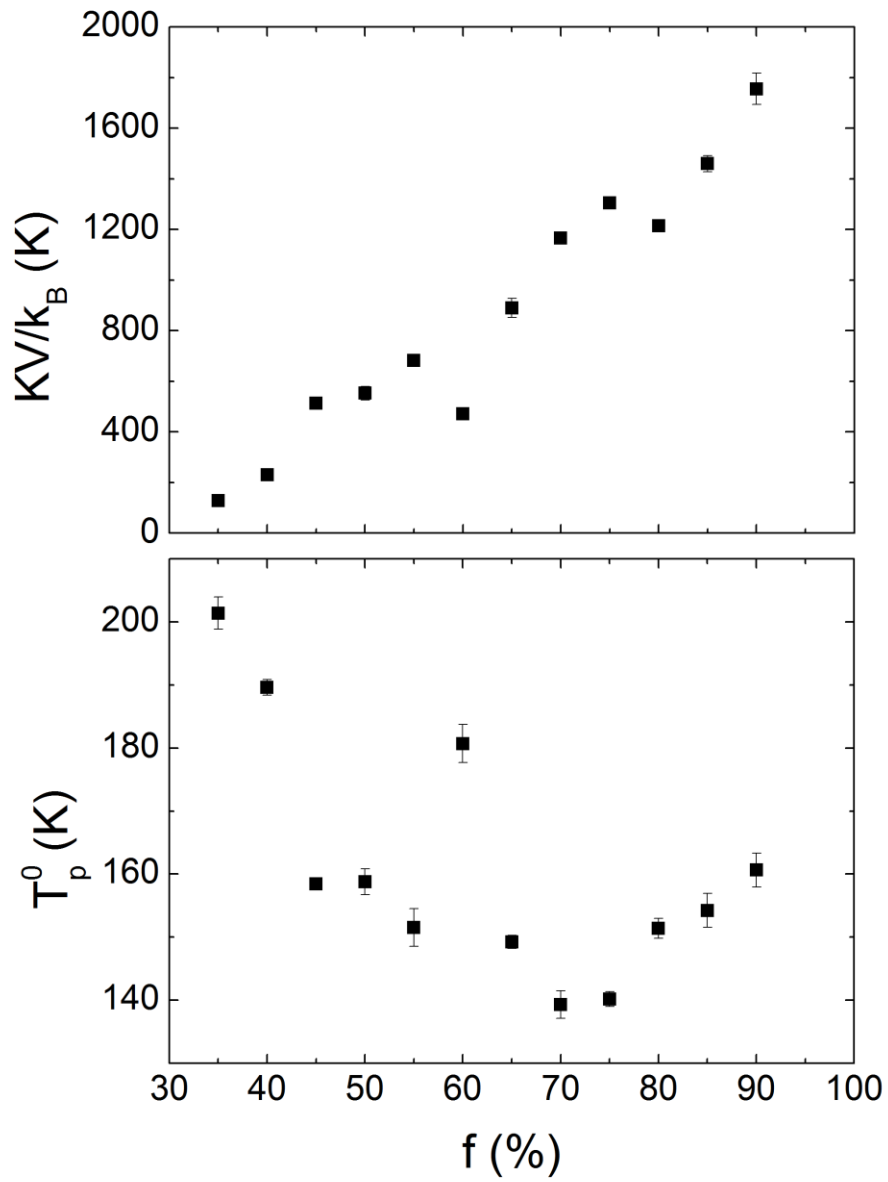
Figure 9

Figure 10

Figure 11
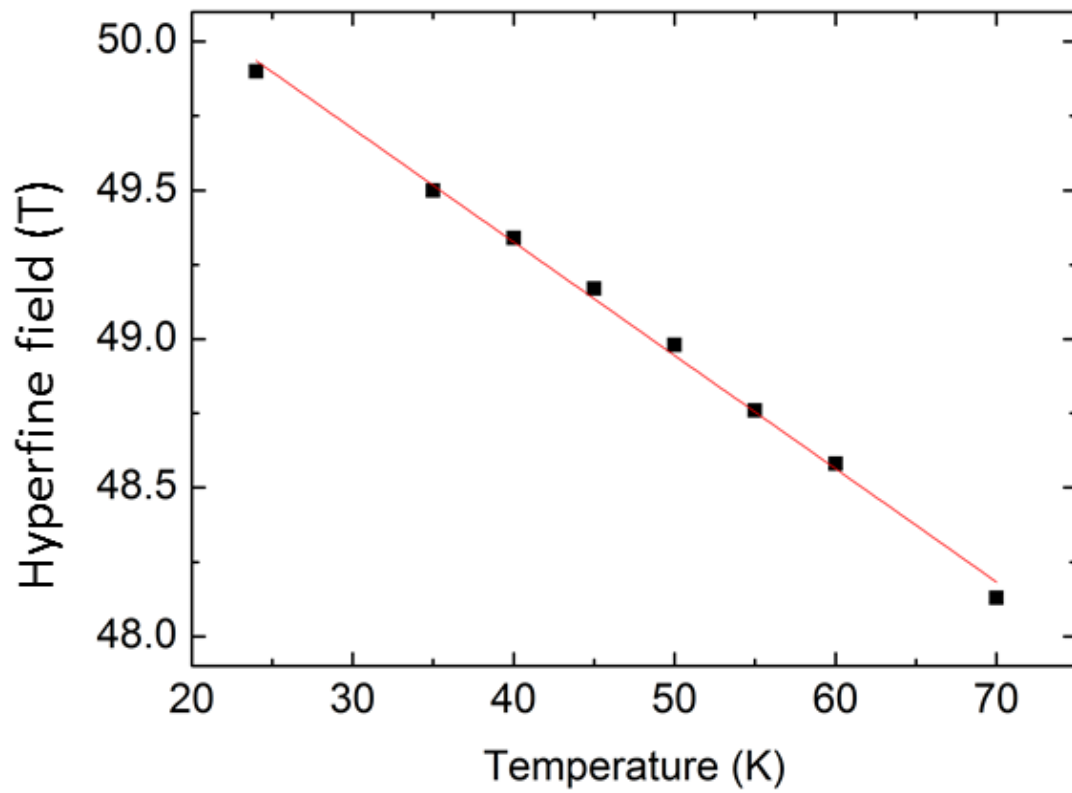
Figure 12

Spin reorientation in α-Fe₂O₃ nanoparticles induced by interparticle exchange interactions in α-Fe₂O₃/NiO nanocomposites

C. Frandsen,[1,*] K. Lefmann,[2,3,4] B. Lebech,[2,4] C. R. H. Bahl,[4,5] E. Brok,[1,6] S. N. Ancoña,[4,†] L. Theil Kuhn,[4,5] L. Keller,[7]
T. Kasama,[6] L. C. Gontard,[6,‡] and S. Mørup[1]

[1]*Department of Physics, Technical University of Denmark, DK-2800 Kgs. Lyngby, Denmark*
[2]*Nano-Science and eScience Centers, Niels Bohr Institute, University of Copenhagen, Universitetsparken 5,
DK-2100 Copenhagen Ø, Denmark*
[3]*European Spallation Source, Lund, Sweden*
[4]*Materials Research Division, Risø DTU, Technical University of Denmark, DK-4000 Roskilde, Denmark*
[5]*Fuel Cells and Solid State Chemistry Division, Risø DTU, Technical University of Denmark, DK-4000 Roskilde, Denmark*
[6]*Center for Electron Nanoscopy, Technical University of Denmark, DK-2800 Kgs. Lyngby, Denmark*
[7]*Laboratory for Neutron Scattering, Paul Scherrer Institute, CH-5232 Villigen PSI, Switzerland*
(Received 30 March 2011; revised manuscript received 14 October 2011; published 22 December 2011)

We report that the spin structure of α-Fe₂O₃ nanoparticles rotates coherently out of the basal (001) plane at low temperatures when interacting with thin plate-shaped NiO nanoparticles. The observed spin reorientation (up to ∼70°) in α-Fe₂O₃ nanoparticles has, in appearance, similarities to the Morin transition in bulk α-Fe₂O₃, but its origin is different—it is caused by exchange coupling between aggregated nanoparticles of α-Fe₂O₃ and NiO with different directions of easy axes of magnetization.

I. INTRODUCTION

Magnetic coupling between different materials in direct contact is a subject of considerable interest. Exchange coupling between a ferro- or ferrimagnetic material and an antiferromagnetic material in, for example, thin film structures can lead to exchange bias,[1–4] which is a key ingredient in read heads in computers. The spin structure at the interface has attracted much attention, and numerous experimental studies and theoretical models for exchange bias have been published.[2–4] In most of this work, the sublattice magnetizations of the antiferromagnetic material and the ferro- or ferrimagnetic material are assumed parallel at the interface, but in some experimental studies, it was surprisingly found that the sublattice magnetizations of the interacting materials may be perpendicular. The latter can be explained by a spin flop induced by the exchange field as proposed by Koon,[5] but anisotropic exchange interaction[6] and spin frustration at the interface may also play an important role.

In samples of antiferromagnetic nanoparticles in close proximity, magnetic interactions can also have a significant influence on the magnetic properties.[7] Antiferromagnetic particles have small magnetic dipole moments and therefore dipole interactions are negligible; yet, Mössbauer studies of antiferromagnetic nanoparticles of hematite (α-Fe₂O₃),[8–11] NiO,[12–14] and ferrihydrite[15] have shown that interparticle interactions between particles, prepared by drying aqueous suspensions, can result in a substantial suppression of the superparamagnetic relaxation. This has been explained by exchange interactions between surface atoms of neighboring particles.[8–11,16–18]

The exchange interaction between two neighboring particles p and q may be written

$$E_{\mathrm{ex}} = -\sum_{i,j} J_{ij} \vec{S}_i^p \cdot \vec{S}_j^q, \tag{1}$$

where $\vec{S}_i^p$ and $\vec{S}_j^q$ are surface spins of the particles p and q, respectively, and J_{ij} is the exchange coupling constant. For simplicity, we consider only one sublattice of particle p interacting with one sublattice of the particle q. Equation (1) can then be written[11]

$$E_{\mathrm{ex}} = -J_{\mathrm{eff}}\, \vec{M}_p \cdot \vec{M}_q = -J_{\mathrm{eff}}\, M_p\, M_q \cos\beta, \tag{2}$$

where $\vec{M}_p$ and $\vec{M}_q$ are the sublattice magnetization vectors of the particles p and q, respectively, J_{eff} is the effective exchange coupling constant, and β is the angle between $\vec{M}_p$ and $\vec{M}_q$.

The observation of strong exchange interactions in dried nanoparticle samples suggests that the drying actually brings the particles closely together and that the exact particle arrangement may include some kind of preferred orientation.[8–15,17] Oriented attachment has also been found in transmission electron microscopy studies of larger α-Fe₂O₃ particles with different morphologies.[19]

In this work, we have studied the influence of interactions between nanoparticles of NiO and α-Fe₂O₃ on the magnetic structure of α-Fe₂O₃. Our findings suggest that the interactions can lead to a spin reorientation in α-Fe₂O₃ nanoparticles out of the interface plane. We compare the studies of α-Fe₂O₃/NiO with studies of α-Fe₂O₃/CoO.

The crystal structure of α-Fe₂O₃ can be described in terms of alternating iron and oxygen layers stacked along the [001] axis of the hexagonal unit cell (see, e.g., Morrish[20]). The Fe layers order antiferromagnetically below the Néel temperature, $T_N \approx 955$ K, such that the magnetization directions of neighboring Fe layers become antiparallel. The sublattice magnetization directions of α-Fe₂O₃ are confined to lie within the (001) plane above the Morin transition temperature, T_M, which in bulk α-Fe₂O₃ is 263 K. Between T_N and T_M, the two sublattices form a small canting angle of about 0.1° away from perfect antiferromagnetic alignment. Below T_M, the sublattice magnetization directions are rotated by 90° out of the (001) plane such that they become parallel to the [001] direction

with no canting. The Morin transition temperature decreases with decreasing particle size, and in α-Fe$_2$O$_3$ particles with diameters less than approximately 20 nm, there is no Morin transition above the temperature of liquid helium.[20,21]

NiO and CoO are face-centered cubic (fcc) antiferromagnetic materials with Néel temperatures of 523 K and 293 K, respectively. Within the (111) planes, the cations are ferromagnetically coupled, and adjacent (111) planes are antiferromagnetically coupled. In NiO, the common direction of the sublattice magnetization is within the (111) plane, whereas for CoO, it is a direction close to the [$\bar{1}\bar{1}$7] axis.[22] However, for nanoparticles, the magnetic structure can be different from that of the bulk materials.[23]

Mössbauer studies of composites of nanoparticles of α-Fe$_2$O$_3$ mixed with NiO or CoO have shown some interesting results.[18,24] Mixing with NiO resulted in faster superparamagnetic relaxation of the α-Fe$_2$O$_3$ particles at finite temperatures, whereas mixing with CoO had the opposite effect. Well below the blocking temperature of α-Fe$_2$O$_3$ particles, a significant reorientation of the spin system of α-Fe$_2$O$_3$ was found in the α-Fe$_2$O$_3$/NiO sample, whereas no spin reorientation was found in the α-Fe$_2$O$_3$/CoO sample. It has also been shown that interactions between α-Fe$_2$O$_3$ nanoparticles with different crystallographic orientations, obtained by freeze-drying particle suspensions, can result in reorientation of the spin structure, such that the sublattice magnetization forms finite angles with the easy axes defined by the magnetic anisotropy.[17] In this paper, we present the results of a detailed investigation of the spin reorientation in α-Fe$_2$O$_3$/NiO nanocomposites by combined use of Mössbauer spectroscopy, neutron scattering, and transmission electron microscopy (TEM).

II. EXPERIMENTAL DETAILS

Nanoparticles of α-Fe$_2$O$_3$ (approximately spherical, $\sim$8 nm in diameter) were synthesized by means of a gel-sol method.[25] NiO particles (plate-shaped, $\sim$15 nm in diameter and $\sim$2 nm thick) were prepared by annealing Ni(OH)$_2$ in air for 3 h,[18] and CoO particles (approximately spherical, 20 nm in diameter) were prepared by annealing Co-acetate in argon for 4 h.[18] All samples were characterized by x-ray diffraction and TEM. The α-Fe$_2$O$_3$ particles are from the same batch as those studied in Refs. 9 and 18, and the NiO particles are similar to those studied in Refs. 14 and 18.

A sample of pure 8-nm α-Fe$_2$O$_3$ nanoparticles with limited interparticle interaction was prepared as a ferrofluid, in which the particles in suspension were coated with oleic acid after intense ultrasonic treatment. A sample of interacting 8-nm α-Fe$_2$O$_3$ particles was prepared by freeze-drying a suspension of noncoated particles from the same batch.

Composites of α-Fe$_2$O$_3$/NiO and α-Fe$_2$O$_3$/CoO nanoparticles were prepared as reported in Ref. 18 by suspending 50 mg of each of these powders into 100 ml of distilled water. Within this, the particles were exposed to intense ultrasound for 15 minutes by use of an ultrasonic horn, with the aim to break apart agglomerates of particles and obtain a homogeneous mixture of the particles. The particles were then allowed to settle and dry at room temperature in an open petri dish. This procedure was repeated several times to obtain sufficient material for neutron diffraction experiments.
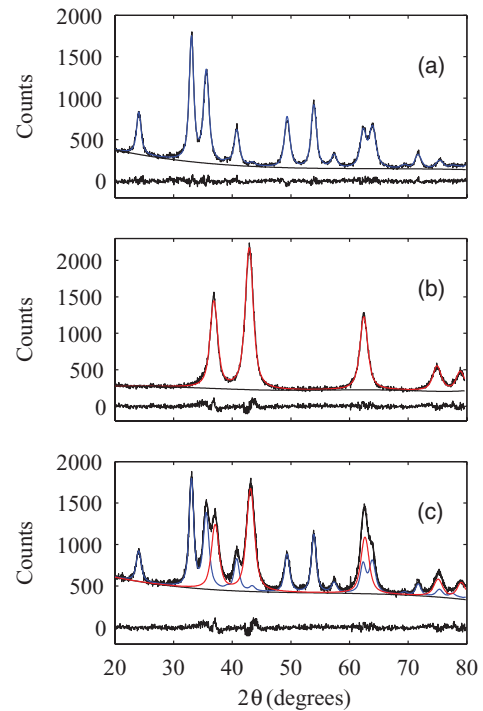

FIG. 1. (Color online) Rietveld refined x-ray diffraction data of (a) 8-nm α-Fe$_2$O$_3$ particles, (b) NiO nanoparticles, and (c) α-Fe$_2$O$_3$/NiO nanoparticle composite. The refinement of α-Fe$_2$O$_3$ is shown in blue/medium gray, that of NiO in red/dark gray, and the total refinement (c) in black.

Figure 1 shows Rietveld refined x-ray diffraction data (Cu Kα, $\lambda = 1.54$ Å) of (a) freeze-dried α-Fe$_2$O$_3$ nanoparticles, (b) NiO nanoparticles, and (c) α-Fe$_2$O$_3$/NiO nanoparticle composite. The refinement shows that the α-Fe$_2$O$_3$ and NiO samples are pure phases and that the particle sizes remain the same in the composite sample [Fig. 1(c)] as in the pure samples [Fig. 1(a) and 1(b), respectively].

The samples were studied by ^{57}Fe Mössbauer spectroscopy using constant acceleration spectrometers with sources of ^{57}Co in Rh. The spectrometers were calibrated using a 12.5 μm foil of α-Fe. Spectra were obtained at temperatures of 20–300 K using a closed-cycle helium refrigerator from APD Cryogenics. Cold neutron powder diffraction data were obtained at temperatures between 20 K and 300 K, using a wavelength of 4.20 Å, at the DMC diffractometer at the Swiss Spallation Neutron Source, SINQ, Paul Scherrer Institute. For all Mössbauer spectroscopy and neutron diffraction studies presented here, the samples were cooled to low temperatures (20 K) and then measured at increasing temperatures (35 K, 50 K, etc). However, we found no thermal hysteresis on the spin orientation by comparison of Mössbauer measurements of the α-Fe$_2$O$_3$/NiO sample obtained at same temperatures after cooling from 295 K and after heating from 20 K. TEM imaging was performed using JEOL 3000F and FEI Technai field-emission gun TEMs (300 keV) equipped with Gatan Imaging Filters. Elemental mapping was acquired using a three-window background-subtracted method with Gatan imaging filter.

III. RESULTS

A. Mössbauer spectroscopy

For studies of spin reorientation relative to the [001] axis in α-Fe$_2$O$_3$ nanoparticles, Mössbauer spectroscopy is a very useful technique. The electric field gradient in α-Fe$_2$O$_3$ is parallel to the [001] axis and the quadrupole shift, ε, is given by

$$\varepsilon = \varepsilon_0(3\cos^2\theta - 1)/2, \qquad (3)$$

where $\varepsilon_0 = 0.20$ mm/s, and θ is the angle between the magnetic hyperfine field (antiparallel to the magnetic moment of the ion) and the [001] axis. Thus, the quadrupole shift changes from $\varepsilon = -0.10$ mm/s above the Morin transition temperature, where $\theta = 90°$ to $\varepsilon = +0.20$ mm/s below T_M, where $\theta = 0°$.

Figure 2(a) shows Mössbauer spectra of the frozen ferrofluid of coated 8 nm α-Fe$_2$O$_3$ nanoparticles with little interparticle interaction. In agreement with previous studies of $\sim$8 nm α-Fe$_2$O$_3$ nanoparticles, where the interparticle interaction was negligible due to coating with oleic acid[18] or phosphate,[11] the spectra in Fig. 2(a) show a typical superparamagnetic behavior (i.e., a gradual transition from a sextet to a doublet in the temperature range 20–80 K, such that the relative area of the doublet gradually increases with increasing temperature). The superparamagnetic blocking temperature, T_B, defined as the temperature at which the sextet and the doublet have identical spectral areas, is around 70 K. At low temperatures, the sextet spectra show, as expected for nanoparticles with no Morin transition, a quadrupole shift, ε, of -0.10 mm/s. At $T \geqslant 180$ K, all the particles are superparamagnetic.

Figure 2(b) shows spectra of the freeze-dried sample of uncoated α-Fe$_2$O$_3$ particles. These spectra are magnetically split at 80 K and even at room temperature, but the absorption lines are substantially broadened and asymmetric above 80 K. This behavior is typical for samples of strongly interacting nanoparticles.[8–11,18] The temperature dependence of such spectra can be described by a mean field model for interacting nanoparticles.[8,23,26,27] The data in Fig. 2(b) also show that there is no Morin transition in these nanoparticles. We fitted the spectra obtained at temperatures $\leqslant$50 K with a sextet [see the spectrum at 20 K in Fig. 2(b)] and found that the quadrupole shift, ε, of the interacting α-Fe$_2$O$_3$ nanoparticles is -0.085 mm/s. This is close to the value of -0.10 mm/s found both in bulk above T_M and in noninteracting α-Fe$_2$O$_3$ nanoparticles [Fig. 2(b)]. The uncertainty of ε is typically around 0.003 mm/s for sextet spectra with well-defined lines, as in those obtained at 25 and 20 K in Figs. 2(a) and 2(b), respectively.[17] The small difference in ε of $\sim$0.015 mm/s between the ferrofluid and the dried sample has been explained by a rotation of the spin structure by an angle of $\sim$15° ($\theta = 75°$) that is induced by interparticle interactions in dried samples, where the easy axis of magnetizations of neighboring particles or chains of particles are nonparallel.[17]

Figure 2(c) shows Mössbauer data of α-Fe$_2$O$_3$ in the α-Fe$_2$O$_3$/NiO nanocomposite. In contrast to Figs. 2(a) and 2(b), the low-temperature spectrum (20 K) shows a positive quadrupole shift (the distance between lines 5 and 6 is larger than the distance between lines 1 and 2). At low temperatures (20–50 K), and more pronounced at intermediate temperatures (80–120 K), the spectra are asymmetric (e.g., lines 2 and 6 are
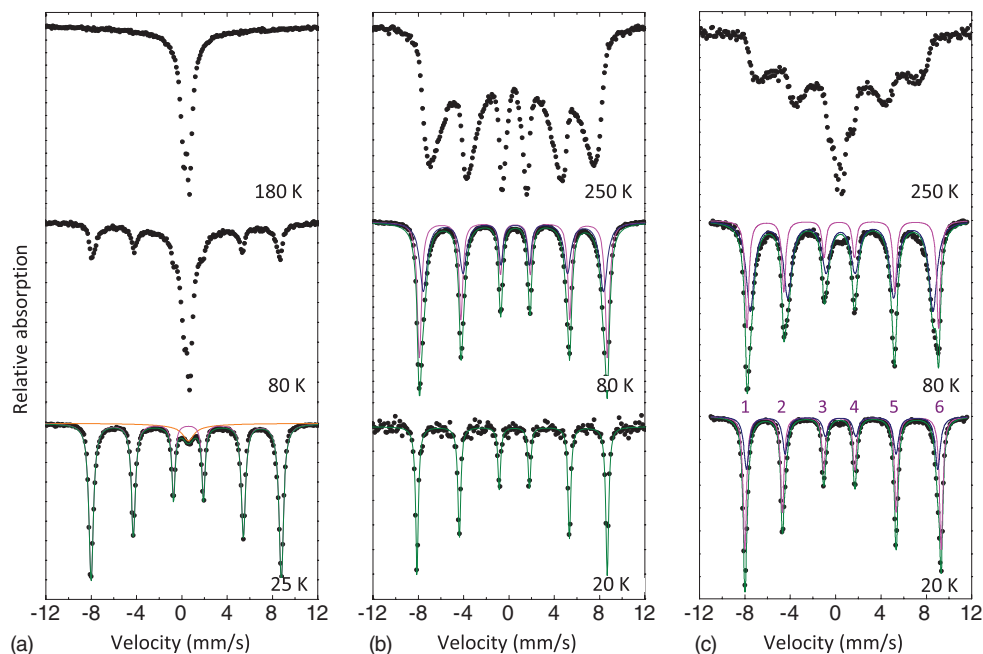
FIG. 2. (Color online) Mössbauer spectra of 8-nm α-Fe$_2$O$_3$ nanoparticles obtained at the indicated temperatures; (a) ferrofluid sample, (b) powder sample, and (c) mixed with NiO nanoparticles. The magenta/light gray numbers in panel c show how the lines are numbered. The solid (magenta/light gray and blue/dark gray) lines in panel b, at 80 K, and in panel c, at 20 K and 80 K, represent fits to the data by two sextets (sextets 1 and 2); the green/gray solid line is the sum of the fit components. The data in panel a at 25 K are fitted with one sextet and a doublet (orange/light gray), due to particles with fast superparamagnetic relaxation. The data in panel b obtained at 20 K are fitted with one sextet. The fit results for all the sextet components in panels a–c are summarized in Table I.

TABLE I. Mössbauer parameters obtained for α-Fe$_2$O$_3$ by fitting with one or two sextets the low-temperature spectra of the α-Fe$_2$O$_3$ ferrofluid sample (α-Fe$_2$O$_3$ (ff)), the α-Fe$_2$O$_3$ nanoparticle powder sample (α-Fe$_2$O$_3$ (fd)), and the α-Fe$_2$O$_3$ nanoparticles mixed with NiO nanoparticles (α-Fe$_2$O$_3$/NiO). The uncertainties of the given values for the hyperfine field (B_{hf}), isomer shift (δ), and quadrupole shift (ε) are ± 0.5 T, ± 0.02 mm/s, and ± 0.02 mm/s, respectively. The spectra are fitted with the area constraint that the sextet lines have the relative area distribution of 3:2:1:1:2:3 and that the line intensities and widths are pairwise equal. The line width (Γ^*) given in the table is an average value obtained by fitting the six lines in each sextet with the same line width.

Sample	T (K)	B_{hf} (T)	δ (mm/s)	ε (mm/s)	Γ^* (mm/s)
α-Fe$_2$O$_3$ (ff)	25	52.0	0.49	-0.10	0.45
α-Fe$_2$O$_3$ (fd)	20	52.5	0.49	-0.09	0.39
α-Fe$_2$O$_3$ (fd)	80	51.5	0.48	-0.09	0.42
		49.3	0.48	-0.08	0.64
α-Fe$_2$O$_3$/NiO	20	53.7	0.49	$+0.16$	0.36
		52.1	0.49	$+0.08$	0.49
α-Fe$_2$O$_3$/NiO	80	52.3	0.49	$+0.15$	0.42
		49.9	0.49	$+0.04$	0.75

broader and less intense than lines 5 and 1, respectively). This shows that Fe^{3+} ions are present in environments with different hyperfine interactions. The Mössbauer parameters obtained from fitting the low-temperature measurements in Fig. 2 are summarized in Table I.

The simplest but still sufficient fit of the Mössbauer data of α-Fe$_2$O$_3$/NiO in the range 20–130 K is composed of two sextets. The fits of the spectra obtained at 20 and 80 K are shown in Fig. 2(c). Fitting the data with just two sextets is only possible up to around 130 K; at higher temperatures, the spectra are too severely influenced by relaxation phenomena (seen as an increase in line width and from the occurrence of a doublet in the central part of the spectra at $T \gtrsim 80$ K). The quadrupole shifts, ε, of the two fitted sextets as a function of temperature are plotted in Fig. 3. At 20 K, one sextet with a relative spectral area of 65% has $\varepsilon = +0.16 \pm 0.02$ mms^{-1}. This corresponds to a spin direction with $\theta \approx 21°$ (i.e., an out-of-plane spin rotation of $\approx 69°$) in part of the α-Fe$_2$O$_3$ nanoparticle sample. The other sextet (with a relative spectral area of 35% at 20 K) has a quadrupole shift of $\varepsilon = +0.08 \pm 0.02$ mm/s, corresponding to $\theta \approx 39°$. At increasing temperature, the quadrupole shifts of both sextets decrease, and at 130 K, the ε-values are close to 0.00 mm/s for both sextets (Fig. 3). We have considered other fitting procedures than using two sextets and found that they produced qualitatively similar results (i.e., untypical ε-values in the range of around $+0.16$–0.00 mm/s are still obtained) or they give less good fits. The spectra cannot be described solely by a superposition of two sextets for α-Fe$_2$O$_3$ being truly above and below the Morin transition. The fact that we get two spin directions, θ, of 21° and 39° is most likely a consequence of fitting with two sextets rather than the spin orientation being preferentially in these two specific directions. Correspondingly, fitting with three sextets gives three spin directions ($\neq 0°$, 90°). Presumably there is a distribution of spin orientations around the mean value of $\theta = 27°$.
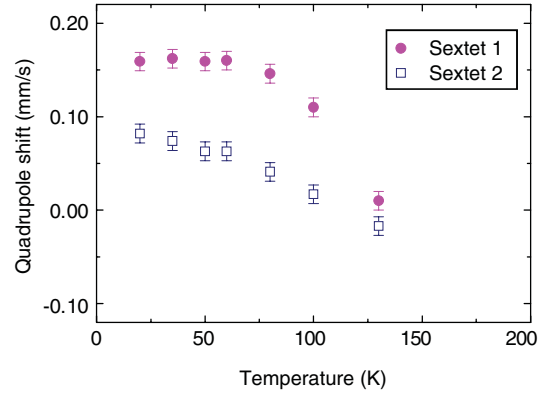
FIG. 3. (Color online) The quadrupole shift of the two sextet components (sextet 1 (filled circles) and sextet 2 (open squares)) in the Mössbauer spectra of the α-Fe$_2$O$_3$/NiO nanoparticles as a function of temperature.

The doublet present in the Mössbauer spectra of α-Fe$_2$O$_3$/NiO at $T > 80$ K [Fig. 2(c), 250 K] also indicates that the magnetic relaxation is faster for some of the α-Fe$_2$O$_3$ particles mixed with NiO particles compared with the pure uncoated α-Fe$_2$O$_3$ sample [Fig. 2(b)], which display only a sextet at the same temperatures. However, the relaxation is still considerably slower compared with the ferrofluid sample [Fig. 2(a)].

B. Neutron diffraction

Neutron powder diffraction is another useful technique to obtain information about spin rotation in α-Fe$_2$O$_3$ relative to the [001] axis. In neutron diffraction data, the dominant contribution to the intensity originating from magnetic scattering is given by the magnetic structure factor, which is proportional to the component of the magnetic moment $\vec{\mu}$ perpendicular to the scattering vector $\vec{q}$. Therefore, for α-Fe$_2$O$_3$ the intensity of the magnetic (003) reflection has its maximum when the spins are perpendicular to the [001] axis and almost vanishes when the spins become parallel to the [001] axis.[28] We can write the variation in intensity I as a function of the angle γ between $\vec{\mu}$ and $\vec{q}$ as

$$I(\vec{q},T) = c(\vec{q},T)\mu^2 \sin^2 \gamma(\vec{q}), \qquad (4)$$

where, for $\vec{q} = $ [003] in hematite and $\gamma(\vec{q})$ is the polar angle between the magnetic moment and the [001] axis (i.e., $\gamma(\vec{q} = [003]) = \theta$ used in Eq. (3)). Within the prefactor $c(\vec{q},T)$ is included the square of the magnetic structure and form factors, which depend on the scatting vector $\vec{q}$, and the Debye–Waller factor, which depends on $\vec{q}$ and T.

Neutron diffraction data for the dried sample of α-Fe$_2$O$_3$ nanoparticles are shown in Fig. 4(a). We have subtracted a linear background and fitted the data with four Lorentzian lines. Within uncertainty, no change is observed for the integrated intensities (the areas) of the reflections in the studied temperature range of 20–300 K (i.e., no spin rotation is observed). The integrated intensities at all measured temperatures (20–300 K) of the magnetic (003) and (101) reflections scaled to that of the structural (104) reflection are
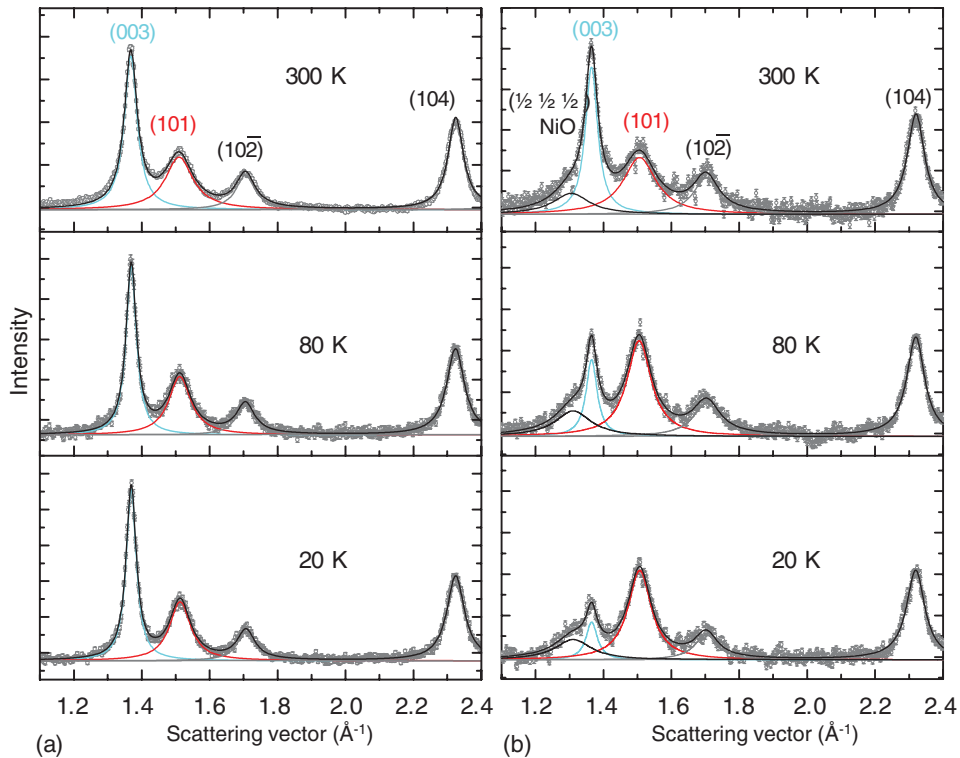
FIG. 4. (Color online) Neutron powder diffraction data obtained at 20, 80, and 300 K of (a) 8-nm α-Fe$_2$O$_3$ particles and (b) α-Fe$_2$O$_3$/NiO nanoparticles. The solid lines are fits to data with Lorentzian lines and a background with constant slope.

$I_F(003) = 0.81 \pm 0.02$ and $I_F(101) = 0.60 \pm 0.02$ (the indices F denote that these results are from the pure α-Fe$_2$O$_3$ sample).

Neutron diffraction data of the composite α-Fe$_2$O$_3$/NiO nanoparticle sample are shown in Fig. 4(b). It is apparent from the changing intensities of the magnetic (003) and (101) reflections that a large spin rotation occurs in α-Fe$_2$O$_3$ at low temperatures. We have applied the same fitting procedure as above but included an extra Lorentzian line to account for the only NiO reflection within the data range, the antiferromagnetic $(\frac{1}{2}\frac{1}{2}\frac{1}{2})$ reflection of NiO observed at around $q = 1.28$ Å^{-1}. The integrated intensities I_N of the magnetic (003) and (101) reflections in the α-Fe$_2$O$_3$/NiO composite scaled to that of the structural (104) reflection (where the indices N denote that these results are from the composite α-Fe$_2$O$_3$/NiO sample) are plotted in Fig. 5. This simple procedure for determining peak intensities is equivalent to using FullProf in the profile matching mode. It was adopted because a full structure refinement with FullProf of just one magnetic NiO peak and four hematite peaks (two nuclear and two magnetic) would need to be too constrained to be meaningful. Between $\sim$180 K and 300 K, the values are close to those found for the pure α-Fe$_2$O$_3$ sample (indicated by the arrows in Fig. 5), but at temperatures below $\sim$150 K, the (003) reflection decreases significantly in intensity, whereas the (101) reflection increases. At 20 K we find that the integrated intensity of the magnetic (003) reflection I_N scaled to the structural (104) reflection, is $I_N(003) = 0.19 \pm 0.02$ (Fig. 5). In the previous paragraph we found $I_F(003) = 0.81 \pm 0.02$ at 20 K, and we know from Mössbauer spectroscopy (Sec. III A) that this corresponds to $\theta_F \sim 75°$.

If we assume that $c(\vec{q},T)$ and μ in Eq. (4) are the same for the (003) reflection of both samples at 20 K, we may write $I_N(003)/I_F(003) = \sin^2\theta_N / \sin^2\theta_F$ and thereby calculate the angle θ_N of the spin orientation relative to [001] of α-Fe$_2$O$_3$ in the composite at 20 K to be $\sim$28°. This corresponds well to the Mössbauer results, in which we found (within the two-sextet model) that approximately 65% of the spins had an angle of 21° and 35% had one of 39° at 20 K, giving a mean value of 27°. Applying the same analysis to the 80 K Mössbauer spectroscopy and neutron diffraction data gives mean values of θ_N of $\sim$37° and $\sim$38°, respectively.

From the broadening of the magnetic (003) and (101) reflections it is possible to estimate the magnetic correlation lengths l_m perpendicular to the (001) and (101) planes as $l_m = 2\pi/(\text{FWHM} - B_i)$, where B_i is the instrumental line broadening and FWHM is the Full Width at Half Maximum of the (003) and (101) reflections obtained from fitting data with Lorentzian lines. We find that the magnetic correlation lengths essentially remain unchanged across the spin rotation temperatures ($l_{m(003)} = 15 \pm 1$ nm and $l_{m(101)} = 6 \pm 1$ nm at 20 K), with values similar to those of the pure α-Fe$_2$O$_3$ sample ($l_{m(003)} = 14 \pm 1$ nm and $l_{m(101)} = 7 \pm 1$ nm). (In all the neutron diffraction data (Fig. 4), the (003) reflection is noticeably narrower than the (101) reflection. This is due to oriented attachment of some of the α-Fe$_2$O$_3$ particles into chains along the [001] direction, combined with formation of magnetic coherence between attached particles as described in detail in Ref. 9.) When comparing the magnetic correlation length to particle size analysis,[9] based on XRD measurements and TEM, we find that the magnetic correlation
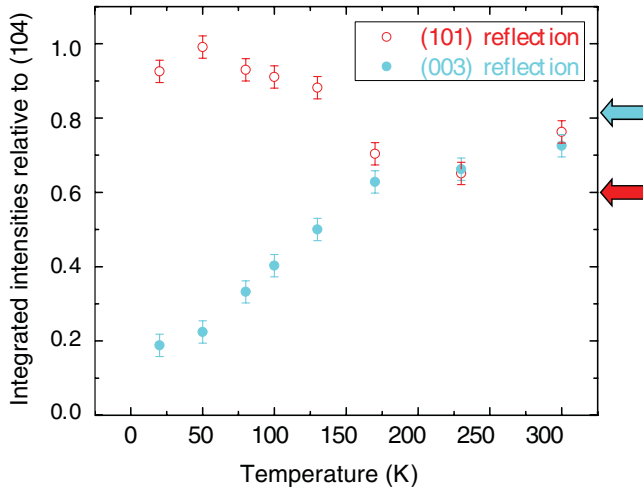
FIG. 5. (Color online) The integrated intensities of the magnetic reflections [(003), filled circles, and (101), open circles] of α-Fe$_2$O$_3$ nanoparticles mixed with NiO particles as a function of temperature. The integrated intensities are given relative to that of the structural (104) reflection. The cyan/medium gray and red/dark gray arrows to the right indicate the mean integrated intensities (scaled) of the (003) and (101) reflections, respectively, found for pure α-Fe$_2$O$_3$ nanoparticles at temperatures between 20 and 300 K.

length is similar to the crystalline correlation length (i.e., the α-Fe$_2$O$_3$ particles are single-domain at all temperatures), both in the pure α-Fe$_2$O$_3$ sample and the α-Fe$_2$O$_3$/NiO sample. This excludes the possibility that the α-Fe$_2$O$_3$ particles may have a multidomain-like magnetic structure, where the spin orientation in part of a particle is different from that in another part of the same particle. The absence of domain walls in the α-Fe$_2$O$_3$ nanoparticles in the α-Fe$_2$O$_3$/NiO composite is in good agreement with the general perception that nanoparticles are too small to have domains. Instead, it can be concluded that, because the particles are single-domain particles at all studied temperatures, the sublattice magnetizations of individual α-Fe$_2$O$_3$ particles rotate coherently out of the (001) plane.

IV. DISCUSSION

The Mössbauer and neutron diffraction data for the α-Fe$_2$O$_3$/NiO sample lead us to the following picture of the spin structure of the α-Fe$_2$O$_3$ nanoparticles in the composite. At low temperatures ($T = 20$ K), the sublattice magnetization directions of the individual particles are rotated coherently out of the (001) plane. The magnetization attains an average direction close to $\theta = 27°$ at 20 K. With increasing temperature (50-180 K) the sublattice magnetization directions approach the (001) plane. Previously, distinct intermediate states ($\theta \neq 0°, 90°$) have been proposed to exist in Al-substituted bulk-like α-Fe$_2$O$_3$ during the Morin transition.[29,30] The spin rotation observed in α-Fe$_2$O$_3$/NiO has similarities with that observed in systems of interacting α-Fe$_2$O$_3$ nanoparticles[17] but it is much larger. In the following, we discuss exchange interaction between neighboring particles with different directions of easy axes as an origin of spin rotation with $\theta \neq 0°, 90°$.

A. Theoretical model for spin rotation in interacting nanoparticles

We first consider a simple example with two particles with uniaxial anisotropy at low temperatures, in which one sublattice of one particle interacts with one sublattice of the other particle. A schematic drawing of the two interacting particles, p and q, with anisotropy constants K_p and K_q and volumes V_p and V_q, respectively, is shown in Fig. 6. Here, the easy axes, $\vec{e}_p$ and $\vec{e}_q$ of the two particles form an angle α. Because of the exchange interaction at the interface, the sublattice magnetization directions $\vec{M}_p$ and $\vec{M}_q$ are rotated by the angles θ_p and θ_q, respectively. For simplicity, we consider only one sublattice of particle p interacting with one sublattice of particle q, and we assume that the exchange interactions between surface spin of neighboring particles result in an interaction energy given by Eq. (2). The magnetic energy may then be written as

$$E(\theta_p, \theta_q) = K_p V_p \sin^2\theta_p + K_q V_q \sin^2\theta_q$$
$$- J_{\text{eff}} M_p M_q \cos(\alpha - \theta_p - \theta_q) \quad (5)$$

where the first two terms are the anisotropy energies of particles p and q, and the last term represents the effective exchange interaction between the two particles. To find energy minima, Eq. (5) is differentiated with respect to θ_p and θ_q, and we obtain

$$\frac{\partial E}{\partial \theta_p} = 2 K_p V_p \sin\theta_p \cos\theta_p + J_{\text{eff}} M_p M_q$$
$$\times \sin(\alpha - \theta_p - \theta_q) = 0 \quad (6)$$

and

$$\frac{\partial E}{\partial \theta_q} = 2 K_q V_q \sin\theta_q \cos\theta_q + J_{\text{eff}} M_p M_q$$
$$\times \sin(\alpha - \theta_p - \theta_q) = 0, \quad (7)$$
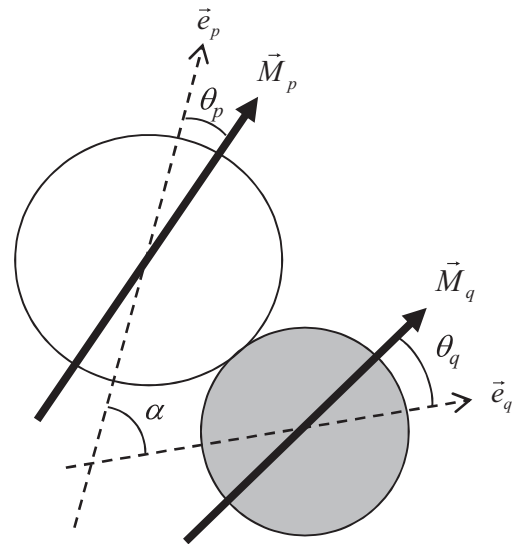
FIG. 6. Schematic illustration of two interacting nanoparticles with easy axes $\vec{e}_p$ and $\vec{e}_q$ and sublattice magnetization directions $\vec{M}_p$ and $\vec{M}_q$. α is the angle between the two easy axes, and θ_p and θ_q denote the angles between the easy axes and the sublattice magnetization of the two particles.
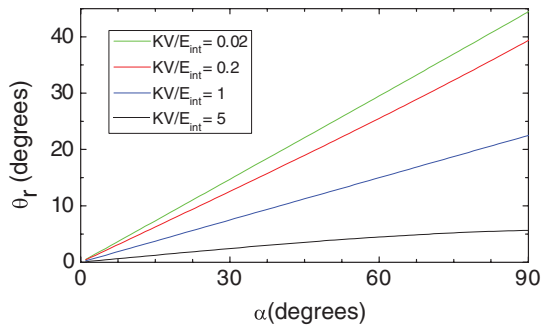
FIG. 7. (Color online) The dependence of θ_r as a function of α, as given by Eq. (10), for $KV/E_{\text{int}} = 0.02, 0.2, 1,$ and 5.

from which we find

$$\sin 2\theta_q = \frac{K_p \, V_p}{K_q \, V_q} \sin 2\theta_p. \qquad (8)$$

Inserting Eq. (8) into Eq. (6), we obtain

$$K_p V_p \sin 2\theta_p - J_{\text{eff}} M_p M_q$$
$$\times \sin\left[\alpha - \theta_p - \frac{1}{2}\arcsin\left(\frac{K_p \, V_p}{K_q \, V_q}\sin 2\theta_p\right)\right] = 0, \quad (9)$$

which may be solved numerically to obtain values of θ_p for given values of the magnetic anisotropy energies, the angle α, and the interaction energy, $E_{\text{int}} = J_{\text{eff}} M_p M_q$.

To illustrate the effects of interactions, we consider the simple case where $K_p V_p = K_q V_q \equiv KV$, for which one can find an analytical solution for the rotation angle $\theta_p = \theta_q \equiv \theta_r$,

$$\cot 2\theta_r = \frac{KV}{E_{\text{int}} \sin\alpha} + \cot\alpha. \qquad (10)$$

The dependence of θ_r as a function of α for $KV/E_{\text{int}} = 0.02, 0.2, 1,$ and 5 is shown in Fig. 7. If the easy axes of the two particles are parallel ($\alpha = 0°$), one finds the intuitive result $\theta_r = 0°$, irrespective of the strength of the interaction energy. However, if the interaction energy is large compared with the anisotropy energy, and the value of the angle α is large, the rotation angle θ will be large at low temperatures. In the above calculations we assumed that $K_p V_p = K_q V_q$, and therefore the rotation angle is the same in both particles, and the maximum rotation is 45° when $\alpha = 90°$. In cases where $K_p V_p > K_q V_q$, rotation angles up to 90° may exist in particle q.

At higher temperatures, the sublattice magnetization directions perform fast fluctuations around the directions corresponding to the energy minima.[8,26,27] Therefore, M_p and M_q should be replaced by the thermal averages $\langle M_p \rangle$ and $\langle M_q \rangle$ such that the interaction energy is given by $E_{\text{int}} = J_{\text{eff}}\langle M_p \rangle\langle M_q \rangle$. With increasing temperature, $\langle M_p \rangle$ and $\langle M_q \rangle$ decrease, leading to an increase of $\cot 2\theta_r$, i.e. a decrease of the spin rotation angle.

B. The α-Fe$_2$O$_3$/NiO composite

The assumption of simple uniaxial anisotropy in the above calculations is not fulfilled in the α-Fe$_2$O$_3$/NiO system. Hematite nanoparticles have a large uniaxial anisotropy for rotations out of the hexagonal (001) plane and a much smaller anisotropy for rotations within the (001) plane.[20,31,32] The

anisotropy of bulk NiO with an fcc structure is also quite complex,[28] with the spins confined in the (111) plane due to a large out-of-plane anisotropy, and the easy direction is in the [11$\bar{2}$] direction within the (111) plane,[22] but the anisotropy in nanoparticles may be different from that of bulk NiO. Moreover, in the model described in Sec. IV A, only interactions between two particles are considered, but in a sample of interacting nanoparticles it is most likely that each particle interacts with more than one neighboring particle. However, the simple model can be used to obtain a qualitative understanding of the influence of interactions on the spin structure in systems of nanoparticles.

According to the model, the relative size of the anisotropy energies of the interacting particles and the interaction energy are important parameters. In α-Fe$_2$O$_3$ nanoparticles, the out-of-plane anisotropy constant is on the order of 10^4–10^5 Jm^{-3}.[21] In 8-nm hematite particles, this corresponds to an anisotropy energy on the order of 200–2000 K. Using the bulk value for the out-of-plane anisotropy constant of NiO ($K_1 \cong 4.3 \times 10^5$ Jm^{-3}),[33] one finds that for the NiO nanoparticles, the anisotropy energy $K_1 V_1$ is around 9000 K.[13] Mössbauer studies of samples of strongly interacting pure α-Fe$_2$O$_3$ and pure NiO particles yielded interaction energies $J_{\text{eff}} M_p M_q$ for ensembles of particles on the order of 600 K[17] and 360 K,[13] respectively. Similarly, studies of the α-Fe$_2$O$_3$/NiO composite[18] indicate interaction energies on the same order of magnitude.

Based on the model discussed in Sec. IV A, the large rotation angles at low temperatures indicate that the easy axes of the NiO nanoparticles form large angles, α, with the easy axis within the (001) plane of the majority of the α-Fe$_2$O$_3$ nanoparticles and may be close to being perpendicular to this. The apparent absence of small rotation angles at low temperatures suggests that the easy axes of neighboring α-Fe$_2$O$_3$ and NiO particles are not completely randomly oriented relative to each other. Assuming that the angle α between the easy axes of neighboring particles has a preferred value might seem too simplistic, considering the random orientation of the easy axes one might expect for particles in a powder. However, oriented attachment between nanoparticles of the same material has been observed in numerous systems and is considered to be a mechanism for crystal growth.[34,35] Correspondingly, there is nothing fundamental that prevents epitaxial assembly of particles of different materials to occur under the right conditions, and therefore it is possible that the particles in the α-Fe$_2$O$_3$/NiO system might have a tendency to assemble with a preferred orientation when mixed in water and subsequently dried. Epitaxial assembly of NiO and α-Fe$_2$O$_3$ can be obtained if the close-packed oxygen structure in the two materials is continued across their interface, such that the [001] axis and a [100] axis of α-Fe$_2$O$_3$ are parallel to a [111] axis and a [11$\bar{2}$] axis of NiO, respectively, as illustrated in Fig. 8. In this case, the antiferromagnetic modulation vectors along [001] of α-Fe$_2$O$_3$ and [111] of NiO can be parallel, too, and hence the antiferromagnetic modulation can continue across the epitaxial assembly at the particle interface.

Because the relative spatial orientation of the particles is crucial for understanding the spin reorientation, TEM can give useful information. TEM has to date been the key
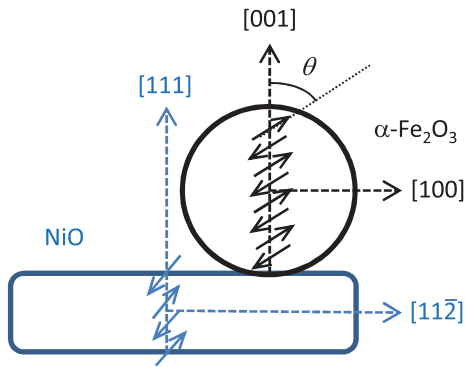
FIG. 8. (Color online) Schematic illustration of epitaxial attachment of α-Fe$_2$O$_3$ and NiO nanoparticles.

technique to verify oriented attachment.[34,35] However, we found it difficult to obtain micrographs that could resolve the particle attachment on composite samples. TEM imaging gives a two-dimensional (2D) projection of the aggregated crystals; therefore, to obtain useful images, the aggregates must have a 2D rather than a 3D complexity. In the case of a composite, it is also somewhat rare to get neighboring particles aligned such that two sets of lattice planes of each particle are visible, as needed for fully establishing crystal orientations. Existence of similar lattice spacings in α-Fe$_2$O$_3$ and NiO further complicates the image interpretation. However, the different morphologies of α-Fe$_2$O$_3$ (spherical) and NiO (plate-shaped) nanoparticles helped image interpretation. A few examples of aggregated α-Fe$_2$O$_3$ and NiO nanoparticles, from which the particle orientations can be established, are shown in Figs. 9(b) and 9(c). The images suggest the existence of preferred attachment of α-Fe$_2$O$_3$ and NiO nanoparticles.

An energy-filtered TEM image [Fig. 9(a)] of the rim of a larger aggregate shows that the α-Fe$_2$O$_3$ and NiO nanoparticles are intimately mixed at a scale of $\leqslant \sim 20$ nm. In Fig. 9(b), a high-resolution bright field image of an agglomerate of at least 14 particles is seen. In the center of this image is a thick nanoparticle (white dashed outline), which is recognized as NiO from its (plate) shape, and 2.4-Å lattice fringes, representing (111) planes, parallel to the plane of the particle. Next to this particle, is another large nanoparticle (black dashed outline), which shows a lattice spacing of 1.46 Å (see enlargement of area in red square). These are presumably (030) planes of α-Fe$_2$O$_3$. It can be seen from the fast Fourier transform (FFT) of the red square image that the (111) planes of NiO are perpendicular to the (030) planes of α-Fe$_2$O$_3$ (i.e., it is a possibility that the [111] axis of NiO is parallel to [001] axis of α-Fe$_2$O$_3$). The nanoparticles (white outlines) in the lower half of the image are NiO particles seen from other angles; their plate shapes make $\sim 70°$ angles with the plate shape of the large NiO particle in the center. In the upper, right part of Fig. 9(b), there appear to be two chain-like assemblies of three α-Fe$_2$O$_3$ particles each. In the upper chain (dashed black outlines), the [001] axis (dashed arrow) is determined from a set of two different lattice planes. In the lower α-Fe$_2$O$_3$ chain (black outlines), only one set of lattice planes is seen, and it is difficult to determine the orientation of the [001] axis, but if we assume that the [001] axis is preferentially oriented parallel to the length of the chain (as found in Ref. 9), then the

[001] axis of this chain (indicated by a solid arrow) appears to be at an angle of $10°$ relative to that of the other chain. The attachment between the NiO particle in the center and the α-Fe$_2$O$_3$ particles in the upper right corner does not seem to have the suggested epitaxial attachment, but the particles may still find the expected arrangement locally. The (111) planes of the small NiO plate (thick white outline) are at an angle close to $90°$ to the [001] axes of the α-Fe$_2$O$_3$ chains. In Fig. 9(c), an image case very similar to that in the center of Fig. 9(b) is seen. Figure 9(c) shows a nanoparticle with lattice spacing of 1.47 Å perpendicular to the 2.4-Å lattice spacing (the (111) planes) of the small agglomerate of NiO nanoparticles (white outlines) next to it. Thus, in the TEM images, there are examples giving the possibility that the particles are attached such that the [001] axis of α-Fe$_2$O$_3$ is parallel to the [111] axis of NiO, but variations exists. Despite the complexity of such studies, further TEM studies are desirable to quantify fully the attachment of nanoparticles of different materials.

Given that the α-Fe$_2$O$_3$ and NiO nanoparticles have a tendency to attach with preferred epitaxial orientation, as described above (Fig. 8), the large rotation of the sublattice magnetization out of the (001) plane in the α-Fe$_2$O$_3$ nanoparticles suggests that the sublattice magnetization directions of the neighboring NiO nanoparticles are not in the NiO (111) plane parallel to the faces of the disc-shaped particles and may form a large angle with this plane. Neutron powder diffraction of NiO nanoparticles has recently been applied to reveal the spin direction relative to the (111) particle plane.[36] Numerous studies of ferromagnetic thin films have shown that there is commonly a spin reorientation transition such that the magnetization is perpendicular to the film plane below a critical film thickness, but within the film plane for larger film thickness. The perpendicular magnetization in very thin films can be explained by a strong magnetic anisotropy perpendicular to the film plane, because surface anisotropy becomes predominant compared with other contributions to the magnetic anisotropy.[37] The critical film thickness is temperature dependent and can be on the order of three to 10 monolayers. A similar spin reorientation transition can also be found in antiferromagnetic thin films,[38] and thus it is possible that plate-shaped NiO particles with a thickness of only 2 nm also have a large surface anisotropy, which may favor the sublattice magnetization to form a large angle to the surface plane. The faces of the disc-shaped NiO particles are (111) planes,[13] but in the fcc structure, there are four equivalent (111) planes, the three others forming angles of $70.5°$ to this. It is likely that the surface anisotropy will favor sublattice magnetization directions within or close to one of these (111) planes.

With the configuration of particle attachment described above, the spin direction in α-Fe$_2$O$_3$ is at a large angle to the α-Fe$_2$O$_3$/NiO interface plane, and the spins in α-Fe$_2$O$_3$ tend to align with the spin direction in NiO. This spin configuration is different from the perpendicular coupling explained by Koon,[5] in which the sublattice magnetization directions of the two constituents are perpendicular, but remain parallel to the interface layer.

The temperature dependence of the quadrupole splitting, shown in Fig. 3, as well as the temperature dependence of the areas of the diffraction peaks, shown in Fig. 5, indicates a
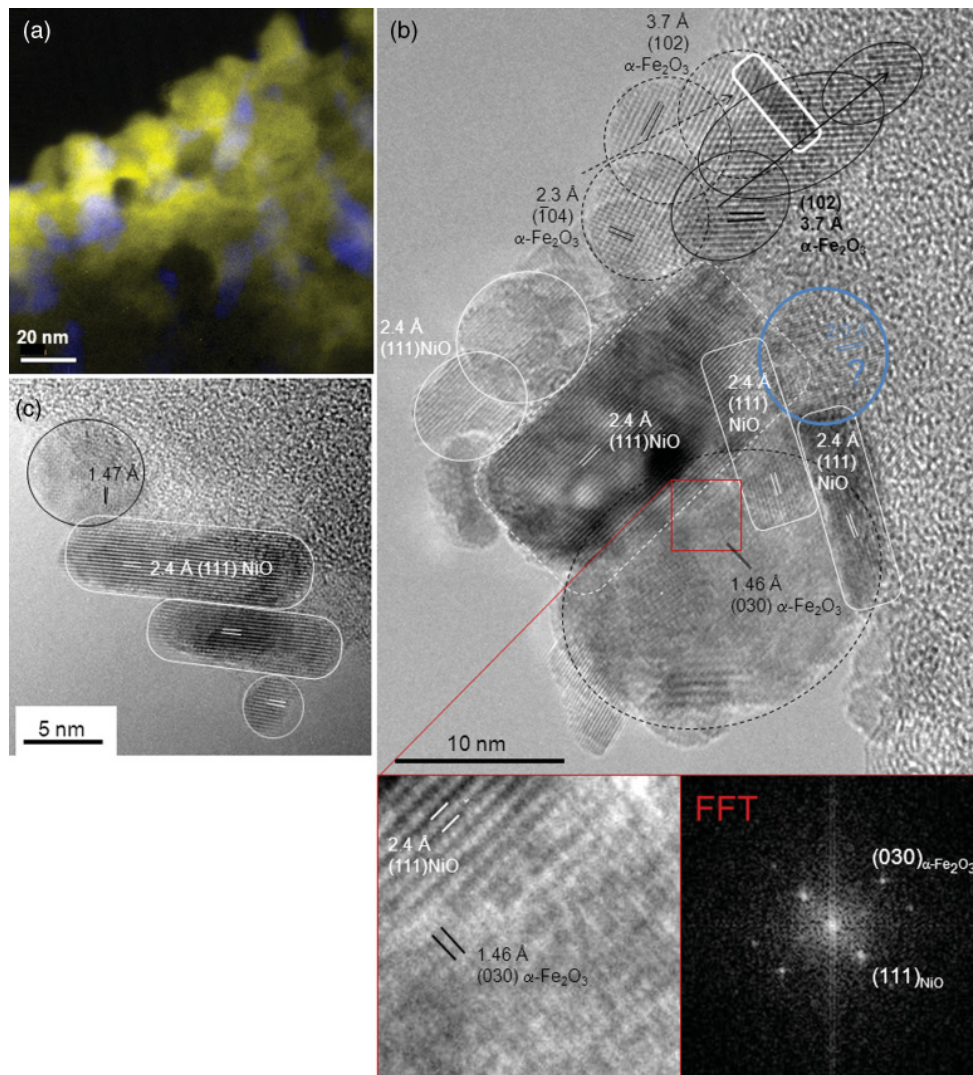
FIG. 9. (Color online) TEM images of α-Fe$_2$O$_3$/NiO nanoparticle composite. (a) Elemental map of aggregate of α-Fe$_2$O$_3$ and NiO particles. Blue/medium gray and yellow/light gray represent enrichment in iron (α-Fe$_2$O$_3$) and nickel (NiO), respectively. (b, c) TEM images of assemblies of more than 14 particles and of four particles, respectively. α-Fe$_2$O$_3$ nanoparticles are indicated by black outlines and NiO nanoparticles by white outlines. The lower panels in panel b show an enlargement of the area with red/dark gray outline and the fast Fourier transform (FFT) of this. The particle with a blue/medium gray outline in panel b is not identified (lattice plane spacings correspond to both α-Fe$_2$O$_3$ and NiO).

decrease of the rotation angle with increasing temperature. This can be explained by the decrease of the averaged sublattice magnetizations $\langle M_p \rangle$ and $\langle M_q \rangle$ with increasing temperature, as discussed in Sec. IV A.

C. Comparison with α-Fe$_2$O$_3$/CoO

In composites of α-Fe$_2$O$_3$ and CoO nanoparticles, the relaxation of the α-Fe$_2$O$_3$ nanoparticles is suppressed much more than in the α-Fe$_2$O$_3$/NiO samples, indicating a very strong interparticle interaction.[18] At first sight, it may therefore appear surprising, that the spin rotation is much smaller in the α-Fe$_2$O$_3$/CoO composite. In fact, the quadrupole shift of the α-Fe$_2$O$_3$ nanoparticles is identical to the bulk value above the Morin transition temperature ($\varepsilon = -0.100$ mm/s). Therefore, it seems that the easy axes of the CoO nanoparticles

are parallel to the (001) plane of the α-Fe$_2$O$_3$ particles. If a hematite nanoparticle is attached to a CoO particle with easy axis parallel to the (001) plane of hematite, the exchange energy can be minimized by rotation of the sublattice magnetization of hematite within the (001) plane. This would not result in any change of either the quadrupole shift in the Mössbauer spectra or of the intensity of the (003) reflection in neutron powder diffraction. Such a parallel (or antiparallel) orientation of the sublattice magnetization directions will also minimize the interparticle exchange coupling energy [Eq. (2)].

V. CONCLUSIONS

By use of Mössbauer spectroscopy, neutron diffraction, and transmission electron microscopy, we have investigated

the spin orientation in α-Fe$_2$O$_3$ nanoparticles mixed with nanoparticles of other antiferromagnetic materials. It is shown that when α-Fe$_2$O$_3$ nanoparticles are wet-mixed with NiO nanoparticles and subsequently dried, a spin reorientation transition somewhat similar to the Morin transition can be induced in the α-Fe$_2$O$_3$ particles. However, in contrast to bulk, where the Morin transition is caused by intrinsic anisotropy in α-Fe$_2$O$_3$, the spin reorientation in the α-Fe$_2$O$_3$ nanoparticles is caused by exchange coupling to the NiO particles with a different direction of easy axis. The spin rotation angle decreases with increasing temperature. This can be explained by a decrease in the average sublattice magnetization. The results presented above on α-Fe$_2$O$_3$/NiO, and compared with data on α-Fe$_2$O$_3$ and α-Fe$_2$O$_3$/CoO, suggest that nanoparticles of different types of materials can be assembled epitaxially and that this has a strong influence on their magnetic properties and, in particular, their spin orientation. It is possible that the assembly can be exploited as a way to construct and tailor, on a larger scale, composites of magnetic materials with new properties.

*fraca@fysik.dtu.dk

†Present address: SimCorp A/S, DK-2300 Copenhagen S, Denmark.

‡Present address: Department of Materials, University of Oxford, Oxford, OX1 3PH, UK.

[1] W. H. Meiklejohn and C. P. Bean, Phys. Rev. **102**, 1413 (1956).

[2] A. E. Berkowitz and K. Takano, J. Magn. Magn. Mater. **200**, 552 (1999).

[3] J. Noqués and I. Schuller, J. Magn. Magn. Mater. **192**, 203 (1999).

[4] J. Noqués, J. Sort, V. Skumryev, S. Suriñach, J. S. Muñoz, and M. D. Baró, Physics Reports **442**, 65 (2005).

[5] N. C. Koon, Phys. Rev. Lett. **78**, 4865 (1997).

[6] Y. Ijiri, T. C. Schulthess, J. A. Borchers, P. J. van der Zaag, and R. W. Erwin, Phys. Rev. Lett. **99**, 147201 (2007).

[7] S. Mørup, M. F. Hansen, and C. Frandsen, Beilstein J. Nanotechnol. **1**, 182 (2010).

[8] M. F. Hansen, C. B. Koch, and S. Mørup, Phys. Rev. B **62**, 1124 (2000).

[9] C. Frandsen, C. R. H. Bahl, B. Lebech, K. Lefmann, L. Theil Kuhn, L. Keller, N. H. Andersen, M. v. Zimmermann, E. Johnson, S. N. Klausen, and S. Mørup, Phys. Rev. B **72**, 214406 (2005).

[10] C. Frandsen and S. Mørup, J. Phys.: Condens. Matter **18**, 7079 (2006).

[11] L. Theil Kuhn, K. Lefmann, C. R. H. Bahl, S. N. Ancona, P.-A. Lindgård, C. Frandsen, D. E. Madsen, and S. Mørup, Phys. Rev. B **74**, 184406 (2006).

[12] F. Bødker, M. F. Hansen, C. B. Koch, and S. Mørup, J. Magn. Magn. Mater. **221**, 32 (2000).

[13] C. R. H. Bahl, K. Lefmann, L. T. Kuhn, N. B. Christensen, H. Vásquez, and S. Mørup, J. Phys.: Condens. Matter **18**, 11203 (2006).

[14] C. R. H. Bahl and S. Mørup, Nanotechnology **17**, 2835 (2006).

[15] T. S. Berquó, J. J. Erbs, A. Lindquist, R. L. Penn, and S. K. Banerjee, J. Phys. Condens. Matter **21**, 176005 (2009).

[16] M. Xu, C. R. H. Bahl, C. Frandsen, and S. Mørup, J. Colloid Interface Sci. **279**, 132 (2004).

[17] C. Frandsen and S. Mørup, Phys. Rev. Lett. **94**, 027202 (2005).

[18] C. Frandsen and S. Mørup, J. Magn. Magn. Mater. **266**, 36 (2003).

[19] L. Wang and L. Gao, J. Colloid Interface Sci. **349**, 519 (2010).

[20] A. H. Morrish, *Canted Antiferromagnetism: Hematite* (World Scientific, Singapore, 1994).

[21] F. Bødker and S. Mørup, Europhys. Lett. **52**, 217 (2000).

[22] W. L. Roth, Phys. Rev. **110**, 1333 (1958).

[23] S. Mørup, D. E. Madsen, C. Frandsen, C. R. H. Bahl, and M. F. Hansen, J. Phys.: Condens. Matter **19**, 213202 (2007).

[24] S. Mørup and C. W. Ostenfeld, Hyperfine Interact. C **5**, 83 (2002).

[25] T. Sugimoto, Y. Wang, H. Itoh, and A. Muramatsu, Colloid. Surf. A **134**, 265 (1998).

[26] S. Mørup, M. B. Madsen, J. Franck, J. Villadsen, and C. J.W Koch, J. Magn. Magn. Mater. **40**, 163 (1983).

[27] D. E. Madsen, L. Cervera-Gontard, T. Kasama, R. E. Dunin-Borkowski, C. B. Koch, M. F. Hansen, C. Frandsen, and S. Mørup, J. Phys.: Condens. Matter **21**, 016007 (2009).

[28] C. G. Shull, W. A. Strauser, and E. O. Wollan, Phys. Rev. **83**, 333 (1951).

[29] R. E. Vandenberghe, E. Van San, and E. De Grave, Hyperfine Interact. C **5**, 209 (2002).

[30] R. E. Vandenberghe, E. Van San, E. De Grave, and G. M. Da Costa, Czech. J. Phys. **51**, 663 (2001).

[31] F. Bødker, M. F. Hansen, C. B. Koch, K. Lefmann, and S. Mørup, Phys. Rev. B **61**, 6826 (2000).

[32] S. N. Klausen, K. Lefmann, P.-A. Lindgård, L. Theil Kuhn, C. R. H. Bahl, C. Frandsen, S. Mørup, B. Roessli, N. Cavadini, and C. Niedermayer, Phys. Rev. B **70**, 214411 (2004).

[33] M. T. Hutchings and E. J. Samuelsen, Phys. Rev. B **6**, 3447 (1972).

[34] R. L. Penn and J. F. Banfield, Geochim. Cosmochim. Acta **63**, 1549 (1999).

[35] J. F. Banfield, S. A. Welch, H. Zhang, T. T. Ebert, and R. L. Penn, Science **289**, 751 (2000).

[36] E. Brok, B. Lebech, K. Lefmann, and C. Frandsen, 5th European Conference on Neutron Scattering, Prague, Abstract **EM24-118** (2011).

[37] P. E. Jensen and K. H. Bennemann, Surf. Sci. Reports **61**, 129 (2006).

[38] D. S. Deng, X. F. Jin, and R. Tao, Phys. Rev. B **69**, 172403 (2004).

Experimental evidence for lamellar magnetism in the mineral hemo-ilmenite by polarized neutron scattering

Erik Brok,[1, 2, *] Morten Sales,[3, 4] Kim Lefmann,[3] Luise Theil Kuhn,[5] Wolfgang F Schmidt,[6]
Bertrand Roessli,[7] Peter Robinson,[8] Suzanne A McEnroe,[8] and Richard J Harrison[9]

[1]*Department of Physics, Technical University of Denmark, DK-2800 Kgs Lyngby*
[2]*Center for Electron Nanoscopy, Technical University of Denmark, DK-2800 Kgs Lyngby*
[3]*Nano-Science Center, Niels Bohr Institute, University of Copenhagen, DK-2100 Copenhagen Ø*
[4]*Department Research with Spallation Neutrons, Helmholtz-Zentrum Berlin Für Materialen und Energie GmBh, D-14109 Berlin*
[5]*Department of Energy Conversion and Storage,*
Technical University of Denmark, DK-4000 Roskilde
[6]*Jülich Centre for Neutron Science, Forschungszentrum Jülich,*
CRG with Institut Laue-Langevin, 38042 Grenoble
[7]*Laboratory for Neutron Scattering, Paul Scherrer Institute, 5232 Villigen*
[8]*Geological Survey of Norway, N-7491 Trondheim*
[9]*Department of Earth Sciences, University of Cambridge, CB2 3EQ UK*
(Dated: September 5, 2013)

Large local anomalies in the Earths magnetic field (for instance observed on large scales in Norway and Canada) have been attributed to the unusual magnetic properties of the naturally occurring mineral hemo-ilmenite, consisting of intergrown nano- to micrometer scale exsolution lamellae of canted antiferromagnetic hematite (α-Fe_2O_3) and paramagnetic ilmenite ($FeTiO_3$). The origin of stable natural remanent magnetization (NRM) in this system has been proposed to be uncompensated magnetic moments in the contact layers between the exsolution lamellae. This lamellar magnetism hypothesis is tested here by using polarized neutron diffraction to measure the orientation of hematite spins as a function of an applied magnetic field in a natural single crystal of hemo-ilmenite from South Rogaland, Norway. Polarized neutron diffraction clearly shows that the ilmenite spins do not contribute to the NRM and that hematite spins account for the full magnetization at ambient temperature. Hematite sublattice spins are shown to adopt an average angle of $56°$ with respect to a saturating magnetic field, which is intermediate between the angle of $90°$ predicted for a pure canted moment and the angle of $0°$ predicted for a pure lamellar moment. The observed NRM is consistent with the vector sum of both lamellar magnetism and canted antiferromagnetic contributions. The relative importance of the two contributions varies with the length scale of the microstructure, with the lamellar contribution increasing when exsolution occurs predominantly at the nanometer rather than the micrometer scale.

I. INTRODUCTION

The mineral intergrowth hemo-ilmenite, consisting of an ilmenite host ($FeTiO_3$) with several populations of hematite (α-Fe_2O_3) exsolution lamellae, has been studied extensively because of its importance as a source of anomalies in the magnetic field of the Earth[1,2] and potentially also on Mars[3], and because of its unusual magnetic properties that are not explained by the magnetic properties of the individual constituent minerals. Natural samples of hemo-ilmenite have a large and extremely stable natural remanent magnetization, which is believed to be related to the fine exsolution structure of the intergrown hematite and ilmenite phases[2,4]. Solid solution hematite-ilmenite [$xFeTiO_3$-$(1-x)Fe_2O_3$] with compositions in the range $0.5 < x < 0.85$ are magnetic semiconductors[5,6] and a detailed understanding of the complex magnetic properties of natural samples of nano-structured hemo-ilmenite could lead to important discoveries that could be utilized in spin-tronics devices.[7–9] Hemo-ilmenite consists of the minerals hematite (α-Fe_2O_3) which is antiferromagnetic (AFM) with a Néel temperature of 955 K [10] and ilmenite ($FeTiO_3$) which is paramagnetic at room temperature, but is AFM ordered below a Néel Temper-

ature of 58 K. [11]

Hematite crystallizes in the $R\bar{3}c$ (corundum) structure with the Fe^{3+} magnetic moments ferromagnetically aligned within the basal (ab) planes of the hexagonal structure, while moments on adjacent planes are antiparallel apart from a small canting of approximately $0.065°$. [10] The canting, which is in the basal plane, gives a small net magnetic moment, and hematite is thus often referred to as a weak ferromagnet (rather than an antiferromagnet). In pure bulk hematite the spins undergo the so-called Morin transition at ($T_M \approx 264$ K [12,13]). The Morin transition is a spin-flop transition, where the two AFM sublattices change their spin direction from perpendicular to parallel to the c-axis. However, substitution of even small amounts ($\approx 1\%$) of Ti in hematite is known to suppress the transition[12,13] and it does not occur in hemo-ilmenite samples. The crystal structure of ilmenite is $R\bar{3}$ and is identical to the hematite structure, but with alternating layers of Fe^{2+} and Ti^{4+} ions instead of Fe^{3+}. In ilmenite below the Néel temperature the Fe^{2+} moments are aligned along the c–axis and antiparallel between adjacent Fe^{2+} layers (see Fig. 1). The lattice parameters of hematite and ilmenite are very similar ($a = b = 5.038$ Å and $c = 13.772$ Å for hematite[10],
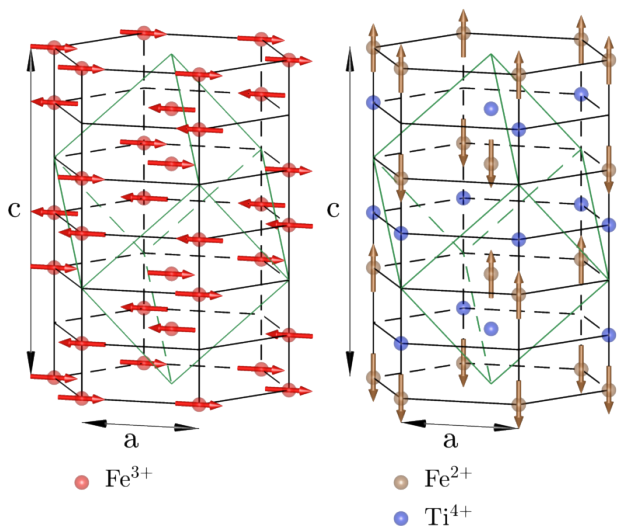
FIG. 1. Antiferromagnetic structure of hematite and ilmenite. Let: Magnetic structure of hematite above the Morin transition. Right: Magnetic structure of ilmenite. The oxygen atoms are left out of the drawing, as is the small canting of the Fe^{3+} moments.
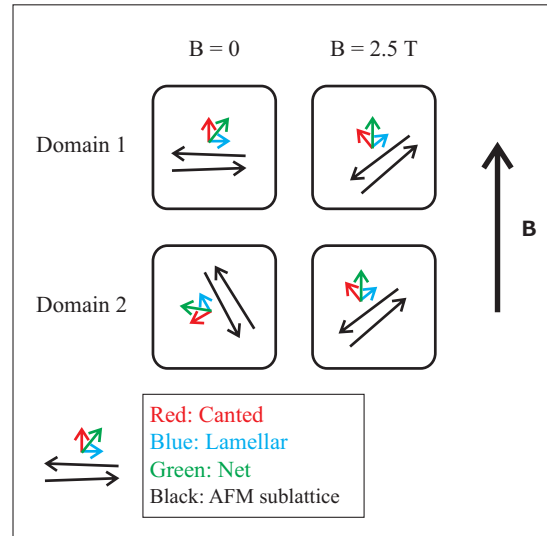

FIG. 2. Sketch of the in-plane hematite spin directions and their response to a magnetic field applied applied in the plane. The net moment is the vector sum of the CAF moment, which is almost perpendicular to the AFM sublattice, and the lamellar moment which is parallel to the AFM sublattice. In zero field the spins are (on average) randomly oriented and the two 'domains' represents two possible configuration. At a saturating field (2.5 T at room temperature) the net moment is aligned with the field and the average spin orientation is no longer random, but makes an an angle with **B** that depends on the proportion of canted and lamellar moments.

and $a = b = 5.088$ Å and $c = 14.085$ Å for ilmenite[14,15]) and the two phases are thus able to grow epitaxially together. In natural samples of hemo-ilmenite that slowly cooled around a billion years ago[16], the two phases exhibit a complex exsolution structure that has been investigated with electron microscopy[17], revealing multiple generations of epitaxially aligned intergrown lamellae ranging in thickness from a few nm to several μm in the direction of the crystallographic c-axis. The lamellae are flattened in the c-direction and extended in the basal plane. While the AFM sublattice direction in hematite above the Morin temperature is usually assumed to be within the basal plane a significant out-of-plane angle of about $30°$ has been observed in a natural hemo-ilmenite sample showing nano-scale exsolution structure.[18]

Natural samples of hemo-ilmenite show a large natural remanent magnetization of around $(1.4 - 4.2) \cdot 10^{-3} Am^2/kg$ [19] that cannot be explained by the ferromagnetic contribution from the canted antiferromagnetic (CAF) hematite. The coercivity of the samples as well as the demagnetization temperature[4] is comparable to that of hematite. The material is not only strongly magnetic, but the magnetism is also very stable. Uncompensated spins in contact layers between hematite lamellae and the ilmenite host, with magnetization aligned with the geomagnetic field at the time the sample solidified[4,20–22] have been proposed as an explanation for the strong remanent magnetization. This hypothesis, which directly links the nanoscale exsolution structure of the hemo-ilmenite samples to their unusual magnetic properties is termed lamellar magnetism and has been backed by Monte Carlo simulations of the cation ordering during exsolution,[4,20]

and measurement of exchange bias have confirmed that the NRM is associated with magnetic moments at the lamellar interfaces [23,24].

The response of the magnetic moments to an applied field can give information about the configuration of the atomic spins. In particular the response of the hematite spins to a saturating field applied in the basal plane can determine whether or not the lamellar magnetism hypothesis is a plausible explanation for the spin structure in the lamellar system. A sketch of the response of the in-plane magnetic moment to a magnetic field applied in the plane is given in Figure 2. Here we use the technique of polarized neutron diffraction to examine a natural hemo-ilmenite sample with an exsolution microstructure showing a range of lamellar sizes from coarse to fine. Through uniaxial polarization analysis we determine the average hematite spin direction in the basal plane as a function of applied magnetic fields up to 2.5 T to directly measure the response of the lamellar moments in order to confirm the validity of the lamellar magnetism hypothesis.

We find that the hematite magnetic moments saturate at an average angle of $56°$ to the applied field, which is consistent with lamellar magnetism as an important mechanism for the NRM.
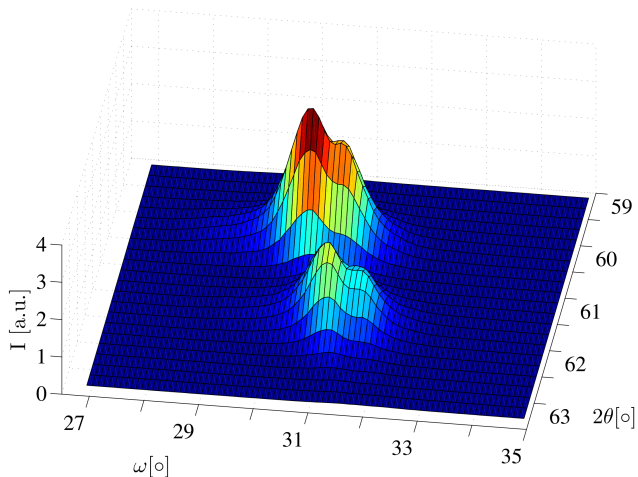
FIG. 3. Mapping of the (003) peaks measured at MOR-PHEUS. 2θ is the scattering angle and ω is the azimuthal rotation angle of the sample. The most intense peak at $2\theta \approx 60°$ is the structural ilmenite reflection and the less intense peak at $2\theta \approx 62°$ is the magnetic hematite reflection. Both peaks have a shoulder, indicating that the sample consists of two distinct crystallites oriented at an angle of approximately $0.6°$ with respect to each other.
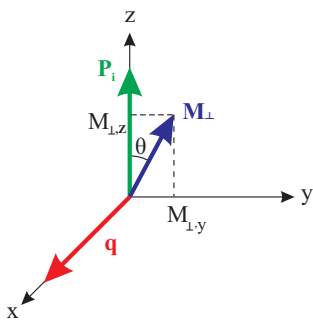

FIG. 4. Geometry in the IN12 experiment. $\mathbf{P}_i$ is the incoming polarization vector, $\mathbf{q}$ is the scattering vector and $\mathbf{M}_\perp$ is the magnetic sublattice magnetization perpendicular to $\mathbf{q}$. The magnetic field is applied in the z-direction (parallel to $\mathbf{P}_i$). The angle between $\mathbf{M}_\perp$ and $\mathbf{P}_i$ is called θ.

where K is the same constant as in (1), and $M_{\perp y}$ is the component of $\mathbf{M}_\perp$ perpendicular to $\mathbf{P}_i$. From the ratio of the SF to the NSF cross-section we can calculate θ – the angle between $\mathbf{P}_i$ and $\mathbf{M}_\perp$.

$$\frac{\sigma^{\text{SF}}}{\sigma^{\text{NSF}}} = \frac{M_\perp^2 \cos^2\theta}{M_\perp^2 \sin^2\theta} = \tan^2\theta. \quad (3)$$

With the external field applied in the z-direction (along $\mathbf{P}_i$), θ is the in-plane spin angle with respect to the applied field. To obtain the true value of the spin-angle from the measurement of the (003) magnetic hematite peak in the polarization analysis experiment we first have to correct the data for imperfect polarization of the neutron beam. Figure 5 shows NSF and SF scans of the (003)
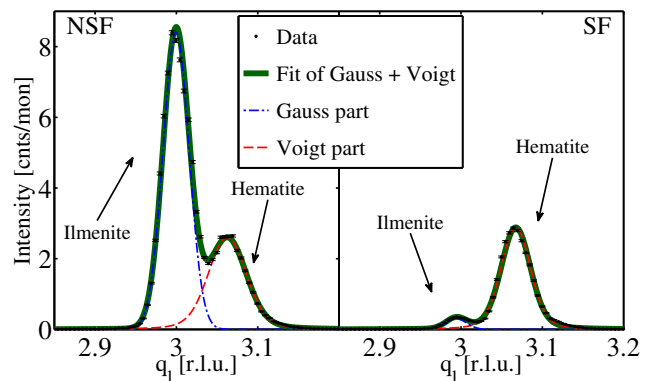

FIG. 5. NSF and SF measurement of the (003) structural ilmenite peak and the (003) magnetic hematite peak. This measurement was in an applied field of 0.25 T and at a temperature of 65 K. This data has not been corrected for imperfect polarization as can bee seen from the nonzero SF-intensity at the position of the structural ilmenite peak.

structural ilmenite and magnetic hematite peaks before the correction. It can be seen that there is a signal at the structural peak position even in the SF measurement. A non-magnetic scattering event cannot change the spin-state of the neutron and the nonzero SF-intensity on the structural position is caused by the fact that the polarization of the beam is not perfect. The data was corrected for imperfect beam polarization using the following formalism:

$$p = \frac{n_\uparrow - n_\downarrow}{n_\uparrow + n_\downarrow} = \frac{R-1}{R+1}, \quad p_\uparrow = \frac{1+p}{2}, \quad p_\downarrow = \frac{1-p}{2}, \quad (4)$$

where p is the beam polarization, $n_\uparrow$ and $n_\downarrow$ are the numbers of neutrons with spin up ($|\uparrow\rangle$) and down ($|\downarrow\rangle$), respectively, and R is the so called flipping-ratio. The probability of finding a neutron in $|\uparrow\rangle$ ($|\downarrow\rangle$) is given by $p_\uparrow$ ($p_\downarrow$). The relationship between the true cross-sections defined in Equations (1) and (2) and the measured intensities I^{NSF} and I^{SF} is then

$$\begin{pmatrix} I^{\text{NSF}} \\ I^{\text{SF}} \end{pmatrix} = \begin{pmatrix} p_\uparrow & p_\downarrow \\ p_\downarrow & p_\uparrow \end{pmatrix} \begin{pmatrix} \sigma^{\text{NSF}} \\ \sigma^{\text{SF}} \end{pmatrix}. \quad (5)$$

The flipping-ratio can be calculated from a measurement of a structural peak ($\sigma^{\text{SF}} = 0$):

$$R = \frac{I_{\text{struct}}^{\text{NSF}}}{I_{\text{struct}}^{\text{SF}}} \quad (6)$$

and the true cross-sections can then be calculated by inverting equation (5). For a full treatment of data corrections in a polarization analysis experiment see the excellent review by Wildes [30]. The flipping ratio was obtained from measurements of the structural (003) ilmenite peak for each combination of temperature and applied field. These R-values were used to obtain the true SF and NSF cross-sections from all measurements.
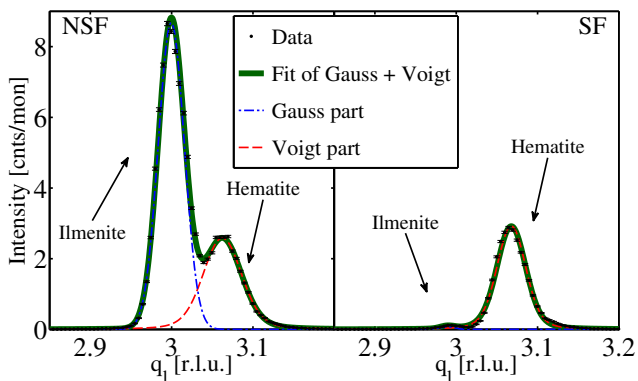
175

FIG. 6. NSF and SF measurement of the (003) structural ilmenite peak and the (003) magnetic hematite peak. This measurement was in an applied field of 0.25 T and at a temperature of 65 K. This data has been corrected for imperfect polarization with a flipping ratio of $R = 43$. The ilmenite reflection is only present in the NSF signal whereas the hematite peak is present in both the NSF and the SF signal.

FIG. 8. Spin orientation as a function of applied field for different temperatures. The error bars were obtained from Monte-Carlo simulations based on the errors on the Voigtian fits.
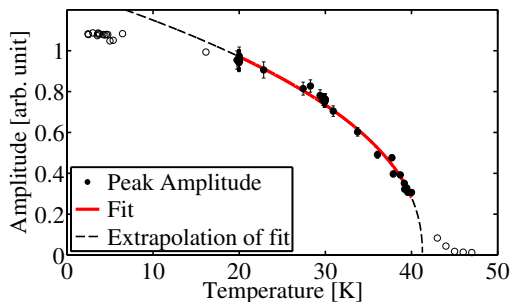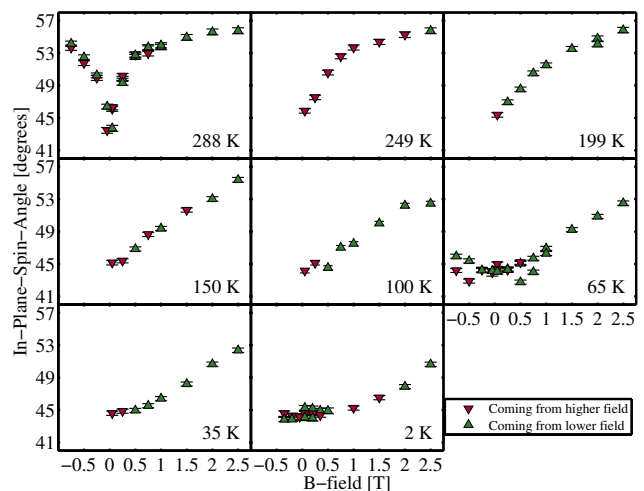

FIG. 7. Temperature variation of the $(10\frac{\bar{1}}{2})$ magnetic ilmenite peak, showing the second order phase transition. Both black and hollow points are peak amplitude measurements, however, the fit is to the black points only, since the power law behavior is only valid within approximately this range.

To confirm the AFM to paramagnetic second order phase transition of ilmenite the $(10\frac{\bar{1}}{2})$ magnetic ilmenite peak was measured and the peak amplitude is displayed as a function of temperature in Figure 7. The data was fitted to the function: $A = A_0(\frac{T_N - T}{T_N})^{2\beta}$ obtaining $T_N = 41.3$ K and $\beta = 0.22$. The Néel temperature of 41.3 K is smaller than the 58 K usually quoted for ilmenite, which is due to partial substitution of Mg^{2+} for Fe^{2+} within the ilmenite lattice.

The intensities of the (003) peaks were obtained through a fit of a Gaussian plus a Voigtian profile to the data (see Fig. 6). The former fits the structural ilmenite peak (bulk material) and the latter fits the magnetic hematite peak (Lorentz broadened peak caused by nano-size effects). Figure 6 shows the data in Figure 5 after correction for imperfect polarization. For each scan of the (003) peaks the data was corrected in the described way, using the obtained polarization. Figure 8 shows the in-plane spin orientation with respect to the applied field

calculated from Equation (3), which is the main result of our investigations. At all temperatures θ is close to 45° in zero field, which is consistent with a random alignment of the probed magnetic moments within the basal plane. When the field is applied θ increases. For the measurements at temperatures of 150 K and higher θ reaches approximately 56° at the maximum field of 2.5 T, while it only reaches angles of 50-53° at lower temperatures. At 2 K, 65 K and 288 K measurements in negative fields of increasing magnitude were performed to investigate the hysteresis of the sample. As can be seen in Figure 8 no significant hysteresis was observed at 288 K and 2 K, while there is a small, but distinct hysteresis feature in the 65 K data. In the measurement at 288 K the material is more magnetically soft than at lower temperatures and the magnetization looks to be approaching saturation at approximately 56°. The change in coercivity may be related to increased pinning of 60° and 120° domain walls in hematite at low temperatures. There is no significant change in the spin orientation or the susceptibility between 65 K and 35 K indicating that the hematite moments are not strongly coupled to the ilmenite which orders at 41.3 K.

It is unclear from the data in Figure 8 whether θ has reached saturation at the applied field of 2.5 T or not. Therefore the intensity of the (101) magnetic hematite peak was measured with unpolarized neutrons at RITA-II in applied fields up to 11 T. The field was applied in the (003) plane, while observing the (101) peak - the same geometry as in the IN12 experiment. The intensity of the (101) peak is proportional to the square of the projection of the magnetic moment perpendicular to the (101) scattering vector and its response to a magnetic field can therefore reveal the saturation field of the hematite moments. The (101) intensity was measured at
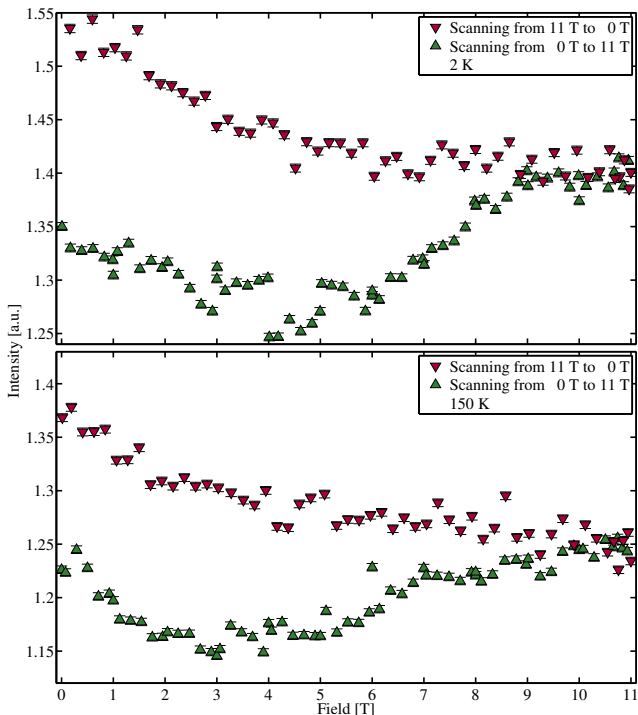
FIG. 9. Unpolarized nuclear diffraction measurement at 2 K and 150 K of the (101) peak, for applied fields between 0 T and 11 T.

2 K and 150 K and thus above and below the Néel temperature of ilmenite. The results are displayed in Fig. 9). In the 150 K data the (101) intensity decreases from 0 T to approximately 2.5 T and then increases to 11 T. This is consistent with a saturation of the (net) hematite moments followed by a rotation of the AFM sublattices away from antiparallel (AFM susceptibility). When the field is decreased to zero again there is a significant hysteresis. The picture is very much the same in the 2 K data, except that the saturation point is not reached before approximately 5 T. This confirms that for the data in Figure 8 the value of θ reaches saturation in the measurements at temperatures above 150 K, whereas it is unsaturated at lower temperatures.

IV. DISCUSSION

The strong NRM in natural hemo-ilmenite samples is believed to be caused by uncompensated magnetic moments in contact layers between exsolution lamellae (lamellar magnetism). The magnetization would then be a combination of these lamellar moments and the CAF moments. In a saturating magnetic field the net moment is expected to align parallel to the field (see Fig. 2). It is important to note that the measured angle θ is not the orientation of the net moment, but the average spin orientation. In a model with CAF moments only the spins

would be expected to align nearly perpendicular to the applied field ($\theta = 90°$). At saturation the only deviation from perpendicular will be the insignificant canting angle. For lamellar moments alone the moments would align themselves parallel to the applied field ($\theta = 0°$), whereas a combined lamellar and CAF moment would align at an intermediate angle. In either case the spin-angles are expected to be randomly distributed in zero field and the measured zero-field value of $\theta \approx 45°$ is what should be expected. The spin angles measured at temperatures above 150 K are believed to be saturated at the 2.5 T field, as confirmed by the high-field measurements at RITA-II displayed in Figure 9. The saturation value of the angle is approximately 56 ° (Fig. 8). The measured spin-angle is an average over all of the hematite spins in the sample and the result is thus consistent with a model with a combination of CAF moments aligning perpendicular to the field and lamellar moments aligning parallel to the field. If all the spins were aligned either perpendicular or parallel to the applied field the 56° would correspond to approximately 62% of the moments being CAF and 38% lamellar moments. The ratio of lamellar to CAF moments will in general depend on the relative surface area of the lamellae and it is likely that the lamellar contribution will be larger in samples with more fine scale lamellae compared to the rather coarse microstructure in the sample investigated here. While this picture is certainly too naive the 56° angle is evidence that a significant proportion of the spins are aligned parallel to the field, consistent with a model with uncompensated moments in contact layers between lamellae as important for producing the large NRM. We note that our experiment cannot determine whether the magnetic moments here termed lamellar moments are uncompensated magnetic layers exactly as described in the lamellar magnetism hypothesis[4,20,23,24] or perhaps randomly placed uncompensated magnetic moments on the interfaces between the two phases like the uncompensated magnetic moment known to produce a significant net magnetization in antiferromagnetic nanoparticles of e.g. NiO.[31,32] The hematite moments respond to the magnetic field in much the same way above and below the ordering temperature of ilmenite indicating that the lamellar moments are not coupled to the ilmenite.

V. CONCLUSION

We have reported results from a neutron diffraction experiment with uniaxial polarization analysis performed on a natural hemo-ilmenite sample with a fine exsolution structure. Measurements of the $(10\bar{1}{}_2)$ ilmenite peak confirms that the ilmenite undergoes a second order phase transition from paramagnetic to antiferromagnetic at a Néel temperature of 41.3 K. Measurements of the (003) hematite peak show that the hematite spin angle is 45° in zero applied field independent of temperature. This corresponds to a random alignment of the hematite mo-

7

ments. When a magnetic field is applied the in-plane hematite moments rotate away from the field. At temperatures from 150 K to 288 K the moment saturates in the maximum applied field of 2.5 T, making an angle of about 56° to the field. At lower temperatures the moment is not saturated in the 2.5 T field. The saturation angle of 56° with respect to the applied field strongly

supports the hypothesis of lamellar magnetism as part of the explanation for the natural remanent magnetism in natural hemo-ilmenite. Our data rule out a model with either lamellar moments or CAF moments as the sole explanation for the NRM and shows that the magnetization is a sum of contributions of similar size of uncompensated moments in contact layers and CAF moments.

---

* erik.brok@fysik.dtu.dk

[1] S. A. McEnroe, R. J. Harrison, M. J. Jackson, A. M. Hirt, P. Robinson, F. Langenhorst, F. Heidelbach, T. Kasama, A. Putnis, L. L. Brown, and U. Golla-Schindler, Journal of Physics: Conference Series **17**, 154 (2005).

[2] S. A. McEnroe, P. Robinson, and P. T. Panish, American Mineralogist **86**, 1447 (2001).

[3] S. A. McEnroe, J. R. Skilbrei, P. Robinson, F. Heidelbach, and F. Langenhorst, Geophysical Research Letters **31**, L19601 (2004).

[4] P. Robinson, R. J. Harrison, S. A. McEnroe, and R. B. Hargreaves, Nature **418**, 517 (2002).

[5] Y. Ishikawa and S.-I. Akimoto, Journal of the Physical Society of Japan **12**, 1083 (1957).

[6] Y. Ishikawa, Journal of the Physical Society of Japan **13**, 37 (1958).

[7] W. H. Butler, A. Bandyopadhyay, and R. Srinivasan, Journal of Applied Physics **93**, 7882 (2003).

[8] H. Hojo, K. Fujita, K. Tanaka, and K. Hirao, Applied Physics Letters **89**, 082509 (2006).

[9] T. Fujii, M. Kayano, Y. Takada, M. Nakanishi, and J. Takada, Solid State Ionics **172**, 289 (2004).

[10] A. H. Morrish, *Canted Antiferromagnetism: Hematite* (World Scientific, Singapore, 1994).

[11] H. Kato, M. Yamada, H. Yamauchi, H. Hiroyoshi, H. Takei, and H. Watanabe, Journal of the Physical Society of Japan **51**, 1769 (1982).

[12] F. J. Morin, Physical Review **78**, 819 (1950).

[13] P. J. Besser, A. H. Morrish, and C. W. Searle, Physical Review **153**, 632 (1967).

[14] R. M. Cornell and U. Schwertmann, *The Iron Oxides* (Wiley, Weinheim, 2003) pp. 3–527.

[15] D. H. Lindsley, Carnegie Inst. Washington Year Book **64**, 144 (1965).

[16] U. Schärer, E. Wilmart, and J. C. Duchesne, Earth and Planetary Science Letters **139**, 335 (1996).

[17] S. A. McEnroe, R. J. Harrison, P. Robinson, and F. Langenhorst, Geophysical Journal International **151**, 890 (2002).

[18] R. J. Harrison, S. A. McEnroe, P. Robinson, and C. J. Howard, American Mineralogist **95**, 974 (2010).

[19] P. Robinson, F. Heidelbach, A. M. Hirt, S. A. McEnroe, and L. L. Brown, Geophysical Journal International **165**, 17 (2006).

[20] P. Robinson, R. J. Harrison, S. A. McEnroe, and R. B. Hargreaves, American Mineralogist **89**, 725 (2004).

[21] S. a. McEnroe, P. Robinson, F. Langenhorst, C. Frandsen, M. P. Terry, and T. Boffa Ballaran, Journal of Geophysical Research **112**, B10103 (2007).

[22] P. Robinson, Fabian K, M. S. A., and F. Heidelbach, Geophysical Journal International **192**, 514 (2013).

[23] S. A. McEnroe, B. Carter-Stiglitz, R. J. Harrison, P. Robinson, K. Fabian, and C. McCammon, Nature nanotechnology **2**, 631 (2007).

[24] K. Fabian, S. A. McEnroe, P. Robinson, and V. P. Shcherbakov, Earth and Planetary Science Letters **268**, 339 (2008).

[25] J. C. Duchesne, Mineralium Deposita **34**, 182 (1999).

[26] P. Böni and P. Keller, PSI Proceedings **2**, 35 (1996).

[27] E. Brok, *Investigation of the unusual magnetic properties of hemo-ilmenite by neutron scattering*, Master thesis, University of Copenhagen (2009).

[28] K. Lefmann, C. Niedermayer, A. B. Abrahamsen, C. Bahl, N. Christensen, H. Jacobsen, T. Larsen, P. Häfliger, U. Filges, and H. Rønnow, Physica B: Condensed Matter **385-386**, 1083 (2006).

[29] R. Moon, T. Riste, and W. Koehler, Physical Review **181**, 920 (1969).

[30] A. R. Wildes, Neutron News **17**, 17 (2006).

[31] J. T. Richardson, D. I. Yiagas, B. Turk, K. Forster, and M. V. Twigg, Journal of Applied Physics **70**, 6977 (1991).

[32] C. R. H. Bahl, M. F. Hansen, T. Pedersen, S. Saadi, K. H. Nielsen, B. Lebech, and S. Mørup, Journal of physics. Condensed matter : an Institute of Physics journal **18**, 4161 (2006).
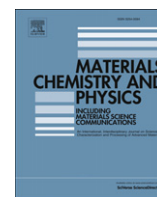
Influence of cation disorder on the magnetic properties of ball-milled ilmenite (FeTiO$_3$)

Steen Mørup [a], Helge K. Rasmussen [a], Erik Brok [a,b], Lukas Keller [c], Cathrine Frandsen [a,*]

[a] Department of Physics, Technical University of Denmark, DK-2800 Kongens Lyngby, Denmark
[b] Center for Electron Nanoscopy, Technical University of Denmark, DK-2800 Kongens Lyngby, Denmark
[c] Laboratory for Neutron Scattering, Paul Scherrer Institute, CH-5232 Villigen PSI, Switzerland

HIGHLIGHTS

► High-energy ball-milling of FeTiO$_3$ results in cation disorder.
► The magnetic hyperfine field of ^{57}Fe is strongly affected by the ball-milling.
► The Néel temperature of FeTiO$_3$ is not significantly affected by cation disorder.

ARTICLE INFO

ABSTRACT

We have investigated the evolution of crystal structure, cation disorder and magnetic properties of ilmenite (FeTiO$_3$) after increasing time of high-energy ball-milling in an inert atmosphere. Refinement of X-ray diffraction data show that the hexagonal crystal structure of ilmenite is maintained after high-energy ball-milling of up to 128 h, but neutron diffraction studies reveal significant cation redistribution of Fe^{2+} and Ti^{4+} ions in the ball-milled samples. Mössbauer spectroscopy studies show that the magnetic hyperfine field of Fe^{2+}, which is around 5 T before ball-milling, increases, and after milling times longer than 4 h a broad distribution of hyperfine fields with values up to around 40 T for Fe^{2+} is seen. This can be explained by the cation disorder induced by the ball-milling which affects the orbital contribution to the magnetic hyperfine field. In contrast to some ball-milled spinel ferrites, the Néel temperature of ilmenite is not significantly affected by the cation disorder.

© 2012 Elsevier B.V. All rights reserved.

1. Introduction

Ilmenite (FeTiO$_3$) is a common mineral, which is often found in igneous rocks. When found in larger massives, ilmenite is often explored for the production of titanium. The crystal structure of ilmenite is hexagonal and very strongly cation-ordered with Fe^{2+} and Ti^{4+}, respectively, located in the so-called A and B layers, that alternate along the [001] hexagonal axis. Ilmenite is antiferromagnetic with a Néel temperature around 58 K [1–3]. Within the A layers, the Fe^{2+} magnetic moments are ferromagnetically coupled, but Fe^{2+} in adjacent A layers have opposite magnetization directions parallel to [001]. The relatively low Néel temperature is due to a weak exchange coupling of the Fe^{2+} layers that are separated by one titanium layer and two oxygen layers. Mössbauer studies of

ilmenite have revealed that the magnetic hyperfine field at low temperatures is on the order of only 5 T [4,5].

Although ilmenite is antiferromagnetic with a low Néel temperature, it plays a surprisingly important role in carrying remanent magnetizations in rocks [6–10]. Rocks of ilmenite that is finely exsolved with hematite (α-Fe$_2$O$_3$) show magnetic properties different from those of simple mixtures of pure FeTiO$_3$ and α-Fe$_2$O$_3$, e.g., larger coercivity and saturation magnetization [6,9,10]. Owing to immiscibility of cation-ordered FeTiO$_3$ and α-Fe$_2$O$_3$ below around 1000 K, very fine exsolution lamellae are formed during slow cooling. It has been suggested that the unusual magnetic properties of the naturally formed α-Fe$_2$O$_3$–FeTiO$_3$ nanocomposite is related to uncompensated magnetic moments at cation-disordered interfaces between α-Fe$_2$O$_3$ and FeTiO$_3$ [6], but this is a subject of investigation in many current studies.

Solid-solutions of ilmenite-hematite [xFeTiO$_3$–(1 − x)Fe$_2$O$_3$], formed by very rapid cooling from ~1000 K, have also attracted much attention because of their interesting magnetic properties,

---

especially the ferrimagnetic properties found at room temperature for compositions of $0.5 \leq x \leq 0.8$ have been of interest [11–17]. The ferrimagnetic properties and the increased magnetic ordering temperature may be explained by the increased amount of magnetic Fe^{3+} ions in the B layers and nanometer-sized hematite clusters within ilmenite that interact to form a cluster-glass [12,17]. Recently, the solid-solution ilmenite–hematite system, with its ability to be a magnetic semiconductor at room temperature, has also been found promising for spintronics applications [18–21].

Generally, the magnetic and electronic properties within the ilmenite-hematite system depend on the cation order/disorder. Typically, this is determined by sample composition and cooling history, but it is interesting for understanding and modifying the magnetic and electronic properties if the cation order/disorder can be controlled otherwise.

The magnetic properties of spinel ferrites can also be strongly dependent on cation order/disorder [22–27], and high-energy ball-milling is known to redistribute cations and thereby create cation disorder in spinels (and in other materials containing more than one type of cations) [22–32]. In $ZnFe_2O_4$, which is a normal spinel, the Zn^{2+} ions are located in the tetrahedral (A) sites in the spinel lattice, whereas Fe^{3+} ions are located in the octahedral (B) sites. The exchange coupling between ions in the B sites is weak, and therefore the Néel temperature is only around 10 K [22,23]. However, after ball-milling $ZnFe_2O_4$, Fe^{3+} is distributed at both A and B sites. Because the exchange coupling between Fe^{3+} ions at A and B sites is strong, the cation disorder in ball-milled $ZnFe_2O_4$ results in an increase in the Néel temperature by more than a factor of ten [22,23,28]. In $Ni_{0.5}Zn_{0.5}Fe_2O_4$, which is essentially a normal spinel with a Néel temperature of 560 K, ball-milling also leads to an increase of the inversion as well as the Néel temperature (by ~ 50 K) [27]. In $MgFe_2O_4$, which is almost an inverse spinel, with a Néel temperature of 648 K, ball-milling leads to a decrease in the inversion and a decrease of the Néel temperature due to a diminished exchange coupling between the A and B sublattices [30]. It may be expected that a more random distribution of Fe^{2+} and Ti^{4+} between the A and B layers in ilmenite may lead to an increased magnetic ordering temperature, but this has not been verified.

A number of studies of ball-milled ilmenite have been published. For example, ilmenite nanoparticles have been prepared by ball-milling of TiO_2 with steel balls [33], and oxidation of ilmenite has been studied after ball-milling at elevated oxygen pressure [34]. It has also been shown that ball-milling of ilmenite in sulfuric acid at elevated temperatures leads to increased dissolution and can be a way to reduce acid waste water in the production of TiO_2 from ilmenite sources [35]. However, no studies of the influence of cation disorder on the magnetic properties of ilmenite have been reported.

In this work, we have ball-milled pure ilmenite in order to elucidate the influence of cation disorder on its magnetic properties. We have studied the structural and magnetic evolution as a function of milling time by use of X-ray and neutron powder diffraction and Mössbauer spectroscopy.

2. Experimental details

$FeTiO_3$ (99.9%) was obtained from Sigma Aldrich. The powder (initial amount 25 g) was high-energy ball-milled in argon using a Fritsch Pulverisette 5 with vial and balls of tungsten carbide at 200 rpm. Samples of 0.5 g were collected after ball-milling for 0 h, 1 h, 4 h, 27 h, 64 h and 128 h.

X-ray diffraction (XRD) was performed using a Panalytical diffractometer with a Cu anode. XRD data from a 2θ-angular range of $20°-145°$ were refined to the hexagonal structure of ilmenite using Rietveld refinements, which were performed using the

program WINPOW, a modified version of the LHMP1 program [36]. The least squares refinement was performed with Voigtian peak profiles and the background was modeled with Chebyshev polynomials. Initial structural parameters, atomic positions and temperature factors for the refinements were taken from [37].

Neutron powder diffraction with a neutron wavelength of 2.4576 Å was performed on a sample of ball-milled ilmenite and the as-prepared ilmenite sample on the DMC instrument at the Paul Scherrer Institute, Switzerland. A sufficient amount of sample of ball-milled ilmenite was obtained by combining the material of the samples that were ball-milled for 128 h, 64 h and 27 h. The as-prepared sample and the combined sample were loaded into 8 mm vanadium cylinders and measured at a temperature of 150 K, well above the Néel temperature of ilmenite. The neutron data were refined in order to obtain the Fe and Ti occupancies in the A and B layers of the ilmenite structure.

Mössbauer spectra were obtained using conventional constant acceleration spectrometers with sources of ^{57}Co in rhodium. The spectrometers were calibrated using a 12.5 μm foil of α-Fe. Spectra were obtained at temperatures of $20-300$ K using a closed cycle helium refrigerator from APD Cryogenics and a liquid nitrogen cryostat. A magnetic field of 0.7 T was applied by use of an electromagnet.

3. Results and discussion

XRD data with Rietveld refinement are shown in Fig. 1. Because of the similar X-ray scattering cross sections of Fe and Ti it was not feasible to refine the XRD data to a model with cation disorder. The occupancies were therefore kept at the cation-ordered values (occupancy of 1 for Fe in the A layers and 0 in the B layers and vice
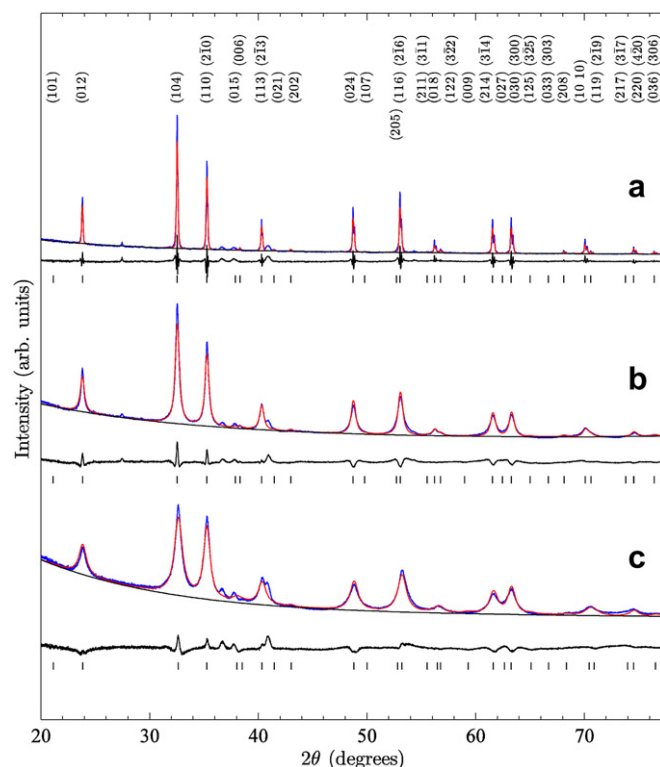

Fig. 1. X-ray diffraction patterns of the as-prepared ilmenite sample (a), the ilmenite sample ball-milled for 1 h (b) and the sample combined of the ilmenite samples ball-milled 27 h, 64 h and 128 h (c). The refined model, the background and the difference between model and experiment are also displayed.

versa for Ti). A few minor discrepancies (e.g. at approximately 27.4°, 36.6°, 37.8° and 40.9°) between the experimental data and the refined model are seen in Fig. 1. This is mainly due to a small amount of an unknown impurity phase present in all the samples. Overall, the refinements show that a hexagonal crystal structure is maintained even after ball-milling for 128 h, but with a small decrease in unit cell size as a function of ball-milling time. The change in unit cell size is preferably along the c-axis which changes from a length of 14.09 Å for the as-prepared sample to 14.00 Å after 128 h of ball-milling. Meanwhile, the length of the a-axis changes from 5.09 Å to 5.08 Å. The unit cell parameters for all the samples are given in Table 1 together with the particle sizes and the weighted pattern residual (R_{wp}) for the refinements. After 1 h of ball-milling the diffraction lines become significantly broadened indicating a decrease in crystallite size and possibly an increase in microcrystalline strain. The line broadening reaches saturation after 4 h of milling, indicating a steady-state grain size due to equilibrium between fracturing and crystal growth [38]. In case the line broadening is solely due to finite crystallite size, we find an average size of about 23 nm after 1 h of ball-milling and after 4 h the size is saturated at about 13 nm. The particle sizes given in Table 1 were estimated under the assumption that there is no microcrystalline strain. To distinguish between the contributions to the peak broadening from strain and finite particle size, the XRD data from the ball-milled sample used in the neutron scattering experiment were analyzed with the Williamson-Hall method [39]. Strain and particle size can be determined from the expression $B \cos \theta = K\lambda/D + 4e \sin \theta$, where B is the non-instrumental peak broadening (FWHM) determined from a Lorentzian fit, K is the Scherrer constant, λ is the X-ray wavelength, θ is the half scattering angle, D is the particle size and e is strain defined as $2e = \Delta d/d$, where d is d-spacing and Δd is the displacement. For XRD data of the ball-milled neutron sample the analysis with K set to 0.9 results in a particle size of $D = 22 \pm 8$ nm and a strain of $e = 0.004 \pm 0.002$.

The neutron diffraction data for the as-prepared and the ball-milled samples are shown in Fig. 2. The cation disorder results in a change in the relative peak intensities. The change is clearly seen from the relative intensities of the (024) peak and the (107) peak: For the as-prepared sample the relative area of the (107) peak is larger than the (024) peak whereas it is smaller in the ball-milled sample. Another piece of evidence is the decreased intensities of the (003) and (101) peaks in the ball-milled sample. The decreased intensity of the (003) peak readily suggests that the cation order with Fe^{2+} in A layers and Ti^{4+} in the B layers gets partially destroyed with ball-milling. The neutron data were refined in a similar way as the XRD data, but with allowance of non-zero occupancies of both Fe and Ti in both A and B layers. Refinements of the neutron data give unit cell parameters of $a = 5.0848 \pm 0.0004$ Å and $c = 14.0893 \pm 0.0009$ Å for the as-prepared sample and
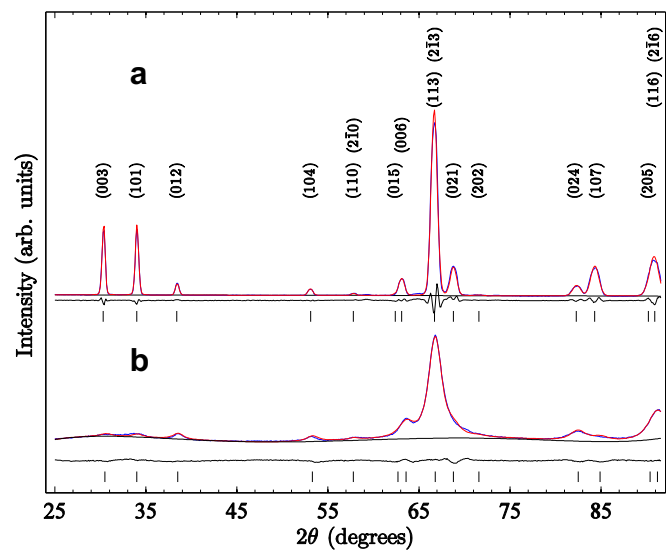

Fig. 2. Neutron diffraction data for the as-prepared sample (a) and the ball-milled sample (b). The refined model, the background and the difference between model and experiment are also displayed.

$a = 5.086 \pm 0.001$ Å and $c = 14.002 \pm 0.003$ Å for the ball-milled sample, in fair agreement with the values found with X-rays. The weighted pattern residuals of the refinements were $R_{wp} = 6.92$ for the as-prepared sample and $R_{wp} = 2.55$ for the ball-milled sample. Assuming that all non-instrumental broadening is due to the finite particle size the refinement of the neutron data gives a particle size of 12.3 ± 0.1 nm for the ball-milled sample in reasonably agreement with the X-ray data. In the refinements the occupancies of both Fe and Ti ions in both layers were constrained such that the total occupancy in each layer is one and so that the amount of Fe and Ti in the system is equal to one atom per formula unit. For the as-prepared sample the refinement resulted in occupancies of 0.997 ± 0.003 Fe and 0.003 ± 0.003 Ti in A layers and 0.003 ± 0.003 Fe and 0.997 ± 0.003 Ti in B layers. The refinements of the neutron data for the ball-milled sample give occupancies of 0.68 ± 0.02 Fe and 0.32 ± 0.02 Ti in the A layers and vice versa in the B layers. Thus, the neutron diffraction data show unambiguously that the ball-milling has resulted in a significant cation disorder.

Mössbauer spectra, obtained at 80 K, are shown in Fig. 3. The spectrum obtained before ball-milling consists of a quadrupole doublet with isomer shift of 1.18 mm s^{-1} and quadrupole splitting of 1.00 mm s^{-1} (green fit lines). These parameters are typical for paramagnetic ilmenite [8,17,35]. After ball-milling for 1 h, a second Fe^{2+}-doublet (blue fit lines) with isomer shift of 1.14 mm s^{-1} and quadrupole splitting of 2.06 mm s^{-1} has appeared. For longer ball-milling times this doublet becomes predominant, and it has relatively broad lines (~ 0.6–0.8 mm s^{-1} (FWHM)) as expected when Fe^{2+} ions are present in many different local environments with different isomer shifts and quadrupole splittings. A similar doublet has been observed in room-temperature Mössbauer spectra of ilmenite after ball-milling in vacuum for 200 h [35]. As the XRD data show that the samples still consist of a single phase with hexagonal structure and lattice constant close to that of ilmenite, we interpret the change in the quadrupole splitting and line width as being due to the cation disorder induced by the ball-milling. After ball-milling for 4 h or more, the line close to zero velocity is slightly asymmetric and more intense than the line close to 2.1 mm s^{-1}. This is due to the appearance of third doublet (red fit lines) with isomer shift around 0.37 mm s^{-1} and quadrupole splitting of about 0.90 mm s^{-1}, which can be ascribed to Fe^{3+}. The relative area of this Fe^{3+} doublet is 6–8%.

Table 1
Unit cell parameters, particle size and residual value from the Rietveld refinement of the XRD data. The statistical uncertainty on the last digit from the refinement is given in parenthesis. $D_{(001)}$ is the particle size in the direction of the crystallographic c-axis under the assumption that there is no microcrystalline strain. The uncertainty in the determination of the particle size chiefly comes from the deviation of the instrumental lineshape from Gaussian and from any non-Lorentzian broadening from the sample. The real uncertainty on the particle size is thus significantly larger than the statistical uncertainty. R_{wp} is the weighted pattern residual.

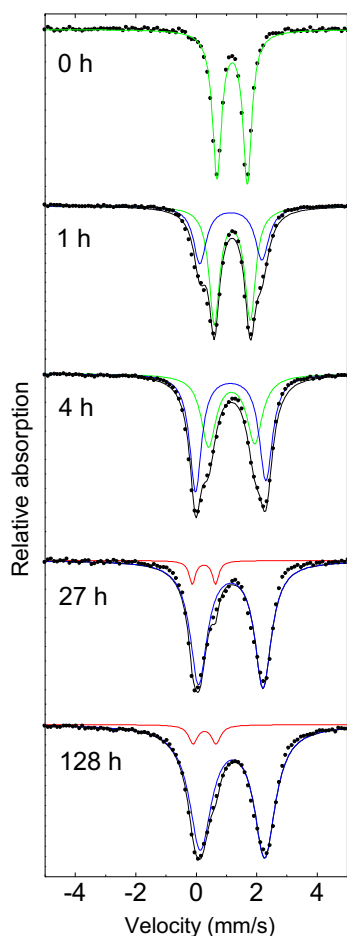| BM time [h]	a [Å]	c [Å]	$D_{(001)}$ [nm]	R_{wp}
0	5.08903 (6)	14.0923 (2)	>100	6.57
1	5.0888 (2)	14.0887 (6)	22.7 (1)	2.99
4	5.0922 (5)	14.0284 (13)	13.7 (1)	2.52
26	5.0870 (4)	14.0081 (8)	13.1 (1)	2.48
64	5.0831 (4)	14.0011 (8)	12.8 (1)	2.07
128	5.0831 (5)	13.9982 (9)	13.6 (1)	2.75

Fig. 3. Mössbauer spectra of ilmenite after ball-milling for the indicated times. The spectra were obtained at 80 K. The colored solid lines are fit to data (see text for details). (For interpretation of the references to color in this figure legend, the reader is referred to the web version of this article.)
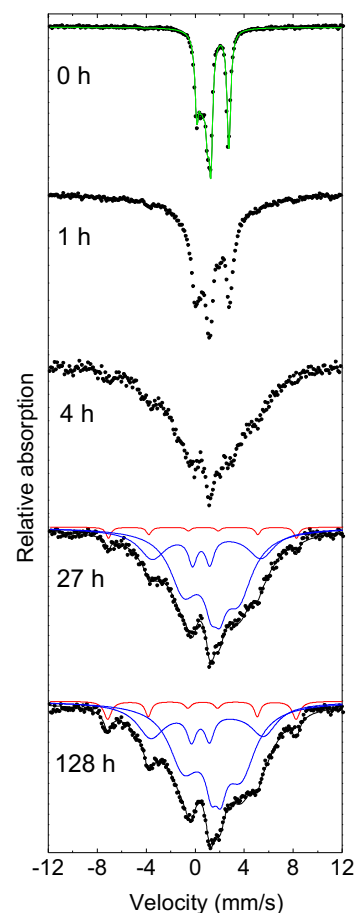

Fig. 4. Mössbauer spectra of ilmenite after ball-milling for the indicated times. The spectra were obtained at 20 K. The colored solid lines are fit to data (see text for details). (For interpretation of the references to color in this figure legend, the reader is referred to the web version of this article.)

Fig. 4 shows Mössbauer spectra, obtained at 20 K, after different ball-milling times. The spectrum obtained before ball-milling (0 h) is typical for pure ilmenite (green fit lines) below its Néel temperature with a magnetic hyperfine field of 4.6 T, an isomer shift of 1.27 mm s^{-1} and a quadrupole shift of 0.73 mm s^{-1} [4,5,8]. After ball-milling for 1 h, the central part of the spectrum has similarities to the spectrum obtained before ball-milling, but the lines are broadened. Moreover, a very broad component has appeared. After ball-milling for 4 h or more, the characteristic ilmenite component with very small magnetic hyperfine field is no longer clearly visible in the spectra. The spectra now consist of very broad sextet components with weak, but relatively well-defined absorption lines at around −7 mm s^{-1} and +8 mm s^{-1} after ball-milling 27 h or more. The spectra have very broad lines, because of distributions of magnetic hyperfine fields, isomer shifts and quadrupole shifts. There is no unique way to fit such spectra. However, reasonably good fits were obtained of the spectra recorded after ball-milling for 27 h and 128 h using a simple model with only three sextets with line area ratios constrained to 3:2:1:1:2:3 and pairwise identical line widths. The spectra have relatively well-defined absorption lines around −7 mm s^{-1} and +8 mm s^{-1} (red fit lines). In the fit, the sextet with these two lines as lines 1 and 6 has a hyperfine field of 48.0 T, an isomer shift of ∼0.60 mm s^{-1} and a quadrupole shift of ∼ −0.04 mm s^{-1}. These Mössbauer parameters indicate that it is due to Fe^{3+}, and the relative area of this component (∼5%) is in accordance with that of the Fe^{3+} doublet

seen at 80 K (around 6–8% for the sample ball-milled for 128 h). The two other sextets (blue fit lines) have very broad lines, indicating a broad distribution of magnetic hyperfine fields. Relaxation effects may also contribute to the line broadening of such spectra [17]. A fit with two sextets is therefore an oversimplification. The two (blue) sextets have isomer shifts of about 0.7 and 1.5 mm s^{-1}, hyperfine fields of around 29 T and 15 T, and relative areas of 35% and 60%, respectively, but the exact values of the parameters should not be considered physically representative. However, from the fits we can conclude that the average isomer shift of the blue sextets is around 1.15 mm s^{-1} and the average hyperfine field is on the order of 20 T, with a distribution in the range around 5–40 T. These parameters are typical for Fe^{2+}. The distribution in the Mössbauer parameters for the Fe^{2+}-sextets is due to Fe^{2+} in varying environments and relates to the cation disorder that has been observed by neutron diffraction.

The unusually small magnetic hyperfine field of Fe^{2+} in perfect ilmenite is due to the fact that the orbital, the dipolar and the Fermi contributions nearly cancel [5]. However, especially the orbital contribution is very sensitive to the local environment of the Fe^{2+} ions, and therefore the cation disorder induced by ball-milling is expected to result in larger magnetic hyperfine fields. Similarly, in quenched solid-solutions of ilmenite-hematite ($x = 0.80$ and $x = 0.70$), where the local environment of Fe^{2+} also differ from that of pure ilmenite, hyperfine fields up to 25–40 T have been observed [17].

In order to estimate the Néel temperature of the ball-milled material we have obtained Mössbauer spectra at different temperatures of the sample, ball-milled for 64 h. The spectra are shown in Fig. 5. At 40 K, the spectrum is similar to those obtained at 20 K for samples ball-milled for more than 4 h, i.e. it is magnetically split with very broad lines. At 50 K, the spectrum is dominated by a doublet, but a broad component is still visible. At higher temperatures (60–70 K) the broad component gradually disappears.

In a recent Mössbauer study of synthetic, rapidly cooled solutions of ilmenite and hematite (α-Fe_2O_3), with $x = 0.95$, it was found that nm-size hematite clusters formed in an ilmenite matrix [17]. Mössbauer spectra obtained at 60 K showed that part of the Fe^{3+} doublet in the zero-field spectrum transformed to a magnetically split component when a large field was applied. This shows that the hematite clusters were superparamagnetic, whereas the ilmenite matrix behaved paramagnetically at this temperature as expected for cation-ordered ilmenite. A spectrum, obtained at 80 K, of the ilmenite sample ball-milled for 64 h with an applied field of 0.7 T only showed a small line broadening compared to the spectrum obtained in zero-field. Therefore, the absence of magnetic splitting in the zero-field spectra above 60 K cannot be explained by superparamagnetic relaxation of ferrimagnetic clusters or antiferromagnetic clusters with a finite uncompensated moment. Thus, the disappearance of the broad, magnetically split component seems to be due to a transition to a paramagnetic phase. The Néel temperature is therefore not much different from that of perfect ilmenite, but there is not a well-defined Néel temperature. Rather, there is a distribution of Néel temperatures in the range 40–70 K.
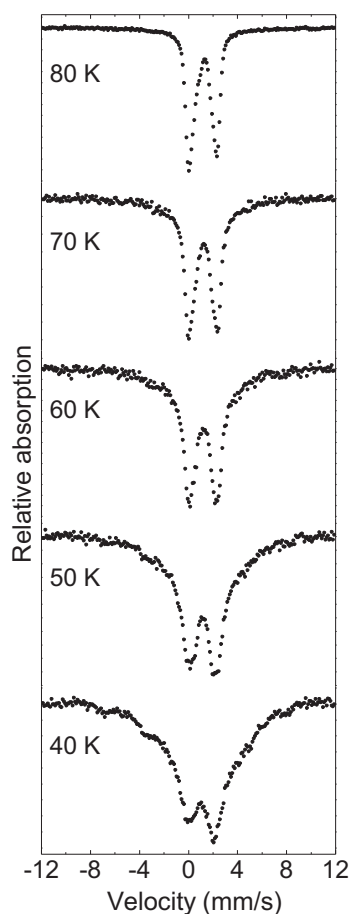
In perfect ilmenite the weak exchange coupling between Fe^{3+} ions in adjacent A layers explains the relatively low Néel temperature. One could expect that the cation disorder, induced by ball-milling leading to a distribution of Fe in both the A and B layers, would result in a stronger exchange coupling and a higher Néel temperature, as it has been seen in studies of ball-milled $ZnFe_2O_4$ [22,23,28] and $Ni_{0.5}Zn_{0.5}Fe_2O_4$ [27]. In the ball-milled ilmenite samples studied here, no noticeable increase in Néel temperature is observed. Part of the reason for this might be that the antiferromagnetic exchange coupling between nearest neighbor Fe^{2+} in adjacent A and B layers is only on the order of −10 K and comparable in size to the in-plane ferromagnetic coupling (~ 10 K per Fe^{2+}–Fe^{2+} interaction) [40], while for the $ZnFe_2O_4$ [22,23,28] and $Ni_{0.5}Zn_{0.5}Fe_2O_4$ [27] ferrites the induced antiferromagnetic coupling between A and B sites can be stronger (e.g. ~ -19 K [41] and as strong as ~ -45 K [42] per cation interaction). Moreover, it is possible that the cation-disordered distribution of Fe^{2+} and Ti^{4+} ions in ball-milled ilmenite leads to significant magnetic frustration, resulting in a reduced effective exchange coupling.

4. Conclusions

We have found that ball-milling of ilmenite reduces the crystallite size to around 20 nm and also results in cation disorder, but the hexagonal crystal structure is maintained. A small oxidation (corresponding to about 5–8% Fe^{3+} of the total Fe) was observed. The defects and cation disorder induced by ball-milling leads to a significant increase of the hyperfine field (up to around 40 T) of Fe^{2+}, but in contrast to some ball-milled ferrites, the Néel temperature is not significantly affected by ball-milling.

Acknowledgments

Fig. 5. Mössbauer spectra of ilmenite, ball-milled for 64 h. The spectra were obtained at the indicated temperatures.

References

[1] Y. Ishikawa, N. Saito, M. Arai, Y. Watanabe, H. Takei, J. Phys. Soc. Jpn. 54 (1985) 312.
[2] H. Kato, M. Yamada, H. Yamauchi, J. Phys. Soc. Jpn. 51 (1982) 1769.
[3] P.F. McDonald, A. Parasiris, R.K. Pandey, B.L. Gries, W.P. Kirk, J. Appl. Phys. 69 (1991) 1104.
[4] B.N. Warner, C. Terry, J.A. Morel, P.N. Shive, J. Geomagn. Geoelec. 23 (1971) 399.
[5] R.W. Grant, R.M. Housley, S. Geller, Phys. Rev. B 5 (1972) 1700.
[6] P. Robinson, R.J. Harrison, S.A. McEnroe, R.B. Hargraves, Nature 418 (2002) 517.
[7] S.A. McEnroe, P. Robinson, F. Langenhorst, C. Frandsen, M.P. Terry, T.B. Ballaran, J. Geophys. Res. 112 (2007) B10103.
[8] C. Frandsen, S. Mørup, S.A. McEnroe, P. Robinson, F. Langenhorst, Geophys. Res. Lett. 34 (2007) L07306.
[9] S.A. McEnroe, B. Carter-Stiglitz, R.J. Harrison, P. Robinson, K. Fabian, C. McCammon, Nat. Nanotechnol. 2 (2007) 631.
[10] S.A. McEnroe, R.J. Harrison, P. Robinson, U. Golla, M.J. Jercinovic, J. Geophys. Res. 106 (2001) 30523.
[11] T. Nagate, Nature 172 (1953) 850.
[12] Y. Ishikawa, S. Akimoto, J. Phys. Soc. Jpn. 12 (1957) 1083.
[13] R.M. Bozorth, D.E. Walsh, A.J. Williams, Phys. Rev. 108 (1957) 157.
[14] G. Shirane, S.J. Pickart, R. Nathans, Y. Ishikawa, J. Phys. Chem. Solids 10 (1959) 35.
[15] G. Shirane, D.E. Cox, W.J. Takei, S.L. Ruby, J. Phys. Soc. Jpn. 17 (1962) 1598.
[16] B.P. Burton, P. Robinson, S.A. McEnroe, K. Fabian, T.B. Ballaran, Am. Miner. 93 (2008) 1260.
[17] C. Frandsen, B.P. Burton, H.K. Rasmussen, S.A. McEnroe, S. Mørup, Phys. Rev. B 81 (2010) 224423.
[18] W.H. Butler, A. Bandyopadhyay, R. Srinivasan, J. Appl. Phys. 93 (2003) 7882.
[19] H. Hojo, K. Fujita, K. Tanaka, K. Hirao, Appl. Phys. Lett. 89 (2006) 142503.

[20] N. Naresh, R.N. Bhowmik, B. Ghosh, S. Banerjee, J. Appl. Phys. 109 (2011) 093913.

[21] A. Hamie, E. Popova, Y. Dumont, E. Chikoidze, B. Warot-Fonrose, B. Berini, N. Keller, Appl. Phys. Lett. 98 (2011) 232501.

[22] G.F. Goya, H.R. Rechenberg, J. Magn. Magn. Mater. 196–197 (1999) 191.

[23] J.Z. Jiang, P. Wynn, S. Mørup, T. Okada, F.J. Berry, NanoStruct. Mater. 12 (1999) 737.

[24] V. Sepelak, Ann. Chim. Sci. Mater. 27 (2002) 61.

[25] M. Hofmann, S.J. Campbell, H. Ehrhardt, R. Feyerherm, J. Mater. Sci. 39 (2004) 5057.

[26] V. Sepelak, I. Bergmann, S. Kipp, K.D. Becker, Z. Anorg. Allg. Chem. 631 (2005) 993.

[27] N. Ponpandian, A. Narayanasamy, C.N. Chinnasamy, N. Sivakumar, J.-M. Greneche, K. Chattopadhyay, K. Shindona, B. Jeyadevan, K. Tohji, Appl. Phys. Lett. 86 (2005) 192510.

[28] S. Deka, P.A. Joy, J. Nanosci. Nanotechnol. 8 (2008) 3955.

[29] D.J. Fatemi, V.G. Harris, V.M. Blomberg, J.P. Kirkland, J. Appl. Phys. 83 (1998) 6867.

[30] V. Sepelak, D. Schultze, F. Krumeich, U. Steinike, K.D. Becker, Solid State Ionics 141-142 (2001) 677.

[31] V. Sepalak, S. Indris, P. Heitjans, K.D. Becker, J. Alloys Compounds 434–435 (2007) 776.

[32] V. Sepelak, I. Bergmann, A. Diekmann, P. Heitjans, K.D. Becker, Rev. Adv. Mater. Sci. 18 (2008) 349.

[33] S. Ohara, K. Sato, Z. Tan, H. Shimoda, M. Ueda, T. Fukui, J. Alloys Compounds 504 (2010) L17.

[34] C. Li, B. Liang, J. Alloys Compounds 459 (2008) 354.

[35] Y. Chen, J.S. Williams, S.J. Campbell, G.M. Wang, Mater. Sci. Eng. A271 (1999) 485.

[36] C.J. Howard, R.J. Hill, AAEC (Now ANSTO) Report M112, Lucas Heights Research Laboratory, 1986.

[37] R.J. Harrison, S.A.T. Redfern, R.I. Smith, Am. Mineral. 85 (2000) 194.

[38] S. Mørup, J.Z. Jiang, F. Bødker, A. Horsewell, Europhys. Lett. 56 (2001) 441.

[39] G.K. Williamson, W.H. Hall, Acta Metall. 1 (1953) 22.

[40] R.J. Harrison, S.A. McEnroe, P. Robinson, B. Carter-Stiglitz, E.J. Palin, T. Kasama, Phys. Rev. B 76 (2007) 174436.

[41] V.G. Vologin, V.D. Parkhomenko, S.F. Dubinin, Yu.G. Chukalkin, B.N. Goshchitskii, S.K. Sidorov, V.V. Petrov, Phys. Status Solidi A 33 (1976) K83.

[42] X. Zuo, Y. He, A. Yang, S. Yan, B. Bernardo, V.G. Harris, C. Vittoria, J. Appl. Phys. 97 (2005) 10F104.

Spin orientation in titanium substituted hematite

Erik Brok[2,3], Cathrine Frandsen[2], Kim Lefmann[4], Suzanne McEnroe[5], Peter Robinson[5] and Richard Harrison[1]

[1]Department of Earth Sciences, University of Cambridge, Downing Street, Cambridge CB2 3EQ, U.K.

[2]Department of Physics, Technical University of Denmark, DK-2800, Kongens Lyngby, Denmark

[3]Center for Electron Nanoscopy, Technical University of Denmark, DK-2800, Kongens Lyngby, Denmark

[4]Nano-Science Center, Niels Bohr Institute, University of Copenhagen, Universitetsparken 5, DK-2100 Copenhagen Ø, Denmark

[5]Geological Survey of Norway, N-7491 Trondheim, Norway

Abstract(less than 800 word, no references) and keywords

Introduction

The ilmenite-hematite [xFeTiO$_3$-(1-x)Fe$_2$O$_3$] solid solution series has been studied extensively because of its complex and interesting magnetic properties and because of the possibility to utilize it in applications. Intermediate compositions are magnetic semiconductors (Ishikawa and Akimoto 1957, Ishikawa 1958) and could conceivably be utilized in spintronics devices (Butler et al. 2003; Fujii et al. 2004). The FeTiO$_3$ - Fe$_2$O$_3$ solid solution series is further interesting because it is a model system for the mineral hemo-ilmenite, which have been studied extensively because of its complex magnetic properties, and because it have been identified as an important contributor to anomalies in the geomagnetic field (McEnroe et al. 2001; Kletetschka et al. 2002), and possibly to the magnetic field of the planet Mars (McEnroe et al. 2004). Interresting properties of natural hemo-ilmenite samples include complicated exsolution structures, very large natural remanent magnetization and giant exchange bias (McEnroe et al. 2002, 2007; Robinson et al. 2002, 2004; Fabian et al. 2008).

In hematite between the Néel temperature of $T_N \approx 955$ K (Morrish 1994) and the Morin temperature of $T_M \approx 264$ K (Besser et al. 1967; Morin 1950) the Fe^{3+} spins are, apart from a small canting, ordered antiferromagneticly along the c-axis of the (nearly) hexagonal crystal structure. The spins are usually assumed to be within, or at least very close to, the basal plane (Morrish 1994, Shull et al. 1951). However, the symmetry of the system does allow for the spins to have an out-of-plane component, as will be discussed in the next section. This was realized by Dzyaloshinsky (1958) who used Landaus theory of phase transitions of the second kind to estimate the size of the out-of-plane angle to be only a tiny fraction of a degree. Below T_M the spins undergo the so-called Morin transition and are oriented close to the c-axis. However, substitution of even small amounts ($\approx 1\%$) of Ti completely suppresses the Morin transition (Besser et al. 1967; Morin 1950) .The majority of experiments have been consistent with a very small out-of-plane spin-angle (Flanders

1971). However, Tobler et al. (1981) have measured α = 3.9° in a synthetic sample, using Mössbauer spectroscopy (MS) and Parise et al. (2006) have measured an α of about 20° in a natural sample, with neutron powder diffraction (NPD), while Frandsen et al. (2011) have measured an out-of-plane angle large as α ≈ 70° in hematite nanoparticles mixed with NiO nanoparticles. Recently, Harrison et al. (2010) investigated the spin orientation in a natural hemo-ilmenite sample with complex exsolution structure, from Modum, Norway, with NPD, finding the spin to be tilted an angle of α ≈ 29.5° out of the basal plane. It is evident that the spin orientation in hematite above the Morin transition may not always be confined to the basal plane, and in particular the spin orientation in Ti-substituted hematite may vary with Ti content.

Here we investigate the spin-orientation in a natural hematite sample and in synthetic samples of solid solution [xFeTiO$_3$-(1-x)Fe$_2$O$_3$] with compositions x ≤ 0.40. We measure the out-of-plane spin-angle with NPD from room temperature to T_N, and use MS to investigate the distribution of spin angles in each sample. We find that the spin in all our hematite-ilmenite samples have a significant out-of-plane component corresponding to α from about 12° to approximately 23°. Surprisingly, even the pure hematite sample has a significant out-of-plane spin-angle of α ≈ 20°.

Group theory and crystallography

Magnetic ordering in hematite at temperatures $T_M < T < T_N$ can be described by a two-dimensional primary magnetic order parameter (Q_1, Q_2) corresponding to the active irreducible representation (mΓ_3^+) of the parent space group (R-3c). Different combinations of Q_1 and Q_2 lead to three possible magnetic space groups: C2/c for $Q_1 \neq 0$, $Q_2 = 0$; C2'/c' for $Q_1 = 0$, $Q_2 \neq 0$; and P-1 for $Q_1 \neq 0$, $Q_2 \neq 0$. The magnetic structure observed by experiment is the C2/c structure with $Q_1 \neq 0$ and $Q_2 = 0$. This structure is a canted antiferromagnet with parallel alignment of the moments within each (001) layer and nearly antiparallel alignment of moments in neighboring (001) layers

(indices refer to the parent hexagonal unit cell). The primary order parameter Q_1, places magnetic moments parallel to the (001) basal plane and nearly perpendicular to the diad (i.e. nearly perpendicular to an *a* crystallographic axis of the parent hexagonal unit cell). A degree of canting within the basal plane is permitted by the C2/c symmetry, such that moments are rotated by ~0.065° to create a weak ferromagnetic (WF) moment along the diad. A secondary irreducible representation (mΓ_1^+) is permitted within C2/c. By itself, mΓ_1^+ would give a strictly antiferromagnetic alignment of moments normal to the (001) basal plane (as observed for $T < T_M$). In combination with mΓ_3^+, the antiferromagnetic moments are rotated about the diad so that they lie at an angle, α, to the basal plane. Note that even when $\alpha \neq 0$, the canted WF moment still lies parallel to the diad and therefore in the basal plane. If we assign a secondary order parameter Q_3 to mΓ_1^+, then Q_1 and Q_3 are proportional to the in-plane and out-of-plane components of magnetic moments, respectively. Given the symmetry relationship between Q_1 and Q_3, it is permitted for these order parameters to couple bilinearly in the expansion of Gibb's free energy. In this case we would expect that Q_3 would vary linearly with Q_1. This proposition can be tested directly by Rietveld refinement of high-temperature NPD data.

Here we follow the crystallographic conventions and refinement procedures described in detail by Harrison et al. (2010). For technical reasons, refinements were performed in a non-standard A2/a setting of the monoclinic C2/c phase described above. For ease of comparison with the high-temperature hexagonal phase the unit cell parameters are presented here using a monoclinic pseudocell with volume equal to that of the high-temperature hexagonal phase: $a_m = (1/\sqrt{3})[210]_{hex}$, $b_m = [010]_{hex}$, $c_m = [001]_{hex}$, $\beta_m \sim 90°$, where $[abc]_{hex}$ refers to the axes of the hexagonal cell. Similarly the refined magnetic moments M_x and M_y in the monoclinic cell are converted to components parallel ($M_{\parallel}$) and perpendicular ($M_{\perp}$) to the basal plane of the hexagonal cell.

4

Methods

Samples

Synthetic powder samples of [xFeTiO$_3$-(1-x)Fe$_2$O$_3$] with nominal compositions of $x = 0.13$, 0.20, 0.35 and 0.40 were prepared by heating followed by rapid cooling of mixtures of Fe$_2$O$_3$ and TiO$_2$. (For details see *reference?*). A natural sample of hematite was obtained from the Sedgwick Museum of Earth Sciences, Cambridge, United Kingdom. The hematite sample was crushed and ground into a fine powder. We refer to these samples as ilm13, ilm20, ilm35, ilm40 and hem.

Neutron powder diffraction

We performed NPD experiments at the OSIRIS instrument at the ISIS spallation neutron source, Oxfordshire, UK and at the D20 instrument at the reactor source at Institut Laue Langevin, Grenoble, France. In both experiments the samples were mounted inside a furnace, providing a temperature range from room temperature to 1100°C (1373 K). The Néel temperatures of the Ti-containing samples are expected to be lower (Besser et al. 1967) than that of pure hematite ($\approx$ 955 K), and the available temperature range should thus allow us to obtain diffraction patterns from all samples at temperatures from hundreds of degrees below, to well above the magnetic phase transition. To minimize background we loaded the samples in vanadium cylinders with very thin walls.

We collected NPD patterns for the samples hem, ilm20, ilm35 and ilm40 at the OSIRIS instrument at ISIS. OSIRIS is a time-of-flight (TOF) spectrometer/diffractometer with a ring of detectors for diffraction placed around the incident beam covering a range of scattering angles 150°<2θ <171°. The accessible d-spacing range is from 0.8 Å to 20 Å with an optimal angular resolution of $\frac{\Delta d}{d} = 2.5 \times 10^{-3}$. With choppers running at a 25 Hz frequency, a 4 Å wide

wavelength range with minimal contamination of higher order neutrons is allowed to reach the sample. To obtain one diffraction pattern we performed 4 measurements with different relative phasings of the choppers in order to span the desired range of *d*-spacings. The four measurements are combined to a diffraction pattern that continuously covers *d*-spacings from approximately 0.72 Å to approximately 5.25 Å.

The ilm13 sample was measured at the high-flux powder diffractometer D20 at the ILL. With a neutron wavelength of 2.4 Å, and a take-off angle of 42° of the HOPG(002) monochromator the detector, covering 153.6°2θ , provided us with diffraction patterns in the *d*-spacing range 1.3 Å - 13.1 Å with a resolution on the order of $\frac{\Delta d}{d} = 10^{-2}$. While the resolution of D20 is inferior to that

of OSIRIS, the high flux at D20 enabled us to measure a diffraction pattern in a few minutes. It was therefore possible to measure a temperature series of closely spaced data points, from room temperature to far above the Néel temperature of the sample (≈ 560 °C), within one day.

Rietveld refinements

To obtain α from the diffraction patterns Rietveld refinements were performed, using the monoclinic model of hematite in the space group A112/a as described in Harrison et al. (2010). The GSAS program (Larson and von Dreele (1994)) was used for the refinements, with appropriate peak shape functions for TOF (OSIRIS) and constant wavelength (D20) data. The background was modeled with Chebyshev polynomials. In all refinements the cations were assumed to be fully disordered.

For all samples, weak lines in the diffraction patterns were identified as belonging to the structure of magnetite. Because of this magnetite impurity, a magnetite phase was added to the refinements for ilm20 and hem where the signal from magnetite was most significant. For the other

samples the impurity was negligible. For the magnetite phase a scale factor, the magnitude of the magnetic moment, and the unit cell parameters were refined.

For the vast majority of the diffraction patterns convergence in the refinements was achieved without problems. However, in a few cases it was necessary to reduce the number of refined parameters, or use Marquardt-damping to achieve convergence. This is almost inevitable when refining the magnetic model very close to T_N, where the magnetic peaks are vanishing.

For the OSIRIS data (ilm20, ilm35 and ilm40), the sample compositions (x) were determined from the refined unit cell volumes using the formula (see *reference?*)

$$V = 1.685\ x^2 + 10.823\ x + 301.740\ \ (x < 0.5)\ , \tag{1}$$

where V is the unit cell volume corresponding to the hexagonal cell. Refinement of the atomic occupation factors was not feasible because of correlation to the absorption factor for the TOF data. For the D20 data (ilm13) x was determined from refinement of the atomic occupation factors of Fe and Ti to the room temperature diffraction pattern, and then fixed at the obtained value in the remaning refinements.

The diffraction patterns of ilm13 taken above T_N was refined to the high-symmetry hexagonal unit cell. A magnetite phase was added for the refinements at the highest temperatures because we observed magnetite diffraction peaks growing in intensity.

Mössbauer spectroscopy

[57]Fe MS measurements at room temperature were performed on samples hem, ilm20, ilm35 and ilm40. To prepare samples for MS a small amount of material was ground to a fine powder in

7

an agate mortar and approximately 30 mg of it was mixed with boron nitride and placed in a plastic holder. The spectra were obtained with a constant acceleration Mössbauer spectrometer with a source of [57]Co in rhodium. The MS data was fitted with a number of sextets. Each sextet fit to data was constrained to have common line width for lines 1 and 6, 2 and 5, and 3 and 4 respectively. The area ratio between lines 1 to 6 was constrained to 3:2:1:1:2:3. The spectrometers were calibrated with a foil of α-Fe and the isomer shifts will be given relative to this calibration value.

<div align="center">**Results**</div>

Neutron powder diffraction

The room temperature diffraction patterns of the samples hem and ilm13 are shown in Figure 1. The positions of the two main magnetic peaks of hematite and the most intense of the peaks from the magnetite impurity are indicated. The difference in peak width in the two diffractograms is because of the much better resolution of OSIRIS as compared to D20. The refined model represents the data reasonably well, and the disagreements between model and measurement originate primarily from misfits of the peak profiles, which is a problem that can never be completely eliminated. For some samples the background was rather significant and nonuniform, which served to deteriorate the agreement between model and measurement. However, it is important to note that the background is rather flat, and well modeled in the d-spacing range close to two main magnetic peaks, which is the most significant for obtaining α.

A two-dimensional representation of the complete set of measurements of the ilm13 sample from room temperature to above 1200 K is displayed in Figure 2. All the most intense lines can be identified as belonging to the chemical or magnetic structure of hematite. The magnetic phase transition is clearly identified by the disappearance of the two main magnetic peaks ($2\theta \approx 30°$ and $2\theta \approx 33°$) at a Néel temperature of approximately $T_N \approx 805$ K. No intensity remains at the positions

8

of the magnetic hematite peaks above T_N, indicating that the assumption of cation disorder is justified. This was the case for all samples. The weak line at $2\theta \approx 27°$ can be identified as a magnetic reflection from magnetite and it completely disappears at the Curie temperature of magnetite (853 K). Weak lines identified as belonging to the chemical structure of magnetite achieve a significant gain in intensity at temperatures around 1100 K, indicating that in addition to an initial impurity of magnetite, part of the sample is reduced to magnetite during heating. The weak and broad line at $2\theta \approx 20°$ is from some other impurity or from the sample environment.

The Rietveld refinement of the room temperature diffraction data resulted in nonzero values of α for all samples. The most important results of the room temperature refinements are given in Table 1. The refined unit cell volume and corresponding composition are given together with the in-plane and out-of-plane magnetic moment ($M_\parallel$ and $M_\perp$) and the calculated spin-angle α. In all cases $M_\parallel$ is larger than $M_\perp$, but the size of $M_\perp$ is significant for all samples, giving a significant out-of-plane spin-angle α. The size of α varies from $11.1 \pm 1.9°$ for ilm13 to $22.8 \pm 0.5°$ for ilm35 and it does not seem to depend systematically on Ti-content. For the pure hematite sample $\alpha = 20.0 \pm 0.7°$.

The temperature dependence of $M_\parallel$ and $M_\perp$ for the samples hem, ilm13, ilm20 and ilm35 are shown in Figure 3. From room temperature until close to the Néel temperature there is a significant $M_\perp$ component. For the hem sample $M_\parallel$ and $M_\perp$ become zero almost simultaneously, while for the most Ti-rich samples (ilm20 and ilm35) $M_\perp$ clearly becomes zero before $M_\parallel$, indicating a reorientation of the spins close to T_N. For ilm13 the data allows for a spin reorientation, but the

uncertainties on the data close to T_N is large. Both components of the magnetic moment as a function of temperature was fitted to an expression of the form (see *reference?)*

$$M(T) = \sqrt{\frac{-a + \sqrt{a^2 + 4b\theta\left(\coth\left(\frac{\theta}{T_N}\right) - \coth\left(\frac{\theta}{T}\right)\right)}}{2b}},$$
(2)

where $\theta = 300$ K was kept fixed leaving a, b and T_N as fit parameters. The Néel temperature of each sample was determined from the fit to the $M_\parallel$-data because $M_\perp$ becomes zero before the total

moment. The model in Equation (2) works well until very close to T_N where the system shows critical behavior. Because of the critical behavior a finite intensity remains in the magnetic peaks at temperatures a few Kelvin above T_N. The saturation values of $M_\parallel$ and $M_\perp$ and the Néel temperatures

determined from the fit are given in Table 2. The Néel temperature is given as a function of composition in Figure 4, where also the results of Dunlop and Ozdemir (1997) are plotted for comparison.

In Figure 5 we show $M_\parallel$ versus $M_\perp$ for the same samples as in Figure 3. At low temperature

(large moment) the relationship between $M_\parallel$ and $M_\perp$ is reasonably well described by a linear fit as

indicated in the figure. This is consistent with the hypothesis that the secondary order parameter Q_3 couples linearly to the primary order parameter Q_1. However, as already discussed, $M_\perp$ becomes

zero before $M_\parallel$ for the Ti-containing samples, indicating a spin reorientation into the basal plane.

This of course means that the linear relationship between Q_3 and Q_1 is not maintained close to T_N. It

is noteworthy that even for the pure hematite sample the linear description does not fit the data very well, indicating a spin reorientation, even in pure hematite.

In Figure 6 (left) α is displayed as a function of the reduced temperature for all 5 samples. The spin reorientation discussed above is reflected in a decreasing α close to the Néel temperature. The uncertainty on α is very large close to T_N, but the tendency of decreasing α is systematic for all samples. For hematite there is a significant change in α between the first and the second point, which are measured at room temperature and at 400°C respectively. The point measured at 400°C seems somewhat anomalous especially given that this measurement is the only one where the refined moments deviate significantly from the fit to Equation (1) (see Fig. 4). The total moment as a function of reduced temperature is displayed in Figure 6 (right) for comparison.

In the experiment at D20 we obtained sufficient data above and below T_N to follow the transformation of the monoclinic unit cell to the high-symmetry hexagonal cell occurring simultaneous with the magnetic phase transition. The change in the unit cell parameters as a function of temperature can be seen in Figure 7. The unit cell parameters for the low-temperature monoclinic phase, a_m, b_m and c_m are given in the reference frame of the monoclinic pseudo-cell and can thus be compared directly to the unit cell parameters of the high-temperature hexagonal cell, a_h and c_h. As the temperature increases a_m and b_m converge towards the value of a_h at T_N. The slope of the curve does not change significantly at the phase transition, indicating that the strain associated with the phase transition is small. The same is true for the transformation of c_m to c_h. At high temperatures (above 1000 K) the slope of the a_h and c_h curves change. This change happens in the same temperature range where the intensity of the magnetite lines start to increase (see Fig. 2) and is probablu associated with the reduction of part of the sample to magnetite. Reduction of the ilm13 to magnetite may change the hematite-ilmenite composition, and in turn the unit cell volume. The transformation of the crystallographic β-angle from monoclinic $\beta_m \neq 90°$ to $\beta_h = 90°$ can be

followed in Figure 8. The value of β_m starts out at about 90.04° at room temperature and decreases to about 90.02° at 700-800 K. Close to the phase transition β_m deviates slightly back towards 90.04°. The magnetic peaks at low d-spacing are important for refining the unit cell, and the anomalous behavior of β_m may be ascribed to the vanishing of the magnetic peaks close to T_N. There is also an anomalous feature in the values of a_m, and b_m in the same temperature range, where the values start diverging, and this may be explained by the same effect.

Mössbauer spectroscopy

Room temperature Mössbauer spectra of hem, ilm20, ilm35 and ilm40 are shown in Figure 10. For the hem sample the spectrum consist of a well defined sextet with narrow lines as expected for pure hematite, whereas the spectra of the Ti-containing sample consist of sextets with much more narrow and asymmetric lines.

There is a small component (10 % of the spectral area) in the hem spectrum that can be ascribed to the magnetite impurity, also observed in the NPD data. The room temperature Mössbauer parameters of the hematite sextet obtained from fitting are: Hyperfine field $B_{hf} = 51.50 \pm 0.03$ T, isomer shift $IS = 0.370 \pm 0.001$ mm/s and quadrupole shift $\varepsilon = -0.094 \pm 0.001$ mm/s independent of whether or not the magnetite impurity is included in the fit. The quadrupole shift (ε) in the Mössbauer spectrum of hematite is sensitive to the angle the Fe^{3+} spins make with the hexagonal c-axis (90°-α), and the fact that the spectrum is well fitted with one symmetric sextet rather than two sextets with different ε indicates that the directions of the Fe^{3+} spins in the sample are grouped around one value of α, rather than being distributed into distinct domains with different spin-directions. In particular we can rule out a scenario with significant proportions of the spins being in the basal plane and along the c-axis respectively. The average value of α can be found from the quadrupole shift of the spectrum from (Morrish 1994)

12

$$\varepsilon = \varepsilon_0 (3 \cos^2(90^\circ - \alpha) - 1)/2, \tag{3}$$

where ε_0 depends on the quadrupole moment of the iron nucleus in the nuclear spin= 3/2 state, and on the electric field gradient along the c-axis. Tobler et al. (1981) have determined the value of ε_0 to 0.21 mm/s. With the measured quadrupole shift of -0.094 ± 0.001 mm/s this corresponds to $\alpha = 11^\circ$.

The much broader and asymmetric lines in the spectra of the Ti-containing samples can be understood because of introduction of a Fe^{2+} component in the spectrum plus a variation in environments for different nuclei depending on the proximity of Fe^{3+}, Fe^{2+} and Ti on the atomic sites surrounding the nucleus. The spectra of the Ti-contaning samples are reasonably well fitted with 4 sextets, where 3 have isomer shifts close to 0.4 mm/s, corresponding to Fe^{3+} and one with isomer shift close to 0.6 mm/s, corresponding to Fe^{2+}. The hyperfine fields of the Fe^{3+} sextets are in the range 47 T - 50 T, which is a few Tesla lower than expected for pure hematite at room temperature (probably due to Ti^{4+} substitution in the hematite structure). The hyperfine field of the Fe^{2+} sextet is 37 - 40 T in all samples. The quadrupole shifts of the Fe^{3+} sextets are in the range between -0.11 mm/s and -0.08 mm/s. For samples containing Ti Equation (3) cannot immediately be used to calculate α, as ε_0 is not expected to be the same as for pure hematite. The fact that the quadrupole shifts of all the Fe^{3+} sextets are close to -0.1 mm/s suggests that, like for hematite, the spin directions are grouped around some average angle, rather than two distinct populations of in-plane and out-of-plane spins.

Discussion

The Rietveld refinement of the NPD data tells us that there is a significant out of plane component of the hematite spins in both the sample of pure hematite ($\alpha = 20.0^\circ$) and in the samples

13

containing Ti ($\alpha = 11.1°$-$22.8°$). While there is a variation in the measured spin-angle α between samples it does not seem to depend systematically on Ti-content. At low temperatures the linear relationship between the primary order parameter Q_1 and the secondary order parameter Q_3 is confirmed by the experiments, but approaching T_N the linear relationship is not maintained as the spin reorients to be within the basal plane just before the magnetic phase transition.

In the refinements the system was assumed to be well described by the R-3C structure of hematite with no ordering of the Fe and Ti cations. Cation order would give rise to diffraction peaks from the R-3 structure of $FeTiO_3$ at the positions of the magnetic hematite reflections. These cation-order diffraction peaks should be visible above T_N, but no such lines were seen. While the NPD data thus exclude a long range ordering of the cations it is not possible to determine whether a short-range cation order exists. Frandsen et al (2010) suggested that for samples with ($x > 0.5$) 1-2 nm clusters of pure hematite exist within the $FeTiO_3$ matrix. We cannot rule out that small populations of similar clusters of $FeTiO_3$ exist within the hematite in our samples, as the diffraction peak of a small population of 1-2nm clusters would likely be to broad and weak to be seen. This type of short range cation order would however be of no significance for the determination of α from Rietveld refinement.

The diffraction patterns suffered from a rather large and nonuniform background. This does, however, not pose a great problem for the determination of α from the Rietveld refinement of the diffraction data, because α is in essence determined from the relative area of the (003) and (101) magnetic peaks at high d-spacing, where the background is rather flat and nicely modeled. For spins along the hexagonal c-axis ($\alpha = 90°$) the (003) peak would disappear completely, whereas the intensity of (003) relative to (101) would be largest if the spins were in the basal plane ($\alpha = 0°$). The two magnetic peaks measured at room temperature, for the hem sample, is given in Figure 11, together with refined models with different values of α. It is seen that the background is nicely

14

modeled in this *d*-spacing range, and that the agreement between model and experiment is good for $\alpha = 19.988°$ (the refined value). It is also seen that the models with other values of α, including $\alpha = 0°$ does not represent the data well.

The Mössbauer spectrum of the hem sample was well described by a sextet with narrow lines and isomer shift and hyperfine field as expected for pure hematite. The fact that the hematite spectrum is well described by a single sextet with narrow lines, rather than a distribution of sextets with different quadrupole shifts indicates that the hematite spins are not distributed into populations with different spin-angles, but grouped around some average value of α. The quadrupole shift in the Mössbauer spectrum of the hem sample gives $\alpha = 11°$ with the value of ε_0 measured by Tobler et al. (1981). There are considerable uncertainties in the determination of ε_0, and values in the range between 0.20 mm/s (Gee et al. 2004; Frandsen et al. 2011) and 0.22 mm/s (Artman et al. 1968) are used in the literature and these give considerable different values of α (8° and 13°). For the Ti-containing samples it is not immediately possible to determine α from the Mössbauer spectrum, but because the quadrupole shifts of the fitted Fe^{3+} sextets are very similar it seems very unlikely that the Fe^{3+} spins in the samples with Ti are distributed into domains with different α.

With NPD we find an out-of-plane spin angle of 20.0° in the pure hematite sample at room temperature, while the Mössbauer spectra indicates an angle of around 11°. Even though the Mössbauer result is not in agreement with the results of Rietveld refinement of the NPD data it does confirm that there is an appreciable out of plane component to the spin in the hematite sample. We do not have a satisfactory explanation for the discrepancy between the results of the two measurements, but note that the angle determined by Mössbauer spectroscopy depends on the value of ε_0 and also that there are other contributions to the quadrupole shift in the Mössbauer spectra of hematite than the spin direction, and it is not impossible that impurities or even strain in the natural sample can explain the lower value of the spin angle found with MS. In Rietveld refinement of the

NPD data the spin-angle is determined largely from the ratio of the intensities of the two main magnetic peaks, which are well fitted by the model. We therefore assume the value from the Rietveld refinement of the NPD data to be most reliable.

Our experiments show unambiguously that there is a significant out of plane spin-angle in all the investigated $FeTiO_3$-Fe_2O_3 samples, and even in the pure hematite sample. While the symmetry of the magnetic structure of hematite does not prohibit an out-of-plane spin-component, it is expected to be orders of magnitudes smaller than found in this work (Dzyaloshinsky 1958). The room temperature spin-angle of 20.0° in hematite fond in this work is thus surprising, even though it is consistent with the measurement of Parise et al. (2006). The spin-angle does not seem to depend systematically on Ti-content. Further our NPD experiments indicate a spin reorientation into the basal plane at temperatures close to T_N. The Mössbauer spectra reveal that the spins are distributed around an average angle, rather than in two discrete populations of spins in the basal plane and perpendicular to it.

Acknowledgments

References

Artman, J.O., Muir, A.H., and Wiedersich, H. (1968) Determination of the Nuclear Quadrupole Moment of Fe^{57m} from α-Fe_2O_3 Data. Physical Review, 173, 337.

16

Besser, P.J., Morrish, A.H., and Searle, C.W. (1967) Magnetocrystalline Anisotropy of Pure and Doped Hematite. Physical Review, 153, 632-642.

Butler, W. H., Bandyopadhyat, A., and Srinivasan, R. (2003) Electronic and Magnetic Structure of a 1000 K Magnetic Semiconductor: α-hematite (Ti). Journal of Applied Physics, 93, 7882.

Dzyaloshinsky, I. (1958). A Thermodynamic Theory of "Weak" Ferromagnetism of Antiferromangetics. Journal of Physics and Chemistry of Solids, 4, 241-255.

Fabian, K., McEnroe, S.A., Robinson P., and S hcherbakov, V.P. (2008) Exchange bias identifies lamellar magnetism as the origin of the natural remanent magnetization in titanohematite with ilmenite exsolution from Modum, Norway. Earth and Planetary Science Letters, 268, 339.

Flanders, P.J., (1972) Observation of a c-Axis Moment in α-Fe_2O_3. Journal of Applied Physics, 43, 2430-2435.

Frandsen, C., Burton, B.P., Rasmussen, H.K., McEnroe, S.A., and Mørup S. (2010) Magnetic clusters in ilmenite-hematite solid solutions. Physical Review B, 81, 224423.

Frandsen, C., Lefmann, K., Lebech, B., Bahl, C.R.H., Brok, E., Ancoña, S.N., Theil Kuhn, L., Keller, L., Kasama, T., Gontard, L.C., and Mørup S. (2011) Spin reorientation in α-Fe_2O_3 induced by interparticle exchange interactions in α-Fe_2O_3/NiO nanocomposites. Physical Review B, 84, 214435.

Fujii, T., Kayano, M., Takada, Y., Nakanishi, M., and Takada, J. (2004) Ilmenite-hematite solid solution films for novel electronic devices. Solid State Ionics, 172, 289-292.

Gee, S.-H., Hong, Y.K., Sur, J.C., Erickson, D.W., Park, M.H., and Jeffers, F. (2004) Spin Orientation of Hematite (α-Fe_2O_3) Nanoparticles During the Morin Transition. IEEE Transactions on magnetic, 40, 4, 2691-2693.

Harrison, R.J., McEnroe, S.A., Robinson, P., Carter-Stiglitz, B., Palin, E.J., and Kasama, T. (2007) Low-temperature exchange coupling between Fe_2O_3 and $FeTiO_3$: Insight into the mechanism of giant exchange bias in a natural nanoscale intergrowth. Physical Review B, 76, 174436.

Harrison, R.J., McEnroe, S.A., Robinson, P., and Howard, C.J. (2010) Spin orientation in a natural Ti-bearing hematite: Evidence for an out-of-plane component. American Mineralogist, 95, 974.

Ishikawa, Y., and Akimoto, S. (1957) Magnetic Properties of the FeTiO3-Fe2O3 Solid Solution Series. Journal of the Physical Society of Japan, 12, 1083-1098.

Ishikawa, Y. (1958) Electrical Properties of FeTiO3-Fe2O3 Solid Solution Series. Journal of the Physical Society of Japan, 13, 37-42.

Kletetschka, G., Wasilewski, P.J., and Taylor, P.T. (2002) The role of hematite-ilmenite solid solution in the production of magnetic anomalies in ground- and satellite-based data. Tectonophysics, 347, 167.

Larson, A.C. and von Dreele, R.B. (1994) General Structure Analysis System (GSAS). Los Alamos National Laboratory Report LAUR 86-748.

McEnroe, S.A., Robinson, P., and Panish, P.T. (2001) Aeromagnetic anomalies, magnetic petrology, and rock magnetism of hemo-ilmenite- and magnetite-rich cumulate rocks from the Sokndal Region, South Rogaland, Norway. American Mineralogist, 86, 1447.

McEnroe, S.A., Harrison, R.J., Robinson, P., and Langenhorst, F. (2002) Nanoscale haematite-ilmenite lamellae in massive ilmenite rock: an example of 'lamellar magnetism' with implications for planetary magnetic anomalies. Geophysical Journal International, 151, 890-912.

McEnroe, S.A., Skilbrei, J.R., Robinson, P., Heidelbach, F., and Langenhorst, F. (2004) Magnetic anomalies, layered intrusions and Mars. Geophysical Research Letters, 31, L19601.

McEnroe, S.A., Carter-Stiglitz, B., Harrison, R.J., Robinson, P., Fabian, K., and McCammon, C. (2007) Magnetic exchange bias of more than 1 tesla in a natural mineral intergrowth. Nature Nanotechnology, 2, 631.

Morin, F.J. (1950) Magnetic Susceptibility of αFe_2O_3 and αFe_2O_3 With Added Titanium. Physical Review, 78, 819-820.

Morrish, A.H. (1994) Canted Antiferromagnetism: Hematite, World Scientific, Singapore.

Parise, J.B., and Locke, D.R., Tulk, C.A., Swainson, I., and Cranswick, L. (2006) The effect of pressure on the Morin transition in hematite (alpha-Fe_2O_3). Physica B – Condensen Matter, 385, 391.

Robinson, P., Harrison, R.J., McEnroe S.A., and Hargreaves, R.B. (2002) Lamellar magnetism in the haematite-ilmenite series as an explanation for strong remanent magnetization. Nature, 418, 517.

Robinson, P., Harrison, R.J., McEnroe S.A., and Hargreaves, R.B. (2004) Nature and origin of lamellar magnetism in the hematite-ilmenite series. American Mineralogist, 89, 725-747.

Shull, C.G., Strauser, W.A., and Wollan, E. (1951) Neutron Diffraction by Paramagnetic and Antiferromagnetic substances. Physical Review, 83, 333-345.

List of Figure captions

Figure 1. Room temperature neutron powder diffraction patterns. (a) Ilm13 measured at D20. (b) Hem measured at OSIRIS.

Figure 2. Two-dimensional representation of the set of diffraction patterns of ilm13 taken at D20. The two lines at $2\theta \approx 30°$ and $2\theta \approx 33°$ are the main magnetic peaks. The weak lines that gain in intensity at temperatures above 1000 K are from the magnetite structure.

Figure3. Refined in-plane ($M_{\parallel}$) and out-of plane ($M_{\perp}$) moment as a function of temperature. The

solid lines are fits to Equation (2).

Figure.4 Néel temperature as determined from the fit to Equation (2) versus the determined sample composition.

Figure 5. Out-of-plane ($M_{\perp}$) versus in-plane moment ($M_{\parallel}$). The black line is a linear fit and the blue

line is the ratio of the fits of $M_{\perp}$ and $M_{\parallel}$ to Equation (2).

Figure 6. Left: Spin-angle as a function of the reduced temperature. Right: Total magnetic moment as a function of reduced temperature.

Figure 7. Unit cell parameters as a function of temperature.

Figure 8. The crystallographic β_m angle as a function of temperature.

Figure 9. Room temperature Mössbauer spectra of the samples hem, ilm20, ilm35 and ilm40. The hem spectrum is fitted with a single sextet for the hematite phase plus two sextets for the magnetite impurity. The spectra of the Ti-containing samples are fitted with 4 sextets and there is further added a small doublet component to the spectrum of ilm35 to account for some unknown phase.

Figure10. The (101) and (003) magnetic peaks of hematite measured at room temperature for the hem sample. The calculated pattern with α fixed at 0°, 10°, 19.988° and 30° are also displayed. The refined value is 19.988°.

Appendix (if any)

20

Tables

	$V(\text{Å}^3)$	x	$M_{\parallel}(\mu_B)$	$M_{\perp}(\mu_B)$	$M_{tot}(\mu_B)$	α (°)
hem	301.413 (5)	0	3.92 (4)	1.43 (4)	4.18 (2)	20.0 (7)
ilm13	303.72 (3)	0.178 (5)	4.00 (11)	0.79 (13)	4.08 (5)	11.1 (19)
Ilm20	304.05 (3)	0.207 (5)	3.82 (4)	1.21 (6)	4.01 (2)	17.6 (9)
Ilm35	305.62 (3)	0.341 (5)	3.22 (2)	1.35 (3)	3.49 (2)	22.8 (5)
Ilm40	306.18 (4)	0.387 (7)	3.48 ± 0.04	1.17 ± 0.05	3.67 ± 0.02	18.6 (9)

Table 1: Unit cell volume, composition, magnetic moment, and spin-angle from refinement of room temperature data (The data on ilm35 was actually measured at 50 °C). The composition of ilm13 is refined, whereas the composition of ilm20, ilm35 and ilm40 are calculated from the unit cell volume from Equation 1.

	$M_{\parallel}(\mu_B)$	$M_{\perp}(\mu_B)$	$M_{tot}(\mu_B)$	T_N (K)
hem	4.12	1.53	4.40	951 (2)
ilm13	4.25	0.92	4.35	805 (2)
ilm20	4.08	1.37	4.31	778 (2)
ilm35	3.54	1.52	3.85	676 (2)
ilm40	3.82	1.36	4.05	608 (2)

Table 2: Saturation moments and Néel temperatures from fit to Equation (2)

Figures

	$M_{\parallel}(\mu_B)$	$M_{\perp}(\mu_B)$	$M_{tot}(\mu_B)$	T_N (K)

Figure 1

Figure 2

Figure 3

Figure 4

Figure 5

Figure 6

Figure 7

Figure 8

Figure 9

Figure 10